Die erste Messung der Tensorstrukturfunktion b_1^{d} des Deuterons mit dem HERMES-Experiment

The First Measurement of the Tensor Structure Function b_1^{d} of the Deuteron with the HERMES Experiment

Den Naturwissenschaftlichen Fakultäten
der FRIEDRICH-ALEXANDER-Universität Erlangen-Nürnberg
zur
Erlangung des Doktorgrades

vorgelegt von

Caroline Riedl

aus Erlangen

Als Dissertation genehmigt von den
Naturwissenschaftlichen Fakultäten
der Universität Erlangen-Nürnberg

Tag der mündlichen Prüfung:	21. Juli 2005
Vorsitzender der Promotionskommission:	Prof. Dr. D. -P. Häder
Erstberichterstatter:	Prof. Dr. K. Rith
Zweitberichterstatter:	Prof. Dr. W. Weise

Contents

1 Spin physics in polarized DIS

1.1 Introduction: the spin puzzle and beyond

High energy experiments in the 1960s, 70s, and early 80s focussed on the measurement of form factors by elastic scattering in order to image the geometric shape of nuclei, and on finding new particles, like the opening of successively new quark channels at higher energies in electron-positron annihilation (J/ψ in the "November revolution" 1974), and the exchange bosons of the weak interaction ($W^{\pm}$ and Z^0 at CERN 1983). Still today the search for theoretically predicted particles goes on – like for the Higgs particle presumably generating the particle masses, or the exotic pentaquark. Before the wide field of spin physics opened in the end of the 1970s, experiments employed mainly unpolarized beams and targets. Then one of the most fundamental properties of elementary particles moved into the focus of interest: the spin of particles, which determines their symmetry behavior under space-time transformations.
Remarkable ideas and concepts associated with angular momentum have a long history in physics. With the emergence of quantum mechanics at the beginning of the 20th century, angular momentum ceased from satisfying human intuition when Niels Bohr postulated the orbital angular momentum of the electron in the hydrogen atom to be quantized in order to provide a concept for its stable states. Soon after, the spin as intrinsic angular momentum of particles entered the models and was confirmed to be quantized 1921 in the Stern-Gerlach experiment. Both the electron (described by the Dirac equation) and the nucleon were found to be spin-$\frac{1}{2}$ particles, although the latter is a complicated compound and thus a thoroughly different object than the point-like electron. The quarks inside the nucleon were identified as spin-$\frac{1}{2}$ particles when the relation which is today known as Callan-Gross equation was 1976 found to be satisfied for the nucleon [1]. In 1988, data from the EMC experiment at CERN [2] indicated that the value of $\frac{1}{2}\,\hbar$ for the spin of the nucleon cannot be obtained by a simple summation of the single spins of the quarks[1]. Their contribution to the nucleon spin does not exceed $\Delta\Sigma \equiv \sum_{q=u,d,s}(\Delta q + \Delta\overline{q}) = 10..20\%$. The *spin puzzle* was born: where does the rest of the nucleon spin originate from? Where do the other contributions "know" they are supposed to sum up to exactly $\frac{1}{2}$? The common decomposition of the nucleon spin $\langle S_z^N\rangle$ nowadays includes the gluonic spin ΔG as well as the orbital angular momenta of quarks and gluons, L_q and L_g, respectively[2]:

$$\langle S_z^N\rangle = \frac{1}{2}\,\Delta\Sigma + \Delta G + L_q + L_g = \frac{1}{2}\,. \tag{1.1}$$

[1] Hereafter, the convention $\hbar = c = 1$ is introduced.

[2] Note that the gluon contribution to the nucleon spin decomposes formally into $\Delta G + L_g$ only in the axial gauge.

After the findings of EMC, a wide variety of experimental approaches have been applied to the investigation of the spin structure of the nucleon. The experiments complement each other in their kinematic coverage and in their sensitivity to possible systematic uncertainties [3]. Typically, beams of polarized electrons or muons are subject to a collision with a fixed target of polarized hydrogen, deuterium, and heavier atoms. Concerning spin effects, the polarized ^{3}He looks very much like a polarized neutron which makes it an ideal polarized neutron target [4]. A large amount of polarized data has been collected within the last 15 years, most of it at SLAC, CERN and DESY. The possibility of generating stable polarized proton beams at high energies has recently opened the field of spin physics at collider facilities; the first collisions of polarized protons are being investigated at BNL with the future plan of a polarized electron-proton-machine (eRHIC).

Deep-inelastic scattering (DIS) with polarized charged lepton beams off polarized nuclei is the key tool in most of these experiments to unravel the nucleon spin. At a squared momentum transfer $Q^2 > 1$ GeV^2, the proton is not seen anymore as elementary particle and the lepton probes the inner structure of the nucleons by the emission of a spacelike virtual photon which is absorbed by a quark inside one of the nucleons, see Fig. 1.1. The nucleus is broken up, causing the struck quark and the target remnants to fragment into hadrons in the final state. In an *inclusive* measurement, the energy and scattering angle of only the scattered lepton are determined. The relevant kinematic variables are compiled in Tab. 1.1. From inclusive scattering, the nucleon spin structure function g_1 and the total quark helicity distribution $\Delta\Sigma$ can be determined. *Semi-inclusive* scattering involves the identification of one or more hadrons from the current jet in coincidence with the scattered beam lepton. Such measurements allow for the flavor separation of helicity distributions if the probability that a quark of certain flavor will fragment into a certain hadron is sufficiently well known (fragmentation functions). In *exclusive* measurements, the complete spectrum of the reaction particles is detected, often using missing mass techniques.

Recently, there has been strong interest in the so-called Generalized Parton[3] Distributions (GPDs) which are accessible through hard exclusive processes. The GPDs carry a wealth of information about the long-distance dynamics from the non-perturbative regime which can be cleanly separated from the hard calculable part of the interaction. In certain kinematic limits, the GPDs hold the electromagnetic form factors and the ordinary parton distribution functions from inclusive DIS. Moreover, they can provide a way to get access to the quarks' total angular momentum [5]. The cleanest tool to constrain GPDs from data is the hard photoproduction of a real photon (DVCS, deeply virtual Compton scattering) as it only involves a single hadron.

From a QCD analysis of the inclusive spin structure function, a substantially positive, however unconstrained contribution from ΔG was found. Semi-inclusive data from

[3] *Parton* is the generic term for nucleon constituent.

4-momenta of involved particles	
$k = (E, \underline{k})$, $k' = (E', \underline{k'})$	4-momenta of the inital, final beam lepton
$q = k - k' = (\nu, \underline{q})$	4-momentum of the spacelike virtual photon
$P \overset{\text{lab}}{=} (M, \underline{0})$, $P' = P + q$	4-momentum of the initial and final target nucleon
Lepton polar scattering angle	
θ	Angle in the lepton scattering plane between the incoming and outgoing lepton
Lorentz invariants	
$W^2 := (P+q)^2 \overset{\text{lab}}{=} M^2 + 2M\nu - Q^2$	Invariant squared mass of the photon-nucleon system
$Q^2 \equiv -q^2 := (k-k')^2$ $\overset{\text{lab}}{\approx} 4EE' \sin^2(\theta/2)$	Negative squared 4-momentum transfer from the lepton to the virtual photon
$\nu := (Pq)/M \overset{\text{lab}}{=} E - E'$	Energy transfer from the lepton to the virtual photon
$y := (Pq)/(Pk) \overset{\text{lab}}{=} (E-E')/E$	Fractional energy of the virtual photon
$x := Q^2/(2Pq) \overset{\text{lab}}{=} Q^2/(2M\nu)$	Bjørken scaling variable ($x = 2$ elastic, $x = 1$ quasi-elastic, $0 < x < 1$ inelastic scattering)
$E = \sqrt{\underline{p}^2 + m^2}$	Relativistic energy-momentum relation (energy E, 3-momentum $\underline{p}$, mass m)
$p = (E, \underline{p})$	General energy-momentum 4-vector
$p^2 = m^2$	Lorentz invariant squared mass (real photon: $p^2 = m^2 = 0$, virtual photon: $p^2 = m^2 \gtrless 0 \begin{smallmatrix}\text{timelike}\\ \text{spacelike}\end{smallmatrix}$)

Table 1.1: Kinematic variables in inclusive deep-inelastic scattering (deuteron target): from the 4-momentum P of the nucleon (with mass $M = 938$ MeV) in the target deuteron and the 4-momenta k and k' of the beam lepton (with initial energy E), a set of Lorentz invariants is derived, characterizing the interaction. Each two are independent due to two degrees of freedom in DIS (e.g. energy of scattered lepton, invariant mass of photon-nucleon-system). It is convenient to boost into the laboratory frame ("lab") as Hermes is a fixed target experiment. The given conditions justify to neglect (indicated by "$\approx$") the electron mass m_e with respect to the electron energies E and E'. Further kinematic factors are compiled in Tab. 1.2. Note that although these kinematic variables characterize a lepton-*deuteron*-reaction, the reference mass is the proton mass M (except for the elastic case where the deuteron does not reveal its inner structure at all): the object which is considered to break up is the proton, and not the deuteron.

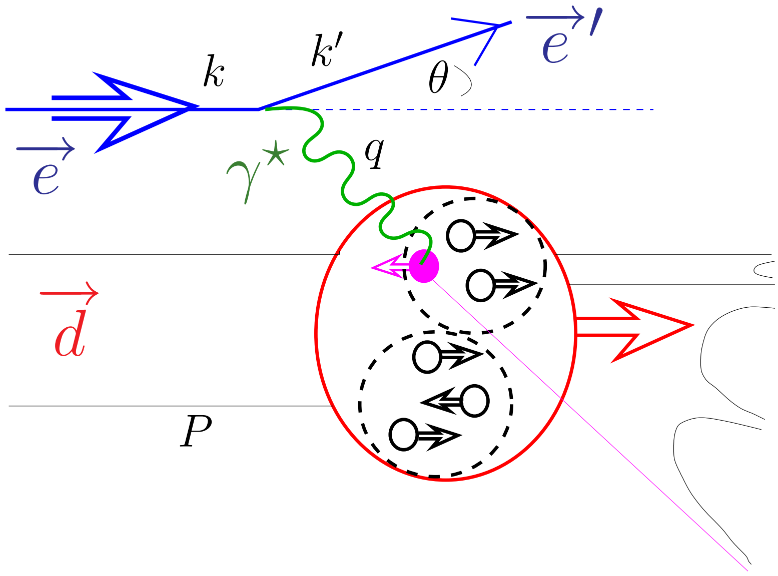

Figure 1.1: Illustration of a polarized deep-inelastic lepton-deuteron reaction in one-photon-approximation: a deuteron $\vec{d}$ with 4-momentum P is probed by a virtual photon $\gamma^\star$ with 4-momentum $q = k - k'$, where k and k' are the 4-momenta of the lepton before ($\vec{e}$) and after ($\vec{e}\,'$) it emitted the photon. The full circle inside the nucleus denotes the struck quark. In the center-of-mass system, the spin orienation of the struck quark has to be opposite to that of the incoming lepton due to angular momentum conservation.

photon-gluon-fusion and photoproduction of hadron pairs with high transverse momenta also indicate a positive gluon polarization [6].
Besides the quark momentum distribution $q(x, Q^2)$ and the quark helicity distribution $\Delta q(x, Q^2)$, another leading order distribution, the transversity distribution $\delta q(x, Q^2)$, is needed for the complete description of the partonic structure. By determining δq, the spin structure can be studied without a gluon contribution because there is no transverse equivalent to ΔG and thus δq does not mix with gluons under evolution. As δq is a chiral-odd object, it can due to helicity conservation not be observed in inclusive measurements, but requires e. g. semi-inclusive methods. The azimuthal asymmetry moment for a transversely polarized target, a rather new observable, allows for access to the quark orbital angular momentum L_q which is related to the transverse parton momenta. The so-called first Sivers moment of the π^+ has recently been found to be non-zero [7], which is an indication for $L_q \neq 0$. A recent review about transversity can be found in Ref. [8].
The structure of the nucleon is reviewed in Ref. [9]. An overview over the latest experimental achievements in spin physics and future facilities has been given in Ref. [10]. The results obtained by the Hermes experiment until the year 2000 are compiled in Ref. [11].

1.2 Appetizer: the Quark Parton Model

In the simple Quark Parton Model (QPM, Feynman 1969) [12], the cross section of the DIS reaction is interpreted as the incoherent sum of elastic scattering processes of leptons off quasi-free point-like constituents (partons[4]) of the nucleus (Fig. 1.2). The photon-parton interactions are considered to happen at such a short time scale that during the interaction the partons do not interact with each other. For data in a limited range of Q^2, this picture was confirmed experimentally[5]. In a frame where the nucleus

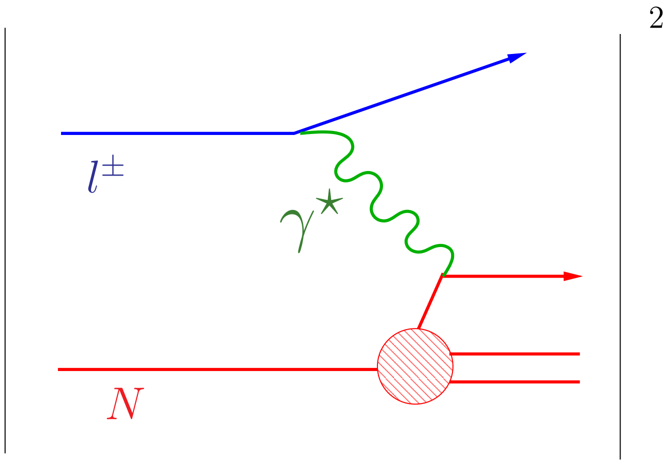

Figure 1.2: In the naive Quark Parton Model (QPM), the nuclear target N is considered to be a cloud of asymptotically free quarks with momentum probability distribution $q(x)$. One of the partons is scattered elastically by the beam lepton $l^\pm$ via the exchange of a virtual photon $\gamma^\star$. The symbolic square indicates that the observable (cross section) is proportional to the squared Feynman amplitude.

moves with large (infinite) momentum, the transverse momenta and rest masses of the partons can be neglected (infinite momentum frame) which is convenient for the interpretation of deep-inelastic scattering because then the structure of the nucleus can be considered to arise only from the longitudinal parton momenta, and the Bjørken scaling variable x is the nucleon's momentum fraction carried by the struck quark [13]. The partons have in general a distribution of momenta. The probability of finding a quark with a momentum fraction x in the interval $x + \mathrm{d}x$ and spin projection m_q inside a nucleus with spin quantum number m is denoted as quark density $q^m_{m_q}(x)$. As illustrated in Fig. 1.3 for the deuteron[6], the distributions are combined in order to distinguish the cases that the struck quark has the same (q^+, 2nd column) or opposite

[4]The electrically charged partons are identified as quarks, the neutral ones as gluons.
[5]Q^2-dependent corrections to the naive model of quasi-free partons are discussed below.
[6]The respective definitions of the quark densities q^+ and q^- also hold for the proton replacing $1 \rightarrow \frac{1}{2}$. There is no q^0. F_2 obtains thus the weighting factor $\frac{1}{2}$ instead of $\frac{1}{3}$, g_1 remains unchanged, and b_1 is not defined.

(q^-, 3rd column) spin orientation as the parent nucleus, or that the quark is in a $m = 0$ nucleus (q^0, right column) [14]. Due to parity conservation in the strong interaction, $q^{m=+1} = q^{m=-1} \equiv q^1$, thus there are only two independent quark densities q^0 and q^1. Their difference is proportional to the tensor structure function (see below).
The total cross section for electron scattering from a cloud of partons is the sum of all individual contributions q

$$\frac{\mathrm{d}^2\sigma}{\mathrm{d}Q^2\mathrm{d}\nu} = \sum_q \int \mathrm{d}x\, q(x) \left(\frac{\mathrm{d}^2\sigma}{\mathrm{d}Q^2\mathrm{d}\nu}\right)_q , \tag{1.2}$$

which is for unpolarized scattering usually parameterized as

$$\frac{\mathrm{d}^2\sigma}{\mathrm{d}Q^2\mathrm{d}\nu} = \frac{4\pi\alpha^2}{Q^4}\frac{E'}{E}\cos^2(\frac{\theta}{2})\frac{1}{\nu}F_2(x) + \sin^2(\frac{\theta}{2})\frac{1}{M}F_1(x), \tag{1.3}$$

introducing the spin-independent structure functions $F_1(x)$ and $F_2(x)$ measured in inclusive unpolarized deep-inelastic scattering. In the discussed framework, F_2 is for scattering off spin-$\frac{1}{2}$ partons connected to F_1 through the Callan-Gross relation (1969) [1]

$$2xF_1(x) = F_2(x). \tag{1.4}$$

Relation 1.4 corresponds to a vanishing longitudinal structure function (F_L) in the Bjørken limit, $0 \equiv F_L = F_2 - 2xF_1$, which is satisfied since massless quarks do not couple to longitudinal photons (helicity 0). Measurements support the idea that spin-$\frac{1}{2}$ partons are dominant. For spin-0 partons, $F_1 \equiv 0$. F_1 has an intuitive interpretation in the QPM as a measure for the quark momentum distribution (see Fig. 1.3). First experimental indications of the Q^2-independence of F_2 (scaling, Bjørken 1969 [12]) led to the conclusion that quarks are point-like objects. To satisfy the scenario that the virtual photon scatters off point-like partons, the deep-inelastic (Bjørken or scaling) limit is assumed with $\gamma^2 = \frac{Q^2}{\nu^2} \to 0$ (with $Q^2 \to \infty$, $\nu \to \infty$ while x fixed)[7].
The spin-dependent structure function $g_1(x)$ measures the difference in the distributions of quarks which have their spin aligned or anti-aligned to the parent nucleus, respectively, as indicated in the figure. In the simple QPM, $g_2 \equiv 0$ since it is related to transverse degrees of freedom [15] which are absent in this model. For polarized spin-1 targets, in addition the tensor structure function $b_1(x)$ arises, measuring the difference in the quark momentum distributions of an $|m| = 1$ and $m = 0$ target. b_1 depends only on quark spin averaged distributions.

1.3 Cross section parameterization

QCD. The theory of strong interactions, quantum chromodynamics (QCD), extends the naive free QPM by allowing interactions between the partons, the quarks (q) and

[7] Then photon and beam direction coincide.

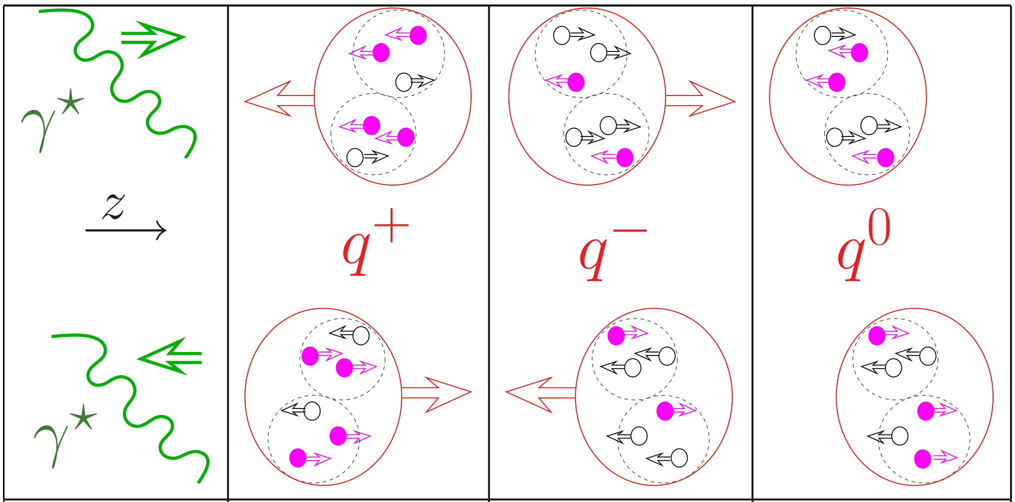

q^+, q^-, q^0	$q^+ \equiv q^{-1}_{-\frac{1}{2}} + q^{+1}_{+\frac{1}{2}}$	$q^- \equiv q^{+1}_{-\frac{1}{2}} + q^{-1}_{+\frac{1}{2}}$	$q^0 \equiv q^0_{-\frac{1}{2}} + q^0_{+\frac{1}{2}}$
q^1	$q^1 \equiv \frac{1}{2}\,(q^+ + q^-)$		
q F_1	$q \equiv q^+ + q^- + q^0$ $F_1 = \frac{1}{3}\,\sum_q e_q^2 q$		
Δq g_1	$\Delta q \equiv q^+ - q^-$ $g_1 = \frac{1}{2}\,\sum_q e_q^2 \Delta q$		
θq b_1	$\theta q \equiv \frac{1}{2}\,(q^0 - q^1)$ $b_1 = \sum_q e_q^2 \theta q$		

Figure 1.3: Illustration of the QPM (deuteron case), top: quarks which can be struck by the virtual photon $\gamma^\star$ with fixed helicity (very left column) are indicated by a full circle, a double arrow $\Rightarrow$ indicates the spin projection of the particles which is denoted by m for the nucleus and by m_q for the quark. Reflection symmetry in the xz-plane implies each quark density $q^m_{m_q}$ in the top row to be identical to the respective density in the bottom row. Bottom: in the QPM, the inclusive structure functions F_1, g_1 and b_1 are related to linear combinations of quark densities. The sums run over all participating quark and anti-quark flavors weighted with the square of the corresponding quark charge e_q in units of the elementary charge. q is the spin-averaged quark distribution, Δq the quark spin (helicity) distribution, and θq the quark tensor distribution. The quark distributions and structure functions depend on x in the simple QPM (scaling) and catch an additional Q^2-dependence in the QCD improved model (scaling violation).

gluons (g), that is not only q-q interactions, but also g-q and g-g interactions due to its construction as non-Abelian gauge theory [16]. These QCD radiative effects dynamically introduce a QCD-scale violating Q^2-dependence of the measured cross section and thus the structure functions[8] and cause the coupling constant of the strong interaction $\alpha_s \sim 1/\ln(Q^2/\Lambda^2)$ to be "running"[9]: the behavior of the partons for $Q^2 \to \infty$ is denoted as asymptotic freedom ('t Hooft 1972), as then $\alpha_s \to 0$, allowing for convergence of the perturbation series. For the other kinematic shore, $Q^2 \to 0$, partons are said to be confined with $\alpha_s \to \infty$. In 2004, the Nobel prize in physics was awarded to Gross, Politzer and Wilczek for the discovery of asymptotic freedom in the theory of the strong interaction.

Cross section and structure functions. In DIS of a charged lepton off a nucleon, the differential cross section for one-photon exchange (Born approximation) can be expressed as the contraction of a leptonic current tensor $L^{\mu\nu}$ and a hadronic tensor $W^{\mu\nu}$:

$$\left.\frac{\mathrm{d}^2\sigma}{\mathrm{d}E'\mathrm{d}\Omega}\right|_{\mathrm{Born}} = \frac{\alpha^2}{2MQ^4}\frac{E'}{E}L_{\mu\nu}W^{\mu\nu} \; . \tag{1.5}$$

The leptonic tensor $L^{\mu\nu}$, describing the emission of the virtual photon, is exactly calculable from QED due to the point-likeness of the lepton. $L^{\mu\nu}$ can be decomposed into a symmetric[10] (denoted by { }) and an anti-symmetric (denoted by [ ]) part,

$$L^{\mu\nu} = L^{\{\mu\nu\}}(k,k') + iL^{[\mu\nu]}(k,k',s), \tag{1.6}$$

leaving the symmetric part *in*dependent of the lepton-spin s (k, k' are the 4-momenta of the ingoing and outgoing lepton).
According to the optical theorem, the imaginary part of the forward scattering Compton amplitude is proportional to the hadronic tensor $W^{\mu\nu}$ which describes the absorption of the virtual photon by the target. It contains the *a priori* unknown non-perturbative structure of the nucleon and can be linearly decomposed into dimensionless Lorentz invariant structure functions. Their number can be determined by counting all possible helicity amplitudes for the virtual Compton scattering process $\gamma^\star_{h_1} + \mathrm{target}_{H_1} \to \gamma^\star_{h_2} + \mathrm{target}_{H_2}$ that are independent of each other after symmetry considerations (time reversal and parity) [14], [17], see Fig. 1.4 for illustration. In the

[8]Illustration: a virtual photon with certain Q_1^2 and fixed ν which interacts with a parton probes the nucleus with a resolution $\sim 1/|\underline{q}_1| = 1/\sqrt{Q_1^2+\nu^2}$. If the photon had probed the same parton at $Q_2^2 > Q_1^2$ and and thus higher resolution $\sim 1/\sqrt{Q_2^2+\nu^2}$ and the parton for example had radiated a gluon not visible at Q_1^2, the photon would have effectively interacted with a parton carrying less momentum.

[9]The quoted expression for α_s holds for leading order QCD. $\Lambda \approx 250$ MeV is the only free parameter in QCD.

[10]Concerning $\mu \leftrightarrow \nu$.

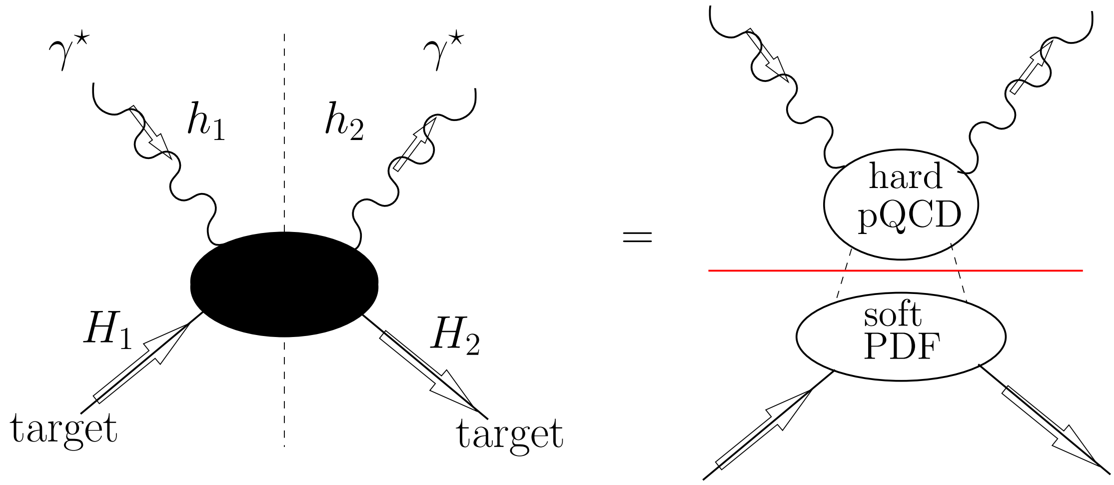

Figure 1.4: Left: definition of forward helicity amplitudes for Compton scattering off a polarized target with initial and final helicity H_1 and H_2, respectively, and corresponding photon helicity h_1 and h_2. Right: illustration of the factorization theorem. The helicity amplitudes are calculated under the assumption that the hard calculable and soft non-perturbative part of the DIS interaction can be separated.

spin-$\frac{1}{2}$ case, this leads to four (F_1, F_2, g_1, g_2), in the spin-1 case to eight (in addition, b_1, b_2, Δ and b_3) independent structure functions. Decomposing the hadronic tensor analogously to $L^{\mu\nu}$ in Eq. 1.6, the spin-independent structure functions F_1 and F_2 fall to its symmetric part as well as the b_i and Δ, whereas g_1 and g_2, being sensitive to the target spin, to the anti-symmetric part (the b_i and Δ, however, depend through momentum terms implicitly on the target spin):

$$W^{\mu\nu} \;=\; W^{\{\mu\nu\}}(F_1, F_2) + iW^{[\mu\nu]}(g_1, g_2) + W^{\{\mu\nu\}}(b_1, b_2, \Delta, b_3). \tag{1.7}$$

As the mixed contributions between symmetric and anti-symmetric components fall away by contracting the two tensors in Eq. 1.5, there is no product term between the symmetric hadronic tensor which depends on the b_i and Δ, and the anti-symmetric, beam-spin dependent leptonic part in the cross section:

$$\text{Inclusive cross section} \sim L_{\{\mu\nu\}}W^{\{\mu\nu\}}(F_1, F_2, b_1, b_2, \Delta, b_3) + iL_{[\mu\nu]}W^{[\mu\nu]}(g_1, g_2). \tag{1.8}$$

The first term in Eq. 1.8 corresponds to the spin-averaged part of the cross section, the second term to the spin-dependent part, involving both the lepton's and nucleon's polarization vectors. Thus, for the measurement of g_1 and g_2, a polarized lepton beam is required, the other structure functions are not sensitive to the lepton spin and can therefore be measured using an unpolarized beam[11]. The explicit form of $W^{\mu\nu}$ and $L^{\mu\nu}$

[11]If the beam *is* polarized, however, then it is preferable to average the cross sections for target spin parallel and anti-parallel to the beam spin in order to avoid contamination by g_1.

and the resulting differential cross section can e. g. be found in Ref. [18].
The structure functions can be calculated using an expansion (OPE[12]) in terms of the twist of the participating operators[13] which boils down to a $1/\sqrt{Q^2}$ expansion [18]. The structure functions of leading twist are F_1, F_2, g_1, b_1, b_2, and Δ. Except for Δ (see Sec. 1.5), they have an interpretation in the partonic picture, respectively are related to such a function by a CALLAN-GROSS-like equation, and they are derived from helicity-conserving COMPTON amplitudes ($H_1 = H_2$ and $h_1 = h_2$). g_2 and b_3 are of higher twist and contain helicity-flip amplitudes.

Factorization theorem, convolution model. An often used tool for drawing information out of a DIS process is the factorization theorem for high-energy scattering: the lepton-nucleus interaction is *assumed* to split (factorize) into two processes:
1.) The parton residing inside the nucleus absorbs the virtual photon. 2.) The fragments propagate into the final state without interaction or interference. The measured cross section σ is then obtained as the convolution integral over the contributions from 1., the photon-parton scattering as hard calculable, short distance process described by $\widehat{\sigma}$, and 2., the hadronization described by a soft non-perturbative, long range PDF[14] p_q [16]:

$$\sigma(x, Q^2) = \sum_q \int_x^1 \frac{\mathrm{d}z}{z} \widehat{\sigma}(z, Q^2, \mu^2) p_q(\frac{x}{z}, Q^2, \mu^2), \tag{1.9}$$

where the factorization scale μ^2 (in units of GeV^2) defines the boundary between the soft and the hard process, and q is the parton flavor. See Fig. 1.4 for illustration.

Scaling violation and next-to-leading order QCD. With more and more precision results from the various DIS experiments covering a wide range in Q^2 ($\sim$ 1-20000 GeV^2 for unpolarized and $\sim$ 0.03-50 GeV^2 for polarized data), a slight Q^2-dependence of F_2 and g_1 was observed. This scaling violation agrees with the predictions of QCD [13]. As shown in Fig. 3.17, $F_2(x, Q_0^2)$ begins to rise at small x-BJØRKEN with increasing Q_0^2. The reason is the depletion of partons with high momenta and an increase of those with low momenta as more and more phase space for QCD radiative processes becomes available. Not only in order to be able to compare data from different facilities[15], but also to calculate integrals of the structure functions (moments) and to parameterize the data (QCD fits) [3], this Q^2-dependence of g_1 has to be modelled.
In leading order QCD, the expression for g_1 in Fig. 1.3 still holds if $\Delta q(x) \rightarrow \Delta q(x, Q^2)$.

[12] **O**perator **P**roduct **E**xpansion with the WILSON coefficients as expansion coefficients.
[13] Twist = dimension minus spin of the operator.
[14] **P**arton **D**ensity **F**unction.
[15] The experimental acceptance imposes a certain correlation between x and Q^2.

OPE with next-to-leading order QCD corrections, however, delivers an expression for $g_1(x, Q^2)$ into which enters in addition to the quark helicity distribution Δq the spin-dependent gluon distribution ΔG which thus affects the Q^2-evolution of g_1. Each of these PDFs is convoluted with the Wilson expansion coefficients in an expression similar to Eq. 1.9. The expansion coefficients correspond to the calculable polarized photon-quark and photon-gluon hard scattering part ($\widehat{\sigma}$ in Eq. 1.9). However, this factorization cannot be defined unambiguously, causing the PDFs to be factorization scheme ("convention") dependent, but straightforward transformable into each other. As physical observable, g_1 is scheme independent. The Q^2-evolution of the polarized PDFs for a chosen scheme is expressed by a closed set of integro-differential equations (DGLAP[16] equations) which include one of the fundamental predictions of QCD: for a PDF measured at arbitrary Q_0^2, the PDF at any Q^2 is calculable.
The fraction of the nucleon spin carried by the quarks $\Delta\Sigma$ is then obtained by integrating the quark spin distributions over x (q runs over all contributing quark and anti-quark flavors):

$$\Delta\Sigma = \int_0^1 \mathrm{d}x \sum_q \Delta q(x). \tag{1.10}$$

This relation also holds in the QPM where $\Delta\Sigma$ is proportional to the first moment of g_1.

1.4 Inclusive asymmetries and structure functions

From the four independent virtual photon amplitudes in photon-nucleon scattering off a spin-$\frac{1}{2}$ target, three ratios are constructed. The asymmetry between the two helicity amplitudes $\sigma^T_{\frac{1}{2}}$ and $\sigma^T_{\frac{3}{2}}$ which describe the absorption of transversely polarized virtual photons (helicity ± 1)[17] is given [11] by

$$A_1 = \frac{\sigma^T_{\frac{1}{2}} - \sigma^T_{\frac{3}{2}}}{\sigma^T_{\frac{1}{2}} + \sigma^T_{\frac{3}{2}}}, \tag{1.11}$$

and the asymmetry arising from an interference between longitudinal (helicity 0) and transverse virtual photon-nucleon amplitudes σ^{TL} by

$$A_2 = \frac{\sigma^{TL}_{\frac{3}{2}}}{\sigma^T_{\frac{1}{2}} + \sigma^T_{\frac{3}{2}}}. \tag{1.12}$$

[16] Dokshitzer-Gribov-Lipatov-Altarelli-Parisi.

[17] The indices $\frac{1}{2}$ resp. $\frac{3}{2}$ are the projections of the total angular momentum of the photon-nucleon system along the incident photon direction. The two cases correspond to the q^+ resp. q^- configuration in Fig. 1.3.

$D = \dfrac{y\left((1+\frac{\gamma^2 y}{2})(2-y) - \frac{2y^2 m_e^2}{Q^2}\right)}{y^2(1-\frac{2m_e^2}{Q^2})(1+\gamma^2) + 2(1+R)(1-y-\frac{\gamma^2 y^2}{4})} \sim y$	Polarization transfer from the lepton beam to the virtual photon
$\gamma = \sqrt{Q^2}/\nu = (2Mx)/\sqrt{Q^2}$	
$\eta = \dfrac{\gamma(1-y-\frac{\gamma^2 y^2}{4} - \frac{y^2 m_e^2}{Q^2})}{(1+\frac{\gamma^2 y}{2})(1-\frac{y}{2}) - \frac{y^2 m_e^2}{Q^2}}$	

Table 1.2: Further kinematic factors in inclusive DIS: the depolarization factor D and η take into account terms depending on m_e^2/Q^2 which cannot be neglected for the low-Q^2 region [19].

The denotation for the virtual photon's polarization state "longitudinal" or "transverse" refers to the electric and magnetic field vectors and not to the spin direction, for which the notation is opposite. A real photon with invariant mass $m^2 = 0$ is purely transversely polarized (i. e. helicity ± 1), a virtual photon with $m^2 \gtrless 0$, however, has also longitudinal admixtures with helicity 0. Thus, the ratio of the longitudinal amplitude σ^L and the transverse amplitudes, which is related to the spin-independent structure functions $F_1(x, Q^2)$ and $F_2(x, Q^2)$ by[18]

$$R(x,Q^2) = 2\frac{\sigma^L}{\sigma^T_{\frac{1}{2}} + \sigma^T_{\frac{3}{2}}} = (1+\gamma^2)\frac{F_2(x,Q^2)}{2xF_1(x,Q^2)} - 1, \tag{1.13}$$

is non-zero in deep-inelastic scattering. From Eq. 1.13 results the (modified) Callan-Gross relation for F_2 (compare to Eq. 1.4 which is only satisfied for lowest-order QCD without radiative effects):

$$2xF_1(x,Q^2) = \frac{1+\gamma^2}{1+R}F_2(x,Q^2). \tag{1.14}$$

The virtual photon absorption asymmetries are related to the nucleon spin structure functions $g_1(x, Q^2)$ and $g_2(x, Q^2)$ (see Tab. 1.2 for the following kinematic factors D, γ and η) by

$$A_1(x,Q^2) = \frac{g_1(x,Q^2) - \gamma^2 g_2(x,Q^2)}{F_1(x,Q^2)}, \tag{1.15}$$

$$A_2(x,Q^2) = \gamma\frac{g_1(x,Q^2) + g_2(x,Q^2)}{F_1(x,Q^2)}. \tag{1.16}$$

[18] $R \to 0$ strongly indicates spin-$\frac{1}{2}$ partons to be dominant rather than spin-1, $R \to \infty$ favors spin-1.

In an experiment, actually $A_\parallel$ is measured, the asymmetry which probes the question how many more quarks have their spin anti-aligned to the parent nucleus' one, than have it aligned (see Eqs. 2.15 and 2.19). $A_\parallel$ is a superposition of the two virtual photon absorption asymmetries:

$$A_\parallel = D(A_1 + \eta A_2). \tag{1.17}$$

Then the ratio g_1/F_1 can be determined by using Eqs. 1.15-1.17:

$$\frac{g_1}{F_1} = \frac{1}{1+\gamma^2}\left(\frac{A_\parallel}{D} + (\gamma - \eta)A_2\right). \tag{1.18}$$

At least some knowledge about the magnitude of A_2 is required for an unambiguous determination of g_1 from the measured cross section. The spin-dependent structure function g_1 is usually extracted by multiplying the measured ratio from Eq. 1.18 by F_1 which has been obtained via Eq. 1.14 from a parameterization of world data on F_2:

$$g_1(x, Q^2) = \left(\frac{g_1}{F_1}\right)(x, Q^2) \cdot F_1(x, Q^2) \tag{1.19}$$

Recent results from g_1 measurements and moments are for example compiled in Ref. [3]. The tensor asymmetry A_{zz} is the inclusive cross section asymmetry for a spin-1 target (like the deuteron) which compares the spin states $|m| = 1$ and $m = 0$ (see Eqs. 2.16 and 2.20). The measurement of the tensor asymmetry allows to extract the ratio b_1/F_1:

$$\frac{b_1}{F_1} = -\frac{3}{2}A_{zz}. \tag{1.20}$$

The tensor structure function b_1 is obtained from the measured ratio b_1/F_1 and world data on F_1:

$$b_1(x, Q^2) = \left(\frac{b_1}{F_1}\right)(x, Q^2) \cdot F_1(x, Q^2). \tag{1.21}$$

Similarily to F_1 and F_2 in Eq. 1.14, b_1 and b_2 are related to each other by

$$2xb_1(x, Q^2) = \frac{1+\gamma^2}{1+R} b_2(x, Q^2). \tag{1.22}$$

1.5 The tensor structure function of the deuteron

The deuteron. The deuteron is a rather dilute neutron-proton bound state with a binding energy of only 2.2 MeV. Among possible nuclear targets, it is the best testing ground for the precise description of nucleon-nucleon interaction since its wave function $|\psi^{\rm d}\rangle$ is known far better than that of any other nucleus. It is a superposition of (primarily) an S-state and a 4% admixture of a D-state, $|\psi^{\mathrm{d}}\rangle = 0.98\,|^3\mathrm{S}_1\rangle + 0.20\,|^3\mathrm{D}_1\rangle$. This deviation of the deuteron shape from a sphere is manifest in a non-vanishing electromagnetic quadrupole moment and in the finding that its magnetic moment $\mu^{\mathrm{d}} = 0.857\mu^{\mathrm{N}}$ is slightly smaller than the sum of the proton and neutron magnetic moments. The D-state admixture is accounted for by a component proportional to $(3\cos^2\theta - 1)$ in the nucleon-nucleon interaction [13]. This so-called tensor force is provided by one pion exchange.

In deep-inelastic scattering, the surrounding nuclear medium is known to have an impact onto the momentum distribution of the quarks (EMC effect [2]). Significant deviations from the idea that the nucleus is a simple compound of nucleons which are interacting via meson exchange are found for heavy nuclei, delivering e. g. a structure function ratio $F_2^{\mathrm{Ca}}/F_2^{\mathrm{d}} < 1$ for $x \lesssim 0.05$ [20]. Also for the kinematic region $0.3 < x < 0.8$, this ratio is found to be smaller than 1 which leads to the conclusion that valence quarks in the nucleus have a lower $\langle x\rangle$ than those in a free nucleon [21]. The missing energy-momentum is supposed to be made up by nuclear excess pions in the nucleus in addition to the pionic field associated with a free nucleon with an extra contribution to F_2^A of the nucleus for small x.

For the weakly bound deuteron, these nuclear effects in unpolarized scattering turn out to be not yet relevant, allowing to write the spin-independent structure function F_2^{d} as the average of the F_2 of the proton and the neutron:

$$F_2^{\mathrm{d}} = \frac{F_2^{\mathrm{p}} + F_2^{\mathrm{n}}}{2}. \tag{1.23}$$

The corresponding relation does not hold for the spin-dependent structure function g_1 due to the fact that the deuteron and the interacting nucleon can be polarized in opposite directions if the deuteron is in a D-state (at a probability of ω_{D}) [17]:

$$g_1^{\mathrm{d}} = (1 - \frac{3}{2}\omega_{\mathrm{D}})\frac{g_1^{\mathrm{p}} + g_1^{\mathrm{n}}}{2}. \tag{1.24}$$

Through Eq. 1.24, g_1^{n} of the neutron can be determined from the spin structure functions of the proton and the deuteron, overcoming the lack of a free neutron target.

Already polarized *elastic* scattering of electrons off the deuteron [22] reveals an additional degree of freedom with respect to the case with the proton as target. For such a spin-1 target, there are three possible values for the spin quantum number m (one more than for the proton). The $m = \pm 1$ state has a dumbbell shape, whereas in the $m = 0$ state, the deuteron exhibits a toroidal shape [23]. It is a long-known effect that the total cross section strongly depends on the polarization state of the deuteron, even if the beam is unpolarized [24], [25]. From polarization asymmetry measurements, the vector and tensor analyzing powers can be extracted and from these the three electromagnetic form factors of the deuteron (electric charge $F_C(Q)$, electric quadrupole $F_Q(Q)$ and magnetic dipole $F_M(Q)$) [26].

Similarily, *deep-inelastic* scattering from a polarized spin-1 target yields qualitative new information which is not available in the spin-$\frac{1}{2}$ case. As mentioned in Sec. 1.3, for a spin-1 target four additional (as compared to the spin- $\frac{1}{2}$ case) independent structure functions are needed to parameterize the deep-inelastic cross section. Of these, the leading twist functions $b_1(x,Q^2)$ and $b_2(x,Q^2)$ are related to each other by the Callan-Gross-like relation Eq. 1.22. In the QPM (Sec. 1.2), b_1 is expressed as

$$b_1(x,Q^2) = \frac{1}{2}\sum_q e_q^2 \left(q^0(x,Q^2) - q^1(x,Q^2)\right), \tag{1.25}$$

thus it does not depend on the quark spin, but on the hadron spin ($|\,m\,| = 0,1$). Studies on the tensor structure function of spin-1 hadrons are in general not restricted to the deuteron. Several other potentially polarizable nuclei have spin-1, of which the light ones are preferable (like ^{6}Li or ^{14}N) because heavy nuclei contain many spin-paired nucleons which contribute to F_1, but not to b_1, and suppress the polarization-dependent effect therefore by $1/A$. The calculation of spin-dependent structure functions is generalized to targets with arbitrary spin J in Ref. [27]. As illustrated below, the tensor structure of mesons like for example the ρ meson reveals an interesting glimpse of the sea quark distribution of hadrons. The importance of studying the Drell-Yan process in proton-deuteron collisions, alternatively to electron scattering, to explore the deuteron tensor structure was pointed out in Ref. [28].

Already these introductory considerations reveal the nature of b_1 as border crosser between nuclear and quark physics: although only accessible in deep-inelastic scattering where due to the high transferred 4-momentum obviously the quark level is probed, it is sensitive only to the spin of the *hadron* embedding the quarks, in contrast to the spin structure function g_1 which probes the helicity of *quarks*. The measurement of b_1 therefore represents the opportunity to obtain new information on nuclear binding effects at the parton level. It could be another signature for exotic modifications in nuclei which appear due to the nuclear medium [14], on equal footing like the before mentioned EMC effect.

In 1992, a proposal was made to measure $b_1^{\rm d}$ of the deuteron by the (never realized) ELFE project [29]. The measurement of $b_1^{\rm d}$ by Hermes had already been proposed during the planning stage of the experiment [30], [31] and was carried out in a dedicated data taking period in 2000 with a deuteron target with high tensor polarization and close-to zero vector polarization which allowed for access to a deuteron sample purely in the $m = 0$ state. The experimental determination of $b_1^{\rm d}$ is presented in Chaps. 2 and 3 and the final result is discussed in comparison to model predictions in Secs. 3.6 and 3.7.

Early models on b_1. In the benchmark paper [14] from 1989, Hoodbhoy, Jaffe and Manohar introduced the leading twist tensor structure function b_1 as novel feature of spin-1 targets. The precursor of the tensor structure function had in 1967 been

discussed for real photons in Ref. [32], and in the early 1980s, b_1 had been calculated for conventional deuteron wave functions in Ref. [33].
In Ref. [14], simple models of nucleons moving in the nuclear target were examined. Trivially $b_1 \equiv 0$ if the nucleus with total angular momentum $J = 1$ consists of two non-interacting spin-$\frac{1}{2}$ nucleons at rest. Two independent nucleons are principally not sensitive to the tensor structure because the quark configuration in the $m = 0$ nucleus is identical to the sum of the $m = +1$ and $m = -1$ configurations (see Fig. 1.3).
They developed further scenarios in a convolution model for DIS off a nucleus [34], in which the virtual photon is considered to incoherently scatter off quarks which are distributed within nucleons which are, in turn, distributed within the nucleus [21]. If the nucleons move non-relativistically in a central potential *and* no D-state admixture is considered, b_1 is suppressed by p^2/M^2. In a more realistic approach, the deuteron was considered in which the proton and the neutron move (non-relativistically) in opposite directions, and the D-state admixture of the deuteron wave function was included in the calculation. The thereby produced tensor structure generates a non-zero b_1^{d} consisting of two terms: one accounts for the D-state (D-D term), the other for S-D interference. Because the D-state admixture is small, $b_1^{\mathrm{d}} \ll F_1^{\mathrm{d}}$. Integrating the explicit expression for $b_1^{\mathrm{d}}(x)$ yields interestingly $\int_0^1 \mathrm{d}x\, b_1^{\mathrm{d}}(x) = 0$ (see below for the discussion of the phenomenological sum rule for b_1).
Relativistic and binding energy corrections were taken into account in Ref. [35]. Non-vanishing contributions to b_1^{d} due to D-D and S-D terms were obtained only for non-zero Fermi motion and nuclear binding. b_1^{d} was found to be at most of the order 10^{-4} with a tendency of the D-D and S-D contributions to cancel each other. The integral of $b_1^{\mathrm{d}}(x)$ was calculated to be -0.000665.
b_1 is also suitable for studying non-nucleonic degrees of freedom in nuclei like meson exchange currents. The tensor structure function $b_1^{\mathrm{d}}(x, Q^2)$ is in that sense a measure for the extent to which the ground state of the deuteron deviates from being a composite of proton and neutron only. The extent to which (excess) pions in the spin-1 nucleus participate in DIS was investigated in Ref. [36] and a link to nuclear shadowing was established. The obtained pionic contribution to b_1^{d} delivers $\int_0^1 \mathrm{d}x\, b_1^{\mathrm{d}}(x) = 0$ [29] and is roughly parametrized as $b_1^{\mathrm{d}}(x)/F_1^{\mathrm{d}}(x) \approx 0.02(x - 0.3)$ for $x \lesssim 0.6$, which corresponds to a $\lesssim 1\%$-effect at small x (see Fig. 3.41).
In a relativistic system, however, b_1 needs not be small. The contribution to b_1 from two massless relativistic quarks (with $J_1 = 1/2$ and $J_2 = 3/2$ which couple to $J = 1$ to form a vector meson) moving in the target like in a central potential was predicted to be substantial from convolution model considerations [14]. In particular, the tensor structure function for the ρ meson was studied in a rather crude estimation by using light-cone wave functions for constituent quarks [37] and the result $b_1^{\rho} \lesssim F_1$ was found. The sum rule $\int_0^1 \mathrm{d}x\, b_1^{\rho}(x) = 0$ is satisfied if the number of sea partons does not depend on the helicity state of the parent hadron.
In summary, these early models predict b_1 of the deuteron to be negligible. A non-

zero, however small $b_1^{\mathrm{d}}(x) \sim \mathcal{O}(10^{-4})$ can at moderate and large $x > 0.2$ be generated through Fermi motion and nuclear binding effects. The exception to this class of models constitute meson exchange currents described in Ref. [36] which lead to a sizable ($b_1^{\mathrm{d}}/F_1^{\mathrm{d}} \lesssim 0.01$) effect.

Double spin-flip structure function $\Delta(x, Q^2)$. Besides $b_1(x, Q^2)$ and $b_2(x, Q^2)$, there is a third leading twist hadronic structure function $\Delta(x, Q^2)$ for spin-1 targets [38]. $\Delta(x, Q^2)$ corresponds to the Compton amplitude that flips both the photon and target helicity by two units each. In parton models, $\Delta(x, Q^2)$ falls off like $1/Q^2$. In QCD, there is a (often neglected) tower of gluon operators with contributing matrix elements for scattering off targets with spin ≥ 1 with *transverse* polarization. The complete cross section for DIS off a spin-1 target of arbitrary polarization is given in Ref. [39]. Because neither nucleons nor pions bound in nuclei can transfer two units of helicity in the target, $\Delta(x, Q^2)$ does not receive contributions from these sources. It rather probes gluon contributions which are not assigned to *individual* nucleons within the nucleus.
$\Delta(x, Q^2)$ is hitherto unmeasured. It can experimentally be determined with an unpolarized lepton beam by measuring the azimuthal asymmetry of the scattered lepton with respect to the direction of the transversely polarized target. The double spin-flip structure function is kinematically supressed for a longitudinally polarized target [39]. It was therefore not taken into account in the extraction of b_1^{d} from Hermes data.

Double-scattering models on b_1. In the late 1990s, a significant contribution to $b_1(x, Q^2)$ at low x ($x < 0.1$) induced by double-scattering mechanisms in the deuteron, along with the presence of the non-vanishing electromagnetic quadrupole moment of the deuteron, was suggested [17], [40], [41]. Low x is the regime in which the coherence length of the virtual photon

$$\lambda \simeq \frac{1}{xM} \left(\frac{Q^2}{M_X^2 + Q^2} \right) \tag{1.26}$$

is larger than the diameter of the deuteron, $\lambda > d \sim 4$ fm, a distance long enough to allow the virtual photon to scatter *subsequently* off the two nucleons[19]. In this process, the virtual photon diffractively produces a hadronic intermediate state with invariant squared mass M_X^2 which subsequently re-scatters from the second nucleon (see Fig. 1.5). The interaction of these excited hadronic states with the nucleons is coherent in the sense that *both* nucleons take part in the scattering process, in contrast to single-scattering where the photon interacts incoherently either with the proton *or*

[19]The argument arises from the uncertainty principle.

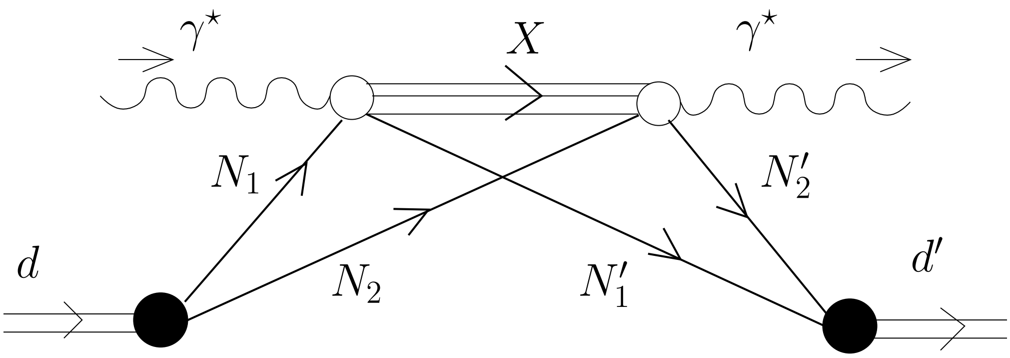

Figure 1.5: Double-scattering diagram for the deuteron d. The virtual photon $\gamma^\star$ interacts with one nucleon N_1 and produces an intermediate hadronic (vector meson) state X which subsequently re-scatters from the second nucleon N_2. The double scattering amplitude contains the sum over all diffractively excited hadronic states X which carry the quantum numbers of the virtual photon.

the neutron. The cross section receives contributions from both single and double scattering processes[20].

The consequence of double scattering is nuclear shadowing for $x < 0.03$, the region where $\lambda > d$ is fulfilled according to Eq. 1.26 ($M_X^2 \sim Q^2$). The momentum transfer Q^2 selects the diffractive states which dominate the shadowing effect, either low-mass vector mesons or heavy hadronic states [42]. As mentioned above, nuclear shadowing is well-known from unpolarized scattering [2], where destructive interference of the single- and double-scattering amplitudes leads to the observed effect [43]. The nucleus cross section is attenuated ("shadowed") and thus smaller than the simple sum of its constituents cross sections since the nucleons on the surface of the nucleus screen the ones deeper in the core: $\sigma(\mathrm{N}\gamma^*) < \sum_{\mathrm{p,n}} [\sigma(\mathrm{p}\gamma^*) + \sigma(\mathrm{n}\gamma^*)]$.

Diffractive nuclear shadowing consequently depends on the alignment of the nucleons, and for the deuteron in particular, the shadowing attenuation is expected to be larger for the $|\,m\,| = 1$ state when proton and neutron are "in front of each other" (dumbbell) than for the $m = 0$ state when the two nucleons are "side by side" (torus). This qualitative explanation gives a first glimpse how $b_1 \sim \sigma(m = 0) - \sigma(|\,m\,| = 1)$ can act as measure for nuclear shadowing caused by double scattering. In this sense, b_1 is absent for single scattering, a process in which the two nucleons are seen as individual spin-$\frac{1}{2}$ particles without sensitivity for the tensor structure which can be regarded as coherent feature of the deuteron.

In particular, coherent double scattering at $x < 0.1$ and $Q^2 \lesssim 3$ GeV^2 was treated in Ref. [17] by an extension of Glauber-Gribov multiple scattering theory to include spin degrees of freedom. The single scattering contributions recover Eqs. 1.23 and 1.24, the latter reflecting the D-state admixture in the deuteron ground state, and

[20]Because in the convolution model the constituents of the nucleus are assumed to scatter *incoherently*, this model breaks down for double scattering.

yield $b_1 \equiv 0$ for the considered kinematic region. Nuclear binding and Fermi motion effects are not relevant for $x < 0.1$ and are therefore neglected. The double scattering amplitude is responsible for shadowing corrections in $F^{\rm d}_{1,2}$ and $g^{\rm d}_1$ leading to a *decrease* of these structure functions for small x. Shadowing is found to be larger by about a factor of two for the latter. The double scattering contribution to b_1 entirely arises from the interference of the deuteron S- and D-state component and dominates b_1 at small x, leading to an *enhancement* in that kinematic region. The resulting size of b_1 is directly related to the relative shadowing correction of $F^{\rm d}_1$; for $x \ll 0.1$, $b^{\rm d}_1$ reaches 2% of the spin-independent structure function $F^{\rm d}_1$ (Eqs. 1.23 and 1.14): $b^{\rm d}_1/F^{\rm d}_1 \approx 0.02$. Two sources of tensor polarization of sea quarks θQ_s (Eq. 1.30) were discussed[21] in Ref. [40] down to very small $x = 10^{-5}$, both leading to a nuclear (Glauber) eclipse effect [24]. The first contribution is the above discussed diffractive nuclear shadowing which was extracted using the pomeron structure function of the proton, the second contribution the nuclear excess of pions (not pomeron, but pion exchange excites the intermediate diffractive state). These excess pions describe the modification experienced by the nuclear medium in the *bound* nucleus due to the pion cloud. Depending on the polarization state of the deuteron, due to the pion's spin-flip coupling pions either deplete or enhance the cross section. Each pion exchange can be described by a skewed parton distribution [44]. The tensor polarization of sea partons θQ_s was found in beyond impulse-approximation at $Q^2 = 10$ GeV^2 to be proportional to $\langle \Delta n^{\pm}_{\pi} \rangle - \langle \Delta n^{0}_{\pi} \rangle = 0.0116$ (where Δn^m_π is the number of nuclear excess pions in a nucleus with spin m). θQ_s rises toward small x, where it is for $x < 10^{-4}$ a 1%-effect. $b^{\rm d}_2 = -\frac{3}{2} A_{zz} F^{\rm d}_2$ is predicted to rise and then fall again in the range $0.01 < x < 0.4$ and then to steeply rise (to negative values) towards very small x.
The diffractive hadronic intermediate state was in Ref. [41] studied in the context of vector meson dominance (VMD), a model in which the virtual photon is considered to fluctuate between the bare photon state and a superposition of hadronic states with the same quantum numbers as the photon. At the Q^2 scale taken into account (0.1 GeV$^2 < Q^2 < 10$ GeV^2), these are the light vector mesons ρ, ω and ϕ. The VMD provides an estimate of the contributions to the structure functions at a low scale, which are then mapped into the large Q^2 domain by standard Q^2-evolution. In qualitative agreement with Refs. [17] and [40], a significant contribution from multiple scattering to $b^{\rm d}_1(x, Q^2)$ for $x < 0.1$ was found, enhancing for $x < 0.01$. $b^{\rm d}_2$ behaves as $(1-x)^{2\delta}/x^{1+2\delta}$. In the context of nuclear shadowing induced by double-scattering, the tensor asymmetry A_{zz} was estimated in Ref. [45], however without explicit calculation, to be of the order of 1% for $x \leq 0.03 - 0.02$. It is worth mentioning in passing that multiple scattering at low x can still lead to $b^{\rm d}_1 \neq 0$ even if the D-state component of the deuteron is neglected [43]. However, this contribution is only $\mathcal{O}(0.001)$ and does not enhance for

[21] Note that the definition of the tensor structure function in Ref. [40] differs by a minus sign with respect to the usual definition.

decreasing x.

Sum rule for b_1. The violation of the Gottfried sum rule found by the NMC collaboration in 1994 [46],

$$\int_0^1 \frac{\mathrm{d}x}{x}(F_2^{\mathrm{p}}(x) - F_2^{\mathrm{n}}(x)) = 0.235 \pm 0.026 \neq \frac{1}{3}\,, \tag{1.27}$$

indicates that the light quark sea is not flavor symmetric, i. e. $\overline{u}(x) \neq \overline{d}(x)$. The Gottfried sum rule is due to the symmetry assumptions made by its derivation not a "strict" sum rule like the Bjørken sum rule $\int_0^1 \frac{\mathrm{d}x}{x}(g_1^{\mathrm{p}}(x) - g_1^{\mathrm{n}}(x)) = \frac{1}{6}|\frac{g_A}{g_V}|$ + QCD corrections [47], [48] which bases on fundamental current algebra. Rather similar to the Gottfried sum rule, the Close-Kumano sum rule for b_1 [49], [29] describes a phenomenological expectation about the tensor polarization of sea quarks basing on the naive parton model. Integrating Eq. 1.25 over x at fixed[22] Q^2 by including all light quark and anti-quark flavors q one obtains with the definition of the quark tensor distribution[23] θq from Fig. 1.3,

$$\theta q = \frac{1}{2}\,(q^0 - q^1), \tag{1.28}$$

after separation of valence and sea quark contributions und introducing the usual subscript v for the valence quark distribution in the proton:

$$\int_0^1 \mathrm{d}x\, b_1(x) = \frac{5}{9}\int_0^1 \mathrm{d}x\,(\theta u_v + \theta d_v) + \frac{1}{9}\theta Q_s, \tag{1.29}$$

where θQ_s is the tensor polarization of the sea quarks:

$$\theta Q_s = \int_0^1 \mathrm{d}x\left(8\theta\overline{u}^{\mathrm{d}} + 2\theta\overline{d}^{\mathrm{d}} + (\theta s^{\mathrm{d}} + \theta\overline{s}^{\mathrm{d}})\right). \tag{1.30}$$

The right hand side of Eq. 1.29 can in the context of the QPM be related to elastic amplitudes Γ_{HH} for scattering off a target with helicity H. Macroscopically, the amplitudes Γ_{00} and $\Gamma_{11} = \Gamma_{-1-1}$ can be expressed as linear combinations of the electric charge and electric quadrupole form factors of the target, $F_C(Q)$ and $F_Q(Q)$, respectively. In the tensor combination of amplitudes, $\Gamma_{00} - \frac{1}{2}\,(\Gamma_{11} + \Gamma_{-1-1})$, the charge form

[22] The Q^2 dependence is skipped for simpliceity in the following.

[23] The sometimes used symbol δq is in the meantime reserved for the transversity distribution. For the same reason, the term *tensor charge* must not be used in this context.

factor cancels out, leaving the quadrupole form factor in the integral of the tensor structure function:

$$\int_0^1 \mathrm{d}x\, b_1(x) = \frac{5}{3} \lim_{t \to 0} \left[-\frac{t}{4M^2} F_Q(t) \right] + \frac{1}{9} \theta Q_s. \tag{1.31}$$

Thus the sum rule for b_1 is closely related to the electric quadrupole structure of the target. As

$$\lim_{t \to 0} \left[-\frac{t}{4M^2} F_Q(t) \right] = 0, \tag{1.32}$$

the integral in Eq. 1.31 vanishes in any model with a not tensor-polarized sea ($\theta Q_s = 0$), like the naive parton model (Close-Kumano sum rule):

$$\int_0^1 \mathrm{d}x b_1(x) = \frac{1}{9} \theta Q_s \equiv 0. \tag{1.33}$$

If $\int_0^1 \mathrm{d}x\, b_1(x) = 0$ then the total number of quarks, both valence and sea, in the parent spin-1 hadron does not depend on its helicity (with respect to $m = 0$ and $|m| = 1$). Thus, the sum rule Eq. 1.33 provides important information about the way in which parton distributions in a spin-1 state feel the polarization of the parent hadron [37].
To illustrate that the sum rule for b_1 is settled on a similar level as the Gottfried sum rule, the integral from Eq. 1.27 is also written in terms of elastic form factors,

$$\int_0^1 \frac{\mathrm{d}x}{x} (F_2^{\mathrm{p}}(x) - F_2^{\mathrm{n}}(x)) = \frac{1}{3} \left(F_C^{\mathrm{p}}(0) - F_C^{\mathrm{n}}(0) \right) + \frac{2}{3} \int_0^1 \mathrm{d}x \left(\overline{u}(x) - \overline{d}(x) \right), \tag{1.34}$$

where $F_C(0)$ is the charge of the target. The value of the integral is not compatible with $\frac{1}{3}$ within uncertainties, i. e. the Gottfried sum rule is broken, if the sea is not $\mathrm{SU}(2)_f$ symmetric.
Models involving nucleons alone (no "exotic" components) deliver a zero integral of b_1^{d}, even when the D-state admixture of the deuteron is taken into account [14], [29]. Models involving pion exchange to generate the tensor force preserve $\int_0^1 \mathrm{d}x\, b_1^{\mathrm{d}}(x) = 0$, those models involving a ρ exchange could give a non-vanishing integral because the ρ can effectively transport a non-zero tensor polarization θQ_s [49], [50]. Tensor polarization of vector mesons from fragmentation processes was studied in Ref. [51], introducing fragmentation function counterparts of $b_1(x, Q^2)$ and $\Delta(x, Q^2)$. The experimental observation of non-zero tensor polarization of diffractive vector mesons was e. g. reported in Refs. [52] (HERA) and [53] (LEP).
The result of the models for which double-scattering leads to a significant contribution to b_1 at small x implies the Close-Kumano sum rule to be violated. In particular, Ref. [40] predicts a tensor polarization of sea partons which is proportional to the difference of nuclear pions for different helicity states of the deuteron.

2 How can HERMES measure b_1^{d}?

2.1 HERMES: setup

The HERMES[1] experiment at DESY[2]/Hamburg is located in the east hall of the HERA[3] complex about 20 meters below the ground, see Fig. 2.1. It is a fixed-target experiment that uses only the lepton beam of the HERA electron-proton storage ring to scatter off a gas target internal to the lepton ring, while the proton beam passes unemployed through the mid plane of the experiment. This section gives a short overview over the

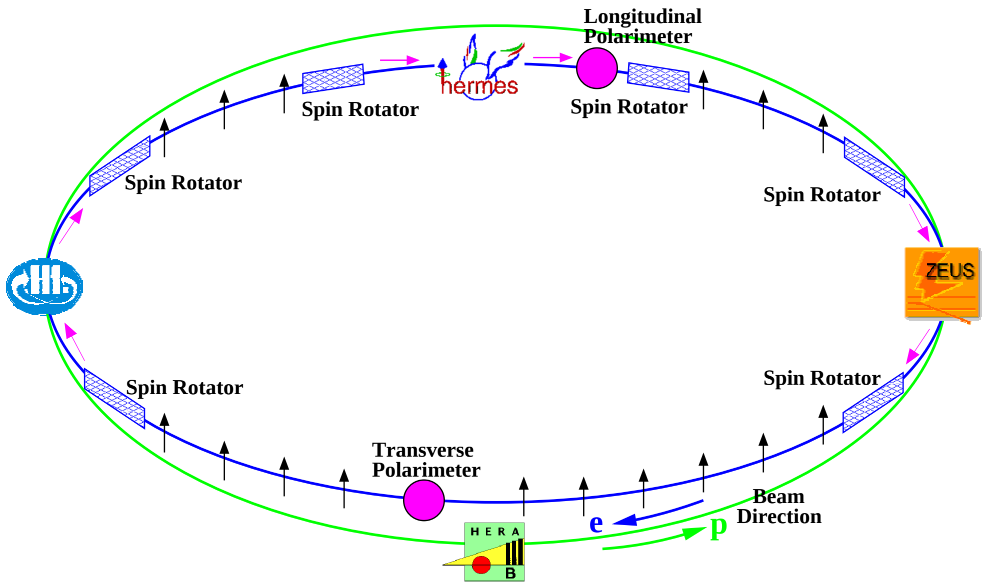

Figure 2.1: Schematic view of the HERA electron-proton storage ring (until 2000 with four experiments); the loations of the spin-rotators and the two polarimeters are indicated (see Sec. 2.1.1)

involved ingredients[4] which allow for the generation and detection of a deep-inelastic scattering (DIS) process of polarized charged leptons off polarized nuclei: the polarized beam, the polarized target, and the spectrometer. All three are described in greater detail elsewhere [11], [54].

[1]**HER**a **ME**asurement of **S**pin.
[2]**D**eutsches **E**lektronen **SY**nchrotron.
[3]**H**adron-**E**lektron **R**ing-**A**nlage.
[4]Restricted to the experimental status during the time the data were collected (July/August 2000).

2.1.1 The polarized HERA lepton beam

The HERA electron[5] bunches have a length of 27 ps and are separated by 96 ns. This allows for at most 220 bunches[6]. Average electron currents at injection are mostly around 40 mA (up to 50 mA) with an injection energy of 12.0 GeV and decrease exponentially within a beam life time of about ten hours (one *fill*, a term which is both used for the time the beam stays in the machine, as well as for the data collected during this period) due to scattering processes off rest gas particles in the beam pipe. After injection is completed, the electrons are ramped up to their final energy of 27.6 GeV.
An electron beam which is injected unpolarized into a high-energy storage ring can become transversely self-polarized by the emission of spin-flip synchrotron radiation (Sokolov-Ternov mechanism [55]). The thereby involved asymmetry in the spin-flip amplitude populates the state with the spin pointing upwards, developing a theoretically stable transverse polarization in time [31]. For a typically reached asymptotic beam polarization of 53%, the *rise time* is about 21 min. The ideal maximum polarization value which can theoretically be achieved at HERA is 92.4%, but depolarization effects can not be eliminated entirely.
At the Hermes interaction point, longitudinal beam polarization is obtained by two spin rotators [56] up- and downstream the experiment (see Fig. 2.1); the first one, located in front of the target region, rotates the electron spins parallel to the beam direction, the second one turns them back into the transverse direction. Beam polarization is measured continuously by two apparatuses which are both based on aymmetries in Compton backscattering of polarized laser light from the electron beam. The *transverse polarimeter* (TPOL) [57], [58] measures the polarization of the beam at a point where it is transversely polarized, exploiting a spatial up-down asymmetry in the Compton backscattering process. The *longitudinal polarimeter* (LPOL) [59] measures the beam polarization some 90 m downstream the Hermes target shortly before the spin orientations are rotated back to the transverse direction. Differently than in the TPOL case, the asymmetry is manifested in the total cross section, allowing for a higher precision measurement.
Principally, the sign of the beam helicity could be changed after every electron fill by reversing the direction into which the spin rotators flip the electron spins. Actually, for the reported data this happened only once roughly after one half of the desired data had been taken; the corresponding beam polarization values are compiled in Tab. D.1.

[5] Throughout Sec. 2.1, the term *electron* stands for both lepton species e^+ and e^-, except when a distinction is necessary; for the presented data, positrons were circulating in HERA.

[6] The HERA ring has a circumference of 6.3 km.

2.1.2 The polarized HERMES atomic-gas target

Vector and tensor polarization. For a spin-$\frac{1}{2}$ target (like the proton), the z-component of the nuclear spin, s_z, has two projections m onto the z-axis[7], namely $+\frac{1}{2}$ and $-\frac{1}{2}$ (Fig. 2.2, left side). Spin-1 particles have one further possibility to set their spin in the $m = 0$ state (Fig. 2.2, right side). For a spin-$\frac{1}{2}$ target, the vector polarization P_z is defined for an ensemble of particles n (see Fig. 2.2) as

$$P_z = \frac{n^+ - n^-}{n^+ + n^-}, \qquad |P|_z \leqq 1 \tag{2.1}$$

and for a spin-1 target

$$P_z = \frac{n^+ - n^-}{n^+ + n^- + n^0}, \qquad |P|_z \leqq 1. \tag{2.2}$$

Only for a spin-1 target, the tensor polarization P_{zz} is defined as:

$$P_{zz} = \frac{(n^+ + n^-) - 2n^0}{n^+ + n^- + n^0}, \qquad -2 \leqq P_{zz} < 1. \tag{2.3}$$

The notations for the vector and tensor polarizations P_z and P_{zz}, respectively, follow the Madison convention [60].

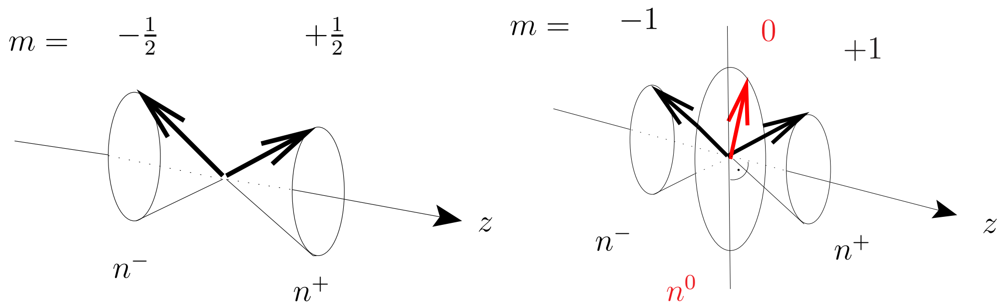

Figure 2.2: Projections m of the spin z-component onto the z-axis for a spin-$\frac{1}{2}$ (left) and spin-1 particle (right). $n^{\mathrm{sign}(m)}$ denotes the number of particles with spin quantum number $\mathrm{sign}(m) \cdot |m|$ in the ensemble.

If only the $m = +1$ *or* $m = -1$ state is populated, the vector polarization reaches its largest (absolute) value of 1. For a spin-1 target, the tensor polarization's absolute value is then also 1. The extreme value of $P_{zz} = -2$ is achieved for *vanishing* populations of $m = \pm 1$. If in the spin-1 case the target is purely vector polarized ($P_{zz} = 0$ and $n^0 = \frac{1}{2}(n^+ + n^-)$), the state $m = 0$ is populated with $\frac{1}{3}$ of the particles, like for an unpolarized ensemble. That means that P_z is restricted to values $|P_z| \leq \frac{2}{3}$. If higher P_z is desired, the state $m = 0$ has to be depopulated resulting in a non-vanishing tensor polarization, except for the very special case that $n^+/(n^+ + n^- + n^0) = 0.66$ (or

[7]Formally, s_z is a quantum mechanical operator with eigenvalues m.

Dilution factor f

Target	SLAC	CERN	DESY/Hermes
Solid targets			
H-butanol	0.13-0.15	0.12	
D-butanol		0.19-0.20	
NH_3	0.15-0.16	0.16	
ND_3	0.24		
LiD	0.36		
Gaseous targets			
^{3}He	0.35-0.55		1
H			1
D			1

Table 2.1: Compilation of fixed targets at DIS facilities [3]. The quoted dilution factor f is the fraction of scattering events that result from the polarized atoms of interest. However, it is the factor $P_B P_z f$ accounting for beam and target polarization P_B and P_z, respectively, which enters the extraction of the inclusive vector asymmetry $A_\parallel$ (Eq. 2.21). The best achieved values of $P_B P_z f$ for SLAC are 0.17 (E154, ^{3}He) and 0.10 (E155′, NH_3), for CERN 0.16 (COMPASS, LiD) and 0.11 (SMC, NH_3), and for Hermes 0.48 (H-gas). Hermes is the only DIS experiment that can for a spin-1 target adjust a high tensor polarization P_{zz} with at the same time close-to zero vector polarization P_z (a combination which is not possible for solid-state polarized targets).

analogously for n^-) and $n^0/(n^+ + n^- + n^0) = 0.33$.
New affects arising from the additional (with respect to spin-$\frac{1}{2}$) degree of freedom for a spin-1 target reside in the tensor structure funstion b_1 which is the main topic of this thesis.

Survey of experimental setup. The Hermes target is unique within the community of targets used for DIS; targets at other DIS facilities are mostly solid-state, see Tab. 2.1. The technique used at Hermes is however not entirely new; an internal gaseous spin-1 target with high tensor polarization has i. e. been used at NIKHEF to study elastic and quasi-elastic electron-deuteron reactions [26], [61].
Since 1996, Hermes has used a gaseous atomic target that allows various combinations of hyperfine states of the gas atoms to enter the target cell[8]. This procedure makes it possible to rapidly reverse the nuclear polarization and to perform measurements without dilution arising from unpolarizable material. Especially the fact that a high

[8]In 1995, a polarized ^{3}He source was used which worked differently than the system described below.

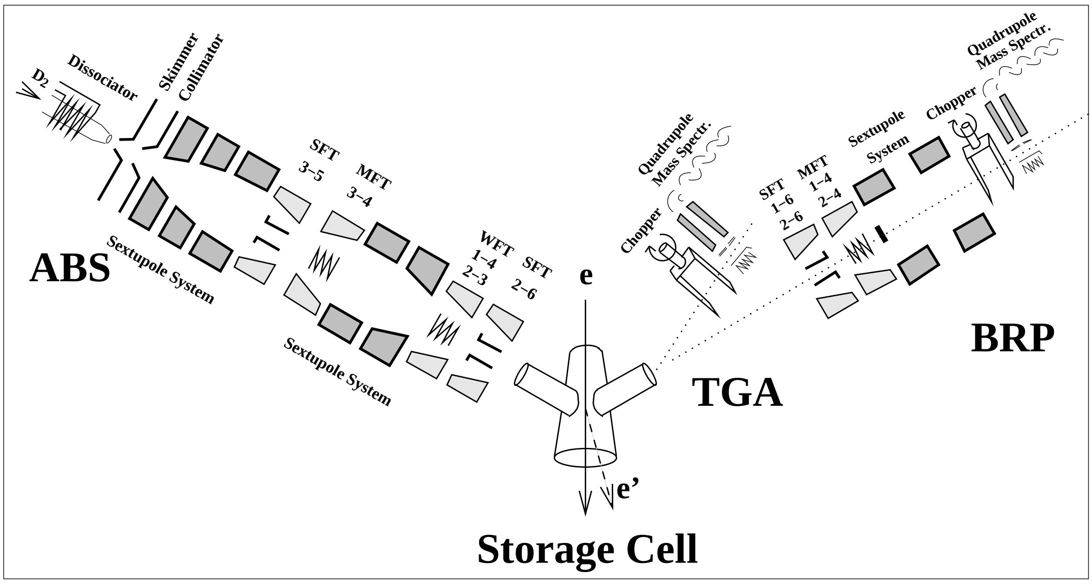

Figure 2.3: Schematic top view of the HERMES-target.

negative tensor polarization with *at the same time* vanishing vector polarization can be achieved makes the HERMES target stand out. The target system is described in detail in Ref. [62]. The polarized target can both be operated with hydrogen and deuterium gas; the reported data have been collected with a deuterium target.
Fig. 2.3 shows a schematic view of the HERMES target. On the left hand side, an atomic beam source (ABS) is located providing polarized deuterium atoms which are injected in the storage cell (middle part) through a feed tube. The storage cell is embedded in a super-conducting magnet which generates a magnetic field of $B = 0.335$ T longitudinal to the electron beam, providing the quantization axis for the nuclear spin and preventing spin relaxation. About 5% of the target gas leaves the cell through the sample tube and is analyzed by two instruments (right hand side): the TGA (target gas analyzer) measures the atomic and molecular gas content, and the BRP (BREIT-RABI polarimeter) monitors the atomic polarization.

ABS. In the ABS [63], the gas molecules provided by the gas feed system are dissociated in a plasma driven by microwave radiation and are formed into a beam by a cooled nozzle (100 K) and two collimators. The energy levels of the atoms entering the ABS sextupole magnets split up into their hyperfine states (ZEEMANN effect). The energy states of a deuterium atom in an external magnetic field are displayed in the BREIT-RABI diagram in Fig. 2.4. There are six such states for deuterium (two possibilities for the electron to adjust times three for the nucleus). The sextupole system allows (STERN-GERLACH-like) only states with an electron polarization of $+\frac{1}{2}$ to pass

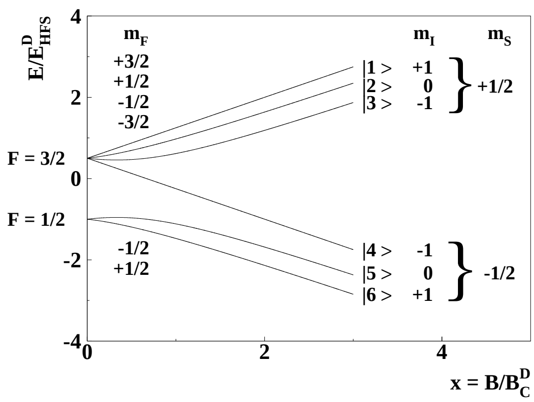

Figure 2.4: Breit-Rabi diagram for deuterium. m_F denotes the spin quantum number of the coupled electron-nucleus system. The decoupled states $|1\rangle$ to $|6\rangle$ are the hyperfine states with spin quantum numbers m_I of the nucleus and m_s of the shell electron (Breit-Rabi basis), arising for $B > B_C$ (only then the states cease from mixing). For deuterium, $B_C = 11.7$ mT.

(in the diagram the upper three). Radio frequency (RF) transitions[9] exchange the populations of the states in such a way that an effective nuclear polarization results. By combining several of these processes, two certain hyperfine states are selected and injected into the storage cell at the same time. The combinations of injected hyperfine states are alternated cyclically every 90 seconds, as indicated in Tab. 2.2.

Storage cell. The storage cell [64] is an open-ended tube of elliptical cross-section (40 cm long, 21×9 mm^2 wide) constructed out of pure aluminium (75 μm thick) and cooled to 70 K (deuterium). It is mounted internal to the HERA storage ring allowing the polarized gas to be confined along the beam line, reaching an areal density of $2.1 \cdot 10^{14}$ nucleons/cm^2. The scattered particles leave the target chamber (which surrounds the storage cell) through a stainless steel exit window in the direction of the spectrometer.

TGA. The TGA [65] is a quadrupole mass spectrometer (QMS) which determines the degree of dissociation in the target gas by measuring the relative fluxes of the atomic mass (D) and the molecular mass (D_2), after background has been subtracted by means of a chopper.

BRP. The BRP [66] is basically set up as a mirror image to the ABS; the sample beam is sent through RF and magnetic sextupole fields. A QMS measures then the relative hyperfine populations of the gas atoms, each three states at one time. Resolving all

[9]So-called Strong Field (SFT), Mean Field (MFT) and Weak Field Transitions (WFT).

target state	inj. hyperfine states	injected particles	m of single nucleus	vector pol. P_z	tensor pol. P_{zz}	ABS trans.
`vector plus`	$\|1>+\|6>$	n^+	$m=+1$	$P_z^+=+1$	$P_{zz}^+=+1$	3-5, 2-6
`vector minus`	$\|3>+\|4>$	n^-	$m=-1$	$P_z^-=-1$	$P_{zz}^-=+1$	2-5, 1-4
`tensor plus`	$\|3>+\|6>$	$n^+ + n^-$	$\|m\|=1$	$P_z^{\Leftrightarrow}=0$	$P_{zz}^{\Leftrightarrow}=+1$	1-4, 2-6
`tensor minus`	$\|2>+\|5>$	n^0	$m=0$	$P_z^0=0$	$P_{zz}^0=-2$	1-4, 3-5

Table 2.2: The injection modes of the HERMES target running with deuterium gas. Each two hyperfine states of the atomic deuterium gas are injected into the target cell at the same time. The resulting vector and tensor polarizations are the ideal values reachable for 100% efficiency in the sextupole and transition units, with no depolarization inside the target cell and infinitely high guide field. The very right column quotes the required RF transitions in the ABS to obtain the two desired hyperfine states.

measurements gives the complete population of the sample. By applying the knowledge about the target magetic field strength, the absolute vector and tensor polarizations and the residual polarizations of the shell electrons in the sample beam can be calculated. Monte Carlo simulations are employed to extrapolate to the conditions in the storage cell (sampling corrections).

Real target polarization values. The nuclear target polarization seen by the HERA positron beam is not identical to the atomic polarization P_a[10] of the sample beam measured by the BRP. Corrections have to be applied due to spin relaxation[11] and recombination[12] processes:

$$P = \alpha_0 \cdot ((1-\alpha_r)\cdot\beta + \alpha_r)\, P_a = \alpha_{\text{eff}} \cdot P_a, \tag{2.4}$$

where α_0 is the inital fraction of nucleons in atoms and α_r the fraction that survived recombination. The polarization of the molecules P_m arising from recombination relative to the atomic polarization is estimated to be $\beta = P_m/P_a \approx 0.5$ [67]. The effective atomic fraction α_{eff} summarizes all dilution processes. In the considered data taking period (year 2000), spin relaxation processes turned out to be negligible. The target showed such a stable performance that the measured polarizations did not fluctuate significantly. For the presented analysis, therefore the corrected *mean* polarization values of this year were used [68], as they are compiled in Tab. D.2.

An overview over polarized gas targets can be found in Ref. [69].

[10] P stands here both for vector and tensor polarization.
[11] By wall collisions; by spin exchange collisions; by resonant interactions of beam and target gas.
[12] The moluecules can thereby keep part of the nuclear polarization.

2.1.3 The Hermes spectrometer

General setup. The Hermes spectrometer is a forward spectrometer typically engaged for fixed-target experiments to detect, track and identify particles emerging from the scattering process. The apparatus is described in great detail in Ref. [54].
A diagram of the spectrometer in side view is shown in Fig. 2.5. Its components are arranged around the electron and proton beam pipes; roughly one fourth of the apparatus is surrounded by a dipole magnet of an integrated field of 1.3 Tm. A horizontal iron plate shields the beam pipes from the spectrometer's magnetic field, limiting the acceptance at small angles. This topology favored the construction of two identical spectrometer halves *top* and *bottom* above and below the pipes. The definition of the Hermes coordinate system is given in Fig. 2.6.

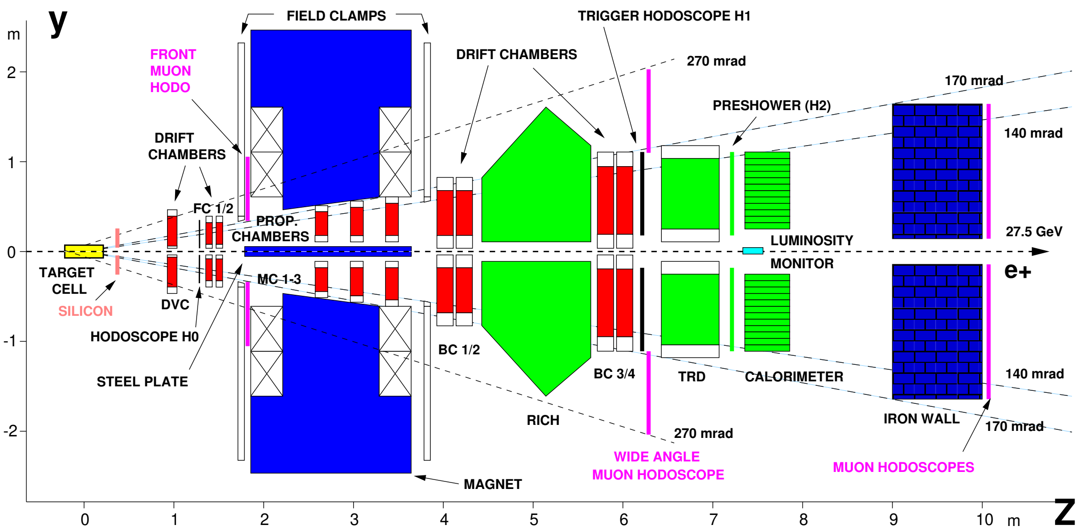

Figure 2.5: Schematic side view of the Hermes spectrometer.

Tracking chambers. Several tracking chambers (microstrip-gas chambers, multiwire proportional chambers and drift chambers) in front of, inside and behind the magnet record the particles' tracks. All wire chambers are assembled as modules consisting of six layers of wires which are tightened in three planes tilted with respect to each other in order to allow for track reconstruction in space. For the here presented analysis, tracking is based on drift chambers: two modules of *Front Chambers* (FC 1/2) and four modules of *Back Chambers* (BC 1/2 and BC 3/4) in each detector half. Signal generation in the drift chambers by a traversing charged particle is based on the Geiger-Müller-counter: the charged particles trigger an ionization avalanche in the inert gas filling the space between the wires. The ions are accelerated to the wires which are set to high voltage und deposit a signal when hitting on them. From the position of the triggering wires, the location of the particle can be deduced, and from

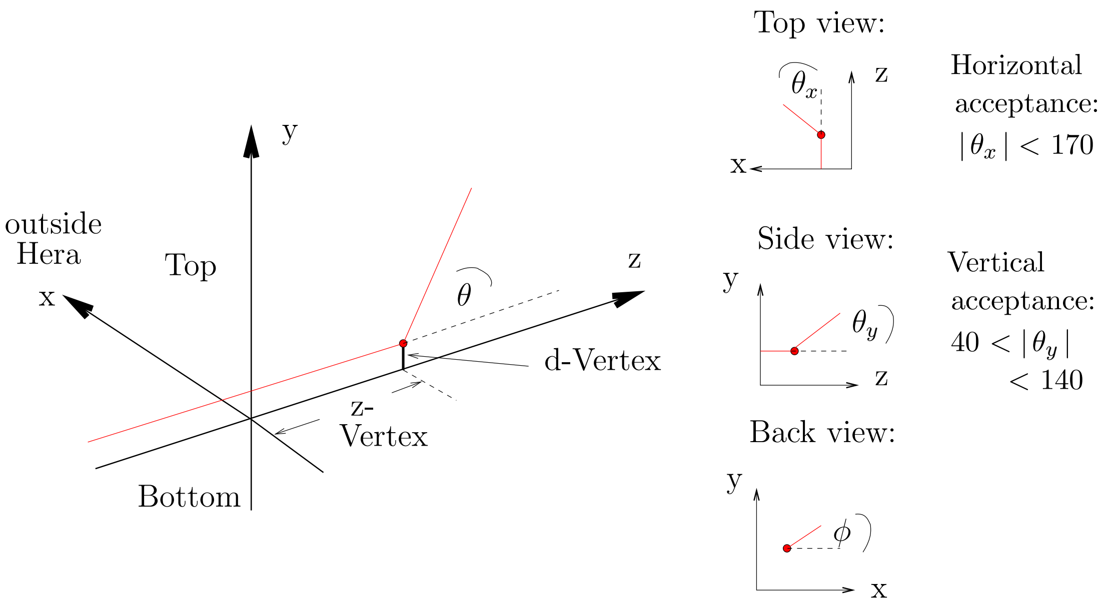

Figure 2.6: The HERMES coordinate system is given by kanonical right-handed spherical coordinates. The dot indicates the location of a DIS event, the solid lines touching it the incoming/emerging beam lepton. The figure defines the polar (θ) and the azimuthal (ϕ) scattering angles, the first one measured in the lepton scattering plane defined by the initial and final lepton tracks. Scattering angles 40 mrad $< \theta <$ 220 mrad can be detected. The zero point of the coordinate system lies in the middle of the target cell. The right hand side of the figure shows projections on each two coordinate planes for a lepton which is deflected in the top detector half to the right upwards (as seen from a spectator in back of the spectrometer); the solid dot symbolizes the event vertex in the target. The d-vertex is the shortest distance of the vertex to the positron beam pipe. The horizontal and vertical acceptances are quoted (in mrad).

the arrangement of many parallel wire layers above each other, its track can be traced.

PID detectors. PID involves the combined responses of four detectors behind the magnet: a *Ring Imaging* ČERENKOV *Detector* (RICH) to separate pions, kaons and protons, a *Transition Radiation Detector* (TRD) to reject hadrons by a factor of more than 300 (only electrons produce transition radiation in the HERMES kinematics), a *Preshower Detector* (referred to as H2 in combination with two radiation lengths of lead preceeding it), which provides a discrimination between electrons and hadrons as the latter ones deposit at least 10 times more energy than leptons and can therefore be reduced by a factor of 10, and an electromagnetic lead-glass *Calorimeter* to suppress pions by measuring the energy deposition of particles.

A description of the track reconstruction and the PID analysis is given in Sec. 2.2.

DIS trigger. The function of the trigger system is to distinguish events of specific interest from background with high efficiency, and to initiate digitization and readout of the detector signals. It therefore stands at the very beginning of the data flow. The most basic physics trigger selects positrons stemming from a DIS reaction; this so-called *DIS trigger* requires hits in the three scintillator hodoscopes H0, H1, and H2, together with sufficient energy (for the presented analysis: 1.4 GeV) deposited in two adjacent columns of the calorimeter, in coincidence with the accelerator bunch signal (HERA clock).

Luminosity monitor. Luminosity measurement is based on Bhabha scattering of the beam positrons off the target gas electrons and their annihilation into photon pairs [70]. The scattered particles exit the beam pipe 7.2 m downstream the target and are detected in coincidence by two small calorimeters made out of highly radiation resistant Čerenkov crystals situated very close to the beam pipe (one on the left and one on the right hand side), achieving a horizontal acceptance of 4.6-8.9 mrad. The lumi monitor is thus the only detector component which is *not* constructed in the top/bottom architecture. The coincident detection of the beam positron and the shell electron (one in each calorimeter) which are emerging from the elastic scattering reaction under symmetrical angles provides a statistical accuracy of the luminosity measurement of 1% within about 100 s.

2.2 Hermes: data collection and processing

Picking up the thread from the previous section where the detector components have been described in short, now the data are considered which are delivered [54], [71] by these detectors, and the data stream from the experimental hall until the screen of the analyzer is being followed.

Online data. The signals of particles in the detectors, like hits in the drift chambers or charge from the photomulitplier tubes, are digitized in the electronic modules of the detectors. Then they are processed by the programs of the online software. The DAQ[13] organizes the incoming data in units and superunits. Every time the detector electronics trigger, the basic unit of one event is recorded, picking up all detector signals caused by the particles emerging from the interaction point of the DIS reaction. The information collected for one particle is denoted as the track of the particle, and the

[13]**D**ata ac**Q**uisition.

sum of all registered particles for one event is usually referred to as its multiplicity. The events collected in 10 seconds are combined to one burst, and the bursts are gathered in one run which is a fixed number of MBytes of information. The slow control reads and records independently of the DAQ hardware information that changes on a slow time scale. The two software packages are carefully synchronized.

Tracking. After the online data have been decoded and detector calibrations have been applied, HRC, the HERMES reconstruction code, translates the wire chamber hits into actual particle tracks provided the information of the wires' actual position in space which is contained in the geometry file. Two classes of straight tracks are reconstructed applying a fast tree-search algorithm: the front partial tracks by using the wire chambers in front of the spectrometer magnet, and back partial tracks using the back chambers. If the projection of each one front and back partial track into the center of the magnet delivers an intersection there, the tracks are declared to stem from the same scattered particle and are combined to a full track. From the angle between the two intersection lines, the bending radius in the magnetic field can be deduced and thus the momentum p and charge sign of the particle (LORENTZ force). Instead of tracing each single particle through the magnet on a track-by-track basis, a fast momentum look-up table is employed which contains the momentum of a given track as a function of the partial track parameters[14]. The momentum resolution is $\delta p/p \approx 2\%$.
HRC calculates for each track the polar angle θ and the azimuthal angle ϕ from the front partial track parameters. HERMES can detect particles with $40 < \theta < 220$ mrad, with an average angular resolution of $\delta\theta = 0.3 - 0.6$ mrad. The chambers in the front region are used to reconstruct the interaction vertex, ensuring the event stems from the target gas (and not from the walls of the target cell or from the collimators upstream of the target). One function of the back chambers is to map the hits in the PID detectors to the tracks of the particles which triggered the hits.

Finally, the post-processed slow control data and the HRC data are merged together into the user-friendly micro-DSTs[15] which contain one run per file. Part of the information in these data files is available once per burst[16], another part once per track[17]. The production of the the micro-DSTs involves offline data quality on burst level. Concerning data quality and detector efficiency, the two halves of the spectrometer are treated as two independent units. Thus, the natural way is to perform analysis on the refined offline data separately for the top and bottom detector half.

[14] The data base contains 520000 tracks.

[15] **D**ata **S**ummary **T**ables. Usually, the data taken within one year are compiled in one offline production.

[16] Like polarizations and luminosity.

[17] Track parameters like momentum and scattering angles.

For a given track, the entire set of inclusive kinematic variables from Tab. 1.1 is accessible through the knowledge of the track momentum p and polar angle θ which are delivered by the tracking system.

PID. The separation of leptons and hadrons[18] is based on a Bayesian algorithm that uses the conditional probability $P(A|B)$ defined as the probability that A is true if B has been observed [72]. The *a priori* available information that a given track with observed momentum p and polar angle θ caused a response R in the PID detectors is linked to the hypothesis H_l (H_h) that the track was a lepton (a hadron) by writing the corresponding conditional probability $P(H_{l(h)}|R,p,\theta)$ according to Bayes' theorem [73] as:

$$P(H_{l(h)}|R,p,\theta) = \frac{P(H_{l(h)}|p,\theta) \cdot P(R|H_{l(h)},p,\theta)}{P(R|p,\theta)}, \tag{2.5}$$

with the denominator

$$P(R|p,\theta) = \sum_{i=l,h} P(H_i|p,\theta) P(R|H_i,p,\theta). \tag{2.6}$$

The numerator in Eq. 2.5 separates in the product of the lepton (hadron) flux $\Phi_{l(h)} = P(H_{l(h)}|p,\theta)$ and the parent distributions $\mathcal{P}_{l(h)}(p,\theta) = P(R|H_{l(h)},p,\theta)$. The latter correspond to the typical detector response triggered by a lepton (a hadron) with p and θ. These responses were extracted in 27 bins in p and 6 bins in θ from measured Hermes data for every of the four PID detectors by imposing cuts on the detectors other than the one considered in order to extract a clean sample of one particle type (lepton or hadron). The total PID detector response for a given particle type is obtained by multiplying the parent distributions $\mathcal{P}^\alpha$ for each detector with each other:

$$\mathcal{P} = \prod_\alpha \mathcal{P}^\alpha. \tag{2.7}$$

For every track, the quantity PID can be calculated from Eq. 2.5 as the logarithmic ratio of lepton and hadron probability [74]:

$$\mathrm{PID} := \log \frac{P(H_l|R,p,\theta)}{P(H_h|R,p,\theta)} = \log \frac{\mathcal{P}_l(p,\theta)}{\mathcal{P}_h(p,\theta)} - \log \frac{\Phi_h}{\Phi_l}, \tag{2.8}$$

with the so far unknown flux ratio Φ_h/Φ_l which can be written as

$$\frac{\Phi_h}{\Phi_l} \equiv \frac{\#\text{ of hadrons with } p,\theta}{\#\text{ of leptons with } p,\theta}. \tag{2.9}$$

[18] For the *inclusive* analysis reported here, only a clean separation of the electron and hadron samples is necessary, rather than a further separation into individual hadron types.

The flux ratio from Eq. 2.9 was calculated iteratively for each (p, θ) bin from Eq. 2.8, starting with the initial value $\Phi_h/\Phi_l = 1$. Then the PID parameter was recalculated for every track; *per constructionem* PID > 0 if a given track is rather a lepton than a hadron, and PID < 0 vice versa. The value

$$\frac{\#\text{ of tracks with PID} < 0}{\#\text{ of tracks with PID} > 0}$$

was fed into the flux ratio Φ_h/Φ_l in the next iteration. Convergence was reached after few iterations. In conclusion, the lepton and hadron peaks in the PID parameter distribution are well separated [72]. Restricting the lepton sample to tracks with PID>1 and the hadron sample to tracks with PID<0, the electron identification reaches an efficiency of 98-99%, with a hadron contamination of less than 1%.

For the presented analysis, the parent distributions and the fluxes were loaded from a separate library[19] which allowed to fetch the PID parameter calculated from all four PID detectors for every track given its momentum, polar angle and detector responses. Tracks with PID>1 were identified as leptons, corresponding to a 10 times higher likelihood that the track *was* actually a lepton than a hadron.

Selection of the inclusive data sample. For the analysis of the inclusive tensor asymmetry, 6121 micro-DST runs[20] with the target in the four-state-mode (Tab. 2.2) were available. Offline data quality on burst level was taken from a database containing the bursts which suffer from specific problems[21].

From the measured data, an inclusive data sample was selected separately for each detector half by the following requirements: the DIS trigger (Sec. 2.1.3) gave a signal for the event, and the data quality criteria on burst level were met. Then the lepton (as identified by the PID scheme described above) with the highest momentum in the event was selected; if the lepton did not originate from inside the target cell ($|\, z_v \,| < 18$ cm), the event was discarded. Furthermore, the event was discarded if it lied outside the phase space defined by the kinematic cuts in Tab. D.4 (left), and/or if it did not traverse the fiducial volume of the spectrometer accurately defined by its active area. If the leading lepton passed all cuts and if it was found to be a positron[22], the number of DIS candidates $N_{\text{cand}}(k)$ for the current target and beam spin state k was incremented by one. If the leading lepton was an electron, it was used for the estimation of the charge symmetric background arising from electron-positron pair production by incrementing the number of charge symmetric events $N_{\text{cs}}(k)$ by one.

The total obtained sample of inclusive DIS candidates is shown in Fig. 2.7 in the $x-Q^2$-plane together with the imposements on the phase space arising from the acceptance

[19] PIDlib version 2.41 including the correction for the not uniform TRD response over the detector area. The micro-DSTs only contain the PID library of the previous production.

[20] 00c1 production.

[21] Like polarization; luminosity; PID detectors; dead-time correction factor.

[22] I. e. the beam particle.

of the spectrometer in θ and the applied kinematic cuts. The geometrical range of accepted positrons with respect to z_v, θ_x, θ_y and ϕ is illustrated in Fig. 2.8. The collected data were divided into six bins in x-Bjørken. The bin borders were arranged in a logarithmically equidistant scheme except for the lowest and the highest border, see Tab. D.4, right side. Every tensor asymmetry presented here was extracted in this binning. Average kinematics for each bin were calculated according to Eq. A.3.
It is not possible to decide wether an inclusive DIS candidate really *is* the scattered beam positron, or if it is the positron from a electron-positron pair production. Because the latter is a secondary reaction of the DIS process, these charge symmetric events are concentrated at low momenta (high y). To eliminate a possible false asymmetry from these background processes, in every x-bin and for every target state k separately, the number of previously collected charge symmetric events $N_{\mathrm{cs}}(k)$ was therefore subtracted from the number of the candidates $N_{\mathrm{cand}}(k)$ in order to obtain the real DIS counts $N(k)$:

$$N(k) = N_{\mathrm{cand}}(k) - N_{\mathrm{cs}}(k). \tag{2.10}$$

In Tab. D.5, the total number of collected inclusive DIS events and in Tab. D.6, the total number of collected charge symmetric events are compiled separately for each target state, x-bin and detector half. These numbers, for all target states summed together, are displayed in Fig. 2.9, together with the ratio of charge symmetric over DIS events, which rises to values larger than 15% for low-x.

Luminosity. The coincidence rate (in Hz) of the lumi monitor (see Sec. 2.1.3) corrected for the effect of the gain drop due to radiation damage to the crystals in the detector, can serve as luminosity estimator in the extraction of cross section asymmetries and is denoted as `lumirate` in the following. In order to cancel out a possible Bhabha asymmetry arising from the interaction of the beam positrons with the target shell electrons (see Sec. 3.4.1), the `lumirate` is subject to a fit[23]. The so obtained `lumifit` is employed for the normalization of the collected DIS count rates, unless otherwise noted. Generally, also the lepton beam current can be used as luminosity estimator; as it does not account for fluctuations in the target density, however, it is only applied for systematic checks. Over $\Delta\mathcal{T}$ integrated luminosity L is obtained by

$$L := \int_{\Delta\mathcal{T}} \mathrm{d}t \; \epsilon(t) \; \mathcal{L}(t), \tag{2.11}$$

where $\mathcal{L}$ can be one of the three `lumirate`, `lumifit`, or beam current. The efficiency factor ϵ accounts for dead-time effects of the detector[24]. In the experiment, the coincidence rate is read out once per burst. The integral in Eq. 2.11 is replaced by a sum

[23] Provided by the lumi experts separately for each positron fill.
[24] ϵ =(accepted/generated) trigger rate; typically, ϵ was less than 10%.

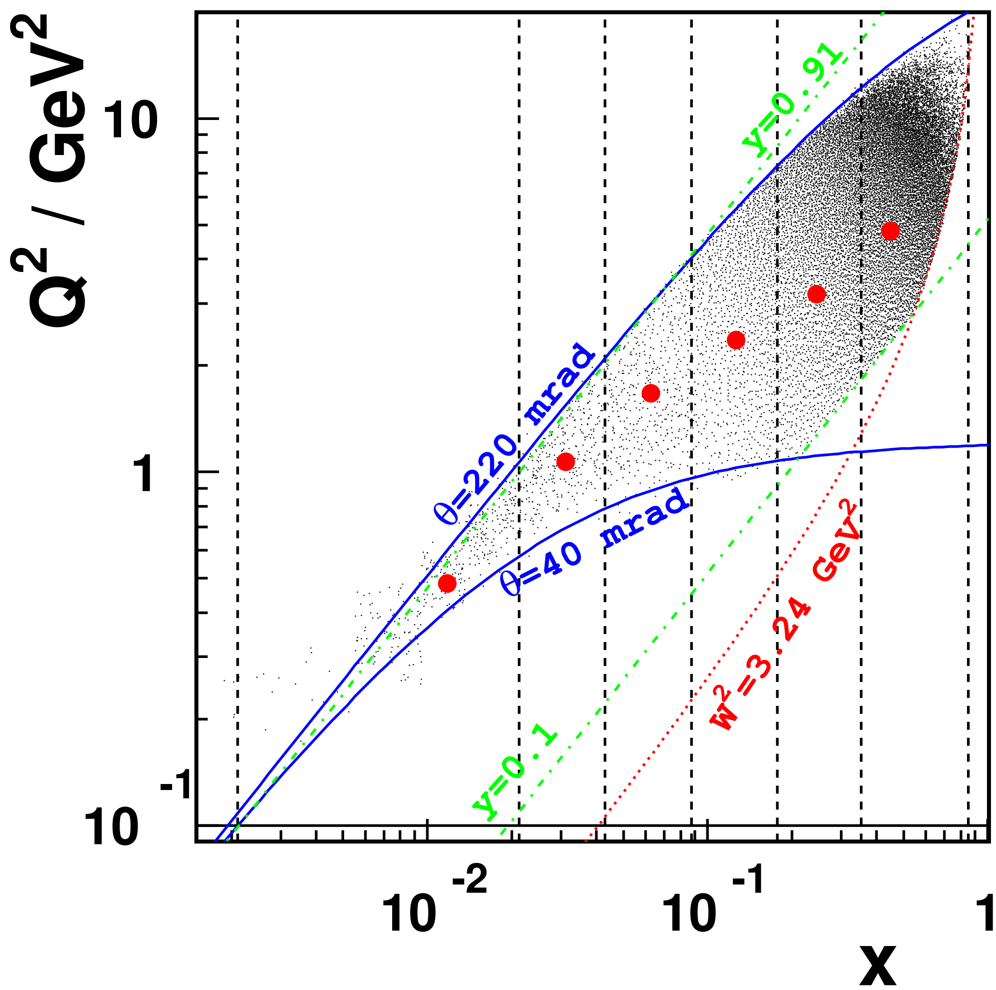

Figure 2.7: The data set of the inclusive DIS candidates $N_{\rm cand}$ after kinematic and geometry cuts in the x-Q^2-plane. The dashed vertical lines indicate the borders of the bins in x-BJØRKEN, the big dots their centers of gravity. The solid curves obeying $Q^2 = Q^2(x, \theta = 220\text{ mrad})$ and $Q^2 = Q^2(x, \theta = 40\text{ mrad})$ indicate the vertical acceptance of the spectrometer, defined by its apperture. In addition the kinematic cuts imposed on the variables Q^2 (horizonal line at $Q^2 = 1\text{ GeV}^2$), y (dashed-dotted curves) and W^2 (dotted curve) define the selected data sample. The lower y cut excludes the region in which the momentum resolution starts to degrade, the upper y cut discards the low momentum region ($p < 2.5$ GeV) where the trigger efficiencies have not reached a momentum plateau yet. The $W^2 > 3.24$ GeV^2 cut suppresses the nuclear resonance region.

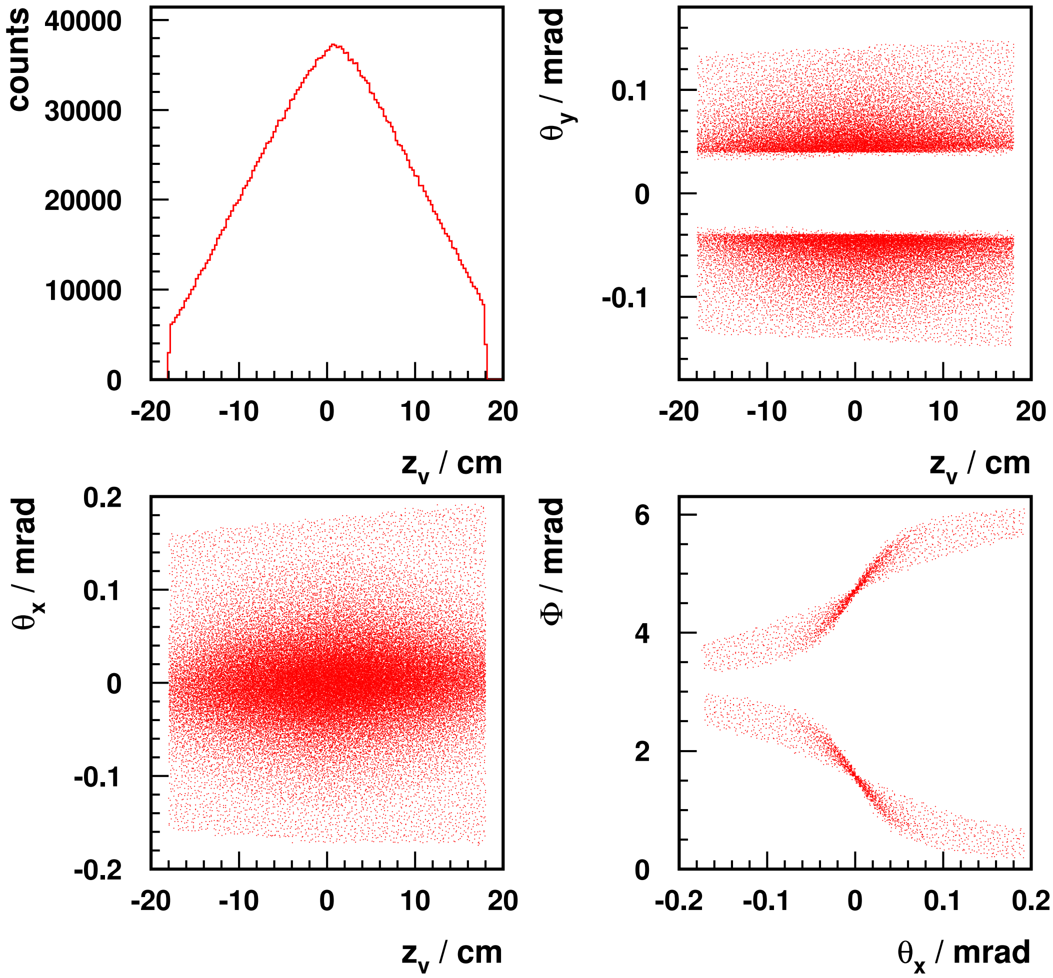

Figure 2.8: The figure illustrates the geometrical range in which the DIS leptons were accepted for this analysis after applying a fiducial volume cut (see text for details) and a cut $|z_v| < 18$ cm on the z-vertex z_v to ensure the lepton scattered off a nucleus of the target gas. Top left panel: z_v reflects the triangular profile of the target gas density along the beam line (z-direction). The top right panel illustrates the acceptance profile in side view (y-z-plane); the bottom left panel in top view (x-z-plane); and the bottom right panel in front view (x-y-plane). For the definition of z_v and the projections of the polar scattering angles θ, θ_x and θ_y, and the azimuthal angle ϕ, see Fig. 2.6.

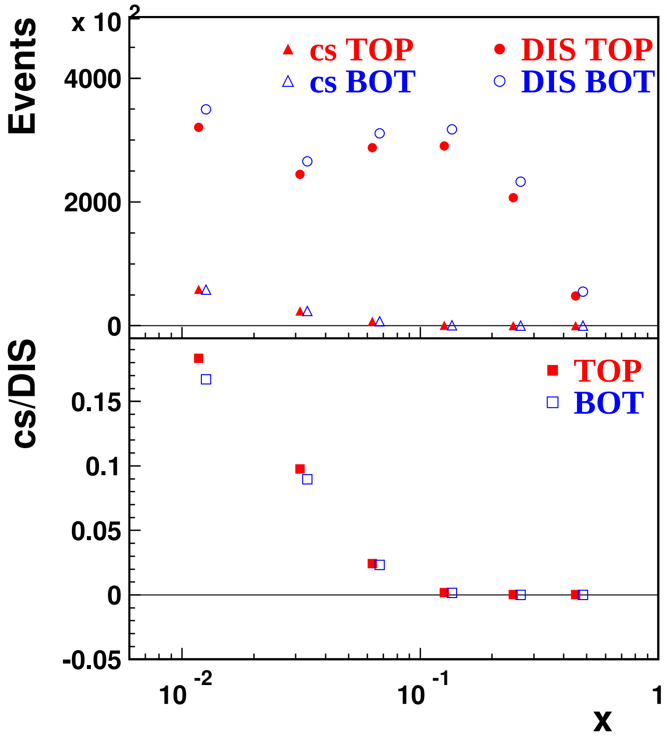

Figure 2.9: Top: the number of collected DIS and charge symmetric (cs) events for each x-bin, separatley for each detector half; bottom: the ratio of the two.

over all bursts i:

$$L = \sum_i \Delta\tau_i \epsilon_i \mathcal{L}_i, \tag{2.12}$$

where $\mathcal{L}_i$ is the luminosity and ϵ_i the dead-time correction factor measured for burst i and $\Delta\tau_i$ its duration. Due to the separate data quality and detector efficiency for the top and bottom detector, luminosity is counted separately for each detector half, even if the measurement of luminosity by the lumi monitor is not sensitive to such a distinction.

2.3 Hermes: extraction of tensor asymmetries

2.3.1 Measured cross section

The measured inclusive cross section σ_{meas} for a polarized lepton beam with polarization P_B scattering on a spin-1 target with vector polarization P_z and tensor polarization

P_{zz} is[25]

$$\sigma_{\text{meas}} = \sigma^{\mathrm{U}} \left[1 - P_B P_z A_{\|} + \frac{1}{2} P_{zz} A_{zz} \right]. \tag{2.13}$$

σ_{meas} can solely be expressed in terms of the spin-independent cross section σ^{U} and the spin-dependent cross section σ^{P}:

$$\sigma_{\text{meas}} = \sigma^{\mathrm{U}} + \sigma^{\mathrm{P}}. \tag{2.14}$$

σ^{P} is the sum of the terms in Eq. 2.13 which depend on beam and target polarizations P and which introduce the inclusive vector and tensor asymmetries $A_{\|}$ and A_{zz}. The contribution of the tensor asymmetry to the measured cross section does not depend on the beam polarization.
Such an asymmetry A compares cross sections σ measured under different polarization conditions of the target (and possibly the beam). Here, two data modes from scattering off a deuteron target are distinguished: For the *vector* modes (data with high vector target polarization P_z), data are discriminated with respect to the particular relative beam and vector target polarization (denoted by $\overset{\rightleftarrows}{\Leftarrow}$ for antiparallel and $\overset{\rightrightarrows}{\Rightarrow}$ for parallel spin orientation), and for the *tensor* modes (data with close-to-zero vector target polarization), with respect to the sign of the tensor polarization P_{zz} (positive for $\Leftrightarrow$, negative for 0), compare to Tab. 2.2.
In these terms, the vector asymmetry $A_{\|}$ compares only subsamples of vector mode data with each other, taking into account the beam helicity:

$$A_{\|} := \frac{\sigma^{\overset{\rightleftarrows}{\Leftarrow}} - \sigma^{\overset{\rightrightarrows}{\Rightarrow}}}{2\sigma^{\mathrm{U}}} \approx \frac{\sigma^{\overset{\rightleftarrows}{\Leftarrow}} - \sigma^{\overset{\rightrightarrows}{\Rightarrow}}}{\sigma^{\overset{\rightleftarrows}{\Leftarrow}} + \sigma^{\overset{\rightrightarrows}{\Rightarrow}}}, \tag{2.15}$$

where the "≈" in Eq. 2.15 refers to the small tensor dilution term for a spin-1 target in Eq. 2.32. A_{zz} is a cross section asymmetry discriminating between target states with the nuclei being in the $|m| = 1$, or $m = 0$ state:

$$A_{zz} := \frac{2\sigma^1 - 2\sigma^0}{3\sigma^{\mathrm{U}}} = \frac{2\sigma^1 - 2\sigma^0}{2\sigma^1 + \sigma^0}. \tag{2.16}$$

The cross section σ^1 has to be weighted *double* in the denominator because σ^0 is $P_{zz}^0 = 2$ (ideal case) times as large as σ^1. As can be seen from Tab. 2.2, there are several compositions possible for the data set with $|m| = 1$; they are compiled in Fig 2.10. If n subsets m_i with $|m| = 1$, $m_i = +1, -1$, or ± 1, are used, then

$$\sigma^1 = \frac{1}{n} \sum_i^n \sigma^{m_i}. \tag{2.17}$$

[25] The symbol σ denotes here a double differential cross section, *double* with respect to any two independent kinematic DIS variables.

Experimentally, an inclusive cross section σ_{meas} is determined by the ratio of the number of collected inclusive particles N (here: positrons) and the dead-time corrected integrated luminosity L:[26]

$$\sigma_{\text{meas}} = \frac{N}{L}. \tag{2.18}$$

The actually measured inclusive vector asymmetry

$$A_{\parallel}^{\text{meas}} = \frac{\left(\frac{N}{L}\right)^{\overrightarrow{\Leftarrow}} - \left(\frac{N}{L}\right)^{\overrightarrow{\Rightarrow}}}{\left(\frac{N}{L}\right)^{\overrightarrow{\Leftarrow}} + \left(\frac{N}{L}\right)^{\overrightarrow{\Rightarrow}}} \tag{2.19}$$

and the inclusive tensor asymmetry

$$A_{zz}^{\text{meas}} = \frac{2\left(\frac{N}{L}\right)^{1} - 2\left(\frac{N}{L}\right)^{0}}{2\left(\frac{N}{L}\right)^{1} + \left(\frac{N}{L}\right)^{0}} \tag{2.20}$$

need, unless beam and target are ideally polarized at 100%, a dilution correction by the real values of the polarizations:

$$A_{\parallel} = \frac{A_{\parallel}^{\text{meas}}}{\langle P_B P_z \rangle} \tag{2.21}$$

$$A_{zz} = \frac{A_{zz}^{\text{meas}}}{\langle P_{zz} \rangle}, \tag{2.22}$$

the brackets around the polarizations indicating average values.
As HERMES uses a gaseous target which is not diluted by unpolarizable material like at facilities which use solid targets (see Tab. 2.1), the dilution factor f usually coming along with the polarization product has been ignored in Eqs. 2.21 and 2.22 as well as in Eq. 2.13.

In the following, the upper index $k \in \{\overrightarrow{\Leftarrow}, \overrightarrow{\Rightarrow}, \Leftrightarrow, 0\}$ (as defined on Pg. 39) of the number of collected inclusive DIS particles N (Eq. 2.10) and dead-time corrected integrated luminosity L (Eq. 2.11) labels the data type. The notations for vector polarization P_z and tensor polarization P_{zz} are taken from Tab. 2.2. P_B^+ denotes the value of the beam polarization for positive beam helicity, P_B^- the one for negative.
Combining Eqs. 2.13 and 2.18 with the expression for the collected luminosity L corrected for the dead-time factor ϵ in Eq. 2.11, the number of inclusive DIS events collected during the data taking time $\Delta\mathcal{T}$ can be written as:

$$N = \int\limits_{\Delta\mathcal{T}} \mathrm{d}t\ \epsilon(t)\ \mathcal{L}(t)\ \sigma = \sigma^{\mathrm{U}} \cdot \int\limits_{\Delta\mathcal{T}} \mathrm{d}t\ \epsilon(t)\ \mathcal{L}(t)\ \cdot \left[1 - P_B P_z A_{\parallel} + \frac{1}{2} P_{zz} A_{zz}\right], \tag{2.23}$$

[26]Note that this ratio has the unit of a (double differential) cross section $\frac{\mathrm{d}^2\sigma}{\mathrm{d}E\mathrm{d}\Omega} \equiv \sigma$, but as HERMES can not detect scattered particles in the full 4π-steradian Ω, the quantity σ is not equivalent to a *total* cross section.

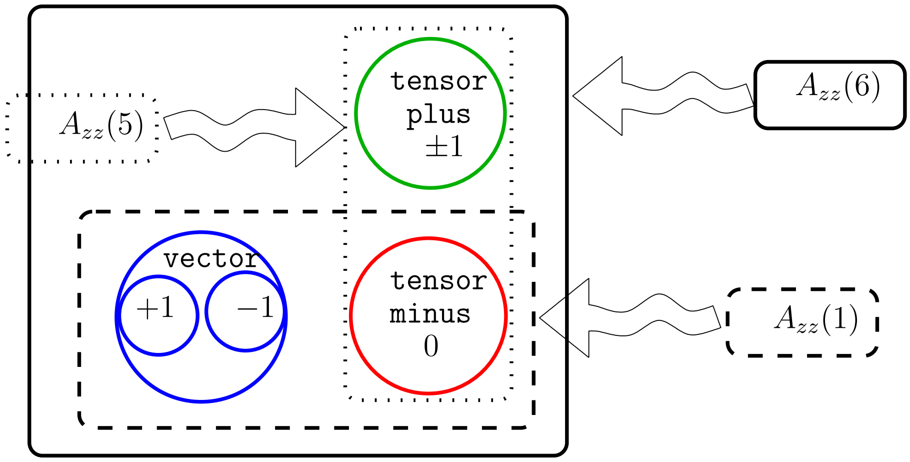

Figure 2.10: Possible combinations of the available data sets to extract a tensor asymmetry A_{zz}. The numbers in the circles denote the nuclei's m value of the corresponding data set. The averaged vector set consists of two subsets. The numbers 1, 5 and 6 are purely historical.

where also the polarizations can have a time dependence. Explicit expressions of collected numbers of events for specific conditions of target and beam are developed in App. B.1.

2.3.2 Cross section tensor asymmetries

The operation mode of the target allowed for at least three different ways of access to the tensor asymmetry, see Fig. 2.10. The `tensor plus` mode has originally been integrated in the flipping modes of the target as a consistency check for the A_{zz} extraction.
In the construction of a tensor asymmetry from the collected data, one has to recall Eqs. 2.20 and 2.22. To account for real polarization values deviating from the ideal ones (see Tab. 2.2), one can choose two approaches: either by directly multiplying each yield N/L in the denominator by the corresponding real polarization values (like for $A_{zz}(5)$), following the $A_{\parallel}$ strategy, or by dividing by a suitably averaged, i.e. *effective* tensor polarization $\langle P_{zz} \rangle$ (like for $A_{zz}(1)$ and $A_{zz}(6)$). No difference in the result is expected between the two approaches, as for all target modes the relation $P_{zz}^{\mathrm{ideal}}/P_{zz}^{\mathrm{real}} \approx 1.2$ holds.
For $A_{zz}(1)$, the equivalence in the results between the standard $A_{zz}(1)$ (weighting with an effective tensor polarization) and the alternative $A_{zz}^{\mathrm{alt}}(1)$ (separate weighting of every yield by P_{zz}) is shown in Fig. 3.3.
The tensor asymmetries were extracted separately for the top and bottom detector half and were finally combined to a statistically weighted average for each measured x-bin according to Eq. A.5.

Vector vs. tensor minus $A_{zz}(1)$. For $A_{zz}(1)$, the averaged `vector` states are weighted against the `tensor minus` state, in Fig 2.10 illustrated by the dashed box. Neglecting the small corrections originating from the vector asymmetry, one obtains the following expressions for the standard $A_{zz}(1)$, which was used for the analysis, and $A_{zz}^{\mathrm{alt}}(1)$, the alternative approach described above on Pg. 41 (for the derivation of the full expression, see App. B.2):

$$A_{zz}(1) \simeq \frac{1}{\langle P_{zz}\rangle_1} \cdot \frac{\left[\left(\frac{N^{\leftrightarrows}}{L^{\leftrightarrows}}\right) + \left(\frac{N^{\rightrightarrows}}{L^{\rightrightarrows}}\right)\right] - 2 \cdot \left(\frac{N^0}{L^0}\right)}{\left[\left(\frac{N^{\leftrightarrows}}{L^{\leftrightarrows}}\right) + \left(\frac{N^{\rightrightarrows}}{L^{\rightrightarrows}}\right)\right] + \left(\frac{N^0}{L^0}\right)}, \tag{2.24}$$

where $\langle P_{zz}\rangle_1 \approx 83\%$ is the effective tensor polarization for the three considered target modes:

$$\langle P_{zz}\rangle_1 = \frac{|\,P_{zz}^{+}\,| + |\,P_{zz}^{-}\,| + 2 \cdot |\,P_{zz}^{0}\,|}{6}. \tag{2.25}$$

Similarily one obtains for the alternative approach:

$$A_{zz}^{\mathrm{alt}}(1) \simeq 2 \cdot \frac{\left[\left(\frac{N^{\leftrightarrows}}{L^{\leftrightarrows}}\right) + \left(\frac{N^{\rightrightarrows}}{L^{\rightrightarrows}}\right)\right] - 2 \cdot \left(\frac{N^0}{L^0}\right)}{|P_{zz}^{0}| \cdot \left[\left(\frac{N^{\leftrightarrows}}{L^{\leftrightarrows}}\right) + \left(\frac{N^{\rightrightarrows}}{L^{\rightrightarrows}}\right)\right] + (|P_{zz}^{+}| + |P_{zz}^{-}|) \cdot \left(\frac{N^0}{L^0}\right)}. \tag{2.26}$$

Tensor only $A_{zz}(5)$. For the calculation of A(5), the two `tensor` states are weighted against each other, in Fig. 2.10 illustrated by the dotted box. One obtains after the neglection of the small vector corrections (see App. B.3):

$$A_{zz}(5) \simeq 2 \cdot \frac{\left(\frac{N^{\Leftrightarrow}}{L^{\Leftrightarrow}}\right) - \left(\frac{N^0}{L^0}\right)}{|\,P_{zz}^{0}\,| \cdot \left(\frac{N^{\Leftrightarrow}}{L^{\Leftrightarrow}}\right) + |\,P_{zz}^{\Leftrightarrow}\,| \cdot \left(\frac{N^0}{L^0}\right)}. \tag{2.27}$$

Cross-check $A(4)$. To check the compatibility of the $A_{zz}(1)$ and the $A_{zz}(5)$ measurement, the two possible constellations with averaged `vector` states are compared to each other: once with the injection of nuclei with $m = \pm 1$ into the target cell at the same time, and once switching roughly every minute between the nuclei's $m = +1$ and $m = -1$ state (see Fig. 3.1 for illustration). This asymmetry is more or less expected to be zero:

$$A(4) := \frac{\left[\left(\frac{N^{\leftrightarrows}}{L^{\leftrightarrows}}\right) + \left(\frac{N^{\rightrightarrows}}{L^{\rightrightarrows}}\right)\right] - 2 \cdot \left(\frac{N^{\Leftrightarrow}}{L^{\Leftrightarrow}}\right)}{\left[\left(\frac{N^{\leftrightarrows}}{L^{\leftrightarrows}}\right) + \left(\frac{N^{\rightrightarrows}}{L^{\rightrightarrows}}\right)\right] + \left(\frac{N^{\Leftrightarrow}}{L^{\Leftrightarrow}}\right)} \approx 0, \tag{2.28}$$

see App. B.4. The experimental result is compiled in Tab. D.8.

Four-in-one $A_{zz}(6)$. For the asymmetry $A_{zz}(6)$, *all* target modes are taken together to build up an asymmetry, as indicated by the solid box in Fig. 2.10. $A_{zz}(6)$ follows the $A_{zz}(1)$-method, the factor 2/3 re-weighting the sum of the three data sets with $|\, m \,| = 1$ such that their effective statistics is relatively double to that of the tensor set. Neglecting the small vector terms, one obtains (for details of the derivation, see App. B.5):

$$A_{zz}(6) \simeq \frac{1}{\langle P_{zz} \rangle_6} \cdot \frac{\frac{2}{3}\left[\left(\frac{N^{\overset{\rightarrow}{\Leftarrow}}}{L^{\overset{\rightarrow}{\Leftarrow}}}\right) + \left(\frac{N^{\overset{\rightarrow}{\Rightarrow}}}{L^{\overset{\rightarrow}{\Rightarrow}}}\right) + \left(\frac{N^{\Leftrightarrow}}{L^{\Leftrightarrow}}\right)\right] - 2 \cdot \left(\frac{N^0}{L^0}\right)}{\frac{2}{3}\left[\left(\frac{N^{\overset{\rightarrow}{\Leftarrow}}}{L^{\overset{\rightarrow}{\Leftarrow}}}\right) + \left(\frac{N^{\overset{\rightarrow}{\Rightarrow}}}{L^{\overset{\rightarrow}{\Rightarrow}}}\right) + \left(\frac{N^{\Leftrightarrow}}{L^{\Leftrightarrow}}\right)\right] + \left(\frac{N^0}{L^0}\right)}, \tag{2.29}$$

with the effective tensor polarization for all target states $\langle P_{zz} \rangle_6 \approx 83\%$:

$$\langle P_{zz} \rangle_6 = \frac{|\, P_{zz}^{+} \,| + |\, P_{zz}^{-} \,| + |\, P_{zz}^{\Leftrightarrow} \,| + 3 \cdot |\, P_{zz}^{0} \,|}{9}. \tag{2.30}$$

The derivations of the expressions for the statistical error δA_{zz} on the tensor asymmetries are compiled in App. B.7.

Vector asymmetry $A_{\parallel}$. Using the ansatz

$$A := \frac{\left(\frac{N^{\overset{\rightarrow}{\Leftarrow}}}{L^{\overset{\rightarrow}{\Leftarrow}}}\right) - \left(\frac{N^{\overset{\rightarrow}{\Rightarrow}}}{L^{\overset{\rightarrow}{\Rightarrow}}}\right)}{\langle |\, P_B \cdot P_z \,|^{\overset{\rightarrow}{\Rightarrow}} \rangle \cdot \left(\frac{N^{\overset{\rightarrow}{\Leftarrow}}}{L^{\overset{\rightarrow}{\Leftarrow}}}\right) + \langle |\, P_B \cdot P_z \,|^{\overset{\rightarrow}{\Leftarrow}} \rangle \cdot \left(\frac{N^{\overset{\rightarrow}{\Rightarrow}}}{L^{\overset{\rightarrow}{\Rightarrow}}}\right)}, \tag{2.31}$$

where $\langle |\, P_B \cdot P_z \,|^{\overset{\rightarrow}{\Rightarrow}(\overset{\rightarrow}{\Leftarrow})} \rangle$ denotes the average product of beam and target polarization when both have the same (opposite) sign, and following the developed formalism, it turns out that for a spin-1 target

$$A_{\parallel} = A \cdot (1 + \frac{1}{2}\, P_{zz} A_{zz}). \tag{2.32}$$

Here P_{zz} is the average tensor polarization of the vector states, assuming

$$P_{zz} \approx P_{zz}^{+} \approx P_{zz}^{-}. \tag{2.33}$$

The $\frac{1}{2}\, P_{zz} A_{zz}$ factor in Eq. 2.32 describes the dilution of the vector asymmetry due to tensor effects, an impact arising from the non-vanishing contribution of the tensor asymmetry to the measured cross section from Eq. 2.13. The asymmetry $A_{\parallel}^{\mathrm{d}}$ extracted from Hermes deuteron data was corrected for this small dilution factor arising from the tensor asymmetry A_{zz} [75].
On the other hand, the impact of the vector asymmetry onto the measurement of the tensor asymmetry, quantified by small vector correction terms, turns out to be negligible because the vector polarizations of the vector states cancel each other except for 1%, because the vector polarizations of the tensor states are closed-to zero ($\mathcal{O}(1\%)$), and because data of opposite beam helicity and approximatively the same statistics are combined (see App. B for details).

3 Tensor asymmetry and structure function as measured by Hermes

3.1 Tensor data mismatch

As illustrated in Fig. 2.10 and developed in Sec. 2.3.2, the periodically alternating target modes allowed for several methods to extract the tensor asymmetry. $A_{zz}(1)$ (Eq. 2.24) and $A_{zz}(5)$ (Eq. 2.27), both combining subsamples of the complete tensor data set, are partially correlated measures for the same quantity. The physical basis for the measurement of the two asymmetries is identical; the only difference is that to obtain the vector averaged states, once the injection took turns between positive and negative vector polarization, and once the vector polarized particles were injected into the storage cell of the target at the same time, as illustrated in Fig. 3.1.

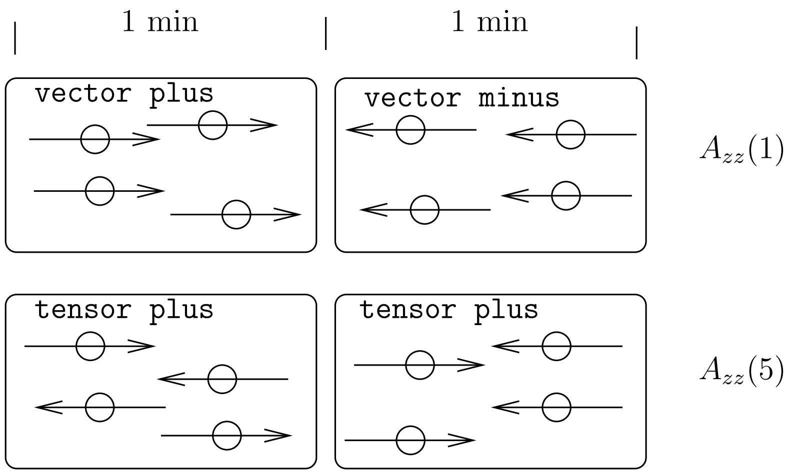

Figure 3.1: The boxes symbolize the content of the target cell for certain injection modes, each with a duration of about one minute. For $A_{zz}(1)$, the vector averaged states are achieved by an alternating sequence of positively and negatively polarized nuclei (upper row), for $A_{zz}(5)$ by their simultaneous injection (lower row).

Rather than combining *all* four target states in one asymmetry $A_{zz}(6)$ from the very beginning, the first step was to check the compatibility of the two vector averaged data samples. Indeed, as mentioned already, the `tensor plus` state has originally been integrated in the ABS cycling mode to check systematic effects.
Fig. 3.2 shows $A_{zz}(1)$ and $A_{zz}(5)$ (left panel) as extracted from Hermes data, revealing a deviation between the two asymmetries for some bins (see also Tab. D.8). This mismatch was quantified to be a 2-sigma-deviation[1], see Fig. 3.2, right panel, for the

[1]Error weighted mean over all x-bins according to Eq. A.5.

difference ΔA between $A_{zz}(1)$ and $A_{zz}(5)$ and its sigma deviation $\Delta A/\delta(\Delta A)$ from zero. The statistical error on ΔA (Eq. B.52) takes into account the partial correlation between the two asymmetries. Also displayed in Fig. 3.2 is the cross-check asymmetry $A(4)$ (Eq. 2.28) and its sigma deviation $A(4)/\delta A(4)$ from zero.
The mismatch is not correlated to the fact that different extraction philosophies were used for $A_{zz}(1)$ (weighting by an average effective tensor polarization) and $A_{zz}(5)$ (weighting each yield N/L separately by the corresponding tensor polarization). Fig. 3.3 illustrates that the two approaches applied to $A_{zz}(1)$ (as discussed in Sec. B) lead to identical results.
The mismatch was subject of systematic studies in which the data were further split with respect to a certain category. Still, splitting the data into many subsamples makes systematic studies a delicate matter from the statistical point of view as one runs the risk of loosing any statistical power, especially when dealing with small (close-to-zero) quantities like tensor asymmetries.

Time stability. In Fig. 3.4, the tensor asymmetries $A_{zz}(1)$, $A_{zz}(5)$ and $A(4)$ averaged over x were split into three time bins (of which the first two are at negative, the third at positive beam helicity, compare to Tab. D.1). The caption of Fig. 3.4 specifies the sigma deviations from bin to bin for each of the asymmetries: the time fluctuations of these quantities with rather small statistics do not appear to be statistically significant. Obviously it happens only by accident that for at least the last 2/5th of the data (those with positive beam helicity), the mismatch between $A_{zz}(1)$ and $A_{zz}(5)$ disappears. This behavior is again shown in Fig. 3.5, in which the tensor asymmetries are displayed versus x separately for the two beam helicities. The over the x-bins averaged $\Delta A/\delta(\Delta A)$ is 2.71 for negative and -0.52 for positive beam helicity ($\Delta A = A_{zz}(1) - A_{zz}(5)$), but only two of the six values $\Delta A(x)/\delta(\Delta A(x))$ for negative helicity deliver values larger than one (not shown in the figure). This means that due to the small remaining statistics in each bin, one cannot conclude that the mismatch *originates* from the time period with negative beam helicity.

Top and bottom detector half. Fig. 3.6 shows the tensor asymmetries extracted separately for the top and bottom detector halves. The deviation between top and bottom result seems to be worse for $A_{zz}(5)$ than for $A_{zz}(1)$. The t-test (lower panel) proves that the deviation is for neither of them statistically significant (see App. A.3), but clearly more pronounced for $A_{zz}(5)$. As a consequence, the tensor mismatch is smaller in the top detector half than in the bottom (see Fig. 3.7): less than one sigma deviation from zero for the top half, but two sigmas for the bottom (in the x-average). Moreover, the separate splitting for the top and bottom asymmetries into three successive time bins, as displayed in the right panel of Fig. 3.4, indicates a smoother time behavior of $A_{zz}(5)$ and $A(4)$ for the top detector than for the bottom one.

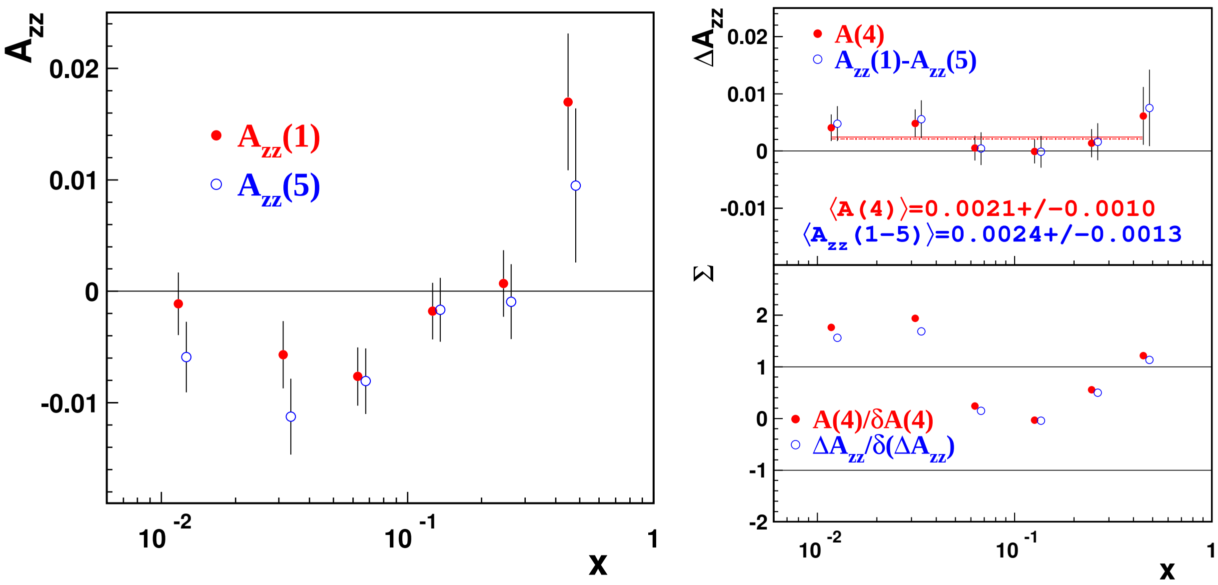

Figure 3.2: Left panel: the two tensor asymmetries $A_{zz}(1)$ and $A_{zz}(5)$; right top panel: tensor mismatch, i. e. the difference between $A_{zz}(1)$ and $A_{zz}(5)$ and the cross-check asymmetry $A(4)$. The denoted values are the error weighted mean values calculated over all x-bins, respectively. The lower right panel shows the sigma deviation Σ from zero.

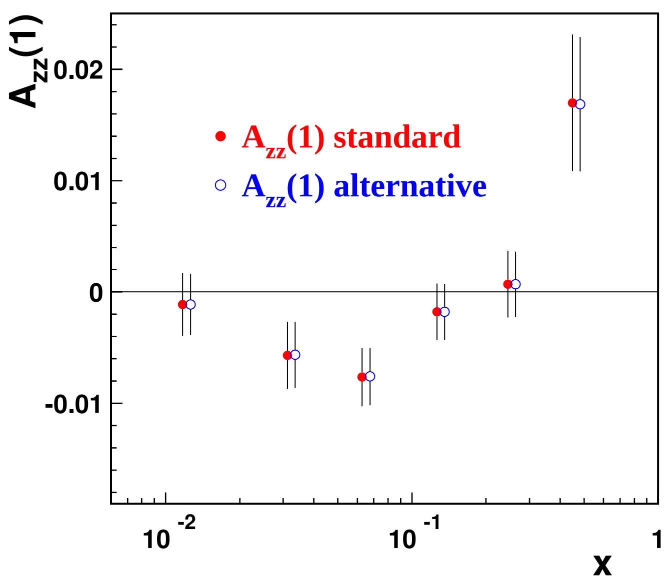

Figure 3.3: Comparison between the two methods to extract $A_{zz}(1)$ (which compares the vector averaged with the `tensor minus` state): once weighting the cross section asymmetry by an average effective tensor polarization (standard) and once weighting each yield N/L separately by the corresponding tensor polarization (alternative).

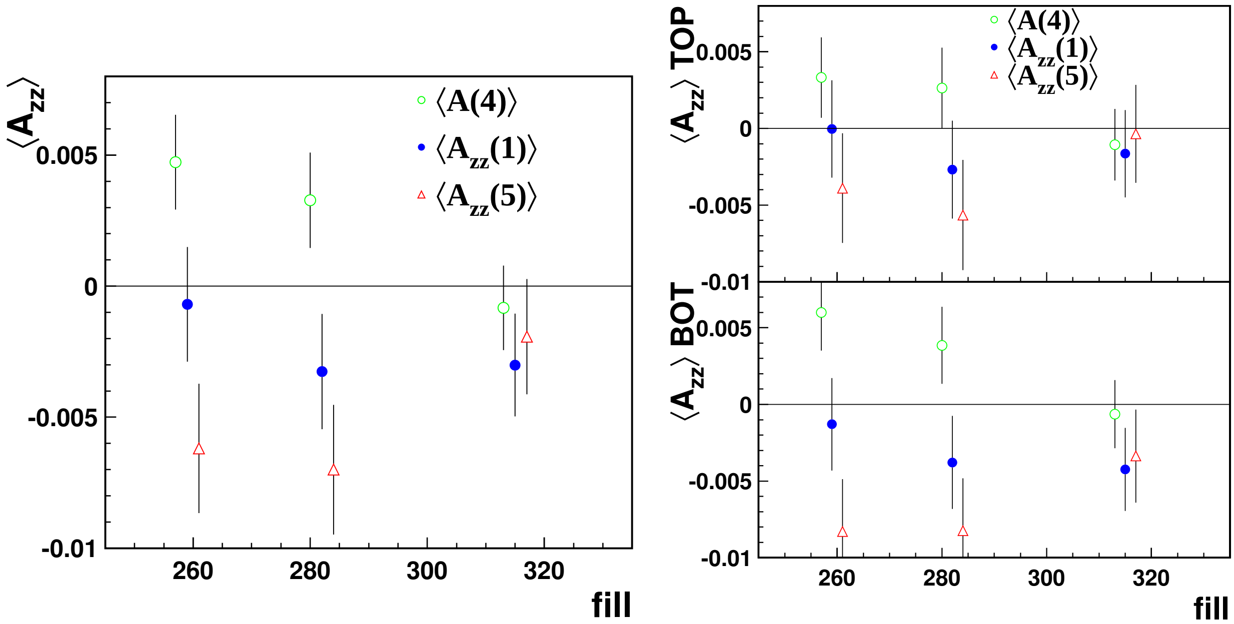

Figure 3.4: Left panel: time variation for $A_{zz}(1)$, $A_{zz}(5)$, and $A(4)$ for three sucessive time bins. Assuming independent measurements between the time bins, the sigma deviations from one time bin to another read: for $A_{zz}(1)$: 0.83, -0.09 (from time bin 1 to 3: 0.79); for $A_{zz}(5)$: 0.23, -1.53 (from time bin 1 to 3: -1.29); for $A(4)$: 0.57, 1.69 (from time bin 1 to 3: 2.30). Right panels: the same separately for top (TOP) and bottom (BOT) detector half.

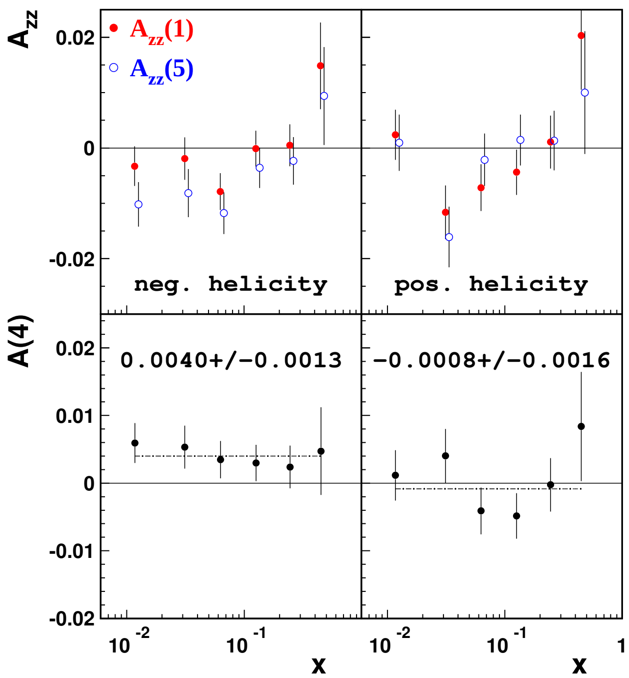

Figure 3.5: Top panels: comparison between $A_{zz}(1)$ and $A_{zz}(5)$ for each beam helicity separately; bottom: comparison for the cross-check asymmetry $A(4)$.

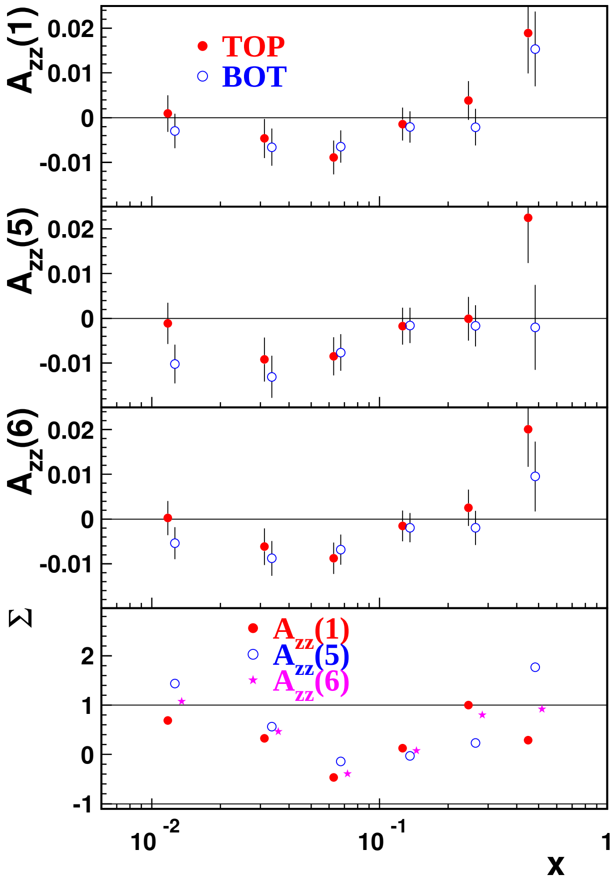

Figure 3.6: A_{zz} extracted separately for top (TOP) and bottom (BOT) detector half; the t-test showing the sigma deviation Σ (bottom panel) assumes independent measurements between the detector halves.

A possible reason for deviating measurements in the top and bottom half can be a misalignment of the detector. But $A_{zz}(5)$, being measured by the same apparatus, can trivially not be affected *to a greater extent* by a misaligned detector than $A_{zz}(1)$. Thus, a possible explanation has to consider a different mechanism.

For the inclusive analysis, the top and bottom detector halves can be regarded as independent of each other, as only one particle is detected in one half, and the other half is not being taken into account. The analysis chains for inclusive events detected in the top and bottom halves are decoupled from each other, as described in Sec. 2.2. The reason for the separate treatment is that the efficiencies and thus the data quality of the two detector halves are independent of each other. The extracted top and bottom asymmetries were averaged in the very end to get a “fair” mean asymmetry according to Eq. A.5.

To quantify the possible impact of data quality onto the result of the measurement, the asymmetries were also extracted *without* separating for top and bottom halves, i. e. all events were taken together from the very beginning, washing out any biases in

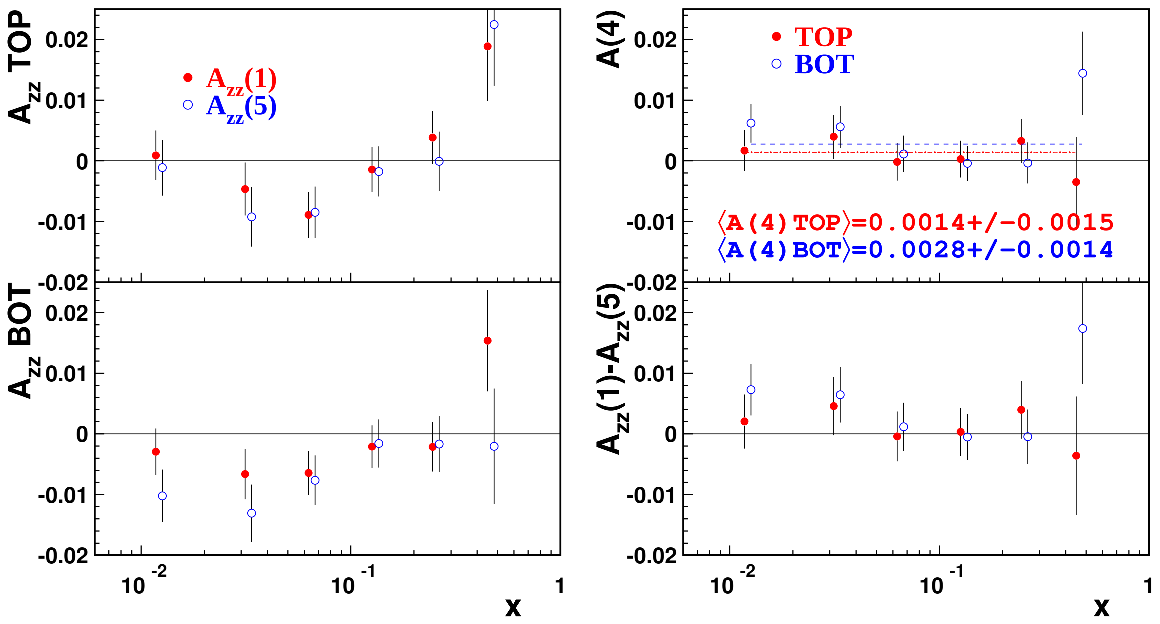

Figure 3.7: Tensor data mismatch separately displayed for top (TOP) and bottom (BOT) detector half. For the top detector half, the tensor mismatch is only one sigma, for the bottom half two sigma (right panel).

data quality between the two independent detetcors. Fig. 3.8 shows the result in comparison to the standard method. There is a constant offset in the absolute difference between asymmetries extracted with the two methods (lower panel): it is about 0.0009 for $A_{zz}(5)$, 0.0006 for $A_{zz}(6)$ and 0.0005 for $A_{zz}(1)$. Again, $A_{zz}(5)$ is mostly affected. This offset should (at least partially) be a measure for how much the efficiency differs between top and bottom halves; obviously, the `tensor plus` state is affected more than the others – but this can be only a pure accident and would probably have dropped out with more statistics.

Helicity balancing and impact of correction terms. The considered data were taken at two different electron beam helicities (see Tab. D.1), resulting in different statistics for each period (62% resp. 38%). The 2-sigma-deviation of $\langle A(4)\rangle$ from zero was checked not to vanish if an approximatively helicity balanced data sample was used by randomly selecting a subsample of the larger samples of the two (the one with negative helicity). The relative difference in luminosities $\Delta L/L$, as it is defined in App. B.2, thereby reduces from 0.22 to 0.02.

$\Delta L/L$ is one component of the small correction terms arising from an $A_{\|}$ contribution in the measurement of the tensor asymmetries (see App. B and there in particular App. B.6). Also the beam polarization and the residual vector polarizations of the tensor states enter these vector correction terms. A close-to-zero linear combination of tensor polarizations is a further correction term. All these correction terms were

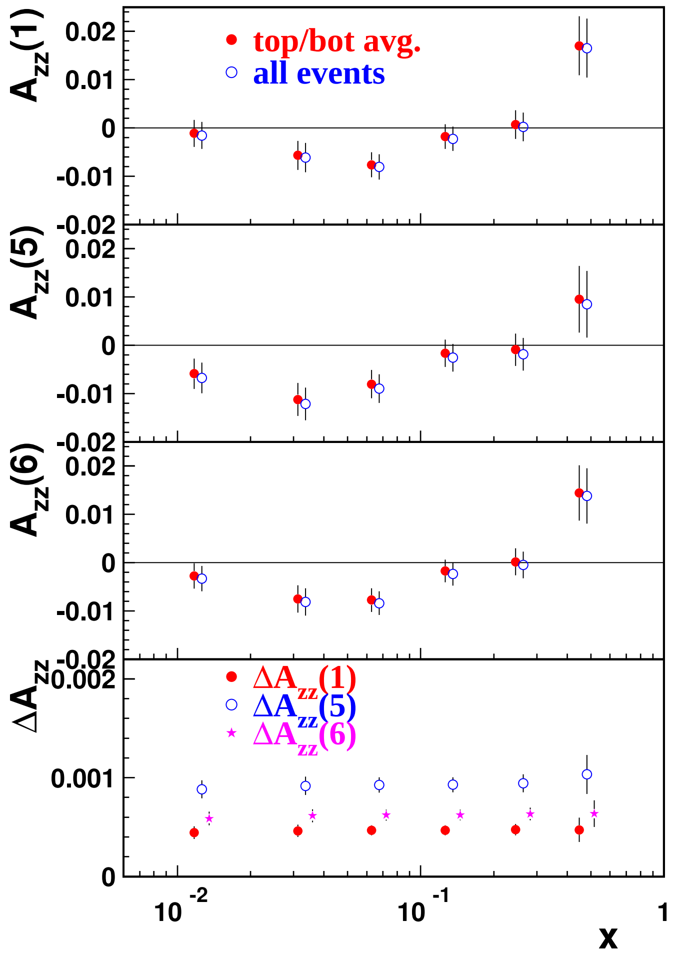

Figure 3.8: Tensor asymmetries (normalized to `lumifit`) extracted in two different ways: once averaged over top and bottom, once all events together. The lowest panel shows the absolute difference between asymmetries extracted with the two methods. This offset is identical for asymmetries normalized to beam current.

neglected in the final extraction of the tensor asymmetries. The mismatch between $A_{zz}(1)$ and $A_{zz}(5)$ was tested to not vanish when these asymmetries are extracted with the full formulas Eqs. B.14 and B.26; thereby, a fit to $A_{\|}^{\mathrm{d}}$ measured by HERMES was used. Furthermore, the order of magnitude of the mismatch is not affected by using even exaggerated assumptions about the actual beam and target polarizations by far exceeding the systematic uncertainties quoted in Tabs. D.1 and D.2. It was thus excluded that the mismatch is generated by a false measurement of the polarizations, which could theoretically be the case due to inefficiencies in the hyperfine transitions of the ABS and/or the BRP.

The performed studies could not reveal a concrete physical or instrumental origin of the mismatch between $A_{zz}(1)$ and $A_{zz}(5)$. Still, the 2-sigma-deviation from zero of the average of the corresponding cross-check asymmetry $A(4)$ does not allow to consider the mismatch to be a pure statistical fluctuation. It might have turned out that with more collected statistics, the difference of the two asymmetries had levelled out. Just as well it is not excluded that indeed a hard- or software problem occurred during data taking which can not be disentangled anymore on the offline stage of the analysis (like a synchronization problem in the target injection mode). Therefore the tensor asymmetry was extracted from all four target modes (the $A_{zz}(6)$ from Eq. 2.29), and the tensor mismatch was accounted for as a systematic uncertainty by assigning symmetrically half of the (over the x-bins) *averaged* $A(4)$,

$$\delta A^{\text{sys}}_{\text{mismatch}} = \frac{1}{2} \langle A(4) \rangle. \tag{3.1}$$

This number corresponds to the difference between $A_{zz}(1)$ and $A_{zz}(5)$, while the latter are partially correlated. In Fig. 3.9, the measured tensor asymmetry from all four target modes is displayed together with the systematic error band for the tensor data mismatch.

3.2 Results for the measured tensor asymmetry

Fig. 3.9 shows the measured tensor asymmetry $A_{zz}(6)$ including all four target states together with its systematic error arising from the tensor mismatch. The values of the measured $A_{zz}(6)$ and its statistical error for each x-bin are compiled in Tab. D.7.
In Fig. 3.10, left panel, $A_{zz}(6)$ is compared to $A_{zz}(5)$ and $A_{zz}(1)$, into which enter only subsamples of the complete tensor data set. The central values for $A_{zz}(6)$ lie between those for $A_{zz}(1)$ and $A_{zz}(5)$, and its statistical error is smaller than for the latter two. As a cross-check for the formalism, in the right panel of this figure $A_{zz}(6)$ is compared to the explicitly averaged $A_{zz}(1)$ and $A_{zz}(5)$ (Eq. B.56 in App. B.8). For the further analysis of the tensor asymmetry, $A_{zz}(6)$ is used solely.

3.3 The Born tensor asymmetry

The measured tensor asymmetry A_{zz} was corrected for radiative effects and detector smearing by the unfolding procedure discussed in App. C. Effects of electromagnetic showers were simultaneously accounted for. These corrections were also applied to the inclusive vector asymmetry $A_{\|}$ measured by Hermes [76], [75].

3.3.1 Event migration ("smearing")

Depending on Q^2 and ν (see Tab. 1.1), three basic channels are distinguished for lepton-nucleus-scattering [77]: elastic scattering where the lepton scatters off the nucleus as

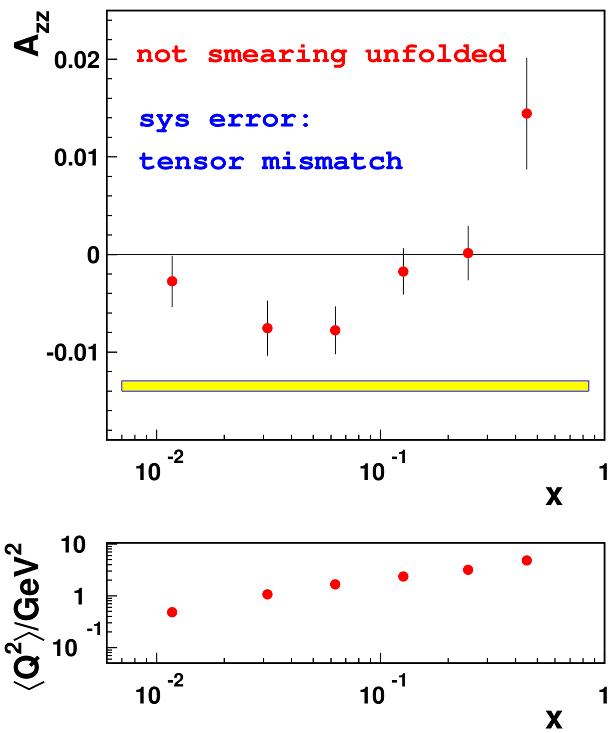

Figure 3.9: The tensor asymmetry $A_{zz}(6)$ including the entire tensor data set versus x-Bjørken; the systematic error band shows the uncertainty due to the tensor mismatch: $\frac{1}{2}\langle A(4)\rangle$ was assigned symmetrically (compare to Fig. 3.2). The lower panel shows the average measured Q^2 at each x-bin.

a whole, leaving the latter in its ground state ($\nu = Q^2/2M_A$, where M_A is the nuclear mass); quasi-elastic scattering where the lepton probes the individual nucleons in the nucleus ($\nu = Q^2/2M$, where M is the proton mass); and, when the pion threshold is reached, inelastic scattering where fragmentation of the nucleus occurs ($\nu \geq Q^2/2M + m_\pi$, where m_π is the pion mass).

On Born level[2], the measurement of the energy and the angle of the scattered lepton unambigiously delivers a set of two independent kinematic variables (like Q^2 and ν); this correlation breaks down as soon as QED radiative processes (internal bremsstrahlung) are involved, requiring to include the 4-momentum of the radiated real photon in the calculation of the event kinematics.

The observed total cross section σ_{obs} contains contributions from second-order QED

[2]The term Born *level* describes the experimentalist's point of view: Contaminated data are measured and have to be corrected in order to arrive at the desired Born level, whereas for the theorist, Born level is the approximation for which only single photon exchange and first-order QED corrections are considered.

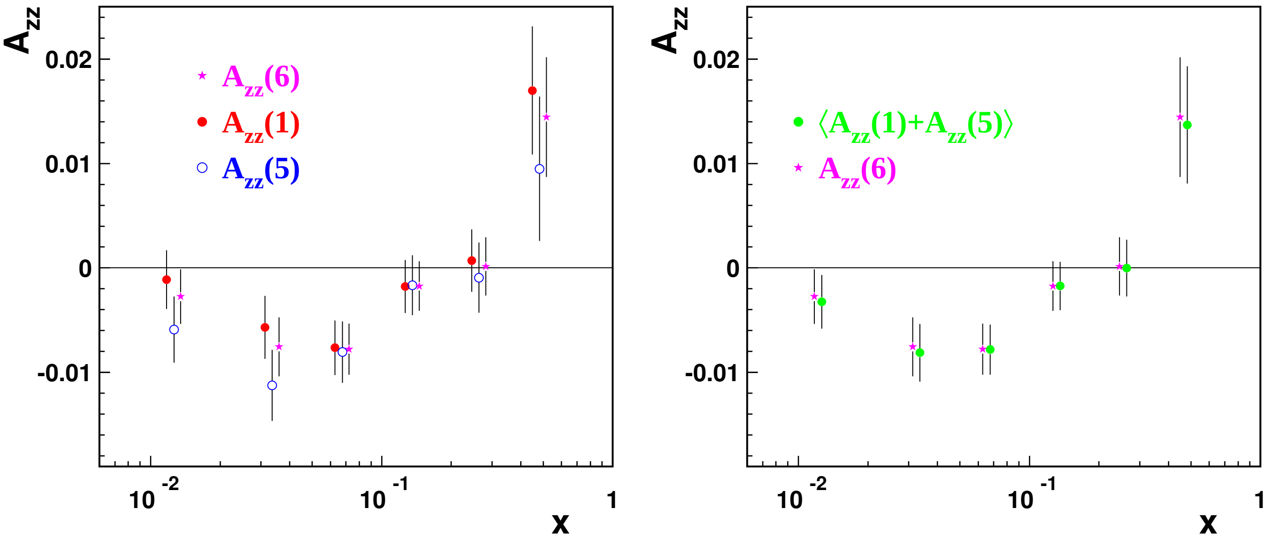

Figure 3.10: Left panel: the measured four-in-one $A_{zz}(6)$ compared to the measured $A_{zz}(1)$ and $A_{zz}(5)$; right panel: the measured $A_{zz}(6)$ compared to the averaged measured $A_{zz}(1)$ and $A_{zz}(5)$.

radiative corrections $\sigma_{\text{RC}} = \sigma_{\text{rad}} + \sigma_{\text{loop}}$ with one additional photon[3]:

$$\sigma_{\text{obs}} = \sigma_{\text{Born}} + \sigma_{\text{rad}} + \sigma_{\text{loop}}, \tag{3.2}$$

where σ_{rad} integrates for all three scattering channels the process that the scattered lepton can radiate a real photon shortly before or after the event vertex, and σ_{loop} further effects from loop corrections (vertex correction or vacuum polarization).

Furthermore, the scattered lepton can radiate a photon in the target or detector material (both called external bremsstrahlung, the latter detector smearing). The observer will thus record an event kinematics (energy of incident lepton E_{Beam}, scattered energy E'', scattering angle θ) which is in general not identical to the kinematics on BORN level (E, E'), see Fig. 3.11, top part.
Thus, when dividing the measured kinematic range into bins for the analysis of the extracted asymmetry, events which are sorted into a certain bin j on BORN level are observed in a possibly different bin i: events undergo a kinematic migration, as it is demonstrated qualitatively in the bottom part of Fig. 3.11. The observed x-BJØRKEN of a QED radiative event is principally *smaller* than the x-BJØRKEN on BORN level:

$$x_{\text{obs}} = \frac{Q^2}{2M\nu} = \frac{4E_{\text{Beam}}E''\sin^2(\theta/2)}{2M(E_{\text{Beam}} - E'')} \overset{\text{RC}}{<} \frac{4EE'\sin^2(\theta_{\text{Born}}/2)}{2M(E - E')} = x_{\text{Born}} \tag{3.3}$$

Events undergoing QED radiative effects thus always migrate to smaller x-bins. This

[3]The nth order of QED corrections contains contributions from $n-1$ additional photons; these contributions enter the perturbation series with a factor $1/\alpha^{n-1}$, where α is the fine structure constant.

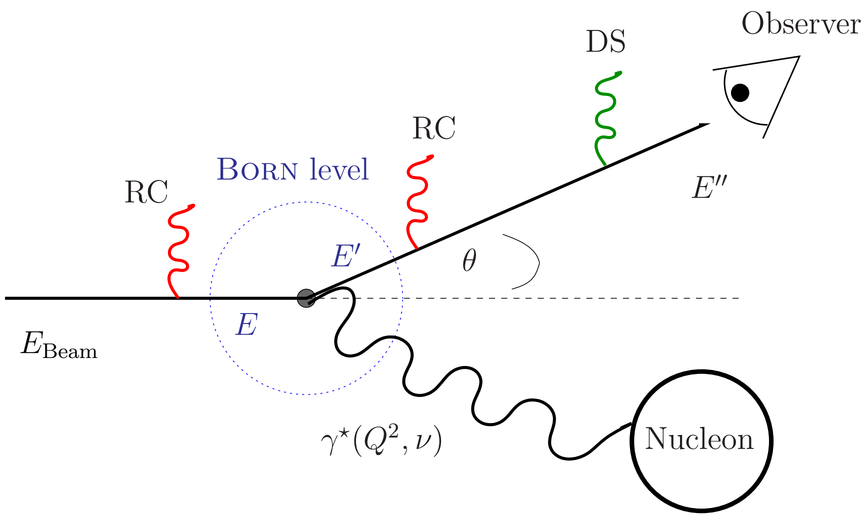

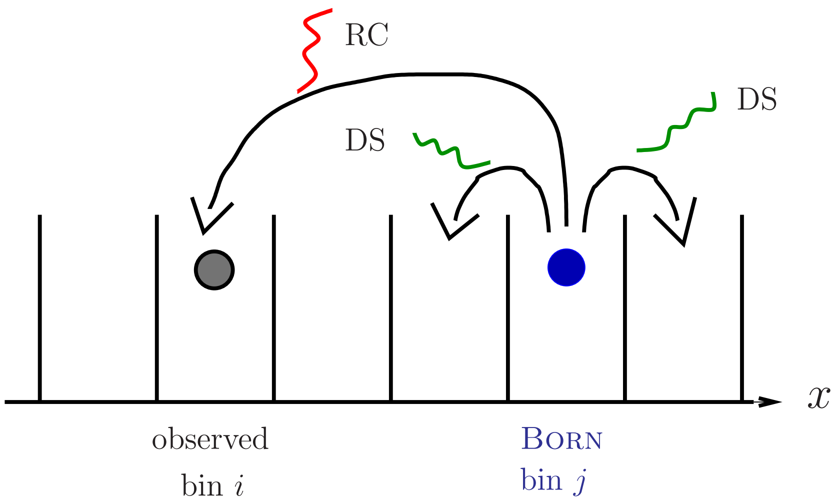

Figure 3.11: Top panel: the observer possibly sees a DIS event kinematics (E_{Beam}, E'') different from the kinematics on BORN level (E, E') due to second order QED radiative corrections (RC) and detector smearing (DS). The QED radiative process can either be Compton scattering (elastic) or inital/final state radiation (ISR/FSR, inelastic). These two contributions (elastic/inelastic) cause peaks in the Bethe-Heitler cross section at different scattering angles [78]. All these processes are summarized as *smearing effects* causing an event migration from BORN bin j to the observed bin i (bottom panel): QED radiative events always migrate to smaller x-BJØRKEN, events undergoing detector smearing migrate with the same probability to higher or lower bins in x. Loop corrections (vertex correction or vacuum polarization, not graphically represented in the top panel) which are as well second order QED radiative corrections, do not alter the kinematics of the scattered lepton and thus do not cause bin migration.

effect applies in particular to elastic and quasi-elastic events migrating to the very low measured x region where they are falsely observed as deep inelastic events (elastic and quasi-elastic background). Detector smearing results in a symmetrical broadening of the kinematic distributions[4]. Such instrumental effects can therefore make an event migrate to both smaller and larger x. For the Hermes detector, detector smearing is distinct for the kinematic region of large x, where the detector resolution (momentum and angle) deteriorates. Furthermore, detector smearing is the overall dominant process causing bin migration at large x, whereas the impact of QED radiative effects dominates the measured region at low x, where the contamination by the (quasi-)elastic background is concentrated.

In order to physically interprete the experimental data, these smearing effects must be taken into account and separated from the Born cross section. Generally, smearing processes occur in a statistical manner. They can therefore not entirely be corrected for by experimental methods; they have to be calculated (in the case of QED radiative effects) or simulated (in the case of external bremsstrahlung). The extent to which corrections have to be applied depends on the concrete experimental situation. Two examples from other facilities are supposed to illustrate that: for the extraction of its $A_{\parallel}$, SMC [79] applied a hadron tagged method for data $x < 0.02$ suppressing the elastic background and an iterative technique requiring a fit of world data on $A_{\parallel}$ [80] to handle the inelastic processes. The correction applied to the measured asymmetry A_{X} to obtain the Born level asymmetry A_{Born} involved a multiplicative term and an additive factor A_{RC}:

$$A_{\mathrm{Born}} = \frac{A_{\mathrm{X}}}{F_{\mathrm{RC}}} + A_{\mathrm{RC}}, \tag{3.4}$$

where F_{RC} serves as a radiative dilution factor. Generally, smearing corrections at SMC (which uses a muon beam) are expected to be smaller than at Hermes because muons radiative much less than electrons (both concerning QED effects as well as detector smearing). Secondly, the DIS experiments E143 [81] and E155 [82] at SLAC also applied the iterative technique[5] from Ref. [80] to their data. External bremsstrahlung is less pronounced (compared to Hermes) because the scattered leptons traverse less material. It is still worth to mention that Hermes has the advantage of operating a gaseous target in which neither external bremsstrahlung nor ionization losses occur.

Hermes has recently used an unfolding technique to correct for smearing effects[6], combining the radiative unfolding with corrections for detector smearing effects [85]. The term *unfolding* refers to the elimination of (systematic) correlations between different kinematic bins caused by the event migration, at the cost of introducing (statistical)

[4] A detector response is not delta-function-shaped, but follows a certain distribution with a finite width.

[5] See Refs. [83] and [84] for technical details.

[6] For the first application, see Ref. [72].

correlations between different kinematic bins: a complete representation of unfolded asymmetries requires not only the quotation of the asymmetry's central values and its statistical errors, but also the correlation matrix (Eq. C.25) of the latter.
The applied correction to obtain the asymmetry on Born level[7] followed the ansatz that not only the unpolarized and polarized Born section $\sigma^{\mathrm{U}}_{\mathrm{Born}}$ and $\sigma^{\mathrm{P}}_{\mathrm{Born}}$ enter the measured asymmetry A_{X}, but also unpolarized and polarized background $\Delta\sigma^{\mathrm{U}}$ and $\Delta\sigma^{\mathrm{P}}$, respectively:

$$A_{\mathrm{X}} = \frac{\sigma^{\mathrm{P}}_{\mathrm{Born}} + \Delta\sigma^{\mathrm{P}}}{\sigma^{\mathrm{U}}_{\mathrm{Born}} + \Delta\sigma^{\mathrm{U}}}. \tag{3.5}$$

With

$$A_{\mathrm{Born}} = \frac{\sigma^{\mathrm{P}}_{\mathrm{Born}}}{\sigma^{\mathrm{U}}_{\mathrm{Born}}}, \tag{3.6}$$

one obtains

$$A_{\mathrm{Born}} = A_{\mathrm{X}} \cdot \left(1 + \frac{\Delta\sigma^{\mathrm{U}}}{\sigma^{\mathrm{U}}_{\mathrm{Born}}}\right) - \frac{\Delta\sigma^{\mathrm{P}}}{\sigma^{\mathrm{U}}_{\mathrm{Born}}}, \tag{3.7}$$

with a multiplicative and an additive term like in Eq. 3.4. Here, *background* refers to that part of the cross section which smears into the selected kinematic bin, i. e. the term integrates both inter-bin migration within the detector acceptance and background from outside the acceptance.

The cross sections σ and the background terms $\Delta\sigma$ from Eq. 3.7 were obtained by Monte Carlo simulations. Each two types of Monte Carlo samples were produced with one certain set of parameterizations (F_2, R, A_{zz}, see Sec. 3.3.2) as input on the generation level GMC[8] by simulating the inclusive DIS cross section, generating DIS events with the PEPSI[9] generator [86]:

1. To obtain the $\Delta\sigma^{\mathrm{P(U)}}$ terms from Eq. 3.7, the *observed* cross section including second-order radiative corrections[10] was simulated ("experimental MC"):

   (a) HRC (**H**ermes **R**econstruction **C**ode): these productions included a description of the detector geometry and a simulation of the detector material based on the GEANT[11] tool [87]. The generated particles were tracked through the detector and were reconstructed as if they were real Hermes data ("fully tracked"), *or alternatively*

[7] With the center-of-mass energy of $\sqrt{s} = 7.5$ GeV at Hermes, only one-photon exchange (no Z^0) takes place.
[8] **G**eneration **M**onte **C**arlo, precisely: `gmc_NC` (**N**ext **G**eneration).
[9] **P**olarized **E**lectron **P**roton **S**cattering **I**nteractions.
[10] In accordance to the contributions to σ_{obs} from Eq. 3.2.
[11] **GE**ometry **AN**d **T**racking.

(b) HSG (**H**ERMES **S**mearing **G**enerator [88]): for these productions, the detector was simulated as one uniform piece of material.

Both HRC and HSG data samples contain thus information about how the kinematic distributions of the events broaden due to the interaction with the detector material (detector smearing). On a second stage, for this type of MC samples QED radiative corrections were applied to the generated kinematics by the RADGEN code [77] to obtain the *true* (BORN) kinematics[12]. Thus, the HRC and HSG productions provide a simulation of the measured cross section σ_{X} and the migration matrix $M_{\mathrm{X}}(i,j)$ containing the information about how many events in a given x-bin on BORN level migrate to which x-bin on the measured level both due to internal and external bremsstrahlung, see Figs. 3.12 and 3.13. The experimental Monte Carlo samples were produced in a slightly larger geometrical range[13] than the HERMES spectrometer does cover[14].

2. To obtain the $\sigma^{\mathrm{U}}_{\mathrm{Born}}$ terms from Eq. 3.7, a Monte Carlo sample without radiative corrections and tracking was produced which simulated the unpolarized BORN cross section within the acceptance of the HERMES spectrometer ("BORN MC"). $\sigma^{\mathrm{U}}_{\mathrm{Born}}$ was used for normalization in the unfolding algorithm (Sec. C.1).

Further details about these MC productions are compiled in App. C.6. The data samples from both MC types were in the subsequent analysis subject to the same kinematic (see Tab. D.4) and geometry cuts (see Fig. 2.2), including a fiducial volume cut, as the real data (see Fig.2.8). For the modelling of a fiducial volume in the BORN Monte Carlo, which does not contain the complete spatial track information, a momentum look-up table was employed which unambigiously maps the known track momentum to the track slope and position (see also Sec. 2.2).
An illustration how the observed and BORN kinematic variables x, Q^2 and ν are related to each other is given in Fig. 3.14. The degree to which the default Monte Carlo sample agrees to the measured data with respect to kinematic and geometrical quantities is illustrated in Fig. 3.15; thereby, a perfectly aligned detector was assumed. A study on the misalignment of the detector is performed in Sec. 3.4.6.
Details about how to extract average kinematic variables and cross section asymmetries from Monte Carlo samples by performing a Monte Carlo weight method are compiled in App. C.6. From there follows that quoting generated event *numbers*[15] does not provide an information about the statistical power of the produced Monte Carlo samples

[12] Only single photon exchange (no Z^0) and pure QED corrections are considered.
[13] The extended range is: $|\,\theta_x\,| < 180$ mrad, 35 mrad $< |\,\theta_y\,| < 150$ mrad.
[14] The box acceptance of the spectrometer is: $|\,\theta_x\,| < 170$ mrad, 40 mrad $< |\,\theta_y\,| < 140$ mrad.
[15] For completeness: the HRC samples were generated with 24 M DIS events, the HSG samples with 150 M DIS events, and the BORN samples with 50 M DIS *per spinstate*.

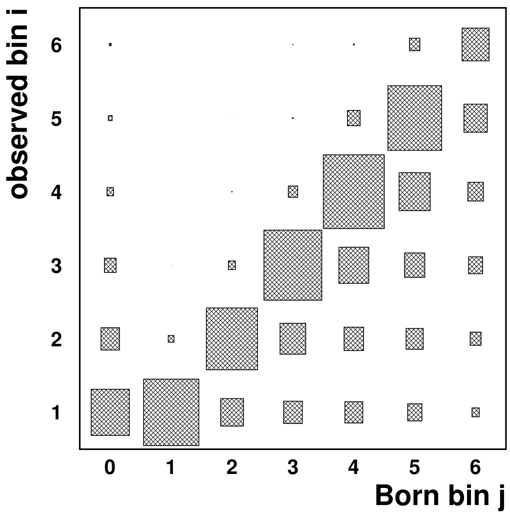

Figure 3.12: Graphical representation of the (unpolarized) migration matrix $M_{\mathrm{X}}(i,j) = 2M^{+}_{\mathrm{X}}(i,j) + M^{-}_{\mathrm{X}}(i,j)$ of the MC production used to obtain the final Born tensor asymmetry. It contains the information how many events (picobarn) from Born bin j (x-axis) migrated to observed bin i (y-axis) due to radiative effects and detector smearing. Born bin 0 integrates all events which smear *into* the Hermes acceptance.

because it is not the pure numbers which enter the asymmetries and their statistical error, but rather a re-weighted number. To compare the statistics available from real data and the Monte Carlo simulations, respectively, one should employ the statistical error on the unfolded data asymmetry $\delta A^{\mathrm{Born}}_{zz}(\mathrm{stat})$ and the statistical error $\delta(\mathrm{MC})$ which is calculated from the MC sample according to Eq. C.29, see Tab. D.10. $\delta(\mathrm{MC})$ gives an estimate on the uncertainty due to the limited MC statistics and scales with the statistical error of the unfolded reconstructed MC asymmetry and is equal to the latter within a 10% range. The default Monte Carlo sample delivers a $(\delta A^{\mathrm{Born}}_{zz}(\mathrm{stat})/\delta(\mathrm{MC}))^2 \approx 3^2 = 9$ times higher statistical accuracy than the measured data sample. This ratio was considered to be sufficiently large in order to neglect $\delta(\mathrm{MC})$.

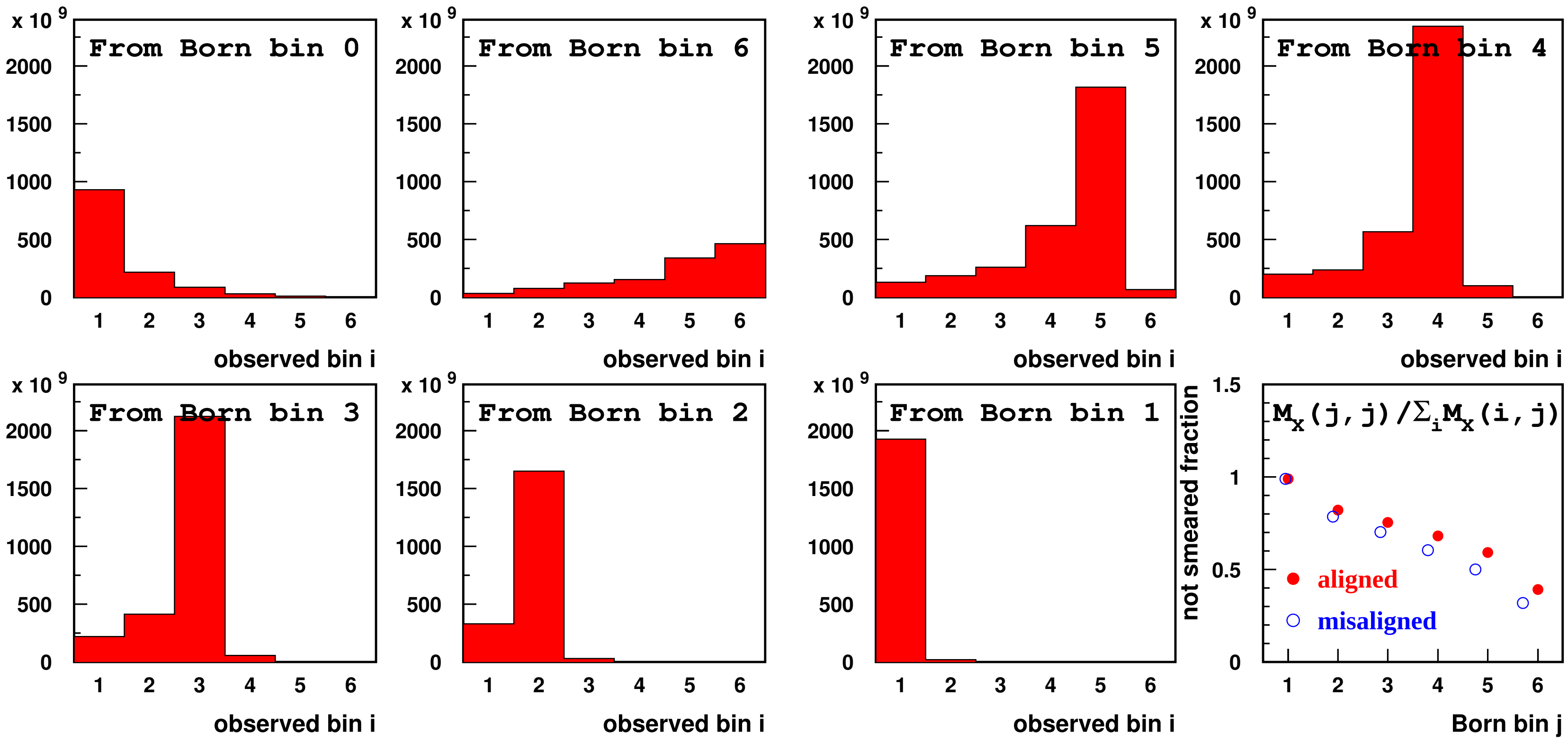

Figure 3.13: Vertical slices through the (unpolarized) migration matrix $M_{\mathrm{X}}(i,j)$ from Fig. 3.12 showing how many events (picobarn) from a given Born x-bin j migrate into which observed x-bin i. The contributions $i \neq j$ are denoted as unpolarized *background* in the observed bin i. Radiative effects make events migrate to *smaller* x, in fact mostly to neighboured x-bins and with a decreasing frequency to x-bins farer away from the given Born bin. The small fraction of events migrating to *higher* x-bins undergoes detector smearing, a process symmetrical in x. The top left panel represents the observed bin distribution of events smearing *into* the detector acceptance (from Born bin 0). The bottom right panel shows the fraction of events which do *not* smear, i. e. which are observed in bin $i = j$. The plot demonstrates that the inter-bin migration within the acceptance is pronounced for large x, the domain where detector smearing is dominant. The open circles illustrate the situation for a misaligned detector: systematically more events migrate (see Sec. 3.4.6).

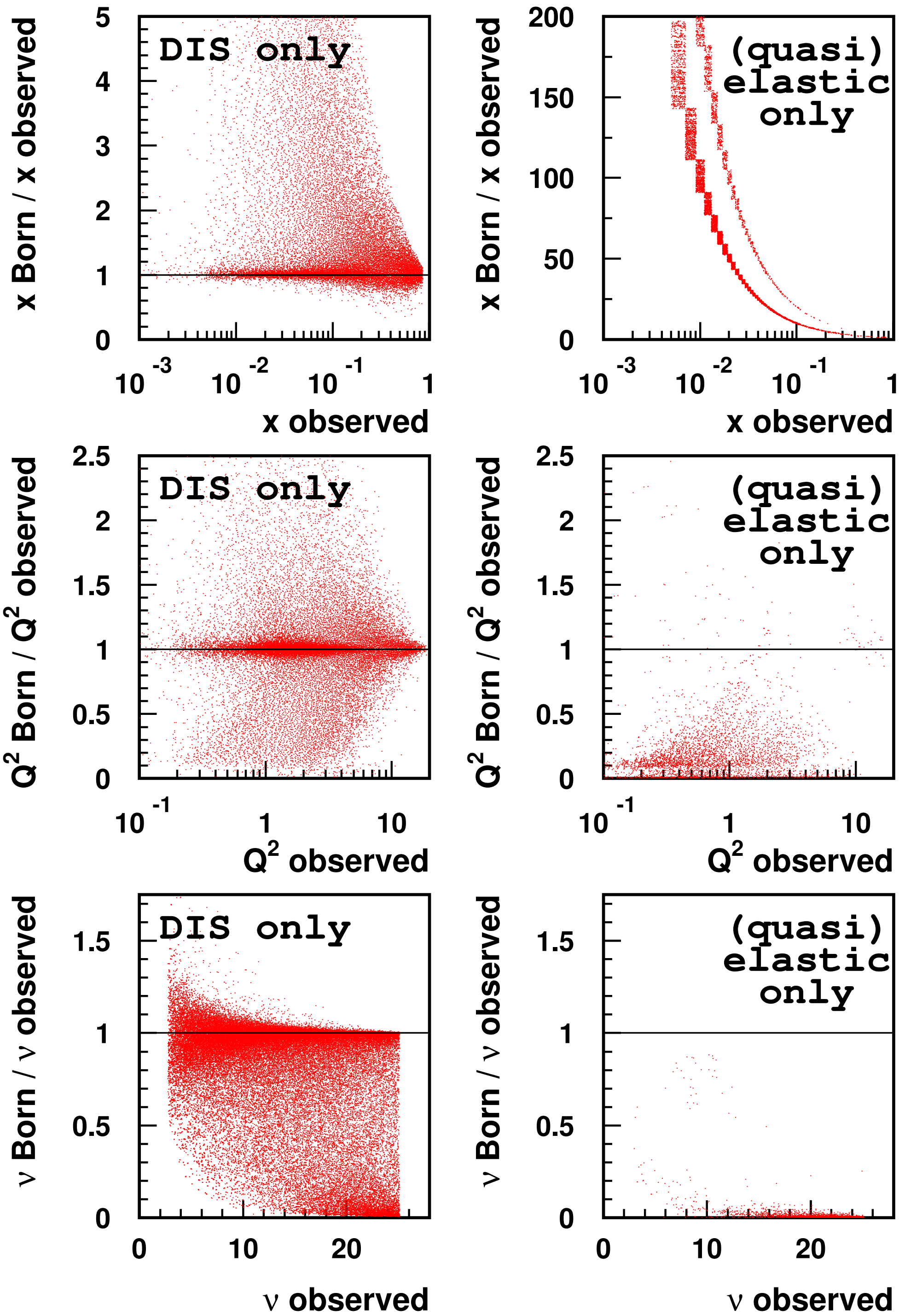

Figure 3.14: The observed kinematics for selected variables is plotted versus the ratio (Born/observed) from a fully tracked MC (after kinematic and geometry cuts), the left panels showing only DIS events, the right panels only elastic and quasi-elastic events. For x-Bjørken (top panels), this reveals that a great part of the inclusive events observed at low x_{obs} actually stems from a wide spread of values of $x_{\mathrm{Born}} > x_{\mathrm{obs}}$ due to QED radiative effects. The right top panel shows the quasi-elastic ($\mathrm{f}(x_{\mathrm{obs}}) = 1/x_{\mathrm{obs}}$) resp. elastic ($\mathrm{f}(x_{\mathrm{obs}}) = 2/x_{\mathrm{obs}}$) hyperbola. The smearing in Q^2 (middle panels) is rather symmetrical. The (quasi-)elastic background is mainly reconstructed at small $Q^2_{\mathrm{obs}} > Q^2_{\mathrm{Born}}$ and large $\nu_{\mathrm{obs}} > \nu_{\mathrm{Born}}$ (bottom panels).

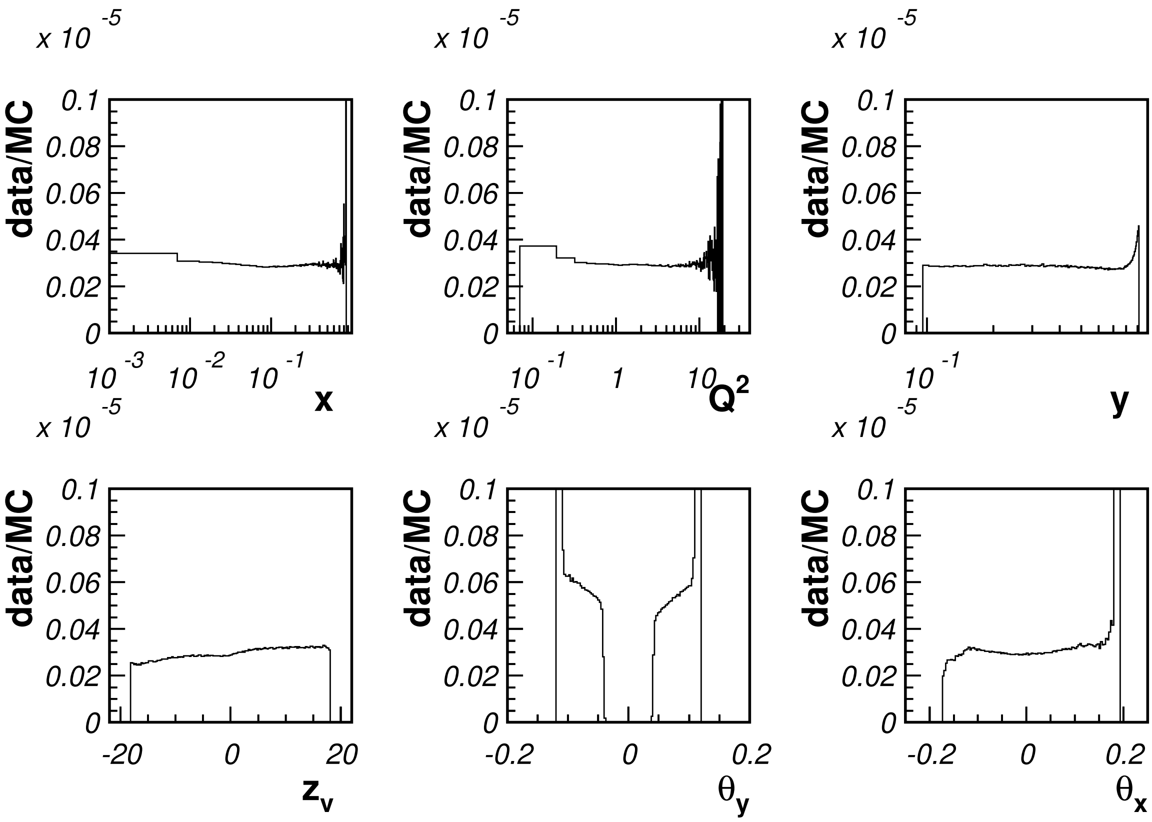

Figure 3.15: Comparison between data and Monte Carlo (fully tracked production): for selected kinematic (top row) and geometrical quantities (bottom row), the ratio data/MC is plotted. The Monte Carlo sample was produced under the assumption of a perfectly aligned detector.

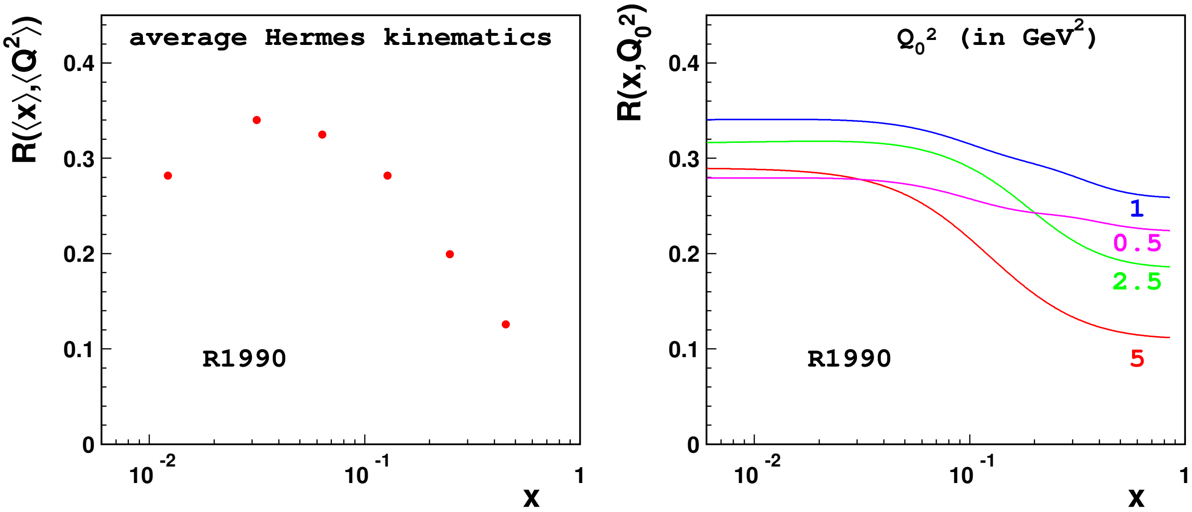

Figure 3.16: $R(x, Q^2)$ in the $R1990$ parameterization; left panel: for average HERMES kinematics $(\langle x\rangle, \langle Q^2\rangle)$ in the binning used to extract the tensor asymmetry, right panel: for fixed Q_0^2.

3.3.2 MC input parameterizations

The unfolding procedure required the production of Monte Carlo data samples with certain input parameterizations to both model the unpolarized and polarized BORN cross section. The latter is needed due to the spin dependence of radiative corrections which are calculated by the RADGEN code. Furthermore, the RADGEN code was fed with parameterizations of the deuteron dipole and quadrupole form factors from Refs. [89], [90] in order to estimate the elastic and quasi-elastic radiative tails. The polarized part of the quasi-elastic radiative tail was neglected, which is justified when the scattering process is considered to happen on a spin-$\frac{1}{2}$ object with no tensor effect [61].

Unless otherwise noted, as default for $R(x, Q^2)$ (Eq. 1.13), the $R1990$ parameterization [91] was used. $R(x, Q^2)$ in the $R1990$ parameterization for average HERMES kinematics and for fixed Q_0^2 is displayed in Fig. 3.16. To simulate the unpolarized BORN cross section, for the spin-independent structure function $F_2^{\rm d}(x, Q^2)$ of the deuteron, the ALLM97 parameterization[16] of the precisely measured $F_2^{\rm p}$ [92] was employed as default, rescaled[17] by the fit to the ratio $F_2^{\rm n}/F_2^{\rm p}$ performed by the NMC collaboration [93]:

$$F_2^{\rm d} = \frac{1}{2}\, F_2^{\rm p}(1 + \frac{F_2^{\rm n}}{F_2^{\rm p}}) \equiv (F_2^{\rm p})_{\rm ALLM} \cdot \left(\frac{F_2^{\rm d}}{F_2^{\rm p}}\right)_{\rm NMC} . \tag{3.8}$$

[16] Obtained by a fit to $F_2^{\rm p}$ world data: H1 (95, 96, 97), ZEUS (94, 96), E665 (1996), BCDMS (1989), NMC (1997) and SLAC (1990) (the numbers in brackets indicate the year of the publication). No errors are quoted for the fit. The ALLM parameterization is based on a Regge motivated approach.

[17] Compare to Eq. 1.23.

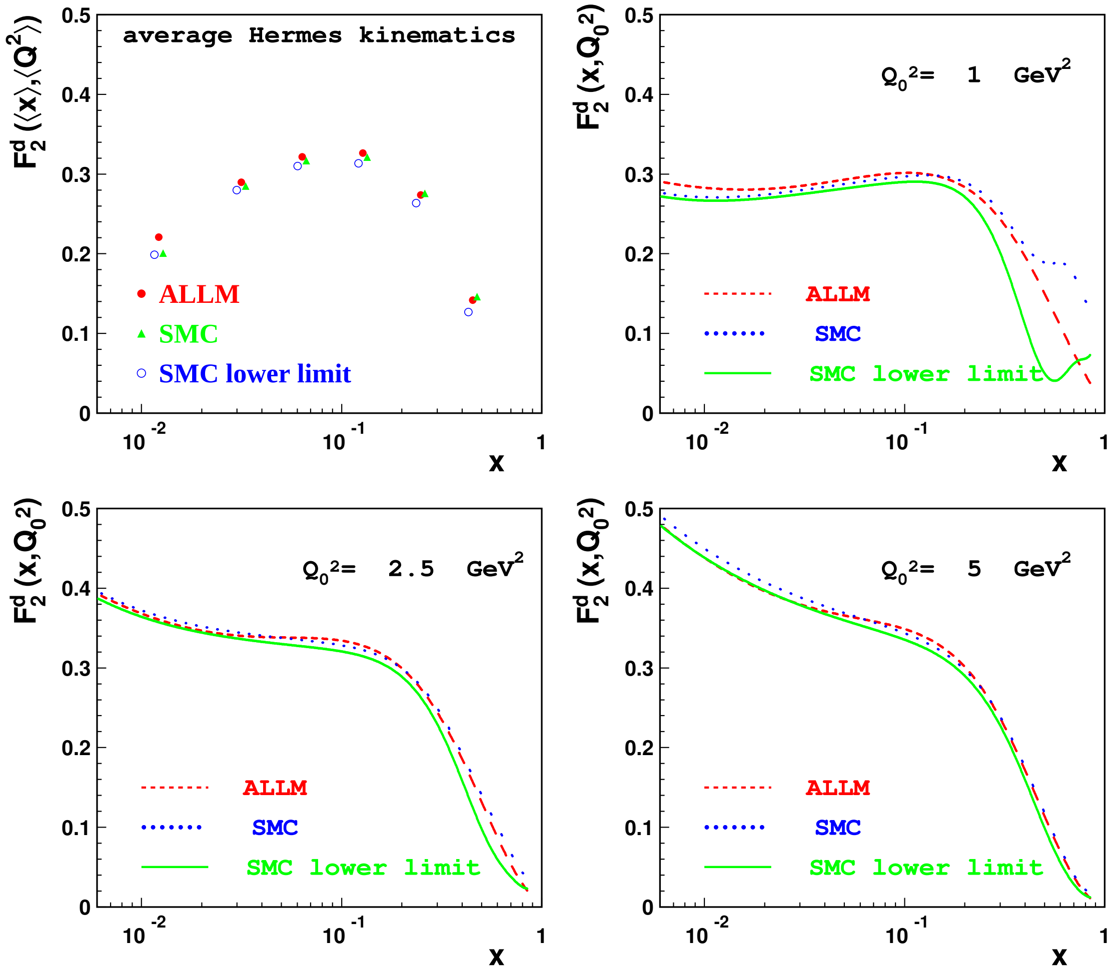

Figure 3.17: Comparison between different parameterizations for $F_2^{\mathrm{d}}(x, Q^2)$: the ALLM97 (for which a fit to proton F_2 data was multiplied by a fit to $F_2^{\mathrm{n}}/F_2^{\mathrm{p}}$ data to obtain the F_2 of the deuteron) and SMC (from 1998); left top panel: for average Hermes kinematics ($\langle x\rangle, \langle Q^2\rangle$) in the binning used to extract the tensor asymmetry, right top and bottom panels: for fixed Q_0^2.

This function is displayed in Fig. 3.17 together with the 15 parameter fit of the SMC collaboration (P15) to $F_2^{\mathrm{d}}(x, Q^2)$ data[18] and its lower limit (P15ℓ) [94] which were employed for systematic studies (Sec. 3.4.4). The lower and upper limits of the P15 fit correspond to its total (statistical and systematic) uncertainty and lie symmetrically around the fit.
To obtain a parameterization of the Born tensor asymmetry needed as input to the Monte Carlo in order to model the polarized Born cross section, the measured asymmetry was corrected for the radiative background on a first level using the POLRAD code [95]. This corrected asymmetry was fitted ("1st fit") and was used as default

[18] The P15 fit for the deuteron contains data from BCDMS (1989), E665 (1996), NMC (1997), SLAC (1992) (the numbers in brackets indicate the year of the publication).

input to the MC in the following. A second fit of A_{zz} on BORN level was obtained from the first unfolding iteration ("2nd fit"). These two input parameterizations of the tensor asymmetry and the BORN asymmetries that were reproduced by the Monte Carlo are shown in Fig. 3.18, left panel. Reconstructed MC and measured asymmetries are seen to agree within statistics, see Fig. 3.18, right panel.

3.3.3 Unfolding of measured data

The BORN tensor asymmetry A_{Born} was obtained from the measured asymmetry A_{X} by applying the unfolding algorithm developed in App. C. The measured asymmetry was corrected in every x-bin for the polarized and unpolarized background due to QED radiative and detector smearing effects according to Eq. C.20.
In order to test the unfolding code, the reconstructed Monte Carlo asymmetry was unfolded; the result is identical to the asymmetry on BORN level[19], see Fig. 3.19 (left panel). Thus, for the low-x-region, data points are shifted down by the unfolding procedure. This can be well understood by comparing the reconstructed MC asymmetry to a MC asymmetry from only elastic and quasi-elastic events and from only DIS events, respectively (Fig. 3.19 right top): the elastic asymmetry is positive, the pure DIS asymmetry negative (to a larger extent than the asymmetry from *all* events) for small-x. One basic goal of the unfolding procedure is to correct for the (quasi-)elastic background; i. e., by removing the positive elastic contribution, it lowers the points. The right bottom panel shows a comparison between the unfolded MC and the DIS only asymmetry, the latter not corrected for *inter*-bin migrations due to radiative and detector smearing effects. In the case of $A_{\|}$, the central values of the asymmetry are shifted down by the unfolding procedure to a by far lesser extent because for A_{zz}, additionally the quadrupole form factor of the deuteron is taken into account, increasing the relative magnitude of the polarized elastic tail.

Apart from the so far discussed fact that as well the incoming beam leptons can radiate a hard photon before they scatter off the target nuclei as the scattered leptons can radiate such a photon or can undergo detector smearing, effects which are both corrected for by the unfolding algorithm, there is a secondary effect which has to be accounted for in the unfolding: the radiated photons can hit the HERMES detector frames surrounding the beam line in the front region of the detector, producing electromagnetic showers with a large amount of photons and soft electron-positron pairs. The latter leave a signal in the multi wire chambers, entailing high event mulitplicities which can cause the electronics not to accept the event – it is lost for analysis (see Refs. [78] and [75] for further details). This tracking inefficiency concerns mainly elastic ($x_{\mathrm{Born}} = 2$) and quasi-elastic ($x_{\mathrm{Born}} = 1$) events[20] in which hard photons are radiated. Not taking

[19]From the BORN MC sample.
[20]Deuterium target.

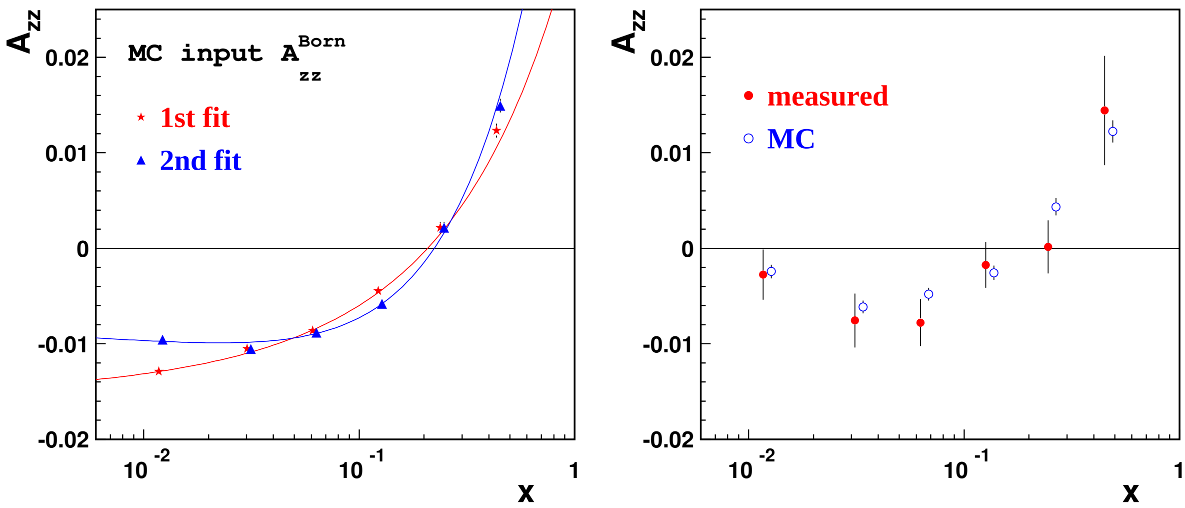

Figure 3.18: Left panel: A_{zz} parameterization used as input in the Monte Carlo (lines) and the Born asymmetries (points) that are reproduced by the Born Monte Carlo using two different fits for A_{zz}; right panel: asymmetries reconstructed from the experimental MC and measured Hermes data ($A_{zz}(6)$).

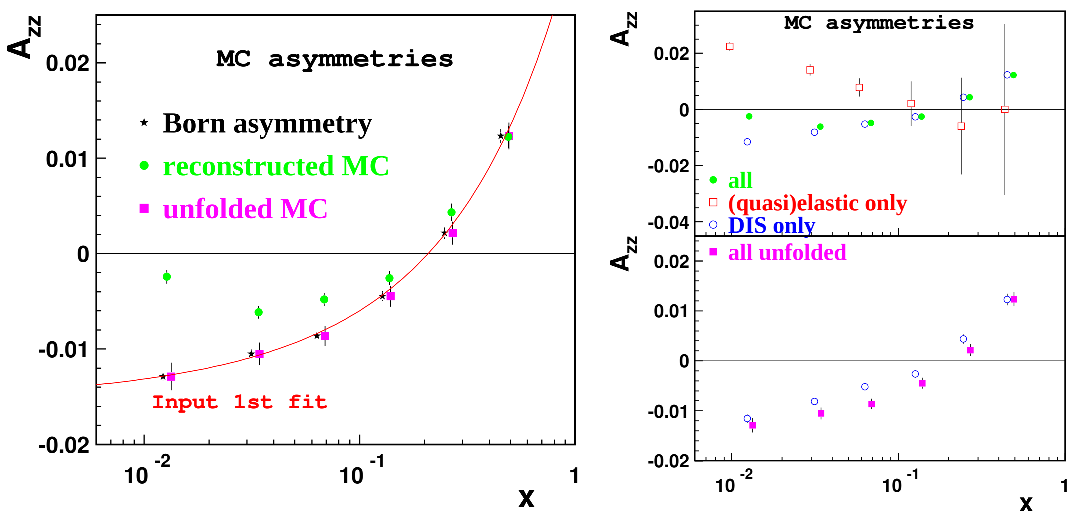

Figure 3.19: Unfolding test (left): the unfolding brings back the MC reconstructed asymmetry to the Born asymmetry; right: asymmetry reconstructed from the experimental MC from (quasi-)elastic and DIS events only, respectively (top), and comparison between the unfolded experimental MC and the DIS only asymmetry (bottom).

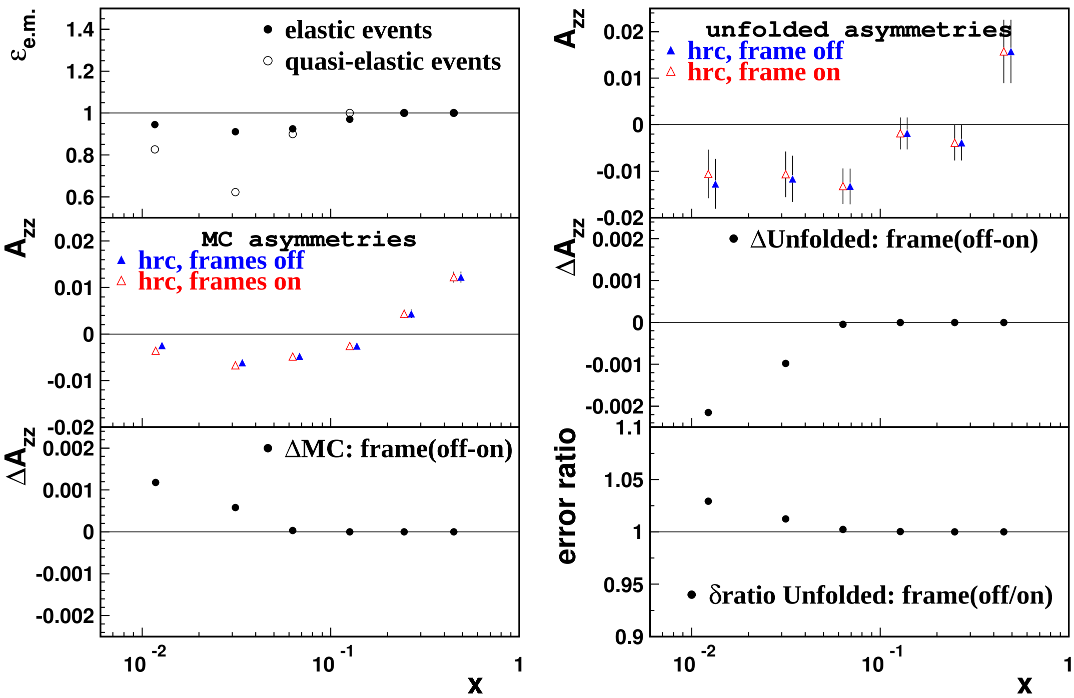

Figure 3.20: Left: detector efficiency for elastic and quasi-elastic events (top) and comparison of MC asymmetries with frame turned on/off (middle and bottom); right: comparison of unfolded asymmetries (not) taking into account electromagnetic shower background.

into account this electromagnetic shower background can pretend the R-ratio to be A-dependent [78].
The treatment of electromagnetic showers from the detector frames (i. e. material outside the acceptance) was *not* implemented in the default tracked Monte Carlo production, as its inclusion in the reconstruction process (HRC) is very CPU-intensive. This Monte Carlo production is therefore not affected by the discussed detector inefficiency and contains more (quasi-)elastic events than real data, for which a certain percentage of these event types was not reconstructed. Thus, when unfolding with such a MC sample, it corrects for *more* (quasi-)elastic events than have actually been reconstructed in the experiment. The actual detector efficiency for elastic and quasi-elastic events $\epsilon_{\text{e.m.}}$ (e.m. $\equiv$ electromagnetic) was determined [96] by comparing the number of (quasi-)elastic events in two parallel sets of Monte Carlo – once with detector frame "turned off" and once "on", see Fig. 3.20 left top panel: for small x, $0 < \epsilon_{\text{e.m.}} < 1$ with a minimum at $x \approx 10^{-2}$ and $\epsilon_{\text{e.m.}} = 1$ for large-x.
In a next step, $\epsilon_{\text{e.m.}}$ was used to correct the weights of the elastic and quasi-elastic events in the standard MC[21]; an estimation of the changes in the reconstructed MC

[21] In the notation from App. C.6, the new weight of event k is $\omega_k \cdot \epsilon_{\text{e.m.}}$. Only the experimental MC is corrected, not the Born MC.

asymmetry associated with this procedure is displayed in the middle and bottom left panels of Fig. 3.20. Finally, A_{zz} was unfolded with the corrected MC. The right part of Fig. 3.20 shows the impact on the unfolding of the data asymmetry: for low-x, data points lie a bit higher, and error bars are a bit smaller for the "on"-case; this is because the unfolding now corrects less. To account for electromagnetic showers in the final unfolded asymmetry, the weight-corrected MC was used for unfolding.

The measured Hermes tensor asymmetry unfolded with the default parameterizations is shown in Fig. 3.21 (left panel) in comparison to the raw measured asymmetry. Tab. D.10 compiles the values for A_{zz} and its statistical error on Born level for each x-bin.
The central values of the tensor asymmetry on Born level represent independent measurements, whereas before unfolding the data points depend on part of the other data points due to the fact that a certain fraction of the events for an individual bin actually stems from a different kinematic region. By removing these systematic correlations between bins, the unfolding procedure introduces a statistical correlation between bin i and j which is encoded in the covariance matrix of the Born statistical errors $\mathrm{cov}(j,i)$ (Eq. C.23); its elements are displayed in Fig. 3.22 and quoted in Tab. D.11. The usual two-dimensional graphical representation of the Born level asymmetry (A_{zz} vs. x-Bjørken with a vertical error bar through every data point), however, reveals only the main diagonal elements of the covariance matrix which are the square of the statistical error on Born level. Every data point on Born level is a stand-alone measurement, its error bar denoting the statistical accuracy to which the measurement has been performed. The inflation of the statistical error coming along with the unfolding procedure is shown in Fig. 3.21 (right panel). One has to interprete this inflation carefully: the statistical error is indeed *underestimated* before unfolding the radiative effects.
As soon as these single measurements are merged together in order to investigate a global property *integrated* over the considered kinematic range like for the calculation of moments (see Sec.3.7) or for the performance of QCD fits, however, these statistical correlations between bins have to be taken into account by including into the integration the mostly negative side diagonal elements, avoiding double-counting of statistical uncertainties (see App. C.5).
In contrast to the Hermes $A_{\parallel}$ analysis [75], [97], there is no decrease of the statistical error after unfolding by binning additionally in Q^2 and averaging afterwards over Q^2 [96]. Unfolding $A_{\parallel}/D(x,Q^2)$ for a given x-bin separately in one high- and one low-Q^2 bin and averaging afterwards over Q^2, results for the x-bin in question in a smaller statistical error compared to *not* binning in Q^2, because events with low Q^2 (corresponding to high D at Hermes) have a higher probability of being detected at lower x (i. e. they cause error inflation coming along with the unfolding to a larger extent) than events with high Q^2 (corresponding to low D at Hermes). Thus, the additional

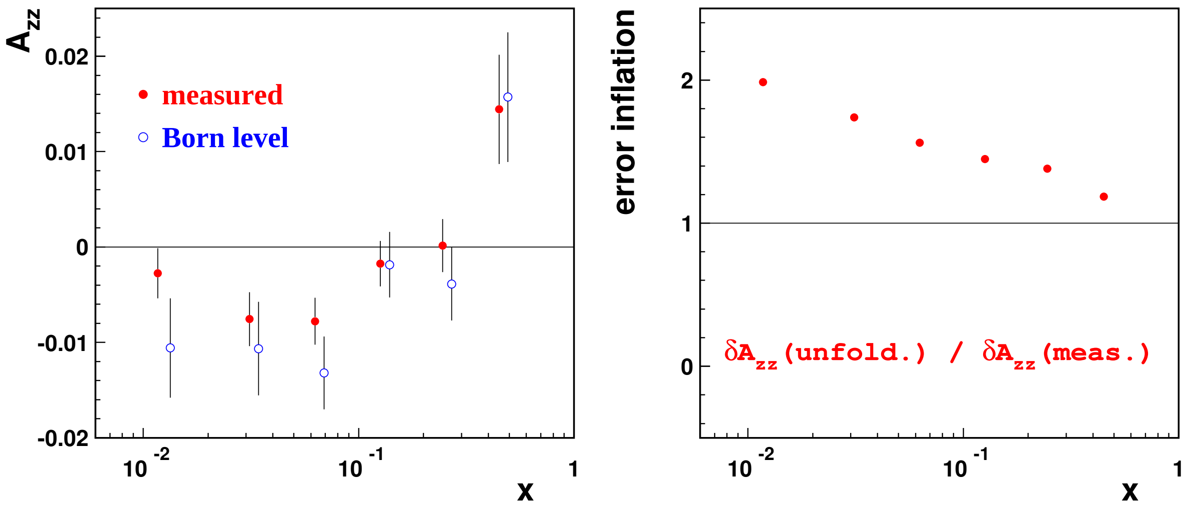

Figure 3.21: Left: the measured tensor asymmetry and the asymmetry corrected for radiative effects and detector smearing, including electromagnetic shower background ($A_{zz}(6)$, default parameterizations); right: the inflation of the statistical error coming along with the unfolding (including electromagnetic shower background).

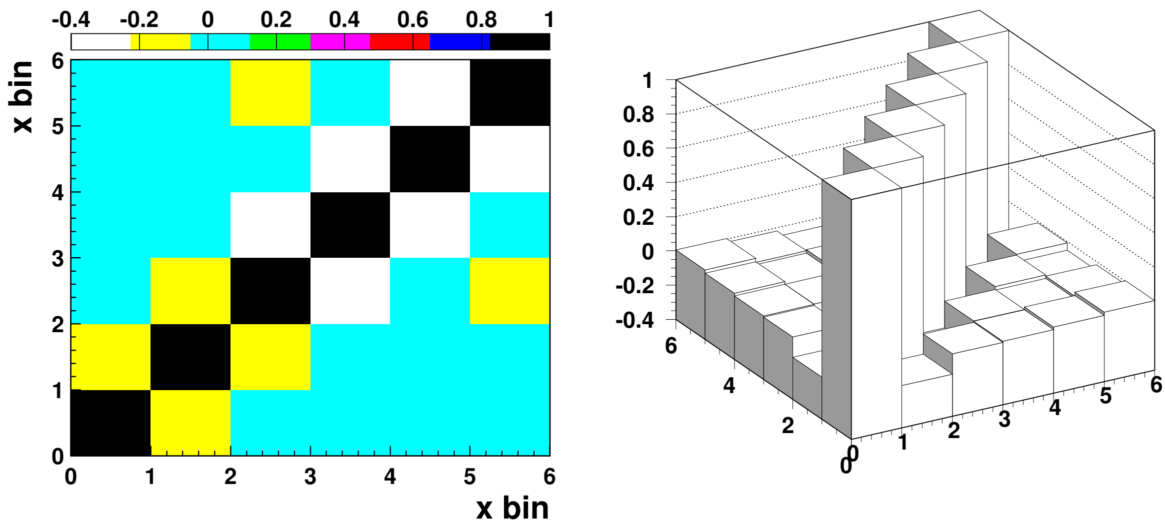

Figure 3.22: The correlation matrix of the statistical error on A_{zz} after unfolding (including electromagnetic shower background). The diagonal elements are 1 (each error is fully correlated to itself), the side diagonal elements close to the main diagonal are non-zero (there are statistical correlations between bins which are close together).

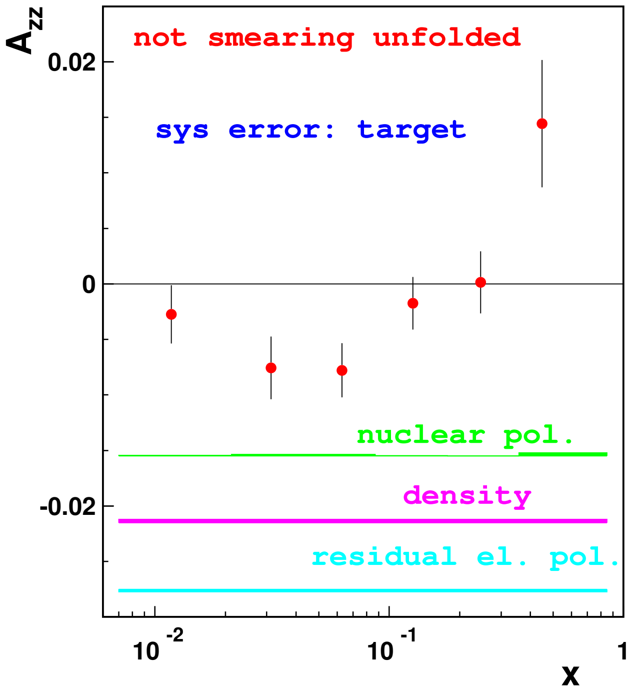

Figure 3.23: Various systematic uncertainties on the measured tensor asymmetry arising from the gaseous deuterium target; the error bands display from top to bottom the systematic error due to: nuclear polarization, density, residual electron polarization.

Q^2-binning weights more the regions with a lower error inflation. Furthermore, the average Q^2 for each bin is increased. As A_{zz} does not couple to the beam polarization and therefore no depolarization factor D enters the tensor formalism, the statistical error of the unfolded A_{zz} is not sensitive to the number of Q^2 bins. Therefore, A_{zz} was extracted in 6 bins in x-BJØRKEN and only 1 Q^2-bin covering the entire kinematic plane used for analysis.

3.4 Systematic studies

3.4.1 Target

The systematic errors arising from uncertainties on target properties are summarized in Fig. 3.23. The particular contributions are discussed in the following subsections. Two independent measures for the lepton beam intensity were available for analysis: the value of the beam current provided by the MDM (machine data module), and the `lumirate` measured by the HERMES lumi monitor (see Sec. 2.1.3). Both measures can be used to normalize the inclusive count rates; differences in the asymmetries built up

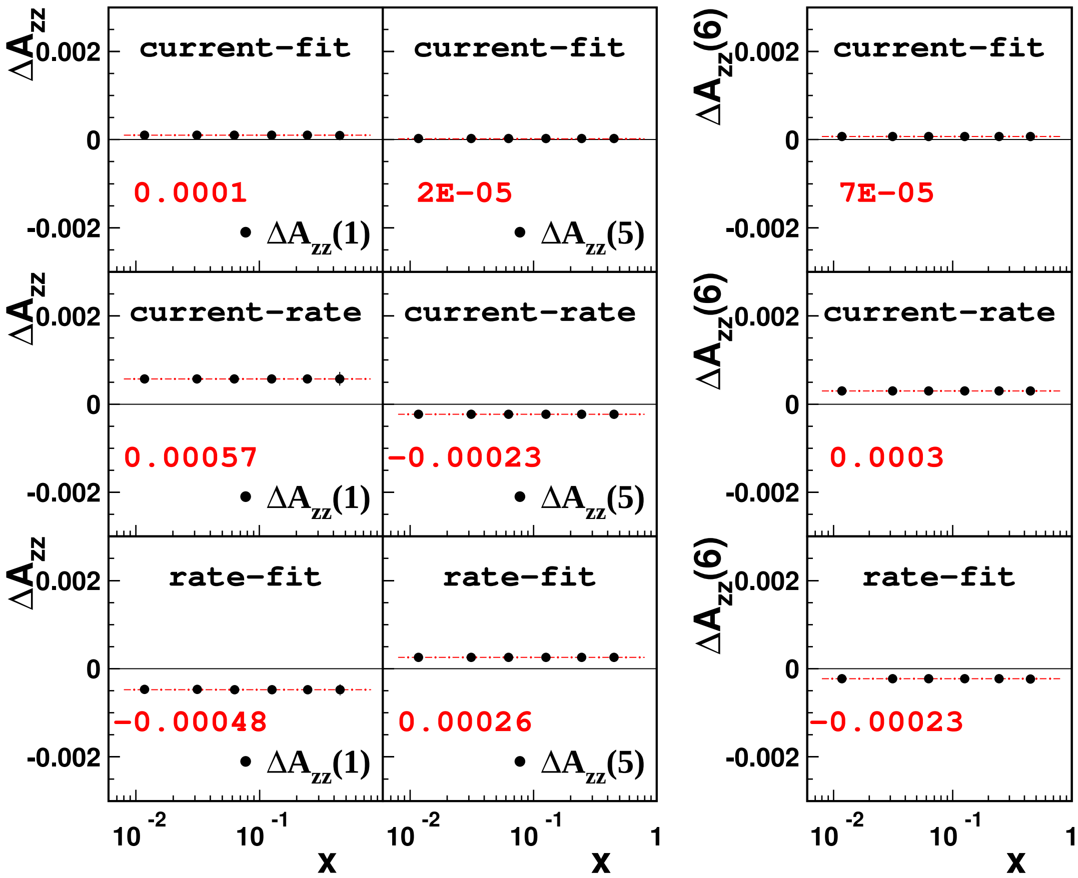

Figure 3.24: Normalization differences from weighting the measured tensor asymmetry with `lumifit` ("fit"), `lumirate` ("rate") resp. beam current ("current"), left panel: for $A_{zz}(1)$ and $A_{zz}(5)$, right panel: for $A_{zz}(6)$. Error bars are so tiny that only the plain (not error weighted) average of the differences was calculated. Each beam current value from tensor states was multiplied by a target density correction factor.

from these yields reveal certain systematic uncertainties.

Target density. The `lumirate` is proportional to the target density because for its measurement an interaction of the beam leptons with the target electrons is involved, whereas the beam current is not sensitive to the target density. From the ratio: `lumirate`(`tensor states`)/`lumirate`(`vector states`)$\approx 0.9965 :=$ TDC ("target density correction") can be estimated that for the tensor states the target density was smaller at a factor TDC. For the calculation of the asymmetry with a normalization on beam current, each beam current value from the tensor states was thus multiplied by the factor TDC. The remaining difference between $A_{zz}(6)$ normalized to beam current and to `lumirate` was taken as the systematic uncertainty on the target density

$\delta A^{\text{sys}}_{\text{tardens}}$:

$$\delta A^{\text{sys}}_{\text{tardens}} := A_{zz}(\text{current}) - A_{zz}(\text{rate}) = 3 \cdot 10^{-4}, \tag{3.9}$$

see Fig. 3.24, right middle panel ("current-rate").

Residual electron polarization. The cross section for BHABHA scattering is spin dependent; thus, if the target shell electrons are afflicted with a residual polarization, a slightly target (and beam) spin dependent `lumirate` is being introduced (BHABHA asymmetry), spoiling the asymmetry measurement. In the $A_\parallel$ case, the procedure of smoothing the `lumirate` to obtain the `lumifit` cancels out this systematic spin dependency of `lumirate`, besides decreasing statistical fluctuations.
In the A_{zz} case, the BHABHA asymmetry is not cancelled out completely as `lumifit` was calculated separately for vector and tensor target states[22]. Generally, the bias should be smaller than in the $A_\parallel$ case, as beam helicities are balanced fairly well (2/5th compared to 3/5th of statistics) for the tensor data sample, annihilating possible BHABHA asymmetries. Furthermore, Fig. 3.26 shows that the tensor asymmetries extracted for one single beam helicity are compatible with the asymmetry which was extracted from the complete data set.
The difference between $A_{zz}(6)$ normalized to `lumirate` and to `lumifit` was taken as the systematic error on the residual electron polarization $\delta A^{\text{sys}}_{\text{reselpol}}$:

$$\delta A^{\text{sys}}_{\text{reselpol}} := A_{zz}(\text{rate}) - A_{zz}(\text{fit}) = 2 \cdot 10^{-4}, \tag{3.10}$$

see Fig. 3.24, right bottom panel ("rate-fit").

Target nuclear polarization. The nuclear target polarization enters $A_{zz}(6)$ as the effective tensor polarization $\langle P_{zz}\rangle_6$ in Eq. 2.29 (linear combination of tensor polarizations, Eq. 2.30) by which A_{zz} is weighted in the very end. The systematic uncertainty was estimated by varying the tensor polarizations P_{zz} by the amount of their systematic errors δP_{zz} (compiled in Tab. D.2) provided by the HERMES target experts [62] (statistical uncertainties are negligible). For each x-bin, the difference in the central values of $A_{zz}(6)$ calculated from P_{zz} and $P_{zz} + \delta P_{zz}$ was summed in quadrature and was taken as systematic error on the target nuclear polarization $\delta A^{\text{sys}}_{\text{tarpo}}$, which is of the order $10^{-6} - 10^{-4}$ (see Tab. D.9):

$$\delta A^{\text{sys}}_{\text{tarpo}} := \sqrt{\sum_{i \in \{+,-,\Leftrightarrow,0\}} \left(A_{zz}(P^i_{zz}) - A_{zz}(P^i_{zz} + \delta P^i_{zz})\right)^2}. \tag{3.11}$$

The resulting error band is displayed in Fig. 3.23.
The fact that the $A_\parallel$-contribution in A_{zz} (Eqs. B.39 and B.40) could be neglected due

[22]For the relevant 00c1 production.

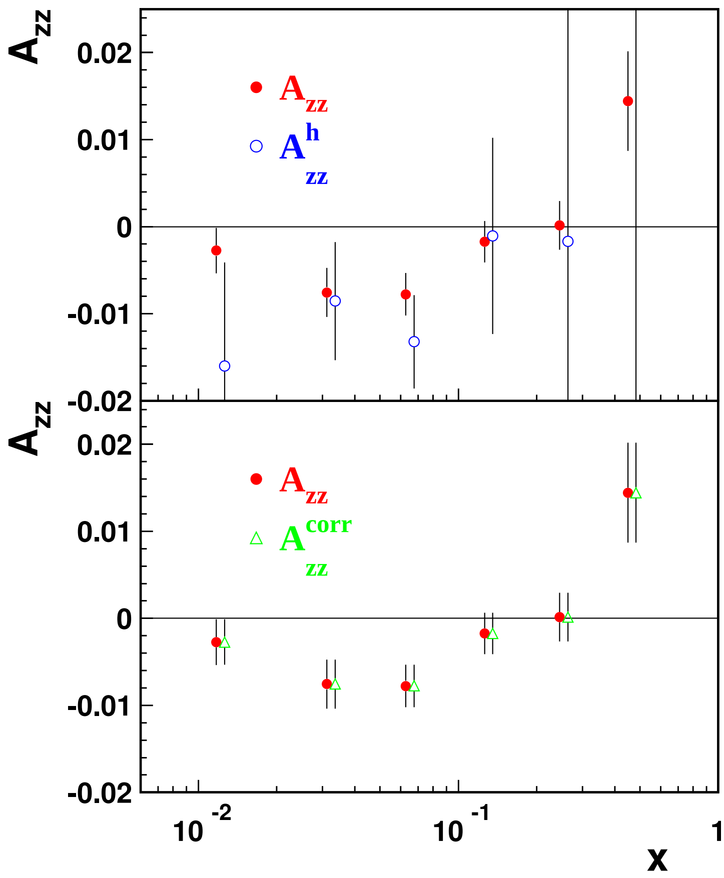

Figure 3.25: Top panel: comparison between default lepton $A_{zz}(6)$ and the hadron tensor asymmetry A^h_{zz} from wrongly identified hadrons; bottom panel: asymmetry A^{corr}_{zz} corrected for hadron contamination in comparison to the uncorrected asymmetry.

to the balance of the vector polarizations and the small residual vector polarization of the tensor states is not spoiled by varying the vector polarizations by the amount of their quoted systematic errors.

3.4.2 Hadron contamination

In order to roughly estimate a possible false asymmetry arising from hadrons misidentified as leptons, the usual cut on the PID parameter (PID>1) to select leptons (see also Sec. 2.2) was strictly reversed to a cut PID<-2. These particles, selected under a consciously wrong assumption, were treated in the analysis as if they were leptons with respect to the search for the leading particle, the calculation of the kinematics and the cuts performed. In Fig. 3.25, the tensor hadron asymmetry A^h_{zz} obtained in this way is compared to the lepton asymmetry in the top panel.

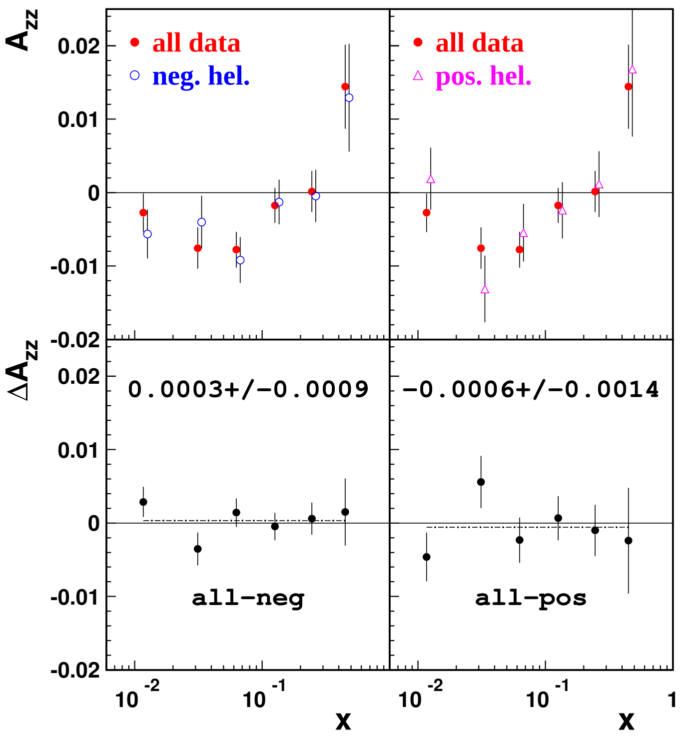

Figure 3.26: Tensor asymmetries measured at single beam helicities (top panels) and their difference to the helicity averaged asymmetry (bottom). For the calculation of the statistical error, completely correlated data sets were assumed in order to estimate an upper bound; the error on the difference for these actually partially correlated data sets is *larger*.

The hadron contamination at Hermes for small-x ($x < 0.1$) was determined in Ref. [98] to be at most $h = 0.002$ for the standard cut PID>1. To account for the hadronic background, a corrected asymmetry A_{zz}^{corr} was calculated:

$$A_{zz}^{\mathrm{corr}} = \frac{A_{zz} - h \cdot A_{zz}^{h}}{1-h}, \tag{3.12}$$

with $h = 0.002$ for x-bins 1-4 and $h = 0$ for x-bins 5-6 (the average x for xbin 4 is $x = 0.126$). A_{zz}^{corr} is shown in the bottom panel of Fig. 3.25 in comparison to the uncorrected one. For each x-bin, the difference in the central values between the uncorrected and the asymmetry corrected for hadronic background, which is of the order $10^{-6} - 10^{-5}$, was taken as systematic error on the hadronic background $\delta A_{\mathrm{hadcont}}^{\mathrm{sys}}$:

$$\delta A_{\mathrm{hadcont}}^{\mathrm{sys}} := A_{zz} - A_{zz}^{\mathrm{corr}}. \tag{3.13}$$

3.4.3 Beam helicity

In contrast to g_1, b_1 is not sensitive to the beam polarization, i. e. one doesn't need a polarized lepton beam to measure b_1. Though, *if* the beam is polarized, there is a contribution from $A_{\parallel}$ entering the cross section. In the analysized data sample, the lepton beam was first negatively and then positively polarized. Both periods are employed for data analysis in order to minimize the vector contribution and further processes sensitive to the beam helicity (like Bhabha asymmetry, see Sec. 3.4.1).
The final $A_{\parallel}$-contribution to the tensor asymmetry depends on the relative *difference* of luminosities at different beam helicities $\Delta L/L$ (and to the residual vector polarization of the tensor states, see Eqs. B.39, B.40). In the dedicated tensor data period, $\Delta L/L$ was about 0.22, keeping the $A_{\parallel}$-contribution small.
Fig. 3.26 shows A_{zz} measured only with negative and positive beam helicity, respectively, in comparison to the helicity averaged (default) asymmetry. No significant deviations were observed; no explicit systematic error was assigned due to beam helicity effects, because the systematic error assigned due to the tensor mismatch (which is prominent for negative beam helicity) vice versa includes possible beam helicity effects, see Fig. 3.5. Moreover, the effect of the Bhabha asymmetry (which is beam spin dependent) was accounted for by assigning a systematic error due to the residual electron polarization (see Sec. 3.4.1).

3.4.4 Unfolding with different input parameterizations

The events of the MC production to obtain the final Born tensor asymmetry by unfolding were fully reconstructed with HRC. This procedure takes quite a long CPU time. A faster possibility to produce MC samples is the HSG which provides already a good tool to simulate the experiment; the MC asymmetries from the fully tracked (HRC) and the smeared production (HSG) match well, see Fig. 3.27 (left), and the unfolding results are compatible within statistics, Fig 3.27 (right). HSG was thus used to generate Monte Carlo samples with changed input parameterizations (each one change at a time):

1. Born A_{zz}: the second fit instead of the first one (Sec. 3.3.2).

2. $R(x, Q^2)$: the low-Q^2-behavior was changed to R = const for $Q^2 < 0.3$ GeV^2 (Rconst) [91] instead of the linear behavior of R1990 in that kinematic region; the rest of the kinematic range corresponds to R1990.

3. $F_2(x, Q^2)$: the 15 parameter fit of the SMC collaboration (P15) and its lower limit (P15ℓ) [94] instead of the ALLM parameterization (Sec. 3.3.2).

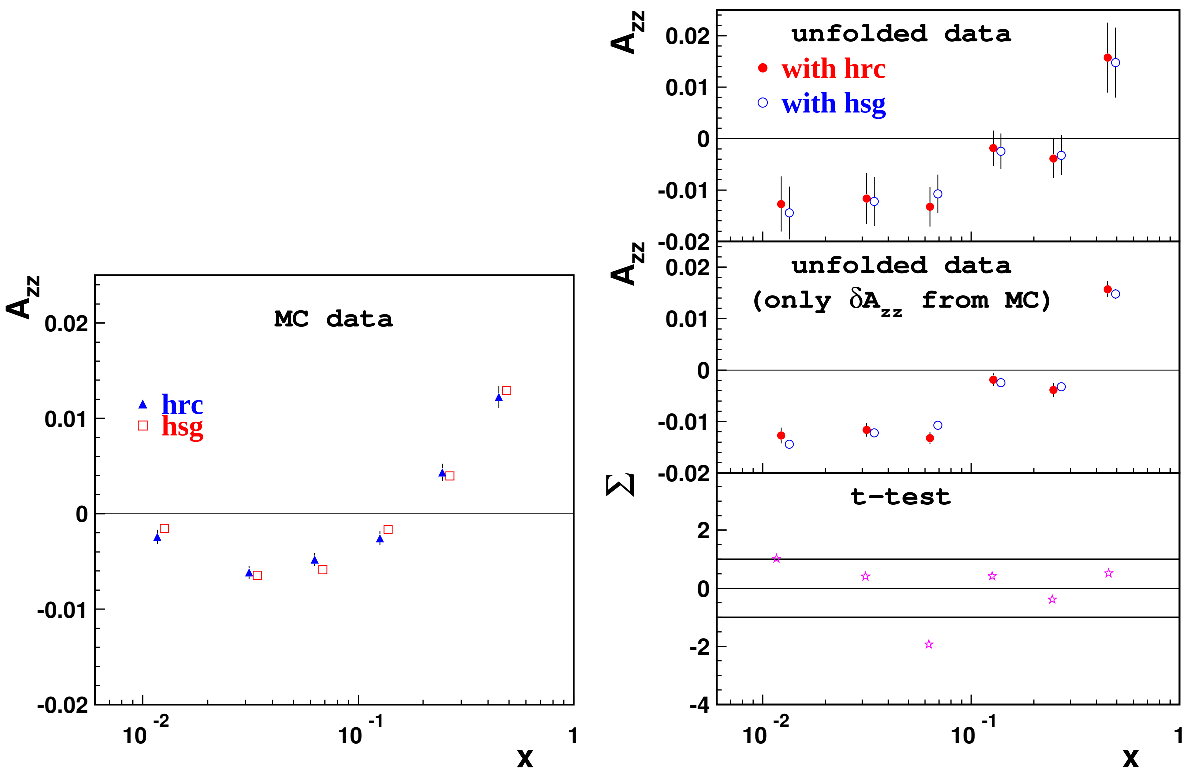

Figure 3.27: Left: comparison between the reconstructed MC asymmetries from a fully reconstructed (HRC) production and from an HSG production (same input parameterizations); right: comparison between the unfolding results using a fully tracked production and an HSG production (same input parameterizations). The t-test uses the MC statistical error δ(MC) (Eq. C.29) and assumes independent data samples.

For these MC productions, the electromagnetic shower background was not taken into account because they were employed for studies for which only differences between asymmetries were considered, expecting the effect to drop out. The MC sample with $F_2 = F_2$(ALLM) as input was reproduced with HSG in order to obtain a default comparison sample. These HSG MC samples reach four times the statistical power of the default tracked MC sample from Sec. 3.3.2, i. e. the statistical error arising from the Monte Carlo δ(MC) (Eq.C.29) is only half of the value in Tab. D.10.
It should be mentioned that the unfolding algorithm is expected not to be dependent on the cross section model *within* the Hermes acceptance because the normalization by the Born cross section (Eq. 3.7), which was generated using input parameterizations identical to the ones in the HRC or HSG Monte Carlo, eliminates any such model dependence except for the polarized background *entering* the acceptance, $\Delta\overset{\frown}{\sigma}^{\mathrm{P}}$ (see Sec. C.1 for details). The unfolding algorithm thus only depends on the detector model used in the GEANT tool, the radiative corrections performed by the RADGEN

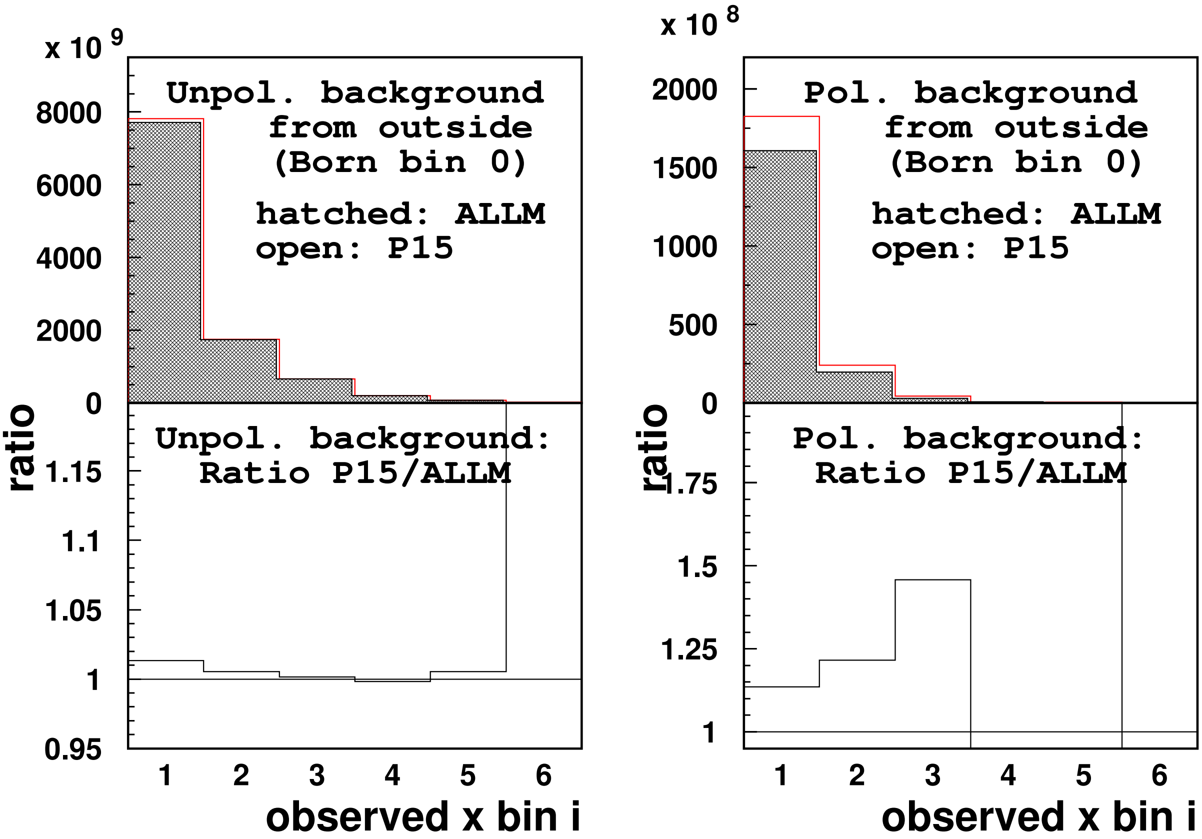

Figure 3.28: Background (column $j = 0$ of the migration matrix $M_X(i, j)$) smearing into the acceptance: absolute (top panels) and relative (bottom panels) comparison between MC samples with different F_2 input parameterizations (ALLM and P15). Left panel: unpolarized background, right panel: polarized background.

code and the models for background processes. Fig. 3.28 shows that the unpolarized background is not sensitive and that the polarized background is only marginally sensitive to the used F_2 input parameterization, thus the effect by unfolding the measured asymmetry with the modified MC samples is expected to be small.

These effects from modelling the DIS cross section outside the acceptance were tested by comparing the unfolding result with the changed input parameterizations to the unfolding result with the default parameterizations, see Fig. 3.29. Each time a t-test was performed to check the statistical significance of deviations (see App. A.3); for that purpose, the statistical error arising from the Monte Carlo sample $\delta(\mathrm{MC})$ (Eq. C.29) was used for the comparison and thus *independent* data samples could be assumed[23]. Each time the unfolding results were compatible within an accuracy of one sigma. Therefore,

[23]The statistical error δA_{zz} of the unfolded asymmetry arising from the measured data set (which stays the same, irrespectively of which modified MC sets are used for unfolding) was not considered and thus statistical correlations were avoided.

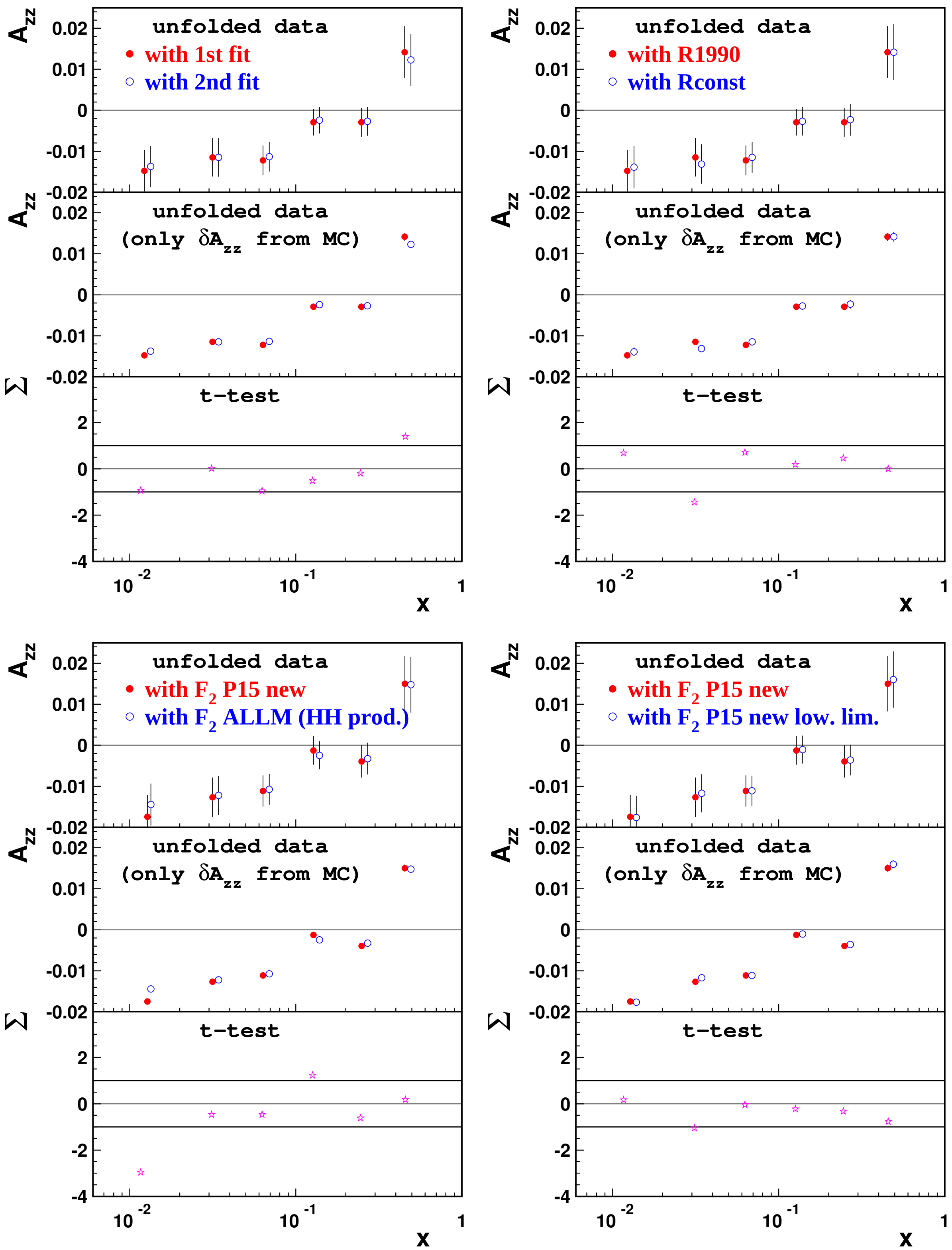

Figure 3.29: The change in the unfolding result if the Born input parameterization is changed (top left) or the R-ratio (top right) or F_2 (bottom). All other parameterizations are the default ones. The t-test uses the MC statistical error δ(MC) (Eq. C.29) and assumes independent data samples.

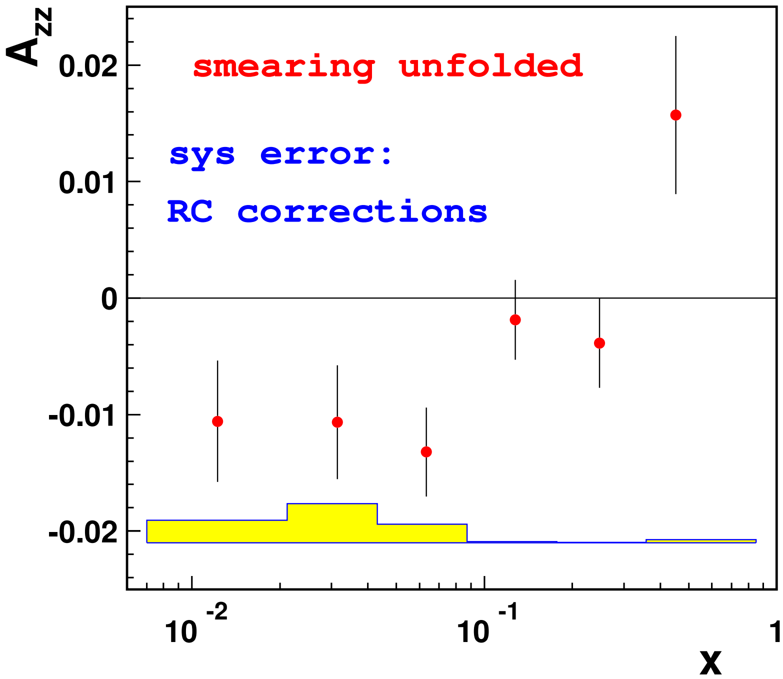

Figure 3.30: The systematic error on the Born level tensor asymmetry on the QED radiative corrections.

no systematic error was assigned due to Monte Carlo input parameterizations[24].

3.4.5 Radiative corrections

A systematic error on the QED radiative corrections $\delta A_{\mathrm{RC}}^{\mathrm{sysMC}}$ was calculated [96]. For this purpose, the complete analysis chain was repeated with modified kinematic cuts ($Q^2 > 0.3$ GeV^2, $y < 0.85$) which reduced the initial elastic background. This analysis included also the treatment of the electromagnetic shower background. An unfolded real data asymmetry $A_{\mathrm{Born}}(\mathrm{mod})$ was obtained which is expected to be as well corrected for the radiative background as the default unfolded asymmetry A_{Born}. Their difference was taken as the systematic uncertainty on the radiative corrections:

$$\delta A_{\mathrm{RC}}^{\mathrm{sysMC}} = A_{\mathrm{Born}} - A_{\mathrm{Born}}(\mathrm{mod}). \tag{3.14}$$

The result is displayed in Fig. 3.30, the values of $\delta A_{\mathrm{RC}}^{\mathrm{sysMC}}$ are compiled in Tab. D.13.

[24] If significant fluctuations *had been* visible, the difference P15-P15ℓ would have been the candidate for such a systematic error, delivering the uncertainty range of the used parameterization.

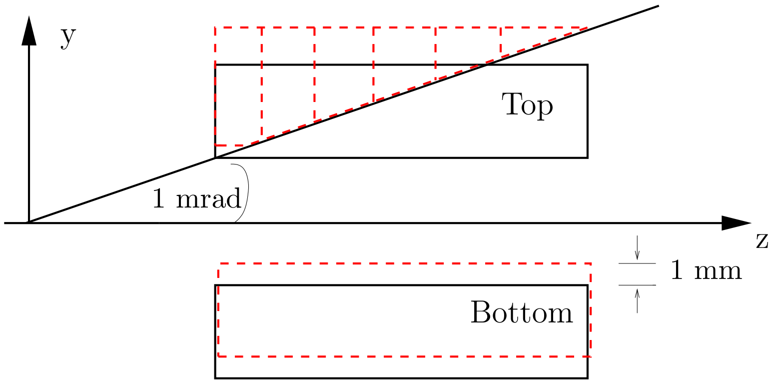

Figure 3.31: Schematic side view of the Hermes spectrometer: the global offset (bottom half) and tilt (top half) of the detector, as it was used as input for a misaligned MC production. Dashed lines: misaligned; solid lines: perfectly aligned. The line of the z-axis denotes the location of the beam pipe.

3.4.6 Detector misalignment

Electromagnetic showers (see Sec. 3.3.3) and their impact onto the R-ratio allow to estimate the amount by which the Hermes spectrometer is misaligned with respect to the beamline [99]: a global shift of the bottom detector of 1 mm in the y-direction and a global tilt of the top detector of 1 mrad with respect to the y-direction was assumed; tilts and offsets in the x-direction turned out to be negligible, and misalignments between individual detector components were not taken into account, see Fig. 3.31 for an exaggerated illustration of the detector misalignment.
With this information, two MC samples with a *mis*aligned geometry file on generator level (GMC) were produced in parallel: once using a *mis*aligned geometry file on reconstruction level (HRC) to simulate perfectly aligned data, and once an aligned geometry file on reconstruction level to mimic real misaligned data, see Fig. 3.32 for illustration.

The statistical power of these two MC samples with respect to δ(MC) (Eq.C.29 and Tab. D.10) is equivalent to the default MC sample from Sec. 3.3.2. The z-vertex-distribution from real data could roughly be reproduced by the misaligned Monte Carlo sample (Fig. 3.33). Fig. 3.34, left panel, shows the misaligned vs. aligned comparison for the reconstructed Monte Carlo asymmetries (top) and the error inflation for real data (bottom) coming along with the unfolding when once the misaligned and once the aligned MC sample was used: when unfolding with a misaligned Monte Carlo, the error inflation reaches a factor of 2 also for *large* x (this is the region where the asymmetry has the steepest slope). Due to an overall misalignment of the detector, much more events than without misalignment get reconstructed in an x-bin which is *different* from their Born bin and have to be resorted, which is resulting in a larger error inflation. This effect can also be observed in Fig. 3.13, left bottom panel. Overall changes in the unfolding result (see t-test, 2nd panel from bottom) are much less pronounced than in

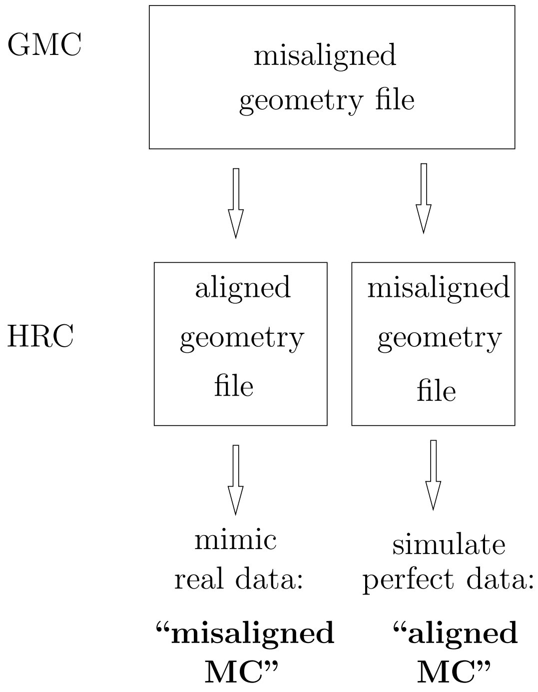

Figure 3.32: In order to mimic real data reconstructed by a misaligned detector, events were generated with a misaligned geometry file on generation level (GMC) and were reconstructed with an aligned geometry file (HRC). This corresponds to the situation in the experiment. When identical geometry files are used on generation and reconstruction level, respectively, one simulates a perfectly aligned detector. In this case, the geometry file was chosen to be misaligned in order to be able to use the *same* generated MC sample twice, employing different geometry files on reconstruction level.

the g_1-case due to the coarser tensor binning [76].
To correct by unfolding for detector misaligment was not considered to be the right procedure, as the detector misalignment doesn't produce a statistically distributed bin misidentification, but one that could in principle be corrected for by a track-by-track algorithm.
Without such an algorithm, rather the difference (misaligned-aligned) in the unfolded *Monte Carlo* asymmetries was chosen to be assigned as systematic error $\delta A^{\mathrm{sysMC}}_{\mathrm{misali}}$:

$$\delta A^{\mathrm{sysMC}}_{\mathrm{misali}} = A^{\mathrm{MCunf}}_{\mathrm{misali}} - A^{\mathrm{MCunf}}_{\mathrm{ali}}, \tag{3.15}$$

where $A^{\mathrm{MCunf}}_{\mathrm{(mis)ali}}$ is the Monte Carlo asymmetry reconstructed from the (mis)aligned MC, unfolded (*both times*) with the aligned MC. The difference in Eq. 3.15 accounts precisely for the error which is inherent in the unfolding due to the detector misalignment: $A^{\mathrm{MCunf}}_{\mathrm{misali}}$ simulates the real data asymmetry; $A^{\mathrm{MCunf}}_{\mathrm{ali}}$ is the asymmetry one would obtain for a perfectly aligned detector. As Monte Carlo statistics are larger than the experimental statistics, fluctuations are smoothed which appear in the case that the

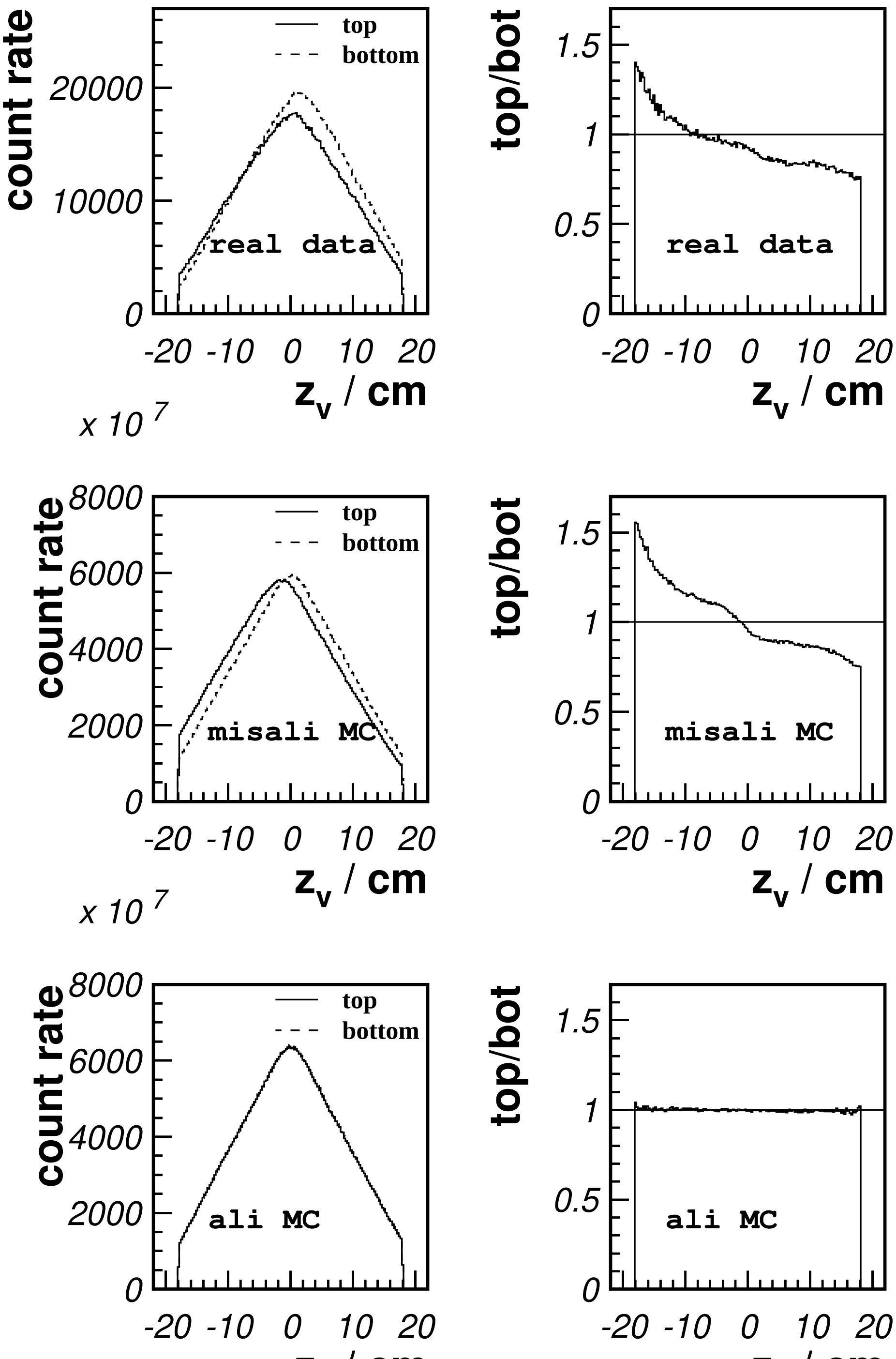

Figure 3.33: The z-vertex-distribution separately for top and bottom detector half (left) and the ratio of top/bottom half (right) for real data (top panels), for the Monte Carlo sample assuming a misaligned detector (middle panels) and the Monte Carlo sample assuming a perfectly aligned detector (bottom panels).

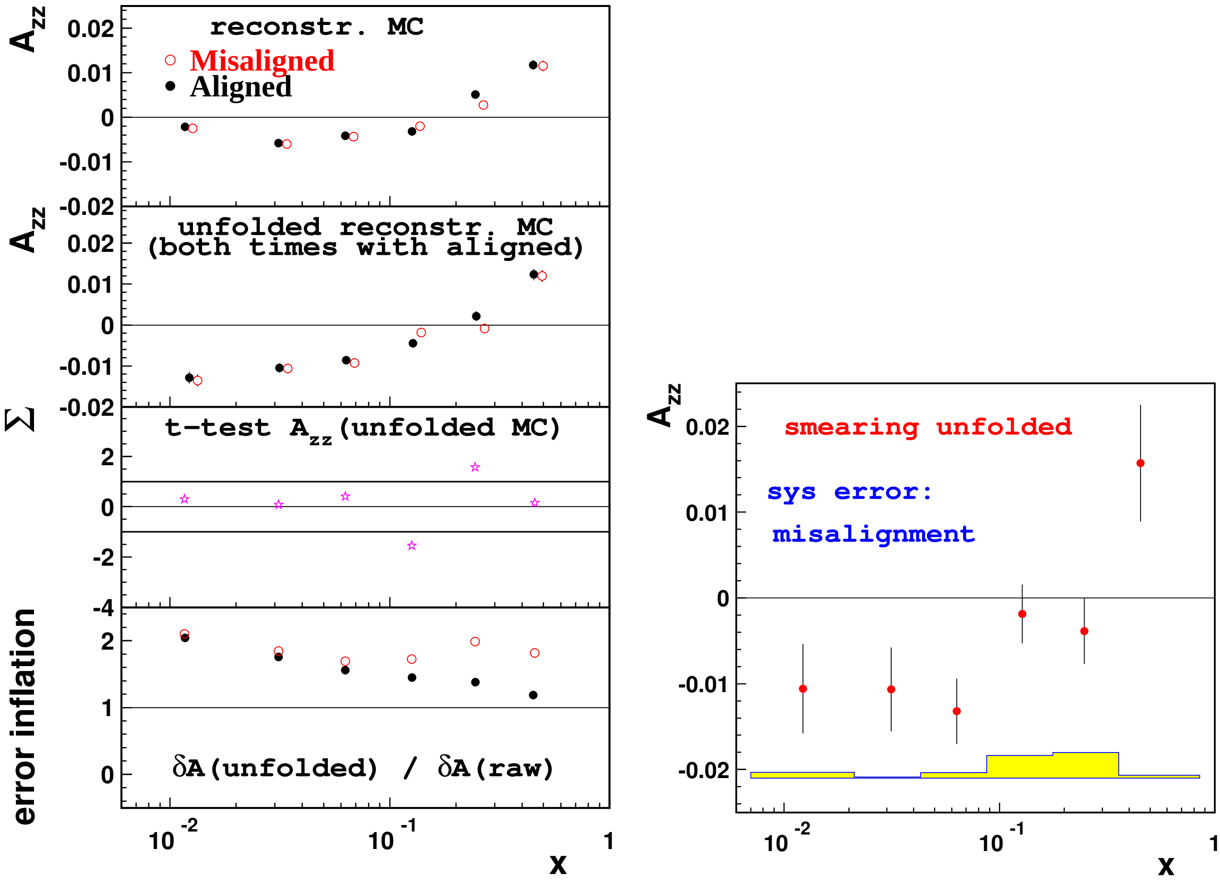

Figure 3.34: Left: misaligned MC versus aligned; two top panels: MC asymmetry on HRC and on Born level; two bottom panels: t-test for unfolded real data asymmetry, and error inflation. The t-test takes the MC statistical error δ(MC) (Eq. C.29) into account and assumes independent data samples. Right: systematic error on the tensor asymmetry on Born level from the misalignment of the detector from the comparison of the unfolding results with an aligned and a misaligned MC.

difference in the unfolded *real* data asymmetries is used for the calculation of this systematic error.
A comparison between the two unfolded MC asymmetries is displayed in Fig. 3.34 in the left, the systematic error band calculated from their difference in the right panel. The values of $\delta A^{\mathrm{sysMC}}_{\mathrm{misali}}$ are compiled in Tab. D.13.

3.4.7 Summary of systematics for A_{zz}

In summary, the systematic errors $\delta A^{\mathrm{sys}}_{zz}$ are (absolute values; A_{zz} itself is at most 10^{-2}):

From experimental data analysis: the total systematic error band is displayed in Fig. 3.35

(left); the single contributions on measured level are compiled in Tab. D.9 for each x-bin:

tensor mismatch: $1 \cdot 10^{-3}$

target polarization: $10^{-6}..10^{-4}$

target density: $3 \cdot 10^{-4}$

residual electron polarization: $2 \cdot 10^{-4}$

hadron contamination: $(0)..10^{-6} - 10^{-5}$

These experimental errors were separately inflated by the unfolding procedure to obtain the uncertainties on BORN level (Tab. D.12). All of them were assumed to be 100% correlated between kinematic bins (Eq. C.27), except for the systematic error arising from the hadron contamination, which was separately determined for each bin and was thus assumed to be uncorrelated between bins (Eq. C.28). After unfolding, systematic uncertainties are uncorrelated between bins.
All the single inflated contributions were added in quadrature to a total experimental systematic error for each x-bin:

$$\delta A^{\mathrm{sys}}_{\mathrm{Born}}(\exp) = \sqrt{(\delta A^{\mathrm{sysinfl}}_{\mathrm{mismatch}})^2 + (\delta A^{\mathrm{sysinfl}}_{\mathrm{tarpo}})^2 + (\delta A^{\mathrm{sysinfl}}_{\mathrm{tardens}})^2 + (\delta A^{\mathrm{sysinfl}}_{\mathrm{reselpol}})^2 + (\delta A^{\mathrm{sysinfl}}_{\mathrm{hadcont}})^2}. \tag{3.16}$$

From MC studies: the error bands are displayed in Fig. 3.35 (right), the values are compiled in Tab. D.13:

radiative corrections: $10^{-5}..10^{-3}$ (large contribution for small x)

detector misalignment: $10^{-4}..10^{-3}$ (large contribution for large x)

These errors refer already to BORN level and thus did not need to be inflated. They were added in quadrature to a total systematic Monte Carlo error:

$$\delta A^{\mathrm{sys}}_{\mathrm{Born}}(\mathrm{MC}) = \sqrt{(\delta A^{\mathrm{sysMC}}_{\mathrm{RC}})^2 + (\delta A^{\mathrm{sysMC}}_{\mathrm{misali}})^2}. \tag{3.17}$$

The total systematic error on A_{zz} on BORN level is then the quadratic sum of the experimental (Eq. 3.16) and Monte Carlo (Eq. 3.17) systematic error:

$$\delta A^{\mathrm{sys}}_{\mathrm{Born}}(\mathrm{tot}) = \sqrt{\delta A^{\mathrm{sys}}_{\mathrm{Born}}(\exp)^2 + \delta A^{\mathrm{sys}}_{\mathrm{Born}}(\mathrm{MC})^2}. \tag{3.18}$$

$\delta A^{\mathrm{sys}}_{\mathrm{Born}}(\mathrm{tot})$ was propagated to $\delta b^{\mathrm{sys}}_{\mathrm{Born}}(\mathrm{tot})$, see Sec. 3.5 and Fig. 3.38.

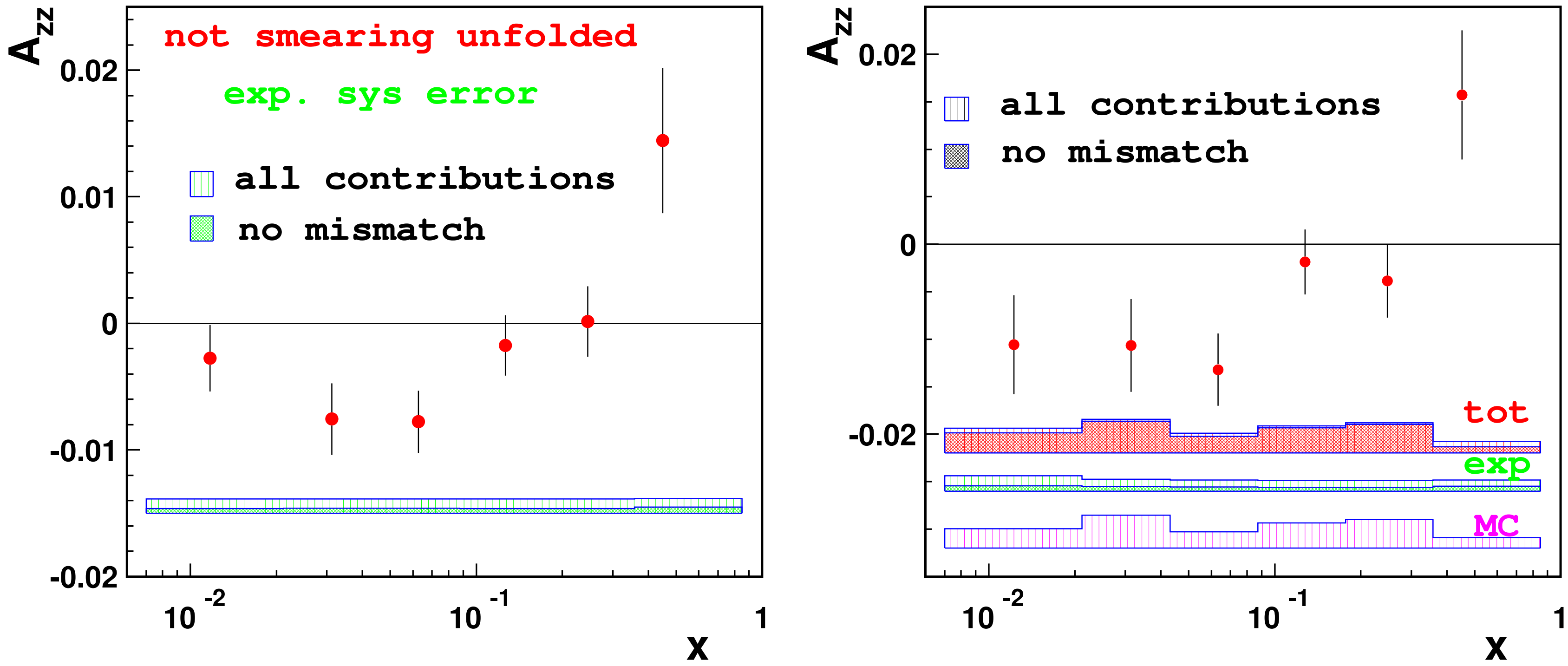

Figure 3.35: Compilation of final tensor asymmetry results and the total systematic uncertainty. The striped error bands contain the total systematic error, the hatched error bands the uncertainty *excluding* the tensor mismatch contribution. Left: measured $A_{zz}(6)$ with its total systematic error from experimental data analysis. The single contributions were added in quadrature: tensor mismatch (which is the prominent contribution), target polarization, target density, residual electron polarization and hadron contamination. Right: unfolded $A_{zz}(6)$ (thereby including electromagnetic shower background) with its total systematic error (error bands as they are denoted in the plot from bottom to top) from MC studies (misalignment and radiative corrections), its total *inflated* systematic error from experiment (compare to the left panel) and the total systematic error on the unfolded tensor asymmetry (for which the latter two contributions were added in quadrature).

Fig. 3.35 shows A_{zz} (before unfolding) with its total systematic error arising from the experiment (left panel). The by far largest contribution stems from the tensor mismatch (Fig. 3.9). The right panel displays the two contributions to the systematic error of the unfolded asymmetry: the inflated experimental uncertainties and the uncertainties stemming from Monte Carlo studies.

3.5 Extraction of b_1^{d}

A daily intake of 1.5 mg vitamin B_1 is recommended. (WHO)

3.5.1 From A_{zz} to b_1^{d} and b_2^{d}

The tensor asymmetry A_{zz} (its statistical error δA_{zz}) is connected to the tensor structure functions b_1 and b_2 (their statistical errors $\delta b_{1,2}$) via:

$$
\begin{aligned}
b_1^{\mathrm{d}}(x,Q^2) &= -\frac{3}{2}A_{zz}(x)F_1^{\mathrm{d}}(x,Q^2), && (3.19)\\
\delta b_1^{\mathrm{d}}(x,Q^2) &= -\frac{3}{2}\delta A_{zz}(x)F_1^{\mathrm{d}}(x,Q^2), && (3.20)\\
b_2^{\mathrm{d}}(x,Q^2) &= -\frac{3}{2}A_{zz}(x)F_2^{\mathrm{d}}(x,Q^2), && (3.21)\\
\delta b_2^{\mathrm{d}}(x,Q^2) &= -\frac{3}{2}\delta A_{zz}(x)F_2^{\mathrm{d}}(x,Q^2), && (3.22)
\end{aligned}
$$

such that one has

$$-\frac{3}{2}A_{zz} = \frac{b_1^{\mathrm{d}}}{F_1^{\mathrm{d}}} = \frac{b_2^{\mathrm{d}}}{F_2^{\mathrm{d}}}. \tag{3.23}$$

The spin-averaged structure function F_1^{d} for the deuteron is obtained from F_2^{d} (Eq. 3.8) by means of the modified Callan-Gross relation (Eq. 1.14):

$$F_1^{\mathrm{d}}(x,Q^2) = F_2^{\mathrm{d}}(x,Q^2)\left(\frac{1+\gamma^2}{2x(1+R(x,Q^2))}\right). \tag{3.24}$$

For the calculation of b_1 and b_2 from A_{zz}, the kinematic quantities x, Q^2 and γ entering F_2, F_1 and R have to be read as the *average* values $\langle x\rangle$, $\langle Q^2\rangle$ and $\langle\gamma\rangle$ for the x-bin in question. $F_2^{\mathrm{d}}(\langle x\rangle,\langle Q^2\rangle)$, $F_1^{\mathrm{d}}(\langle x\rangle,\langle Q^2\rangle)$ and $R(\langle x\rangle,\langle Q^2\rangle)$ were evaluated at this point of averaged kinematics. The average kinematic variables on Born level were obtained from Eq. C.30.

Both the statistical and the systematic error on b_1 were obtained from Eq. 3.20, treating

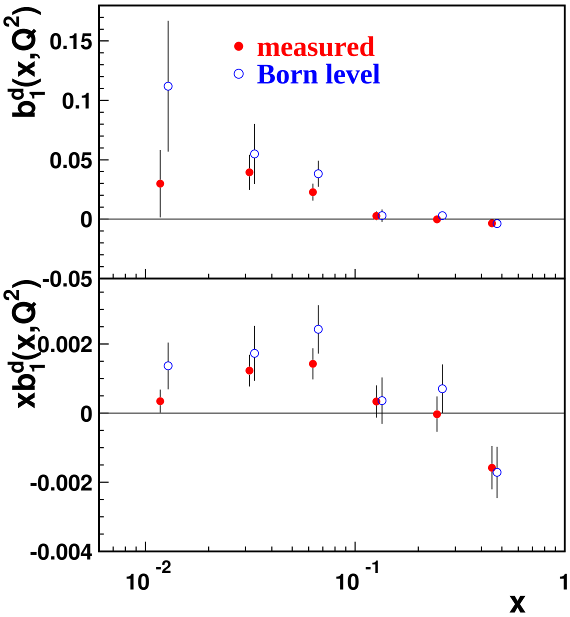

Figure 3.36: Tensor structure function: comparison between before and after unfolding (default parameterizations; electromagnetic shower background included); upper panel: b_1, lower panel: xb_1; note that the steep rise behavior for b_1 at small-x is only present for the unfolded result.

the x- and Q^2-dependent functions and the averaged kinematics as constants in the error propagation. By multiplying $b_1(x, Q^2)$ for each x-bin with the average x-value for that bin, one arrives at xb_1.
For the extraction of b_1, $R = R1990$ and $F_2 = F_2(\text{ALLM})$ were used as default (see Sec. 3.3.2). Fig. 3.36 shows the changes from the measured to the BORN level tensor structure function b_1 (and xb_1) for the default parameterizations. The BORN b_1 is obtained from the BORN tensor asymmetry. The values for b_1 and its statistical error on BORN level are compiled in Tab. D.14.

3.5.2 Systematic errors on b_1^{d}

The extraction of b_1 was repeated with other F_2 parameterizations than the ALLM one (P15, P15ℓ, see Sec. 3.3.2). In the used binning, b_1 is not sensitive to a transition $R1990$ $\rightarrow$ Rconst, as the change affects only the $Q^2 < 0.3$ GeV^2 region, which is completely contained in the first x-bin. For the unfolding of A_{zz} and the extraction of b_1 from A_{zz}, consistent parameterizations were used, respectively. The t-test (see App. A.3) comparing the b_1 results for $F_2 = F_2(\text{P15})$ resp. $F_2 = F_2(\text{P15}\ell)$ to the default result (Fig. 3.37) shows that deviations are not statistically significant. Therefore, also to b_1 no systematic error was assigned due to parameterizations. The total systematic error on the BORN level tensor asymmetry from Eq. 3.18 was propagated to the total

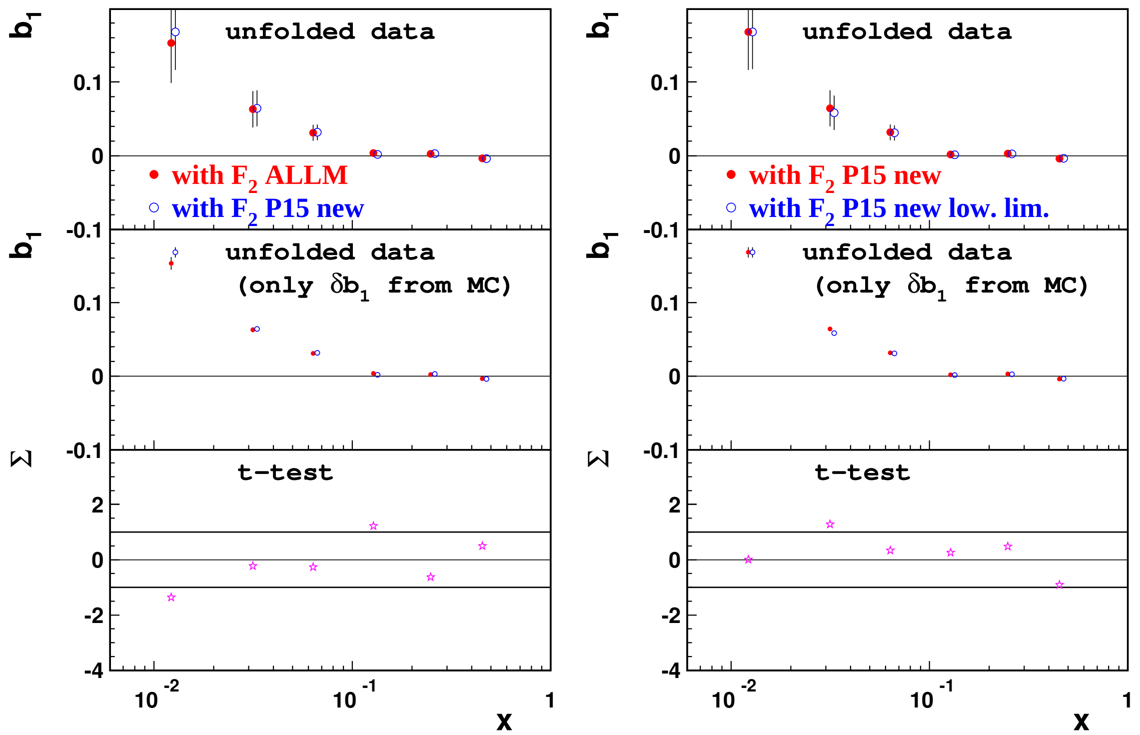

Figure 3.37: b_1 on Born level from different F_2 parameterizations (left: P15, right: P15ℓ) compared to the default b_1 with ALLM as F_2 parameterization (top two panels, where the middle panel displays the statistical error from the MC samples) and the corresponding t-test (bottom panels). Consistent parameterizations were used for the extraction of b_1 and the preceding unfolding of A_{zz}, respectively.

systematic error on b_1, $\delta b_{\mathrm{Born}}^{\mathrm{sys}}(\mathrm{tot})$, by using Eq. 3.20. In Fig. 3.38, the final results for b_1 and xb_1 on Born level are presented together with their systematic error bands.

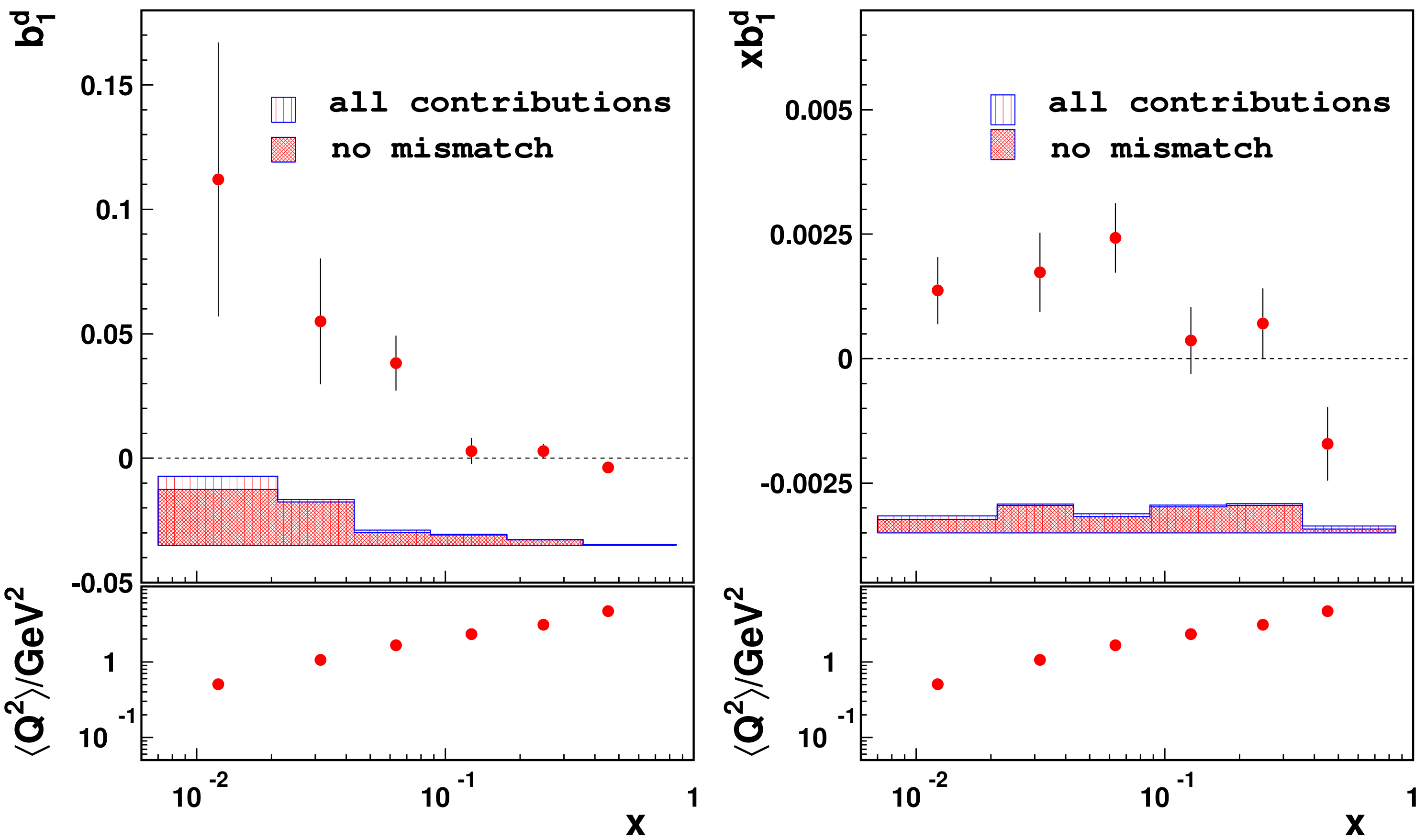

Figure 3.38: The HERMES result for b_1^{d} (left) and xb_1^{d} (right) corrected for radiative effects (including electromagnetic shower background) and detector smearing (default parameterizations), together with the total systematic error bands (striped) and the error bands excluding the tensor mismatch (hatched).

3.6 Final results of tensor asymmetry and structure function

Fig. 3.39 shows the final result [100] of the tensor asymmetry A_{zz} of the deuteron on Born level. Its central values and uncertainties are compiled in Tab. D.10. The asymmetry is positive for large values of x-Bjørken and reaches there a magnitude of more than 1%. It crosses zero at approximately $x \simeq 0.2$ and becomes $\approx -1\%$ for $x < 0.1$.

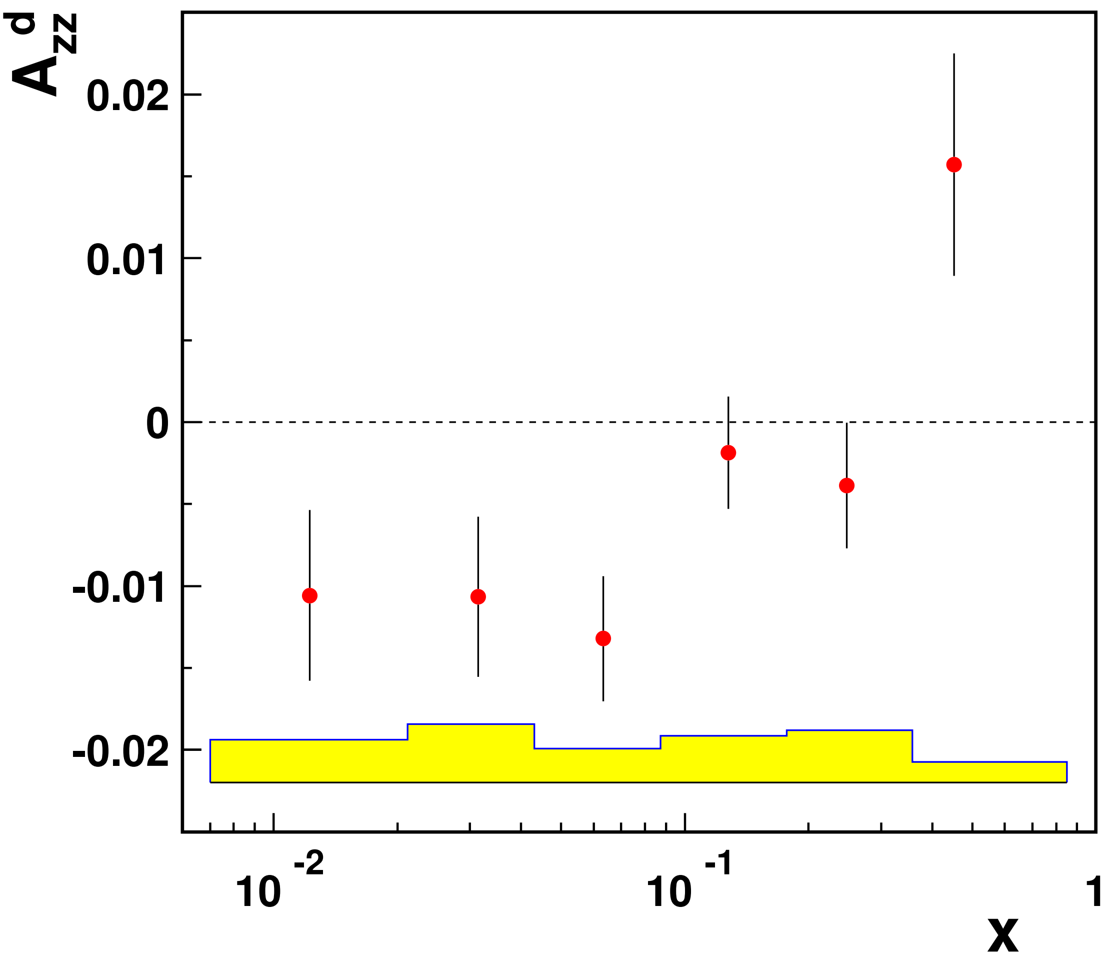

Figure 3.39: The final inclusive tensor asymmetry A_{zz} of the deuteron on Born level versus x-Bjørken. The error band displays the total systematic uncertainty.

Fig. 3.40 displays the final result [100] of the tensor structure function b_1^{d} of the deuteron on Born level. Its central values and uncertainties are compiled in Tab. D.14. The structure function is slightly negative for $x \geq 0.4$ and rises steeply for $x < 0.1$ until it reaches a magnitude of about 11% for $x = 0.01$.
The measured behavior of the tensor structure function $b_2^{\mathrm{d}} = -\frac{3}{2} A_{zz} F_2^{\mathrm{d}}$ on Born level is shown in Fig. 3.41, left panel (see also Tab. D.15). Because $F_2^{\mathrm{d}}(x)$ is exclusively

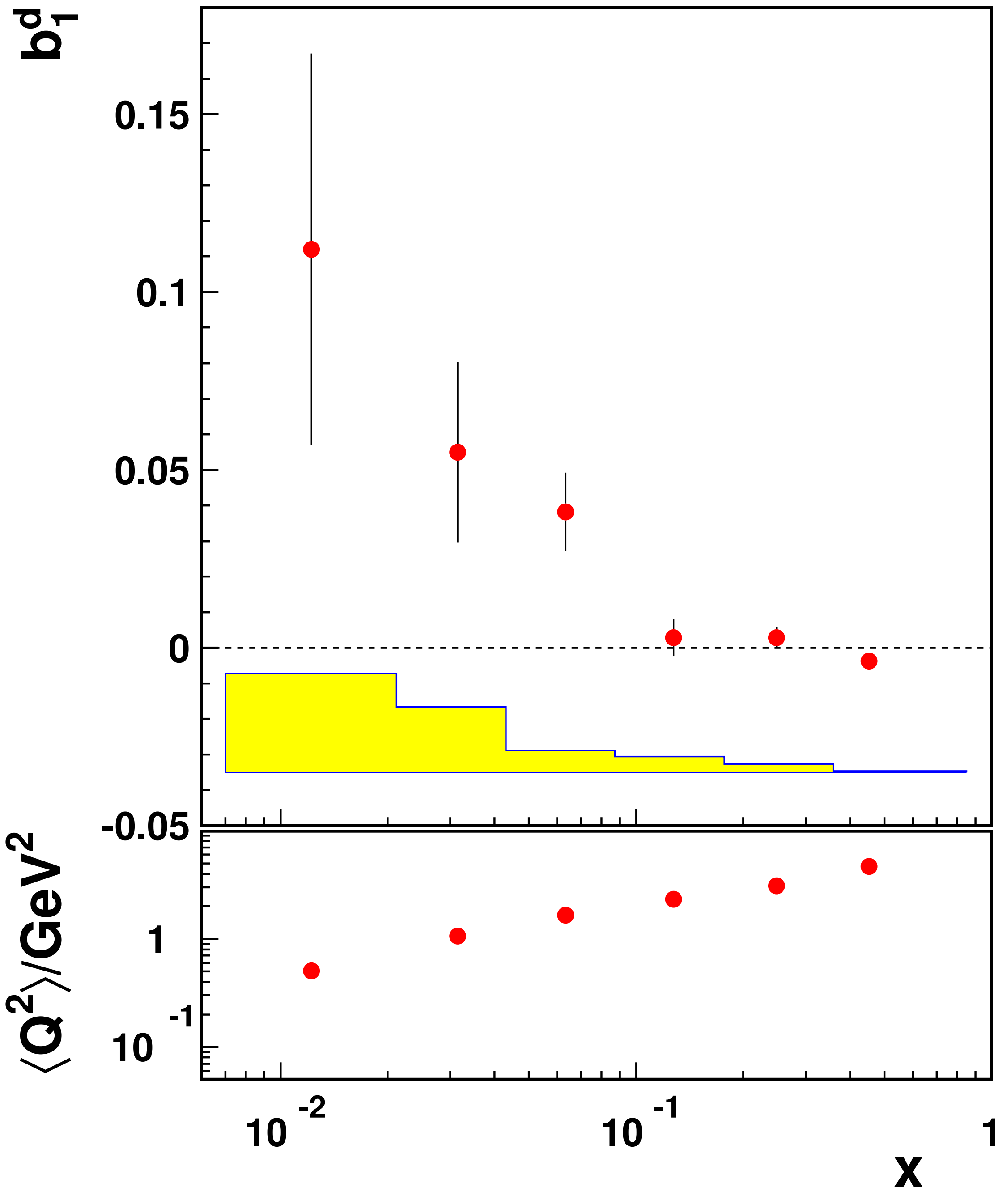

Figure 3.40: The final inclusive tensor structure function b_1^{d} of the deuteron on Born level versus x-Bjørken and the average Q^2 for each x-bin. The error band displays the total systematic uncertainty.

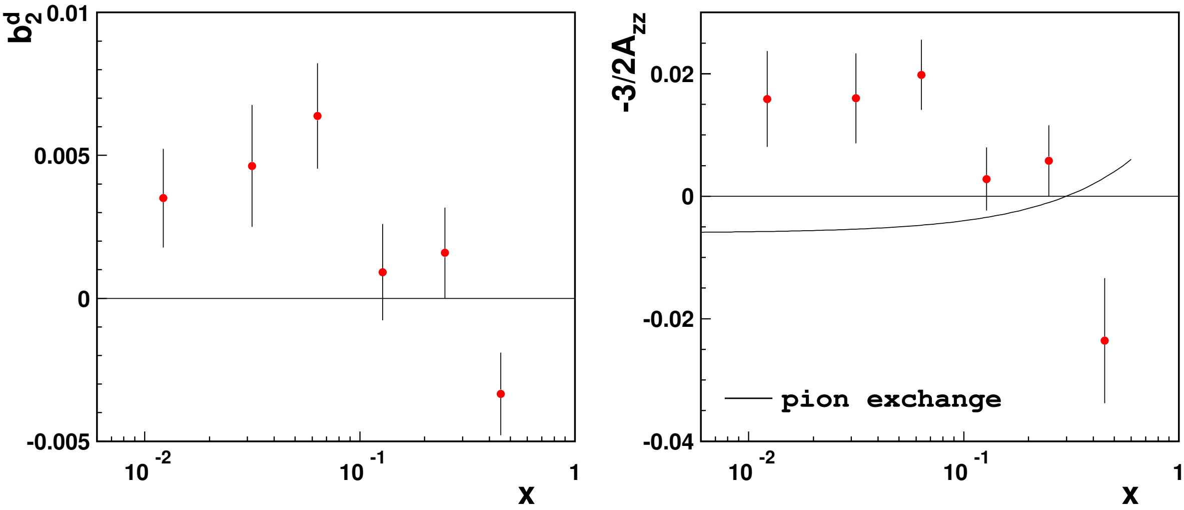

Figure 3.41: Left panel: tensor structure function $b_2^{\rm d} = -\frac{3}{2}A_{zz}F_2^{\rm d}$ of the deuteron on Born level versus x-Bjørken. Right panel: the points indicate the experimentally determined $b_1^{\rm d}/F_1^{\rm d} = -\frac{3}{2}A_{zz}$ on Born level, the curve the pionic contribution as estimated in Ref. [36] for $x < 0.6$. Errors bars are statistical only.

positive, b_2 has the same zero crossing point as the asymmetry A_{zz}.
A set of models predicted a small contribution of the order of 10^{-4} to $b_1^{\rm d}$ through Fermi motion and nuclear binding effects for moderate and large $x > 0.1$. The measured values of $b_1^{\rm d}$ which were found to be rather of the order 10^{-3} (Tab. D.14) in this kinematic region exceed this estimate by one order of magnitude. The contribution to $b_1^{\rm d}$ at $x < 0.6$ which was estimated in Ref. [36] from pion exchange currents is shown in Fig. 3.41 (right panel) together with the measured tensor asymmetry $-\frac{3}{2}A_{zz} = b_1^{\rm d}/F_1^{\rm d}$. The estimated contribution is large for small x, almost 1%, its sign is however opposite to that of the result of the measurement.
The behavior of the measured $b_1^{\rm d}$ for $x < 0.1$ is in qualitative agreement with coherent double scattering mechanisms that were predicted to significantly contribute to the tensor structure function for such small x. These models are discussed in detail in Sec. 1.5.
In particular, the observed steep rise of $b_1^{\rm d}$ was predicted in Ref. [17], see Fig. 3.42 in which the measured values are superimposed to the model curve. The calculated behavior of $b_1^{\rm d}$ in the range $0.01 < x < 0.1$ fits well to the measured structure function. The quantitative estimate for $x < 0.1$ was $b_1^{\rm d}/F_1^{\rm d} \approx 0.02$. The measured $b_1^{\rm d}/F_1^{\rm d}$ is displayed in Fig. 3.41. For $\langle x\rangle = 0.06$, a ratio of $b_1^{\rm d}/F_1^{\rm d} = 0.020 \pm 0.006(\text{stat})$ and for the lowest x-bin of $\langle x\rangle = 0.01$ a ratio of $b_1^{\rm d}/F_1^{\rm d} = 0.016 \pm 0.008(\text{stat})$ were observed (see also Tab. D.15).
Ref. [41] predicts an enhancement of $b_1^{\rm d}$ for $x < 0.01$. The estimated $b_2^{\rm d}$ at different values of Q^2 is shown in Fig. 3.43 in comparison to the measured values. In particular, for $x = 0.01$, $b_2^{\rm d}(x) \approx 0.002...0.009$ (with Q^2 between 0.1 GeV^2 and 1

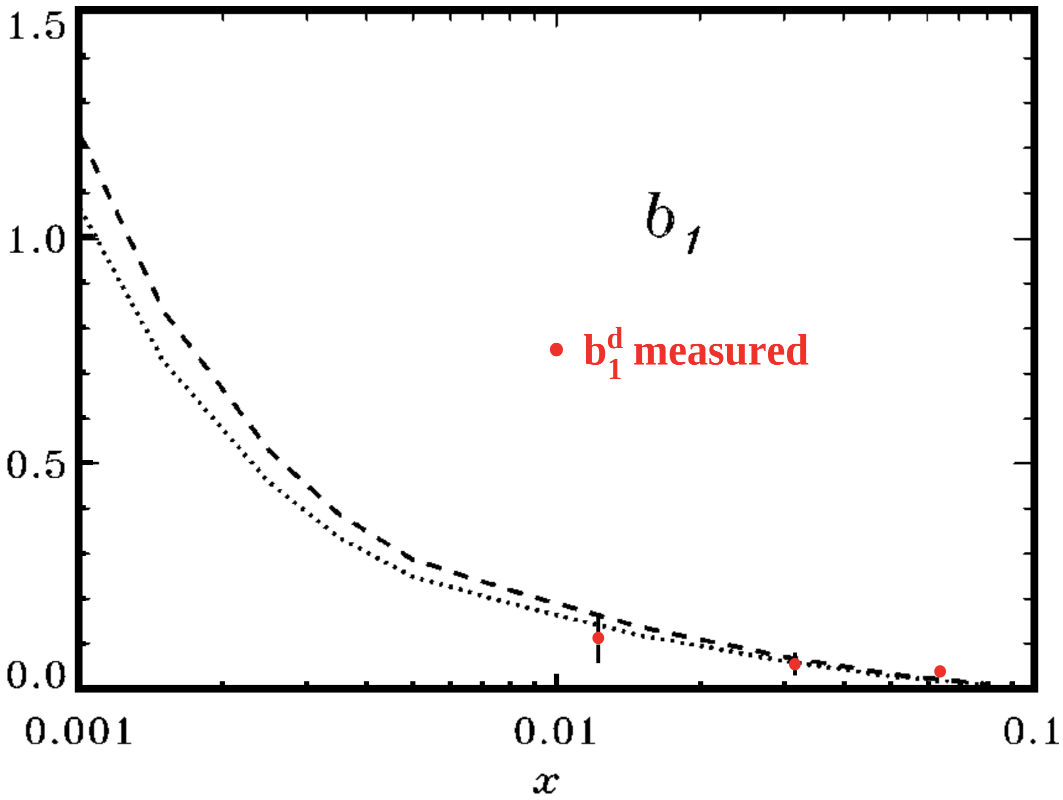

Figure 3.42: Theoretical prediction for $b_1^{\rm d}$ from Ref. [17] in comparison to the measured values (statistical error bars only). The plot is taken from the reference. The dotted and dashed curves correspond to the Bonn OBE and Paris potential, respectively.

GeV^2) is estimated, which is not ruled out by the observed value of $b_2^{\rm d}(x = 0.01, Q^2 = 0.51{\rm GeV}^2) = 0.0035 \pm 0.0017({\rm stat})$ (Tab. D.15). In Ref. [40], the tensor structure function $b_2^{\rm d} = -\frac{3}{2}A_{zz}F_2^{\rm d}$ was predicted to rise and then fall again in the range $0.01 < x < 0.4$. Fig. 3.44 shows the comparison between the predicted behavior and the measurement of the tensor structure function and asymmetry. The estimated magnitude of $b_2^{\rm d}$ at $x = 0.01$ does not reach the order of magnitude of the observed value $b_2^{\rm d} = 0.0035$ (see Tab. D.15).

The estimate of $A_{zz} \sim \mathcal{O}(1\%)$ for $x \leq 0.03 - 0.02$ which was made in Ref. [45] also in the context of nuclear shadowing induced by double scattering processes, however without explicit calculation, is in agreement with the measurement.

Fig. 3.45 compares vector and tensor asymmetries (structure functions) as extracted from Hermes deuteron data [101], [75] to each other. For small values of $x < 0.05$, the ratio of the spin structure function and the spin-averaged function $g_1^{\rm d}/F_1^{\rm d} \approx A_{\|}/D$ drops down to zero, in contrast to the tensor asymmetry $b_1^{\rm d}/F_1^{\rm d} = -\frac{3}{2}A_{zz}$ which does not vanish in that kinematic region. This finding is somewhat surprising as the tensor asymmetry originates from a rather small binding correction in the deuteron wave function. Nevertheless, the impact on the extraction of g_1/F_1 from a deuteron tar-

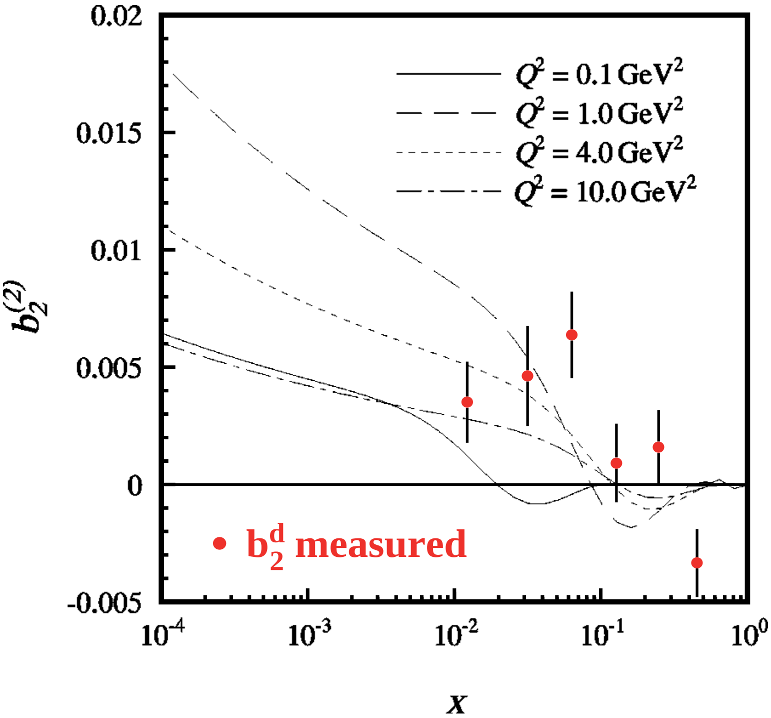

Figure 3.43: Theoretical prediction for $b_2^\mathrm{d} = -\frac{3}{2} A_{zz} F_2^\mathrm{d}$ from Ref. [41] with the Bonn potential for the deuteron in comparison to the measured values (statistical error bars only). The plot is taken from the reference.

get (Eqs. 1.18 and 2.13) is rather small. The tensor asymmetry delivers only a 1% contribution to the vector asymmetry which was taken into account in its extraction. The structure function level is even more impressive; g_1^d vanishes for $x < 0.05$, the region where b_1^d rises steeply up to 2% of the spin-averaged structure function and is significantly larger than the spin structure function g_1^d.

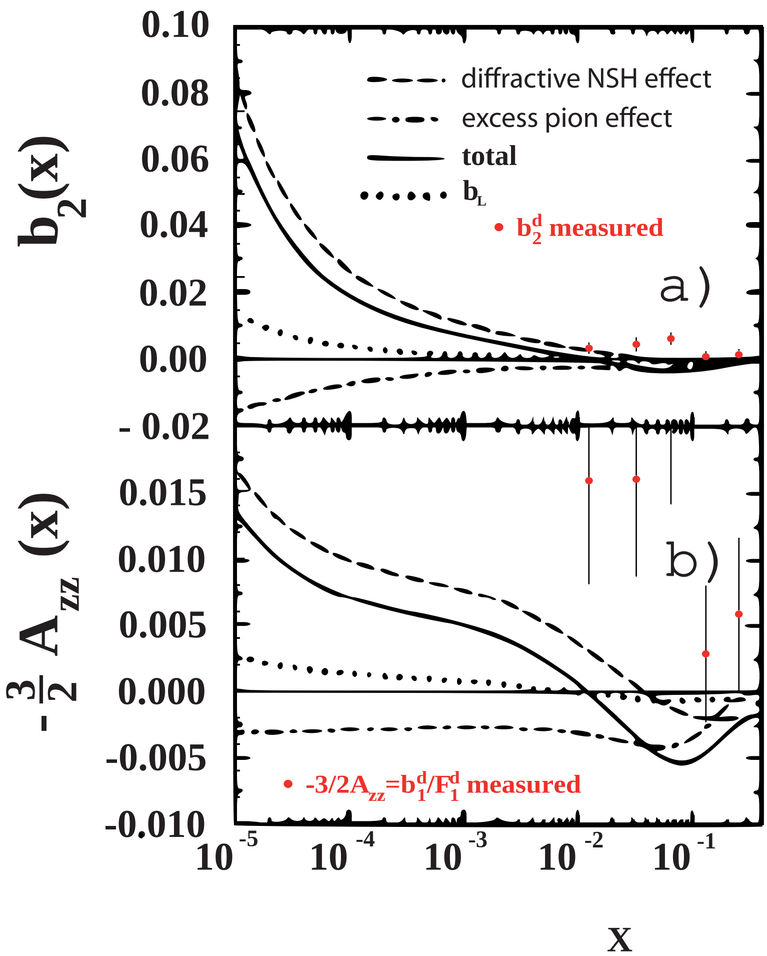

Figure 3.44: Theoretical prediction for $b_2^{\mathrm{d}} = -\frac{3}{2}A_{zz}F_2^{\mathrm{d}}$ (top panel) and $-\frac{3}{2}A_{zz} = b_1^{\mathrm{d}}/F_1^{\mathrm{d}} = b_2^{\mathrm{d}}/F_2^{\mathrm{d}}$ (lower panel) from Ref. [40] in comparison to the measured values (statistical error bars only). Note that the definition of both the tensor structure function and the asymmetry in Ref. [40] differ by a minus sign with respect to the experimentally extracted ones. The plot is slightly modified taken from the reference. All numerical results are for $Q^2 = 10$ GeV^2.

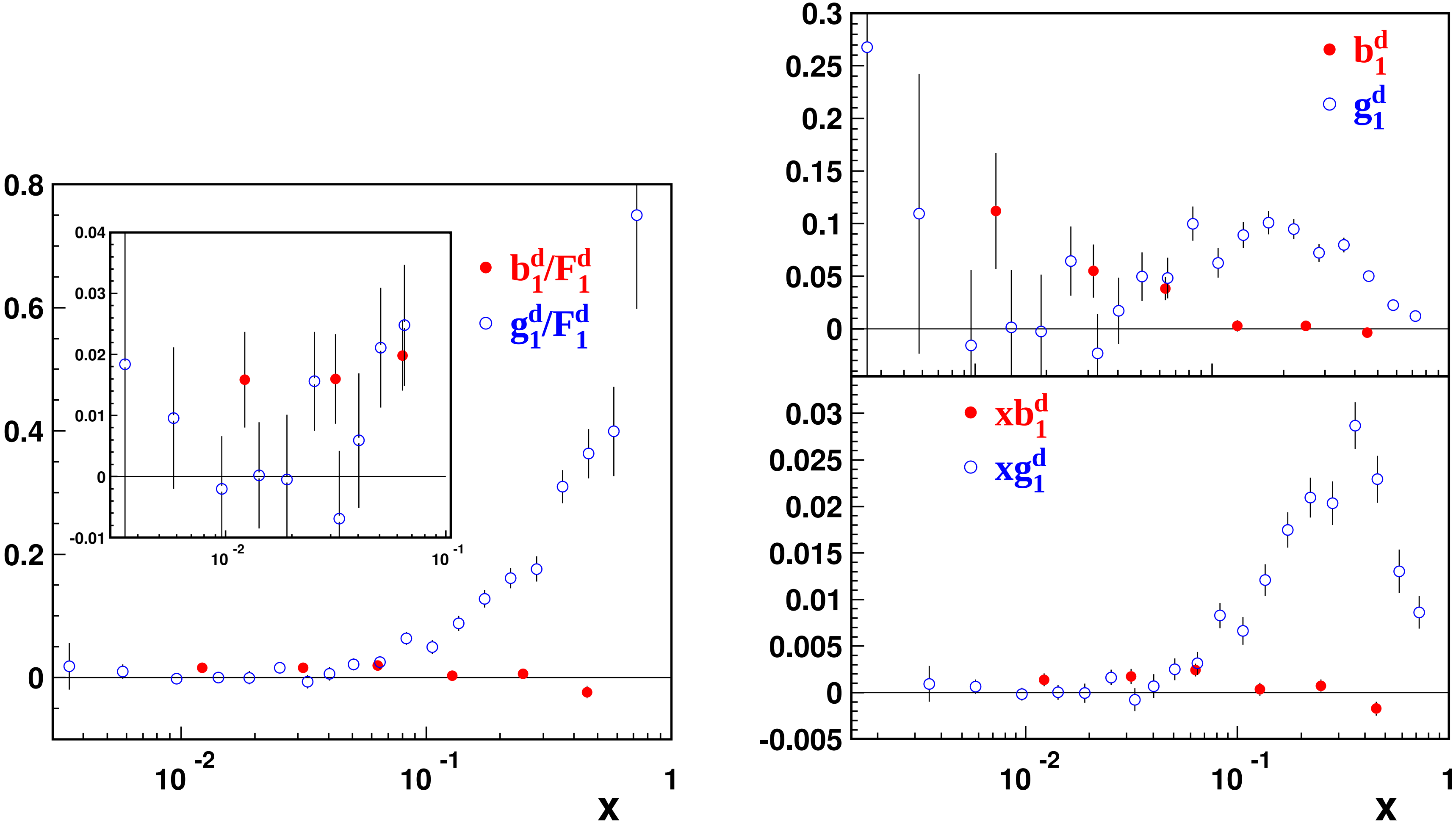

Figure 3.45: HERMES inclusive asymmetries and structure functions from deuteron data; left: $b_1^{\rm d}/F_1^{\rm d} = -\frac{3}{2}A_{zz}$ compared to $g_1^{\rm d}/F_1^{\rm d} \approx A_{\parallel}/D$, right: $b_1^{\rm d}$ and $g_1^{\rm d}$ (top), $xb_1^{\rm d}$ and $xg_1^{\rm d}$ (bottom).

3.7 First moment of b_1^{d}

The first moment of b_1^{d} in the range $x_{\mathrm{min}} < x < x_{\mathrm{max}}$ at fixed $Q^2 = Q_0^2$

$$M = \int_{x_{\mathrm{min}}}^{x_{\mathrm{max}}} b_1^{\mathrm{d}}(x, Q_0^2)\mathrm{d}x \tag{3.25}$$

was calculated using the relation

$$b_1^{\mathrm{d}}(x, Q_0^2) = \left(\frac{b_1^{\mathrm{d}}}{F_1^{\mathrm{d}}}\right)(x) F_1^{\mathrm{d}}(x, Q_0^2). \tag{3.26}$$

For the calculation of the first moment of the tensor structure function, b_1^{d} was assumed to obey the same scaling equations as F_1^{d} does. This ansatz does not fit *a priori* to the interpretation of b_1 in the context of double-scattering models since the scaling behavior arises in the QCD picture from radiative processes of involved partons. Indeed the model calculation of Ref. [41] shows a somewhat stronger Q^2-dependence for the tensor structure function b_2 (see Fig. 3.43) than the one known for F_2 (see e. g. Fig. 3.17). In particular, the curves for $Q^2 = 0.1$ GeV^2 and $Q^2 = 1$ GeV^2 exhibit a sifnificant difference which is explainable by the fact that at $Q^2 = 0.78$ GeV^2 the ρ becomes available for diffractive shadowing, delivering an additional contribution to the tensor structure function.
Still, because there is no better solution at hand, b_1^{d} was assumed to obey the same Q^2-evolution as F_1^{d} does. With Eqs. 3.19 and 3.24, the substitution was made:

$$\left(\frac{b_1^{\mathrm{d}}}{F_1^{\mathrm{d}}}\right)(x) = -\frac{3}{2} A_{zz}(x). \tag{3.27}$$

Then the first moment was evaluated as the discrete sum over $(n - i_1 + 1)$ x-bins from bin i_1 to n (where x_i is the lower bin border of bin i), involving the integral of F_1^{d} between each two bin borders:

$$M = -\frac{3}{2} \sum_{i=i_1}^{n} \left(A_{zz}(\langle x_i \rangle) \cdot \int_{x_i}^{x_{i+1}} F_1^{\mathrm{d}}(x, Q_0^2)\mathrm{d}x \right), \tag{3.28}$$

and its statistical error, using the full covariance matrix of A_{zz} from Eq. C.23

$$\delta M = \frac{9}{4} \sum_{i=i_1}^{n} \left(\sum_{j=j_1}^{n} \mathrm{cov}(i,j) \cdot \int_{x_i}^{x_{i+1}} F_1^{\mathrm{d}}(x, Q_0^2)\mathrm{d}x \int_{x_j}^{x_{j+1}} F_1^{\mathrm{d}}(x, Q_0^2)\mathrm{d}x \right). \tag{3.29}$$

$F_1^{\mathrm{d}}(x, Q_0^2)$ was calculated from Eq. 3.24 at $Q^2 = Q_0^2$, using $F_2^{\mathrm{d}}(x, Q_0^2)$ obtained from a combination of the ALLM parameterization for $F_2^{\mathrm{p}}(x, Q_0^2)$ and the NMC fit to the

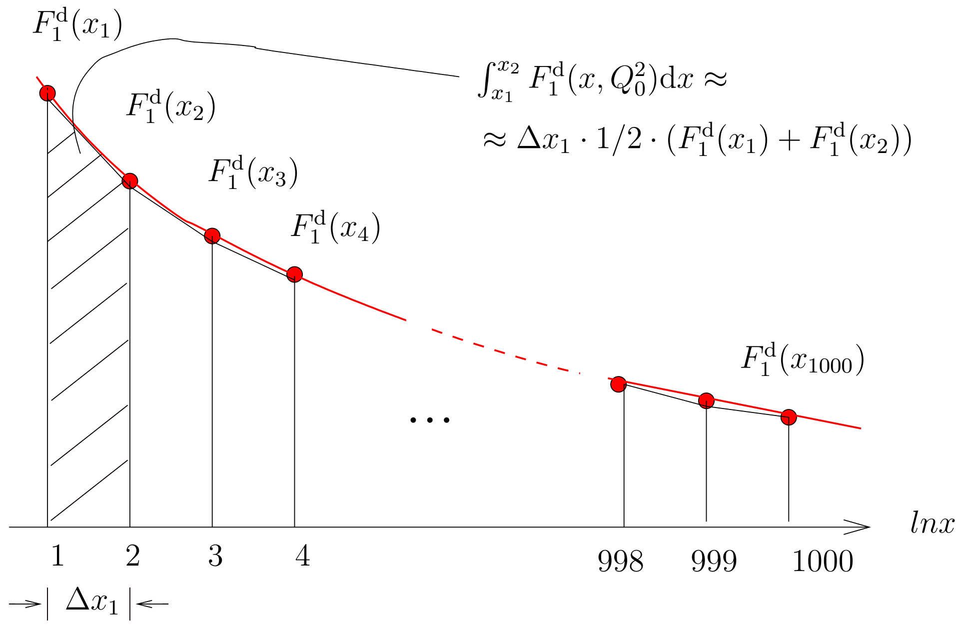

Figure 3.46: $F_1^{\rm d}(x, Q_0^2)$ was integrated by dividing the area below the graph in e. g. $N-1 = 1000$ trapezoids .

$F_2^{\rm n}/F_2^{\rm p}$ ratio (Eq. 3.8). $F_1^{\rm d}(x,Q_0^2)$, $F_2^{\rm d}(x,Q_0^2)$ and $R(x,Q_0^2)$ for $Q_0^2 = 5$ GeV^2 are displayed in Figs. 3.47, 3.17, resp. 3.16.
$F_1^{\rm d}(x,Q_0^2)$ was integrated for each x-bin i by summing up $N(i)-1$ trapezoids between x_i and x_{i+1} that approximate the area below the function graph, see Fig. 3.46, using the area formula for a trapezoid:

$$\int\limits_{x_i}^{x_{i+1}} F_1^{\rm d}(x,Q_0^2){\rm d}x \approx \sum_{j=j_1(i)}^{N(i)-1} \Delta x_j \cdot \frac{1}{2} \cdot \left[F_1^{\rm d}(x_j) + F_1^{\rm d}(x_{j+1})\right], \tag{3.30}$$

where $x_{j_1(i)}$ is the smallest choice for which $x_{j_1(i)} \geq x_i$ is true and $x_{N(i)}$ the largest choice for which $x_{N(i)} \leq x_{i+1}$ is true, and $\Delta x_j = x_{j+1} - x_j$. The total number of trapezoids is $N-1$, where

$$N = \sum_{i=1}^{n} N_i. \tag{3.31}$$

An illustration of the two x-dependent contributions entering Eq. 3.28 is shown in Fig. 3.47; $A_{zz}(\langle x\rangle)$ is presented by a histogram (in the top panel scaled by a factor 1000) and $F_1^{\rm d}(x,Q_0^2 = 5\ {\rm GeV}^2)$ as it was evaluated at each of the $N = 1000$ points used for integration.

If one assumes four significant digits for both the moment and its error, 1000 bins are a sufficient number to use for the F_1 integration, see Fig. 3.48. Then M (δM), calculated according to Eq. 3.28 (Eq. 3.29) at $Q_0^2 = 5$ GeV^2 and including all x-bins (i. e. $0.0021 < x < 0.85$) is found to be

$$M = 0.010473 \pm 0.003411({\rm stat}). \tag{3.32}$$

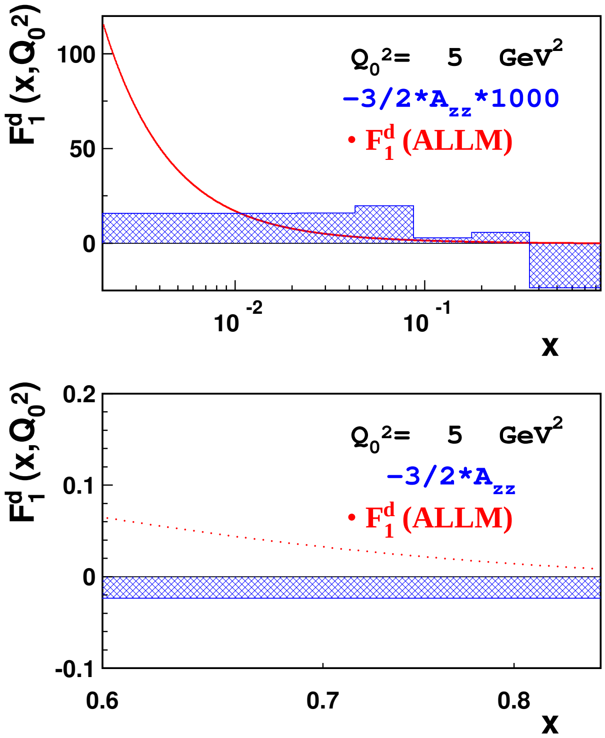

Figure 3.47: Illustration of the contributions to the first moment of b_1^{d}: the histogram represents $-3/2 * A_{zz}$, the dots $F_1^{\mathrm{d}}(x, Q_0^2 = 5\ \mathrm{GeV}^2)$; in the top panel, $-3/2 * A_{zz}$ is scaled by a factor 1000, showing the entire x-range, whereas in the bottom panel the original -3/2*A_{zz} is compared to $F_1^{\mathrm{d}}(x, Q_0^2 = 5\ \mathrm{GeV}^2)$ for the x-region ($x > 0.6$) in which the two are of about the same size.

If one sums up only the main diagonal elements in Eq. 3.29 for the calculation of the statistical error on the moment, i. e. takes only into account the error bars as they are e. g. drawn in Fig. 3.40, the statistical error on the moment is $\delta M(\mathrm{stat}) = 0.0037$. Though, this way of calculation overestimates the error, as the latter is correlated between individual bins. Including the side diagonal elements of the covariance matrix in the calculation of the moment removes the multiple counting of statistical uncertainies coming along with the re-sorting of events because these elements are mostly negative (see Tab. D.11) and thus decrease the error (see also Sec. C.5).
Including only x-bins with an average $Q^2 > 1\ \mathrm{GeV}^2$ (commonly referred to as DIS-region), which means practically leaving out the first x-bin (i. e. $0.02 < x < 0.85$), the moment of b_1^{d} results in

$$M = 0.0035 \pm 0.0010(\mathrm{stat}). \tag{3.33}$$

Two systematic uncertainties of the analysis contributed to the systematic error on the b_1^{d} moment: the experimental and the Monte Carlo uncertainties to obtain A_{zz} on BORN level. To estimate them, two modified moments M_{exp} and M_{MC} were calculated from the tensor asymmetries to which for each bin the corresponding systematic error was

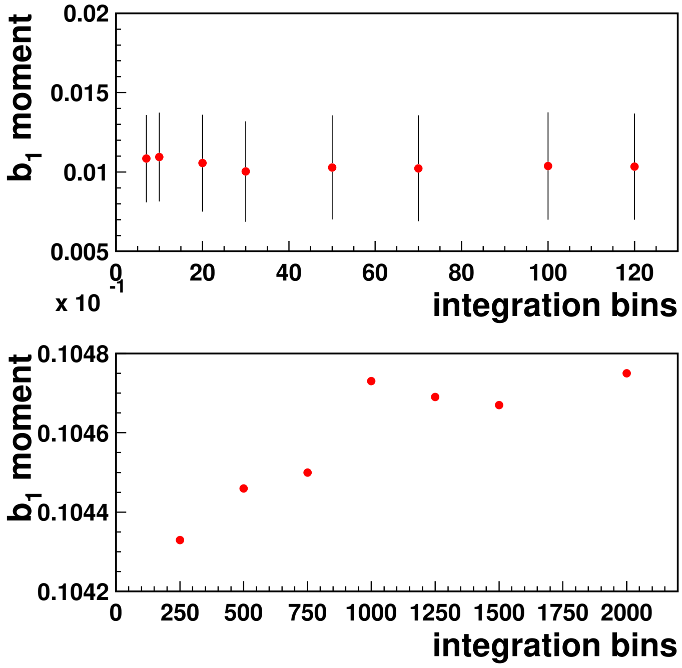

Figure 3.48: The first moment of b_1^{d} in dependence on the numbers of bins used for integration (in the bottom panel, error bars are skipped). Already 50 integration bins provide an stable result within the statistical error bars (top). For latest 1000 bins, the result has converged in the fourth digit behind the comma.

added: M_{exp} from $A_{zz}+\delta A_{\mathrm{Born}}^{\mathrm{sys}}(\mathrm{exp})$ (see Eq. 3.16) and M_{MC} from $A_{zz}+\delta A_{\mathrm{Born}}^{\mathrm{sys}}(\mathrm{MC})$ (see Eq. 3.17). The single systematic errors were calculated by subtracting these moments from the default one (Eq. 3.32):

$$\delta M^{\mathrm{sys}}(\mathrm{exp}) = M - M_{\mathrm{exp}} \tag{3.34}$$
$$\delta M^{\mathrm{sys}}(\mathrm{MC}) = M - M_{\mathrm{MC}}; \tag{3.35}$$

these contributions from Eqs. 3.34 and 3.35 were added in quadrature to obtain the total systematic error $\delta M^{\mathrm{sys}}(\mathrm{tot})$:

$$\delta M^{\mathrm{sys}}(\mathrm{tot}) = \sqrt{\delta M^{\mathrm{sys}}(\mathrm{exp})^2 + \delta M^{\mathrm{sys}}(\mathrm{MC})^2} = 0.0035. \tag{3.36}$$

This leads, in summary, to the first moment of b_1^{d} of

$$\int_{0.0021}^{0.85} b_1^{\mathrm{d}}(x, Q_0^2 = 5\,\mathrm{GeV}^2)\mathrm{d}x = 0.0105 \pm 0.0034(\mathrm{stat}) \pm 0.0035(\mathrm{sys}). \tag{3.37}$$

The discussed contributions to the first moment of b_1^{d} and its statistical and systematic error for the x-range $0.0021 < x < 0.85$ are compiled in Tab. D.16, moreover, results for another (smaller) range of integration ($0.021 < x < 0.85$) are presented there.

The comparison between the prediction of the phenomenological CLOSE-KUMANO sum rule $\int_0^1 \mathrm{d}x\, b_1(x) = 0$ (see Sec. 1.5) and the experiment would require to form the integral of the measured $b_1^{\mathrm{d}}(x, Q_0^2)$ of the deuteron over the full x range from $0 \to 1$ at fixed Q_0^2. Thus extrapolations are necessary in order to include regions of unmeasured x, both at high and low x. As no quantitatively satisfying model calculation for b_1^{d} (yet) exists, sensible extrapolations are out of reach. The first moment of b_1^{d} in the measured range $0.002 < x < 0.85$ of $\int_{0.002}^{0.85} \mathrm{d}x\, b_1^{\mathrm{d}}(x, Q_0^2 = 5\mathrm{GeV}^2) = 0.0105 \pm 0.0034(\mathrm{stat}) \pm 0.0035(\mathrm{sys})$ constitutes a clear non-zero value *possibly* indicating a tensor-polarized quark sea and thus a breaking of the CLOSE-KUMANO sum rule. If merely nuclear binding and FERMI motion contributed to b_1^{d}, its first moment would be expected to vanish. However, due to the x-regions not covered by HERMES, the statement about the breaking or not breaking of the sum rule has to keep vague.
The finding of a possibly tensor polarized quark sea contradicts the generic expectation [40] that cross sections cease to depend on beam and target polarizations at high energies ($x \to 0$). Such tendency was for example confirmed by first results for the individual sea quark (*vector*) polarizations $\Delta\overline{u}/\overline{u}$, $\Delta\overline{d}/\overline{d}$ and $\Delta s/s$ obtained in Ref. [75], which are consistent with zero.
This is the place to go back to Fig. 3.45 which compares deuteron tensor and vector asymmetries and structure functions. The vector asymmetry $A_{\|}/D \approx g_1^{\mathrm{d}}/F_1^{\mathrm{d}}$ is significantly different from zero for $x > 0.04$, where valence quarks play the dominant role and the difference in quarks is probed which have their spin aligned respectively anti-aligned to the spin of parent nucleus. The integral of g_1^{d} is mostly fed from this medium and large x region. At $x < 0.05$, $g_1^{\mathrm{d}}/F_1^{\mathrm{d}}$ drops down to zero. This is the kinematic region where the tensor asymmetry $-\frac{3}{2}A_{zz} = b_1^{\mathrm{d}}/F_1^{\mathrm{d}}$ rises to values significantly different from zero and larger than $g_1^{\mathrm{d}}/F_1^{\mathrm{d}}$. The main contribution to the integral of b_1^{d} stems from the low x region, where double scattering processes begin to contribute to the cross section and probe the tensor polarization of sea quarks.
There is (still) no clear interpretation of the somewhat hybrid b_1^{d} in either the partonic *or* nucleonic picture. Its non-zero value for small x indicates the breakdown of the convolution model in which the *nucleon* distributions inside the nucleus clearly separate from the *quark* distributions inside the nucleon. This result is possibly indicative of extra degrees of freedom possessed by partons in a nucleus relative to a nucleon [43]. At least, b_1^{d} is a fingerprint for the rich structure of the deuteron and diffractive processes taking place inside the deuteron when it is probed in deep-inelastic scattering.

4 Summary

The HERMES experiment at DESY/Hamburg has provided the first measurement ever of the tensor asymmetry A_{zz} and the tensor structure function $b_1^{\rm d}$ of the deuteron in inclusive deep-inelastic positron-deuteron scattering for average values of the BJØRKEN scaling variable $0.01 < \langle x \rangle < 0.45$ and the negative squared 4-momentum transfer 0.5 $\mathrm{GeV}^2 < \langle Q^2 \rangle < 5\ \mathrm{GeV}^2$. The employment of an atomic beam source technique allowed for the generation of a pure deuterium gas target with high tensor polarization and at the same time close-to zero vector polarization, a condition crucial for the experimental access to the cross section tensor asymmetry. The scattered positrons were detected by a forward spectrometer and were cleanly separated from the hadron sample. The extracted tensor asymmetry was corrected for QED radiative and detector smearing effects in order to obtain the asymmetry on BORN level by using an algorithm that keeps track of bin migrations of events without sensitivity to the BORN model input. For this purpose, Monte Carlo simulations of the deep-inelastic scattering process and the subsequent interaction of the scattered particles with the detector material were performed.

The deep-inelastic cross section receives for a spin-1 target like the deuteron in addition to the spin-averaged und spin-dependent structure functions $F_{1,2}(x, Q^2)$ and $g_{1,2}(x, Q^2)$ a contribution from the tensor structure function $b_1(x, Q^2)$ which is of leading twist. $b_1^{\rm d}$ probes the difference in cross sections when the deuteron is in an $|\,m\,| = 1$ respectively an $m = 0$ state and is consequently sensitive to the tensor structure of the deuteron which arises from its non-vanishing electromagnetic quadrupole moment.

The BORN tensor asymmetry $A_{zz}(x, Q^2)$ was found to be different from zero for $x < 0.1$ within uncertainties. This is a striking finding because other spin asymmetries are well known to vanish for $x \to 0$. The resulting tensor structure function $b_1^{\rm d} = -3/2 A_{zz} F_1^{\rm d}$ shows a steep rise in x for this kinematic region and reaches for $\langle x \rangle = 0.01$ a magnitude of $\approx 2\%$ of the spin-averaged structure function $F_1^{\rm d}$ of the deuteron. Effects of nuclear binding and FERMI motion in the deuteron cannot generate such behavior, models involving those effects lead to a contribution to $b_1^{\rm d}$ only at moderate and large $x > 0.2$ which is negligible.

The observed behavior of $b_1^{\rm d}$ at $x < 0.1$ is in qualitative agreement with coherent double scattering models which predict an *enhancement* of the tensor structure function generated by the same mechanism that leads to nuclear shadowing in unpolarized deep-inelastic scattering and thus a *decrease* of the spin-averaged nuclear structure function compared to the free nucleon one. The double scattering reaction involves the subsequent interaction of the virtual photon with both the proton and the neutron and the breaking up of the photon into an intermediate hadronic state. This diffractive nuclear shadowing is considered to be one source of tensor polarization of sea quarks in the deuteron. Another source could be nuclear pions from which b_1 also receives a sizable contribution. The integral $\int_0^1 b_1^{\mathrm{d}}(x, Q_0^2)\mathrm{d}x$ can therefore provide information about the sea tensor polarization. Within the measured range, the integral was calculated to be $\int_{0.0021}^{0.85} b_1^{\mathrm{d}}(x, Q_0^2 = 5\,\mathrm{GeV}^2)\mathrm{d}x = 0.0105 \pm 0.0034(\mathrm{stat}) \pm 0.0035(\mathrm{sys})$. This clear non-zero value indicates a *possibly* tensor-polarized quark sea and the breaking of the related phenomenological Close-Kumano sum rule.

Zusammenfassung

Mit dem Geschirrwaschen ist es doch genau wie mit der Sprache. Wir haben schmutziges Spülwasser und schmutzige Küchentücher, und doch gelingt es, damit die Teller und Gläser schließlich sauberzumachen. So haben wir in der Sprache unklare Begriffe und eine in ihrem Anwendungsbereich eingeschränkte Logik, und doch gelingt es, damit Klarheit in unser Verständnis der Natur zu bringen.
(Niels Bohr beim Abwasch zu Werner Heisenberg)

Das HERMES-Experiment am DESY in Hamburg ermöglichte die überhaupt erste Messung der Tensorasymmetrie A_{zz} und der Tensorstrukturfunktion b_1^{d} des Deuterons in inklusiver tief-inelastischer Positron-Deuteron Streuung an nuklearen Targets für durchschnittliche Werte der BJØRKEN Skalenvariable $0.01 < \langle x \rangle < 0.45$ und des negativen Quadrats des Viererimpulses $0.5\ \mathrm{GeV}^2 < \langle Q^2 \rangle < 5\ \mathrm{GeV}^2$. Durch die Verwendung einer Atomstrahlquelle konnte ein reines atomares Deuteriumgas-Target mit hoher Tensorpolarisation bei gleichzeitig fast verschwindender Vektorpolarisation erzeugt werden; diese Konstellation ist ausschlaggebend für den experimentellen Zugang zur Streuquerschnitts-Tensorasymmetrie. Die gestreuten Positronen wurden mit einem Vorwärts-Spektrometer registriert und sauber von dem Hadronen-Ensemble getrennt. Die gemessene Tensorasymmetrie wurde von Effekten bereinigt, die ein Verschmieren der kinematischen Verteilungen bewirken (QED Strahlungsprozesse und instrumentelle Effekte) und so die Asymmetrie auf BORN-Ebene gewonnen. Dazu wurde ein Algorithmus verwendet, der Buchhaltung über die kinematischen Wanderungen der Ereignisse führen kann, ohne auf das verwendete BORN-Modell empfindlich zu sein. Der tief-inelastische Streuprozeß und die darauffolgende Wechselwirkung der gestreuten Teilchen mit dem Detektormaterial wurden in Monte-Carlo-Rechnungen simuliert. Zusätzlich zu den spingemittelten und spinabhängigen Strukturfunktionen $F_{1,2}(x, Q^2)$ und $g_{1,2}(x, Q^2)$ trägt zum tief-inelastischen Wirkungsquerschnitt für ein Spin-1 Target wie dem Deuteron die Tensorstrukturfunktion $b_1(x, Q^2)$ bei, die von führendem Twist ist. b_1^{d} untersucht den Unterschied in den Wirkungsquerschnitten für ein Deuteron im $|m| = 1$ bzw. $m = 0$ Zustand und ist demnach empfindlich auf die aus dem nichtverschwindenen Quadrupolmoment des Deuterons erwachsende Tensorstruktur.
Die BORN Tensorasymmetrie $A_{zz}(x, Q^2)$ wurde für $x < 0.1$ innerhalb der Fehler zu von Null abweichenden Werten bestimmt. Dies ist ein verblüffender Befund, denn andere Spinasymmetrien fallen bekanntlicherweise für $x \to 0$ auf Null ab. Die resultierende Tensorstrukturfunktion $b_1^{\mathrm{d}} = -3/2 A_{zz} F_1^{\mathrm{d}}$ zeigt in dieser kinematischen Region einen steilen Anstieg in x und erreicht für $\langle x \rangle = 0.01$ eine Größe von etwa 2% der spingemittelten Kernstrukturfunktion F_1^{d} des Deuterons. Weder Kernbindungseffekte noch FERMI-Bewegung im Deuteron können solch ein Verhalten erzeugen; Modelle, die jene

Effekte berücksichtigen, sagen einen Beitrag zu b_1^{d} lediglich bei moderaten und großen Werten von $x > 0.2$ vorher, der vernachlässigbar ist.
Das beobachtete Verhalten von b_1^{d} für $x < 0.1$ steht qualitativ im Einklang mit kohärenten Doppelstreu-Modellen, die dort ein *Anwachsen* der Tensorstrukturfunktion vorhersagen. Dieses Anwachsen wird von dem gleichen Mechanismus erzeugt, der für Abschattungseffekte in unpolarisierter tief-inelastischer Streuung verantwortlich ist und daher zu einem *Abfall* der spingemittelten Strukturfunktion für in Kernen gebundene Nukleonen relativ zu der von freien Nukleonen führt. Bei der Doppelstreu-Reaktion wechselwirkt das virtuelle Photon nacheinander mit dem Proton und dem Neutron und bricht dabei in einen hadronischen Zwischenzustand auf. Diese sogenannte diffraktive Kernabschattung gilt als eine Quelle von Tensorpolarisation der See-Quarks im Deuteron. Eine weitere Quelle könnten Pionen im Kern sein, von denen ebenfalls ein beträchtlicher Beitrag zu b_1 erwartet wird. Das Integral $\int_0^1 b_1^{\mathrm{d}}(x, Q_0^2)\mathrm{d}x$ kann daher Informationen über die Tensorpolarisation der See-Quarks liefern. Das Integral wurde im von der Messung abgedeckten kinematischen Bereich zu $\int_{0.0021}^{0.85} b_1^{\mathrm{d}}(x, Q_0^2 = 5\,\mathrm{GeV}^2)\mathrm{d}x = 0.0105 \pm 0.0034(\mathrm{stat}) \pm 0.0035(\mathrm{sys})$ berechnet. Dieses Ergebnis stellt einen deutlich von Null verschiedenen Wert dar. Es gibt einen Hinweis auf einen *möglicherweise* tensorpolarisierten Quark-See und eine Verletzung der damit verknüpften phänomenologischen Close-Kumano-Summenregel.

A Statistical uncertainties and weights

This section serves as reference for the numerous error calculations and tests of statistical compatibility which were performed for the analysis presented in this thesis.

A.1 Gaussian distribution

A number of measured values of a quantity x is said to be normal distributed if for a sufficiently large number of measurements of this quantity the measured values scatter around the mean value μ following a Gaussian distribution $P(x)$ with the standard deviation σ:

$$P(x) = \frac{1}{\sigma\sqrt{2\pi}} \mathrm{e}^{-\frac{(x-\mu)^2}{2\sigma^2}}, \tag{A.1}$$

see Fig. A.1. The assumption of a Gaussian distribution of the measured values is

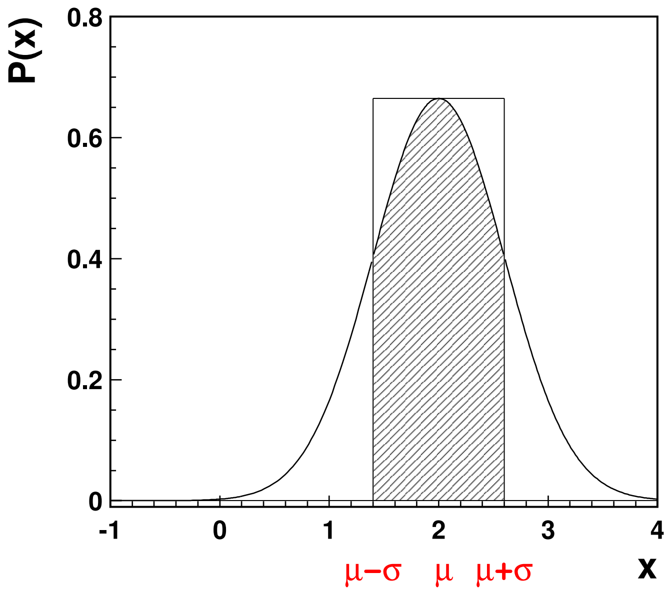

Figure A.1: Gaussian distribution $P(x)$ for a mean value of $\mu = 2$ and a standard deviation of $\sigma = 0.6$. 68.3% of the measured values lie in the one-sigma interval $\pm\sigma$ around μ (0.683 is the content of the shaded area which can be calculated by using the Gaussian error function erf(x) [102]. The Gaussian probability distribution is normalized: $\int_{-\infty}^{+\infty} \mathrm{d}x \, P(x) = 1$).

the precondition for the statistical tests which have been performed for the presented analysis. 68.3% of the measured values lie in the interval $\mu \pm \sigma$. This one-sigma interval is chosen as confidence level for the quotation of the statistical error which arises from the scattering of the measured values. For count rate measurements with N measured events, the one-sigma interval corresponds to a statistical error of $N \pm \sqrt{N}$.

A.2 Error propagation and averages

General error propagation (independent case). To determine the statistical error on a quantity $A = A(N^1, ..., N^R)$ which depends on R independent measured quantities N^j, the statistical error δN^j inherent in the latter has to be propagated to the composed function:

$$\delta A = \sqrt{\sum_{j=1}^{R} \left(\frac{\partial A}{\partial N^j} \delta N^j \right)^2}. \tag{A.2}$$

Average. In the simple case that a large number of N independent measurements A_i of the quantity A have been performed of which each have equal statistical weights, the average $\langle A \rangle$ is calculated as

$$\langle A \rangle = \frac{1}{N} \sum_{i=1}^{N} A_i \tag{A.3}$$

and the one-sigma standard deviation as

$$\langle \delta A \rangle = \sqrt{\frac{1}{N-1} \sum_{i=1}^{N} (A_i - \langle A \rangle)^2}, \tag{A.4}$$

where Eq. A.4 holds only for $N >> 1$. According to Eq. A.3, the average kinematic variables are determined, for example. If it comes to calculating the average of a quantity A which has been determined in n bins[1], and each of the measurements A_i is afflicted with a statistical uncertainty δA_i, the average of these values $\langle A \rangle$ and its statistical error $\langle \delta A \rangle$ are calculated as the statistically weighted mean:

$$\begin{aligned} \langle A \rangle &= \sum_{i=1}^{n} \frac{A_i}{\delta A_i^2} / \sum_{i=1}^{n} \frac{1}{\delta A_i^2}, \\ \langle \delta A \rangle &= 1 / \sqrt{\sum_{i=1}^{n} \frac{1}{\delta A_i^2}}. \end{aligned} \tag{A.5}$$

Error on simple composed functions. Consider two quantities A and B (cross section asymmetries, for example). To determine the statistical error of their difference or their ratio, one must distinguish between the cases that A and B are independent (the intersection set of the data samples entering them is empty), or that they are

[1]Like in the top and bottom detector half ($n = 2$) or in x-Bjørken (here $n = 6$).

correlated (there are data samples which enter both A and B) [103]. In the first case, Eq. A.2 holds for the propagation of the statistical uncertainties δA and δB of A and B, respectively, to the composed function $F = F(A, B)$:

$$\delta F = \sqrt{\left(\frac{\partial F}{\partial A}\delta A\right)^2 + \left(\frac{\partial F}{\partial B}\delta B\right)^2}, \tag{A.6}$$

whereas for the latter case, a correlation term enters the error expression:

$$\delta F = \sqrt{\left(\frac{\partial F}{\partial A}\delta A\right)^2 + \left(\frac{\partial F}{\partial B}\delta B\right)^2 + 2 \cdot \frac{\partial F}{\partial A} \cdot \frac{\partial F}{\partial B} \cdot \mathrm{cov}(A, B)}. \tag{A.7}$$

The covariance $\mathrm{cov}(A, B)$ between A and B is defined as (compare to the definition of the standard deviation in Eq. A.4; also Eq. A.8 holds only for $N >> 1$):

$$\mathrm{cov}(A, B) = \frac{1}{N-1}\sum_{i=1}^{N}(A_i - \langle A\rangle) \cdot (B_i - \langle B\rangle) \tag{A.8}$$

with

$$\mathrm{cov}(A, A) = \delta A^2. \tag{A.9}$$

The covariance for independent A and B is zero; for the special case of completely correlated quantities A and B,

$$\mathrm{cov}(A, B) = \delta A^2, \quad B \subseteq A, \tag{A.10}$$

and for partially correlated quantities A and B,

$$\mathrm{cov}(A, B) = \frac{\delta A^2 \cdot \delta B^2}{\delta(A \cap B)^2}, \tag{A.11}$$

where $\delta(A \cap B)$ denotes the statistical error on the intersection set $A \cap B$. An illustration of the latter case can be found in App. B.8 where an exemplary expression for the correlation term is obtained.
Tab. A.1 compiles the statistical error on $F = A - B$ and $F = A/B$ for both the independent and the completely correlated case.

A.3 Compatibility check of two quantities: t-test

The considerations in Apps. A.1 and A.2 allow to check wether the n measurements F_i of the quantity F are compatible with the expected mean value μ within the defined confidence level, or not. The ratio

$$\Sigma_i = F_i/\delta F_i \tag{A.12}$$

Table A.1: . Statistical error on a simple composed function $F = F(A, B)$ of two measured quantities A and B with statistical uncertainties δA and δB, respectively, and the function Σ employed for the t-test. Once the case is considered that A and B are independent (the intersection set of the data samples entering A and B is empty), and once that A and B are completely correlated (the data sample entering one quantity enters entirely the other quantity). Some examples are given for which cases the given formulas apply (with the number of the section in which they appear in brackets).

	independent	completely correlated
$\delta F = \delta(A - B)$ t-test: $\Sigma = F/\delta F$	$\sqrt{\delta A^2 + \delta B^2}$ $\frac{A-B}{\sqrt{\delta A^2+\delta B^2}}$	$\sqrt{\lvert \delta A^2 - \delta B^2 \rvert}$ $\frac{A-B}{\sqrt{\lvert \delta A^2-\delta B^2 \rvert}}$
$\delta F = \delta(A/B)$	$\frac{A}{B}\sqrt{\frac{\delta A^2}{A^2} + \frac{\delta B^2}{B^2}}$	$\frac{A}{B}\sqrt{\frac{\delta A^2}{A^2} + \frac{\delta B^2}{B^2} - \frac{2}{AB}\delta A^2}$
examples	A_{zz} in different time periods (3.1) A_{zz} in different x-bins (3.1) A_{zz} in top & bottom detector (3.1) A_{zz}^{Born} from different parameterizations (δA, $\delta B = \delta(\text{MC})$) (3.4.4)	A_{zz}(lumi)-A_{zz}(current) (3.4.1) $N_{\text{cand}} - N_{\text{cs}}$ (2.2) N_{cs}/N (2.3.1)

scatters around μ (see Fig. A.2). In the first case (compatibility), at least 68.3% (the previously chosen confidence level) of the n points lie *within* the one-sigma band $\mu \pm \sigma$. In the latter case (no compatibility), less than 68.3% lie inside the band: there are statistically significant deviations from the mean value μ. This statistical check is usually referred to as t-test. An expected value of $\mu = 0$ is often of special interest (zero-measurement). If $F = A - B$, then the t-test on F around $\mu = 0$ checks wether A and B are statistically compatible, or not. The explicit formulas for the t-test on $F = A - B$ for independent and totally correlated quantities, respectively, are compiled in Tab. A.1.

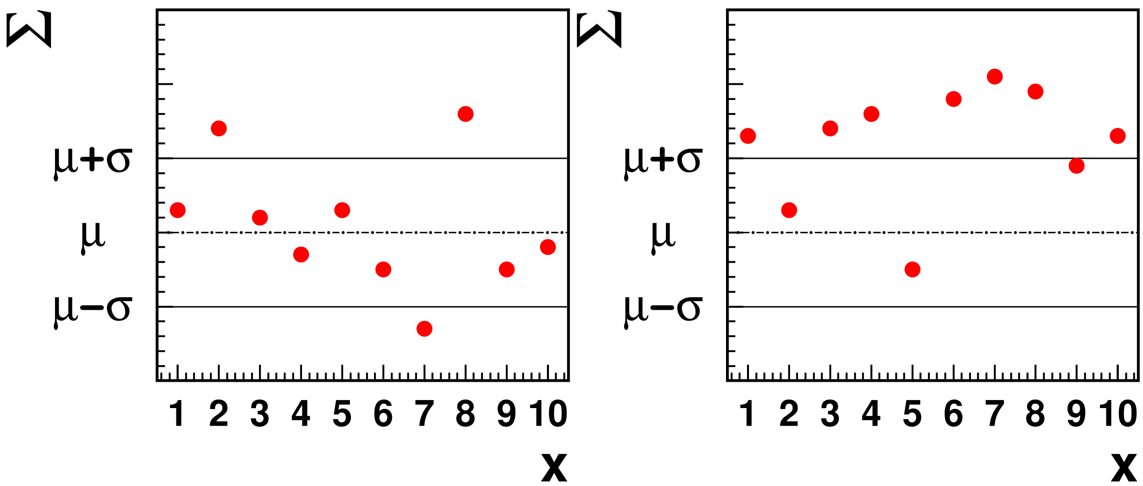

Figure A.2: t-test: the ratio $\Sigma = F/\delta F$ for n (here $n = 10$) measurements of the quantity $F(x)$. δF corresponds to one standard deviation σ. Left panel: Σ scatters around the mean value μ, and more than 68.3% of the points (7 out of n =10) lie within the one-sigma band $\mu \pm \sigma$; the measurement is compatible with μ. Right panel: less than 68.3% of the points lie within the one-sigma band; furthermore, the deviations are biased in one direction. One can thus conclude that the measurement reveals statistically significant deviations from the mean value μ. For the special case that $F = A - B$, the t-test checks the statistical compatibility of A and B, with an expected mean value of $\mu = 0$.

B Tensor formalism

The expressions for the tensor asymmetries in Sec. 2.3.2 are derived.

B.1 Number of events

Let $\Delta\mathcal{T}$ denote the total integration time for a data taking mode with given beam helicity and target polarization). For the target polarizations P_z and P_{zz}, throughout the analysis the average values from Tab. D.2 were used; this assumption is reasonable due to the stable performance of the target in the considered data taking period. Thus, the target polarization can be treated as constant and can be drawn in front of the integral in Eq. 2.23, such that the tensor term becomes:

$$\int_{\Delta\mathcal{T}} \mathrm{d}t\ \epsilon(t)\ \mathcal{L}(t)\ P_{zz}(t)A_{zz} = P_{zz}A_{zz}\cdot L, \tag{B.1}$$

where Eq. 2.11 for the integrated luminosity L corrected for the dead-time ϵ was used. The vector term from Eq. 2.23 will below turn out to be a correction term; this justified to consider the time variation of the beam polarization P_B over one positron fill not to be relevant for the estimation of this term. Thus, P_B is also written in front of the integral in Eq. 2.23:

$$\int_{\Delta\mathcal{T}} \mathrm{d}t\ \epsilon(t)\ \mathcal{L}(t)\ P_B(t)P_z(t)A_{\parallel} = P_BP_zA_{\parallel}\cdot L. \tag{B.2}$$

To write down explicit expressions for collected events, a two-exponent-notation is introduced, the first exponent denoting the sign of the beam polarization (+ or -), the second the target injection mode (as defined in Tab. 2.2). The collected event numbers N and luminosities L as introduced on Pg. 39 on are splitted with respect to different beam helicities for the purpose of systematic studies:

$$\begin{aligned} N^{\rightleftarrows} &= N^{+-}+N^{-+} \\ N^{\rightrightarrows} &= N^{++}+N^{--} \\ N^{0} &= N^{+0}+N^{-0} \\ N^{\Leftrightarrow} &= N^{+\Leftrightarrow}+N^{-\Leftrightarrow} \end{aligned} \tag{B.3}$$

The terms on the right hand side in Eq. B.3 explicitly read, starting from Eq. 2.23:

Vector data:

$$
\begin{aligned}
N^{++} &= \sigma^{\mathrm{U}} L^{++} \left(1 - |P_B^+| \cdot |P_z^+| A_\parallel + \frac{1}{2} |P_{zz}^+| A_{zz}\right) \\
N^{-+} &= \sigma^{\mathrm{U}} L^{-+} \left(1 + |P_B^-| \cdot |P_z^+| A_\parallel + \frac{1}{2} |P_{zz}^+| A_{zz}\right) \\
N^{+-} &= \sigma^{\mathrm{U}} L^{+-} \left(1 + |P_B^+| \cdot |P_z^-| A_\parallel + \frac{1}{2} |P_{zz}^-| A_{zz}\right) \\
N^{--} &= \sigma^{\mathrm{U}} L^{--} \left(1 - |P_B^-| \cdot |P_z^-| A_\parallel + \frac{1}{2} |P_{zz}^-| A_{zz}\right)
\end{aligned}
\tag{B.4}
$$

Tensor data:

$$
\begin{aligned}
N^{+\Leftrightarrow} &= \sigma^{\mathrm{U}} L^{+\Leftrightarrow} \left(1 + |P_B^+| \cdot |P_z^{\Leftrightarrow}| A_\parallel + \frac{1}{2} |P_{zz}^{\Leftrightarrow}| A_{zz}\right) \\
N^{-\Leftrightarrow} &= \sigma^{\mathrm{U}} L^{-\Leftrightarrow} \left(1 - |P_B^-| \cdot |P_z^{\Leftrightarrow}| A_\parallel + \frac{1}{2} |P_{zz}^{\Leftrightarrow}| A_{zz}\right) \\
N^{+0} &= \sigma^{\mathrm{U}} L^{+0} \left(1 + |P_B^+| \cdot |P_z^0| A_\parallel - \frac{1}{2} |P_{zz}^0| A_{zz}\right) \\
N^{-0} &= \sigma^{\mathrm{U}} L^{-0} \left(1 - |P_B^-| \cdot |P_z^0| A_\parallel - \frac{1}{2} |P_{zz}^0| A_{zz}\right)
\end{aligned}
\tag{B.5}
$$

Then one obtains

$$
\begin{aligned}
N^{\rightleftarrows} &= N^{-+} + N^{+-} = \sigma^{\mathrm{U}} \left(L^{\rightleftarrows} + \Sigma L_V^{\rightleftarrows} A_\parallel + \frac{1}{2} (|P_{zz}^+| L^{-+} + |P_{zz}^-| L^{+-}) A_{zz}\right) \\
N^{\rightrightarrows} &= N^{++} + N^{--} = \sigma^{\mathrm{U}} \left(L^{\rightrightarrows} - \Sigma L_V^{\rightrightarrows} A_\parallel + \frac{1}{2} (|P_{zz}^+| L^{++} + |P_{zz}^-| L^{--}) A_{zz}\right) \\
N^{\Leftrightarrow} &= N^{+\Leftrightarrow} + N^{-\Leftrightarrow} = \sigma^{\mathrm{U}} \left(L^{\Leftrightarrow} + \Delta L_V^{\Leftrightarrow} A_\parallel + \frac{1}{2} |P_{zz}^{\Leftrightarrow}| L^{\Leftrightarrow} A_{zz}\right) \\
N^{0} &= N^{+0} + N^{-0} = \sigma^{\mathrm{U}} \left(L^0 + \Delta L_V^0 A_\parallel - \frac{1}{2} |P_{zz}^0| L^0 A_{zz}\right),
\end{aligned}
\tag{B.6}
$$

using the short notations ΣL_V for the sum of two luminosity integrals (*vector* case) and ΔL_V for the difference (*tensor* case):

$$
\begin{aligned}
\Sigma L_V^{\rightleftarrows} &:= |P_B^+| \cdot |P_z^-| \cdot L^{+-} &+& \quad |P_B^-| \cdot |P_z^+| \cdot L^{-+} \\
\Sigma L_V^{\rightrightarrows} &:= |P_B^+| \cdot |P_z^+| \cdot L^{++} &+& \quad |P_B^-| \cdot |P_z^-| \cdot L^{--} \\
\Delta L_V^{\Leftrightarrow} &:= |P_B^+| \cdot |P_z^{\Leftrightarrow}| \cdot L^{+\Leftrightarrow} &-& \quad |P_B^-| \cdot |P_z^{\Leftrightarrow}| \cdot L^{-\Leftrightarrow} \\
\Delta L_V^{0} &:= |P_B^+| \cdot |P_z^0| \cdot L^{+0} &-& \quad |P_B^-| \cdot |P_z^0| \cdot L^{-0}.
\end{aligned}
\tag{B.7}
$$

The terms containing ΣL_V and ΔL_V, both entering the cross section multiplicatively with $A_\parallel$ and describing the *vector contamination* of the tensor measurement, are kept in the further extraction of the tensor asymmetries in order to be able to quantify their impact.

B.2 Vector vs. Tensor minus $A_{zz}(1)$

One starts with writing down the full expression for an *ideal* asymmetry $A(1)$ without a dilution from real polarizations, accounting for the factor 2 in the denominator (see Eq. 2.16) by letting enter twice as many vector as tensor yields:

$$A(1) := \frac{\left[\left(\frac{N^{\overset{\rightarrow}{\Leftarrow}}}{L^{\overset{\rightarrow}{\Leftarrow}}}\right) + \left(\frac{N^{\overset{\rightarrow}{\Rightarrow}}}{L^{\overset{\rightarrow}{\Rightarrow}}}\right)\right] - 2 \cdot \left(\frac{N^0}{L^0}\right)}{\left[\left(\frac{N^{\overset{\rightarrow}{\Leftarrow}}}{L^{\overset{\rightarrow}{\Leftarrow}}}\right) + \left(\frac{N^{\overset{\rightarrow}{\Rightarrow}}}{L^{\overset{\rightarrow}{\Rightarrow}}}\right)\right] + \left(\frac{N^0}{L^0}\right)}. \tag{B.8}$$

By inserting into Eq. B.8 the (beam helicity averaged) collected eventnumbers from Eq. B.6 and introducing the expressions κ_1, κ_2 and τ_1 and the effective tensor polarization $\langle P_{zz}\rangle_1$

$$\kappa_1 = \left(\frac{\Sigma L_V^{\overset{\rightarrow}{\Leftarrow}}}{L^{\overset{\rightarrow}{\Leftarrow}}} - \frac{\Sigma L_V^{\overset{\rightarrow}{\Rightarrow}}}{L^{\overset{\rightarrow}{\Rightarrow}}} + \frac{\Delta L_V^0}{L^0}\right) \tag{B.9}$$

$$\kappa_2 = \left(\frac{\Sigma L_V^{\overset{\rightarrow}{\Leftarrow}}}{L^{\overset{\rightarrow}{\Leftarrow}}} - \frac{\Sigma L_V^{\overset{\rightarrow}{\Rightarrow}}}{L^{\overset{\rightarrow}{\Rightarrow}}} - 2 \cdot \frac{\Delta L_V^0}{L^0}\right) \tag{B.10}$$

$$\tau_1 = \left(|\,P_{zz}^+\,| \left(\frac{L^{-+}}{L^{\overset{\rightarrow}{\Leftarrow}}} + \frac{L^{++}}{L^{\overset{\rightarrow}{\Rightarrow}}}\right) + |\,P_{zz}^-\,| \left(\frac{L^{+-}}{L^{\overset{\rightarrow}{\Leftarrow}}} + \frac{L^{--}}{L^{\overset{\rightarrow}{\Rightarrow}}}\right) - |\,P_{zz}^0\,|\right) \tag{B.11}$$

$$6\langle P_{zz}\rangle_1 = \left(|\,P_{zz}^+\,| \left(\frac{L^{-+}}{L^{\overset{\rightarrow}{\Leftarrow}}} + \frac{L^{++}}{L^{\overset{\rightarrow}{\Rightarrow}}}\right) + |\,P_{zz}^-\,| \left(\frac{L^{+-}}{L^{\overset{\rightarrow}{\Leftarrow}}} + \frac{L^{--}}{L^{\overset{\rightarrow}{\Rightarrow}}}\right) + 2 \cdot |\,P_{zz}^0\,|\right) \tag{B.12}$$

(here, the short notations from Eq. B.7 have been used), one obtains:

$$A(1) = \frac{3\langle P_{zz}\rangle_1 \cdot A_{zz} + \kappa_2 \cdot A_\parallel}{3 + \tau_1 \cdot \frac{1}{2}\,A_{zz} + \kappa_1 \cdot A_\parallel}. \tag{B.13}$$

Solving for $\frac{1}{2}\,A_{zz}|_{A(1)} \equiv \frac{1}{2}\,A_{zz}(1)$ delivers:

$$\frac{1}{2}\,A_{zz}|_{A(1)} = \frac{A(1)\left(3 + \kappa_1 \cdot A_\parallel\right) - \kappa_2 \cdot A_\parallel}{6\langle P_{zz}\rangle_1 - \tau_1 \cdot A(1)}. \tag{B.14}$$

The vector correction terms κ_1 and κ_2 and the term τ_1 in Eq. B.14 can be estimated by making the following approximations:

Luminosity for vector states. One can assume the two vector target states to undergo the same luminosity separately for each beam helicity; this is expected as the target injection mode was switched roughly every minute, compared to many days of data taking, averaging out possible differences on a small scale; furthermore, the beam helicity was switched only long term:

$$\begin{aligned} L^{-+} &\approx L^{--} \\ L^{+-} &\approx L^{++}. \end{aligned}$$

Deviations don't exceed 2 permill (see Tab. D.3). Thus, the following approximations hold:

$$\begin{aligned} &\frac{L^{-+}}{L^{\overset{\rightarrow}{\Leftarrow}}} + \frac{L^{++}}{L^{\overset{\rightarrow}{\Rightarrow}}} \approx 1 && \text{actual value}: \ 0.9992 \\ &\frac{L^{+-}}{L^{\overset{\leftarrow}{\Leftarrow}}} + \frac{L^{--}}{L^{\overset{\leftarrow}{\Rightarrow}}} \approx 1 && \text{actual value}: \ 1.0008. \end{aligned} \tag{B.15}$$

Then the term τ_1 (Eq. B.11) becomes, inserting the average target polarization values from Tab. D.2:

$$\tau_1 = \left(|\,P^+_{zz}\,| + |\,P^-_{zz}\,| - |\,P^0_{zz}\,|\right) = (0.800 + 0.853 - 1.655) = -2 \cdot 10^{-3}, \tag{B.16}$$

and the effective tensor polarization $\langle P_{zz}\rangle_1$ (Eq. B.12) is

$$6\langle P_{zz}\rangle_1 = |\,P^+_{zz}\,| + |\,P^-_{zz}\,| + 2 \cdot |\,P^0_{zz}\,| = 0.800 + 0.853 + 2 \cdot 1.655 = 4.963 \approx 5. \tag{B.17}$$

Beam polarization. The absolute value of P_B for negative and positive beam helicity was assumed to be equal and was chosen to be some rounded number:

$$|P^+_B| \approx |P^-_B| \equiv |P_B| := 0.5.$$

The actual values (see Tab. D.1) differ by 3%.

Luminosity.

1. Each data type ($\overset{\rightarrow}{\Leftarrow}, \overset{\rightarrow}{\Rightarrow}, \Leftrightarrow, 0$) received the same luminosity:

   $$L^{\overset{\rightarrow}{\Leftarrow}} \approx L^{\overset{\rightarrow}{\Rightarrow}} \approx L^0 \approx L^{\Leftrightarrow} =: L$$

   The deviation from this assumption is at most (namely for the two tensor target states) 0.7%, see Tab. D.3.

2. Like 1., but for each beam helicity separately:

$$L^{++} - L^{-+} \approx L^{+-} - L^{--} \approx L^{+\Leftrightarrow} - L^{-\Leftrightarrow} \approx L^{+0} - L^{-0} =: \Delta L$$

The relative difference between luminosities at different beam helicities is estimated to be $\Delta L/L \approx 0.22$, see Tab. D.3.

Thus, the *vector* expressions entering multiplicatively with $A_{\|}$ in the numerator in Eq. B.14 can be simplified:

$$\begin{aligned}
\Sigma L_V^{\leftrightarrows} - \Sigma L_V^{\rightrightarrows} &\approx -|\,P_B\,| \cdot (|\,P_z^+\,| - |\,P_z^-\,|)\Delta L \\
\Delta L_V^{\Leftrightarrow} &\approx |\,P_B\,| \cdot |\,P_z^{\Leftrightarrow}\,|\Delta L \\
\Delta L_V^0 &\approx |\,P_B\,| \cdot |\,P_z^0\,|\Delta L.
\end{aligned}$$

The multiplicative vector term κ_1 then becomes:

$$\begin{aligned}
\kappa_1 &= -\frac{\Delta L}{L} \cdot |\,P_B\,| \left(|\,P_z^+\,| - |\,P_z^-\,| - |\,P_z^0\,|\right) \approx \\
&\approx -0.22 \cdot 0.5 \cdot (0.851 - 0.840 - 0.010) = -1.1 \cdot 10^{-4};
\end{aligned} \tag{B.18}$$

and the additive vector term κ_2:

$$\begin{aligned}
\kappa_2 &= -\frac{\Delta L}{L} \cdot |\,P_B\,| \cdot \left(|\,P_z^+\,| - |\,P_z^-\,| + 2 \cdot |\,P_z^0\,|\right) \approx \\
&\approx -0.22 \cdot 0.5 \cdot (0.851 - 0.840 + 2 \cdot 0.010) = -3.4 \cdot 10^{-3}.
\end{aligned} \tag{B.19}$$

Altogether one obtains for the tensor asymmetry from Eq. B.14 after neglecting the vector correction terms κ_1 (Eq. B.18) and κ_2 (Eq. B.19) and the term τ_1 (Eq. B.16) (under the further assumption that both $A_{\|}$ and $A(1)$ are small compared to 1) and using the effective tensor polarization $\langle P_{zz}\rangle_1$ (Eq. B.17):

$$\begin{aligned}
A_{zz}(1) &:= A_{zz}|_{A(1)} \approx \underbrace{\frac{1}{\langle P_{zz}\rangle_1}}_{\approx 1.2} \cdot A(1) = \\
&= \frac{6}{|\,P_{zz}^+\,| + |\,P_{zz}^-\,| + 2 \cdot |\,P_{zz}^0\,|} \cdot \frac{\left[\left(\frac{N^{\leftleftarrows}}{L^{\leftleftarrows}}\right) + \left(\frac{N^{\rightrightarrows}}{L^{\rightrightarrows}}\right)\right] - 2 \cdot \left(\frac{N^0}{L^0}\right)}{\left[\left(\frac{N^{\leftleftarrows}}{L^{\leftleftarrows}}\right) + \left(\frac{N^{\rightrightarrows}}{L^{\rightrightarrows}}\right)\right] + \left(\frac{N^0}{L^0}\right)}
\end{aligned} \tag{B.20}$$

The alternative approach[1] is to start (in parallel to $Azz(5)$) with

$$A(1)^{\text{alt}} := \frac{\left[\left(\frac{N^{\leftleftarrows}}{L^{\leftleftarrows}}\right) + \left(\frac{N^{\rightrightarrows}}{L^{\rightrightarrows}}\right)\right] - 2 \cdot \left(\frac{N^0}{L^0}\right)}{|P_{zz}^0| \cdot \left[\left(\frac{N^{\leftrightarrows}}{L^{\leftrightarrows}}\right) + \left(\frac{N^{\rightrightarrows}}{L^{\rightrightarrows}}\right)\right] + (|P_{zz}^+| + |P_{zz}^-|) \cdot \left(\frac{N^0}{L^0}\right)}, \tag{B.21}$$

[1]It is a historical issue that in this thesis different methods for $A_{zz}(1)$ and $A_{zz}(5)$ are used.

which leads to

$$A_{zz}^{\text{alt}} = 2 \cdot A(1)^{\text{alt}} = 2 \cdot \frac{\left[\left(\frac{N^{\leftleftarrows}}{L^{\Leftarrow}}\right) + \left(\frac{N^{\rightrightarrows}}{L^{\Rightarrow}}\right)\right] - 2 \cdot \left(\frac{N^0}{L^0}\right)}{|P_{zz}^0| \cdot \left[\left(\frac{N^{\leftleftarrows}}{L^{\leftleftarrows}}\right) + \left(\frac{N^{\rightrightarrows}}{L^{\rightrightarrows}}\right)\right] + (|P_{zz}^{+}| + |P_{zz}^{-}|) \cdot \left(\frac{N^0}{L^0}\right)}. \tag{B.22}$$

The multiplicative correction term barely differs: $\kappa_1^{\text{alt}} = -1.9 \cdot 10^{-4}$, and the additive term κ_2 keeps unchanged.

B.3 Tensor only $A_{zz}(5)$

Already the ansatz for $A(5)$ accounts for real polarizations:

$$A(5) \;:=\; \frac{\left(\frac{N^{\Leftrightarrow}}{L^{\Leftrightarrow}}\right) - \left(\frac{N^0}{L^0}\right)}{|\,P_{zz}^0\,| \cdot \left(\frac{N^{\Leftrightarrow}}{L^{\Leftrightarrow}}\right) + |\,P_{zz}^{\Leftrightarrow}\,| \cdot \left(\frac{N^0}{L^0}\right)} = \tag{B.23}$$

$$= \frac{(L^0 \Delta L_V^{\Leftrightarrow} - L^{\Leftrightarrow} \Delta L_V^0)\, A_{\parallel} + \frac{1}{2}\, L^0 L^{\Leftrightarrow}\, (|\,P_{zz}^{\Leftrightarrow}\,| + |\,P_{zz}^0\,|)\, A_{zz}}{L^{\Leftrightarrow} L^0\, (|\,P_{zz}^0\,| + |\,P_{zz}^{\Leftrightarrow}\,|) + (|\,P_{zz}^0\,|\Delta L_V^{\Leftrightarrow} L^0 + |\,P_{zz}^{\Leftrightarrow}\,|\Delta L_V^0 L^{\Leftrightarrow})\, A_{\parallel}}.$$

Introducing the vector correction terms κ_3 and κ_4

$$\kappa_3 = \left(\frac{|\,P_{zz}^0\,|\Delta L_V^{\Leftrightarrow} L^0 + |\,P_{zz}^{\Leftrightarrow}\,|\Delta L_V^0 L^{\Leftrightarrow}}{L^0 L^{\Leftrightarrow}(|\,P_{zz}^{\Leftrightarrow}\,| + |\,P_{zz}^0\,|)}\right) \tag{B.24}$$

$$\kappa_4 = \frac{\Delta L_V^{\Leftrightarrow} L^0 - \Delta L_V^0 L^{\Leftrightarrow}}{L^0 L^{\Leftrightarrow}(|\,P_{zz}^{\Leftrightarrow}\,| + |\,P_{zz}^0\,|)}, \tag{B.25}$$

$\frac{1}{2}\, A_{zz}|_{A(5)} \equiv \frac{1}{2}\, A_{zz}(5)$ reads:

$$\frac{1}{2}\, A_{zz}|_{A(5)} = A(5)\left(1 + \kappa_3 \cdot A_{\parallel}\right) - \kappa_4 \cdot A_{\parallel}. \tag{B.26}$$

With the assumptions from Pg. 113 ff, one obtains:
$\Delta L_V^{\Leftrightarrow} = |\,P_z^{\Leftrightarrow}\,| \cdot |\,P_B\,|\Delta L$ and
$\Delta L_V^0 = |\,P_z^0\,| \cdot |\,P_B\,|\Delta L$.
Thus, the multiplicative vector term κ_3 becomes:

$$\begin{aligned} \kappa_3 &= \frac{\Delta L}{L} \cdot \frac{|\,P_B\,| \cdot (|\,P_{zz}^0\,| \cdot |\,P_z^{\Leftrightarrow}\,| + |\,P_{zz}^{\Leftrightarrow}\,| \cdot |\,P_z^0\,|)}{|\,P_{zz}^{\Leftrightarrow}\,| + |\,P_{zz}^0\,|} = \\ &= 0.22 \cdot \frac{0.5 \cdot (1.655 \cdot 0.010 + 0.891 \cdot 0.010)}{0.891 + 1.655} = 1.1 \cdot 10^{-3}, \end{aligned} \tag{B.27}$$

and the additive term κ_4:

$$\kappa_4 = \frac{\Delta L}{L} \cdot \frac{|P_B| \cdot (|P_z^{\Leftrightarrow}| - |P_z^0|)}{|P_{zz}^{\Leftrightarrow}| + |P_{zz}^0|} = 0.22 \cdot \frac{0.5 \cdot (0.010 - 0.010)}{0.891 + 1.655} \to 0. \tag{B.28}$$

Neglecting κ_3 (Eq. B.27) and κ_4 (Eq. B.28), $A_{zz}(5)$ simplifies to:

$$A_{zz}(5) := A_{zz}|_{A(5)} \approx 2 \cdot A(5) = 2 \cdot \frac{\left(\frac{N^{\Leftrightarrow}}{L^{\Leftrightarrow}}\right) - \left(\frac{N^0}{L^0}\right)}{|P_{zz}^0| \cdot \left(\frac{N^{\Leftrightarrow}}{L^{\Leftrightarrow}}\right) + |P_{zz}^{\Leftrightarrow}| \cdot \left(\frac{N^0}{L^0}\right)}. \tag{B.29}$$

B.4 Cross-check $A(4)$

The numerator of Eq. 2.28 becomes:

$$\begin{aligned}
& \left(\frac{\Sigma L_V^{\leftleftarrows}}{L^{\leftleftarrows}} - \frac{\Sigma L_V^{\rightrightarrows}}{L^{\rightrightarrows}} - 2 \cdot \frac{\Delta L_V^{\Leftrightarrow}}{L^{\Leftrightarrow}}\right) \cdot A_{\parallel} + \\
+ \quad & \left(|P_{zz}^+| \left(\frac{L^{-+}}{L^{\leftleftarrows}} + \frac{L^{++}}{L^{\rightrightarrows}}\right) + |P_{zz}^-| \left(\frac{L^{+-}}{L^{\leftleftarrows}} + \frac{L^{--}}{L^{\rightrightarrows}}\right) - 2 \cdot |P_{zz}^{\Leftrightarrow}|\right) \cdot \frac{1}{2} A_{zz} \approx \\
\approx \quad & -\frac{\Delta L}{L} |P_B| (|P_z^+| - |P_z^-| - 2|P_z^{\Leftrightarrow}|) A_{\parallel} + (|P_{zz}^+| + |P_{zz}^-| - 2 \cdot |P_{zz}^{\Leftrightarrow}|) \frac{1}{2} A_{zz} = \\
= \quad & 9.9 \cdot 10^{-4} A_{\parallel} - 0.065 A_{zz} \approx 0
\end{aligned}$$

B.5 Four-in-one $A_{zz}(6)$

$$A(6) := \frac{\frac{2}{3}\left[\left(\frac{N^{\leftleftarrows}}{L^{\leftleftarrows}}\right) + \left(\frac{N^{\rightrightarrows}}{L^{\rightrightarrows}}\right) + \left(\frac{N^{\Leftrightarrow}}{L^{\Leftrightarrow}}\right)\right] - 2 \cdot \left(\frac{N^0}{L^0}\right)}{\frac{2}{3}\left[\left(\frac{N^{\leftleftarrows}}{L^{\leftleftarrows}}\right) + \left(\frac{N^{\rightrightarrows}}{L^{\rightrightarrows}}\right) + \left(\frac{N^{\Leftrightarrow}}{L^{\Leftrightarrow}}\right)\right] + \left(\frac{N^0}{L^0}\right)}; \tag{B.30}$$

by inserting the (beam helicity averaged) collected eventnumbers from Eq. B.6 and introducing the expressions κ_5, κ_6 and τ_2 and an effective tensor polarization $\langle P_{zz}\rangle_6$:

$$\kappa_5 = \left(\frac{\Sigma L_V^{\leftleftarrows}}{L^{\leftleftarrows}} - \frac{\Sigma L_V^{\rightrightarrows}}{L^{\rightrightarrows}} + \frac{\Delta L_V^{\Leftrightarrow}}{L^{\Leftrightarrow}} + \frac{3}{2} \cdot \frac{\Delta L_V^0}{L^0}\right) \tag{B.31}$$

$$\kappa_6 = \left(\frac{\Sigma L_V^{\leftleftarrows}}{L^{\leftleftarrows}} - \frac{\Sigma L_V^{\rightrightarrows}}{L^{\rightrightarrows}} + \frac{\Delta L_V^{\Leftrightarrow}}{L^{\Leftrightarrow}} - 3 \cdot \frac{\Delta L_V^0}{L^0}\right) \tag{B.32}$$

$$\tau_2 = \left(|P_{zz}^+| \left(\frac{L^{-+}}{L^{\leftleftarrows}} + \frac{L^{++}}{L^{\rightrightarrows}}\right) + |P_{zz}^-| \left(\frac{L^{+-}}{L^{\leftleftarrows}} + \frac{L^{--}}{L^{\rightrightarrows}}\right) + |P_{zz}^{\Leftrightarrow}| - \frac{3}{2} \cdot |P_{zz}^0|\right) \tag{B.33}$$

$$9\langle P_{zz}\rangle_6 = \left(|P_{zz}^+| \left(\frac{L^{-+}}{L^{\leftleftarrows}} + \frac{L^{++}}{L^{\rightrightarrows}}\right) + |P_{zz}^-| \left(\frac{L^{+-}}{L^{\leftleftarrows}} + \frac{L^{--}}{L^{\rightrightarrows}}\right) + |P_{zz}^{\Leftrightarrow}| + 3 \cdot |P_{zz}^0|\right) \tag{B.34}$$

(here, the short notations from Eq. B.7 have been used), one obtains:

$$A(6) = \frac{9\langle P_{zz}\rangle_6 \cdot A_{zz} + 2 \cdot \kappa_6 \cdot A_{\parallel}}{9 + \tau_2 \cdot A_{zz} + 2 \cdot \kappa_5 \cdot A_{\parallel}}. \tag{B.35}$$

Solving for $\frac{1}{2}\,A_{zz}|_{A(6)} \equiv \frac{1}{2}\,A_{zz}(6)$:

$$\frac{1}{2}\,A_{zz}|_{A(6)} = \frac{A(6)\left(\frac{9}{2} + \kappa_5 \cdot A_{\parallel}\right) - \kappa_6 \cdot A_{\parallel}}{9\langle P_{zz}\rangle_6 - \tau_2 \cdot A(6)}. \tag{B.36}$$

Using the assumptions from Pg. 113 ff and inserting the average target polarization values, one obtains for the term τ_2 (Eq. B.33):

$$\begin{aligned} \tau_2 &= |\,P^{+}_{zz}\,| + |\,P^{-}_{zz}\,| + |\,P^{\Leftrightarrow}_{zz}\,| - \frac{3}{2}|\,P^{0}_{zz}\,| = \\ &= 0.800 + 0.853 + 0.891 - \frac{3}{2} \cdot 1.655 = 0.0615 \end{aligned} \tag{B.37}$$

and for the effective tensor polarization $\langle P_{zz}\rangle_6$ including all target states (Eq. B.34):

$$\begin{aligned} 9\langle P_{zz}\rangle_6 &= \left(|\,P^{+}_{zz}\,| + |\,P^{-}_{zz}\,| + |\,P^{\Leftrightarrow}_{zz}\,| + 3 \cdot |\,P^{0}_{zz}\,|\right) = \\ &= 0.800 + 0.853 + 0.891 + 3 \cdot 1.655 = 7.509 \approx 7.5. \end{aligned} \tag{B.38}$$

The vector correction terms κ_5 (Eq. B.31) and κ_6 (Eq. B.32) turn out to be:

$$\begin{aligned} \kappa_5 &= -\frac{\Delta L}{L} \cdot |\,P_B\,| \left(|\,P^{+}_{z}\,| - |\,P^{-}_{z}\,| - |\,P^{\Leftrightarrow}_{z}\,| - \frac{3}{2}|\,P^{0}_{z}\,|\right) \approx \\ &\approx -0.22 \cdot 0.5 \cdot (0.851 - 0.840 - 0.010 - \frac{3}{2} \cdot 0.010) = 1.54 \cdot 10^{-3}, \end{aligned} \tag{B.39}$$

$$\begin{aligned} \kappa_6 &= -\frac{\Delta L}{L} \cdot |\,P_B\,| \cdot \left(|\,P^{+}_{z}\,| - |\,P^{-}_{z}\,| - |\,P^{\Leftrightarrow}_{z}\,| + 3 \cdot |\,P^{0}_{z}\,|\right) \approx \\ &\approx -0.22 \cdot 0.5 \cdot (0.851 - 0.840 - 0.010 + 3 \cdot 0.010) = -3.4 \cdot 10^{-3}. \end{aligned} \tag{B.40}$$

Altogether one obtains from Eq. B.36 after neglecting the vector correction terms κ_5 (Eq. B.39) and κ_6 (Eq. B.40) and the term τ_2 (Eq. B.37) and using the effective tensor polarization $\langle P_{zz}\rangle_6$ (Eq. B.38):

$$\begin{aligned} A_{zz}(6) := A_{zz}|_{A(6)} &\approx \underbrace{\frac{1}{\langle P_{zz}\rangle_6}}_{\approx 1.2} \cdot A(6) = \\ = \frac{9}{|\,P^{+}_{zz}\,| + |\,P^{-}_{zz}\,| + |\,P^{\Leftrightarrow}_{zz}\,| + 3 \cdot |\,P^{0}_{zz}\,|} &\cdot \frac{\frac{2}{3}\left[\left(\frac{N^{\leftleftarrows}}{L^{\leftleftarrows}}\right) + \left(\frac{N^{\rightrightarrows}}{L^{\rightrightarrows}}\right) + \left(\frac{N^{\Leftrightarrow}}{L^{\Leftrightarrow}}\right)\right] - 2 \cdot \left(\frac{N^{0}}{L^{0}}\right)}{\frac{2}{3}\left[\left(\frac{N^{\leftleftarrows}}{L^{\leftleftarrows}}\right) + \left(\frac{N^{\rightrightarrows}}{L^{\rightrightarrows}}\right) + \left(\frac{N^{\Leftrightarrow}}{L^{\Leftrightarrow}}\right)\right] + \left(\frac{N^{0}}{L^{0}}\right)}. \end{aligned} \tag{B.41}$$

B.6 Vector contamination in the tensor measurement

The impact of $A_{\parallel}$ onto the A_{zz} measurement, quantified by the vector terms κ_1 to κ_6 (Eqs. B.18, B.19, B.27, B.28, B.39, B.40), turns out to be negligible. This is due to several reasons: In all these correction terms, the product of the relative difference in luminosities between different beam helicities, $\frac{\Delta L}{L}$, and a linear combination of vector polarizations enters. In the dedicated tensor data period, luminosities for different settings of the beam helicity were approximatively balanced out, such that $\frac{\Delta L}{L} \approx 0.22$; using only one beam helicity would have meant blowing up the factor $\frac{\Delta L}{L}$ to 1. Furthermore, in the linear combination of vector polarizations the term

$$|P_z^+| - |P_z^-| \tag{B.42}$$

appears, being close to zero, such that it is crucial that the further vector polarizations of the tensor states entering the equation are small compared to 1. This is the case at HERMES due to the special features of the gaseous target.

For $A_{zz}(5)$, no fully polarized vector states like in Eq. B.42 need to be averaged, but only the close-to-zero residual vector polarizations of the tensor states enter the additive correction term κ_4 (Eq. B.28). Therefore, κ_4 is one magnitude smaller than κ_2 and κ_6. All correction terms enter multiplicatively with $A_{\parallel}$; for the deuteron, in the kinematic region measured at HERMES can safely be assumed that $A_{\parallel} \lesssim 0.1$. This further suppresses the correction terms.

B.7 Statistical errors on tensor asymmetries

The statistical errors on the tensor asymmetries were obtained by usual error propagation (Eq. A.2). The number of collected DIS candidates N^i_{cand} (where i is the data type, $i \in \{\overleftarrow{\Leftarrow}, \overrightarrow{\Rightarrow}, \Leftrightarrow, 0\}$) with a statistical error (see App. A.1) $\delta N^i_{\text{cand}} = \sqrt{N^i_{\text{cand}}}$ were corrected for the number of charge symmetric events N^i_{cs} with a statistical error $\delta N^i_{\text{cs}} = \sqrt{N^i_{\text{cs}}}$ to obtain the event numbers N^i which enter the asymmetries: $N^i = N^i_{\text{cand}} - N^i_{\text{cs}}$ (see Sec. 2.2). The statistical error of the latter, δN^i, was obtained by error propagation:

$$\delta N^i = \sqrt{N^i + 2N^i_{cs}}. \tag{B.43}$$

The statistical uncertainties on the luminosity measurement were negligible and thus no luminosity errors were propagated to the asymmetries. The explicit expressions for the asymmetries' errors were obtained as:

$$\delta A_{zz}(5) = 2\cdot(|\,P_{zz}^{\Leftrightarrow}\,|+|\,P_{zz}^{0}\,|)\cdot\frac{L^0L^{\Leftrightarrow}\sqrt{(N^0\delta N^{\Leftrightarrow})^2+(N^{\Leftrightarrow}\delta N^0)^2}}{(|\,P_{zz}^{0}\,|L^0N^{\Leftrightarrow}+|\,P_{zz}^{\Leftrightarrow}\,|L^{\Leftrightarrow}N^0)^2} \tag{B.44}$$

$$\begin{aligned}\delta A_{zz}^{\mathrm{alt}}(1) &= 2\cdot(|\,P_{zz}^{+}\,|+|\,P_{zz}^{-}\,|+2|\,P_{zz}^{0}\,|)\times\\ &\times\ \frac{L^{\vec{\Rightarrow}}L^{\vec{\Leftarrow}}L^0\sqrt{(N^0L^{\vec{\Rightarrow}}\delta N^{\vec{\Leftarrow}})^2+(N^0L^{\vec{\Leftarrow}}\delta N^{\vec{\Rightarrow}})^2+(N^{\vec{\Leftarrow}}L^{\vec{\Rightarrow}}+N^{\vec{\Rightarrow}}L^{\vec{\Leftarrow}})^2(\delta N^0)^2}}{\Big(|\,P_{zz}^{0}\,|L^0(N^{\vec{\Leftarrow}}L^{\vec{\Rightarrow}}+N^{\vec{\Rightarrow}}L^{\vec{\Leftarrow}})+(|\,P_{zz}^{+}\,|+|\,P_{zz}^{-}\,|)L^{\vec{\Leftarrow}}L^{\vec{\Rightarrow}}N^0\Big)^2}\end{aligned} \tag{B.45}$$

$$\begin{aligned}\delta A_{zz}(1) &= \frac{6}{(|\,P_{zz}^{+}\,|+|\,P_{zz}^{-}\,|+2\cdot|\,P_{zz}^{0}\,|)}\times\\ &\times\ \frac{3L^{\vec{\Rightarrow}}L^{\vec{\Leftarrow}}L^0\sqrt{(N^0L^{\vec{\Rightarrow}}\delta N^{\vec{\Leftarrow}})^2+(N^0L^{\vec{\Leftarrow}}\delta N^{\vec{\Rightarrow}})^2+(N^{\vec{\Leftarrow}}L^{\vec{\Rightarrow}}+N^{\vec{\Rightarrow}}L^{\vec{\Leftarrow}})^2(\delta N^0)^2}}{\Big((N^{\vec{\Leftarrow}}L^{\vec{\Rightarrow}}+N^{\vec{\Rightarrow}}L^{\vec{\Leftarrow}})L^0+N^0L^{\vec{\Leftarrow}}L^{\vec{\Rightarrow}}\Big)^2}\end{aligned} \tag{B.46}$$

$$\begin{aligned}&\delta A_{zz}(6) = \frac{9}{(|\,P_{zz}^{+}\,|+|\,P_{zz}^{-}\,|+|\,P_{zz}^{\Leftrightarrow}\,|+3\cdot|\,P_{zz}^{0}\,|)}\times\\ &\times\frac{18L^{\vec{\Rightarrow}}L^{\vec{\Leftarrow}}L^{\Leftrightarrow}L^0\cdot\sqrt{\begin{aligned}&(N^0L^{\vec{\Rightarrow}}L^{\Leftrightarrow}\delta N^{\vec{\Leftarrow}})^2+(N^0L^{\vec{\Leftarrow}}L^{\Leftrightarrow}\delta N^{\vec{\Rightarrow}})^2+(N^0L^{\vec{\Leftarrow}}L^{\vec{\Rightarrow}}\delta N^{\Leftrightarrow})^2\\ &\quad+(N^{\vec{\Leftarrow}}L^{\vec{\Rightarrow}}L^{\Leftrightarrow}+N^{\vec{\Rightarrow}}L^{\vec{\Leftarrow}}L^{\Leftrightarrow}+N^{\Leftrightarrow}L^{\vec{\Leftarrow}}L^{\vec{\Rightarrow}})^2(\delta N^0)^2\end{aligned}}}{\Big(2L^0(N^{\vec{\Leftarrow}}L^{\vec{\Rightarrow}}L^{\Leftrightarrow}+N^{\vec{\Rightarrow}}L^{\vec{\Leftarrow}}L^{\Leftrightarrow}+N^{\Leftrightarrow}L^{\vec{\Leftarrow}}L^{\vec{\Rightarrow}})+3N^0L^{\vec{\Leftarrow}}L^{\vec{\Rightarrow}}L^{\Leftrightarrow}\Big)^2}\end{aligned} \tag{B.47}$$

$$\delta A(4) = \frac{3L^{\vec{\Rightarrow}}L^{\vec{\Leftarrow}}L^{\Leftrightarrow}\sqrt{(N^{\Leftrightarrow}L^{\vec{\Rightarrow}}\delta N^{\vec{\Leftarrow}})^2+(N^{\Leftrightarrow}L^{\vec{\Leftarrow}}\delta N^{\vec{\Rightarrow}})^2+(N^{\vec{\Leftarrow}}L^{\vec{\Rightarrow}}+N^{\vec{\Rightarrow}}L^{\vec{\Leftarrow}})^2(\delta N^{\Leftrightarrow})^2}}{\Big((N^{\vec{\Leftarrow}}L^{\vec{\Rightarrow}}+N^{\vec{\Rightarrow}}L^{\vec{\Leftarrow}})L^{\Leftrightarrow}+N^{\Leftrightarrow}L^{\vec{\Leftarrow}}L^{\vec{\Rightarrow}}\Big)^2}. \tag{B.48}$$

B.8 Difference and average of $A_{zz}(1)$ and $A_{zz}(5)$

As the cross-check asymmetry $A(4)$ is not corrected for real polarizations, there is a small offset between $A(4)$ and $A_{zz}(1) - A_{zz}(5)$, which can be approximated by dividing $A(4)$ by the averaged tensor polarizations of all states with $|m| = 1$:

$$A_{zz}(1) - A_{zz}(5) \approx \frac{3}{|P_{zz}^{+}| + |P_{zz}^{-}| + |P_{zz}^{\Leftrightarrow}|} \cdot A(4) \approx 1.18 \cdot A(4). \tag{B.49}$$

For the proper calculation of the statistical error of $[A_{zz}(1) \pm A_{zz}(5)]$ one has to take into account the partial correlation of the data entering the asymmetries[2], as mentioned in App. A.2. The straight forward way is to perform an error propagation (Eq. A.2) directly for the sum (the difference): with

$$\Delta A := [A_{zz}(1) - A_{zz}(5)] \tag{B.50}$$

$$\Sigma A := [A_{zz}(1) + A_{zz}(5)]\,, \tag{B.51}$$

$$\delta(\Delta A) = \sqrt{\left(\frac{\partial \Delta A}{\partial N^{\overset{\rightarrow}{\Rightarrow}}} \cdot \delta N^{\overset{\rightarrow}{\Rightarrow}}\right)^2 + \left(\frac{\partial \Delta A}{\partial N^{\overset{\rightarrow}{\Leftarrow}}} \cdot \delta N^{\overset{\rightarrow}{\Leftarrow}}\right)^2 + \left(\frac{\partial \Delta A}{\partial N^{\Leftrightarrow}} \cdot \delta N^{\Leftrightarrow}\right)^2 + \left(\frac{\partial \Delta A}{\partial N^{0}} \cdot \delta N^{0}\right)^2}$$

$$= \sqrt{\left(\frac{\partial A_{zz}(1)}{\partial N^{\overset{\rightarrow}{\Rightarrow}}} - \underbrace{\frac{\partial A_{zz}(5)}{\partial N^{\overset{\rightarrow}{\Rightarrow}}}}_{=0}\right)^2 \cdot (\delta N^{\overset{\rightarrow}{\Rightarrow}})^2 + \left(\frac{\partial A_{zz}(1)}{\partial N^{\overset{\rightarrow}{\Leftarrow}}} - \underbrace{\frac{\partial A_{zz}(5)}{\partial N^{\overset{\rightarrow}{\Leftarrow}}}}_{=0}\right)^2 \cdot (\delta N^{\overset{\rightarrow}{\Leftarrow}})^2 + \ldots}$$

$$\overline{\ldots + \left(\underbrace{\frac{\partial A_{zz}(1)}{\partial N^{\Leftrightarrow}}}_{=0} - \frac{\partial A_{zz}(5)}{\partial N^{\Leftrightarrow}}\right)^2 \cdot (\delta N^{\Leftrightarrow})^2 + \underbrace{\left(\frac{\partial A_{zz}(1)}{\partial N^{0}} - \frac{\partial A_{zz}(5)}{\partial N^{0}}\right)^2}_{\text{correlation}} \cdot (\delta N^{0})^2} =$$

$$= \sqrt{\delta A_{zz}^2(1) + \delta A_{zz}^2(5) - 2 \cdot \frac{\partial \delta A_{zz}(1)}{\partial N^0} \cdot \frac{\partial \delta A_{zz}(5)}{\partial N^0} \cdot (\delta N^0)^2} \tag{B.52}$$

Formula (4.29) also holds for Σ, replacing all Δs by a Σ, but the final result for Σ differs by a minus sign:

$$\delta(\Sigma A) = \sqrt{\delta A_{zz}^2(1) + \delta A_{zz}^2(5) + 2 \cdot \frac{\partial \delta A_{zz}(1)}{\partial N^0} \cdot \frac{\partial \delta A_{zz}(5)}{\partial N^0} \cdot (\delta N^0)^2}, \tag{B.53}$$

[2] The `tensor minus` set is both part of $A_{zz}(1)$ and $A_{zz}(5)$, see Fig. 2.10

with the correlation terms reading

$$\frac{\partial A_{zz}(1)}{\partial N^0} = \frac{-3L^{\stackrel{\rightarrow}{\Leftarrow}} L^{\stackrel{\rightarrow}{\Rightarrow}} L^0 \left(N^{\stackrel{\rightarrow}{\Leftarrow}} L^{\stackrel{\rightarrow}{\Rightarrow}} + N^{\stackrel{\rightarrow}{\Rightarrow}} L^{\stackrel{\rightarrow}{\Leftarrow}} \right)}{\left[(N^{\stackrel{\rightarrow}{\Leftarrow}} L^{\stackrel{\rightarrow}{\Rightarrow}} + N^{\stackrel{\rightarrow}{\Rightarrow}} L^{\stackrel{\rightarrow}{\Leftarrow}}) L^0 + N^0 L^{\stackrel{\rightarrow}{\Leftarrow}} L^{\stackrel{\rightarrow}{\Rightarrow}} \right]^2} \tag{B.54}$$

and

$$\frac{\partial A_{zz}(5)}{\partial N^0} = 2 \cdot \frac{-N^{\Leftrightarrow} L^{\Leftrightarrow} L^0 (|\,P_{zz}^0\,| + |\,P_{zz}^{\Leftrightarrow}\,|)}{(|\,P_{zz}^0\,| L^0 N^{\Leftrightarrow} + |\,P_{zz}^{\Leftrightarrow}\,| L^{\Leftrightarrow} N^0)^2}. \tag{B.55}$$

The averaged tensor asymmetry $\langle A_{zz}(1) + A_{zz}(5) \rangle$ was calculated as an error weighted mean[3] according to Eq. A.5:

$$\langle A_{zz}(1) + A_{zz}(5) \rangle = \left(\frac{A_{zz}(1)}{(\delta A_{zz}(1))^2} + \frac{A_{zz}(5)}{(\delta A_{zz}(5))^2} \right) \cdot \left(\frac{1}{(\delta A_{zz}(1))^2} + \frac{1}{(\delta A_{zz}(5))^2} \right)^{-1}, \tag{B.56}$$

and its statistical error, taking into account the partial correlation between the two asymmetries, was approximated as:

$$\delta \langle A_{zz}(1) + A_{zz}(5) \rangle \approx \frac{1}{2}\, \delta \left[A_{zz}(1) + A_{zz}(5) \right] = \frac{1}{2}\, \delta(\Sigma A). \tag{B.57}$$

[3]The correlation between the two asymmetries is neglected here. The obtained result is sufficient for a cross-check; it does not enter any final result, however.

C QED and instrumental radiative corrections

This section describes an algorithm to correct DIS cross section asymmetries for kinematic bin migrations due to QED radiative and detector smearing effects to obtain the asymmetry on Born level without the need of iterated fitting, producing a close-to model-independent result [85]. A description of the Hermes Monte Carlo chain (HMC) is given in Sec. C.6.

C.1 Unfolding of kinematic migrations

The unfolding of event migrations is not performed by shifting each single event kinematically, i. e. by correcting event numbers, but by an effective correction of the observable, the measured inclusive asymmetry, in every kinematic bin.
Let A denote an asymmetry which is obtained by comparing two DIS cross sections from different target states + and -. For the case of the here investigated inclusive tensor asymmetry A_{zz}, "+" corresponds to the $|m| = 1$ state (`vector` averaged), and "-" to the $m = 0$ state of the target (`tensor minus`). The tensor asymmetry between the experimental yields[1] $X^{\pm}(i)$ observed in the kinematic bin i, $i = 1...n$, is:

$$A_{\mathrm{X}}(i) = \frac{2X^+(i) - 2X^-(i)}{2X^+(i) + X^-(i)}. \tag{C.1}$$

The goal of the unfolding algorithm is to obtain the asymmetry between the *unknown* yields on Born level $B^{\pm}(j)$ in Born bin j, $j = 0...n$:

$$A_{\mathrm{Born}}(j) = \frac{2B^+(j) - 2B^-(j)}{2B^+(j) + B^-(j)}. \tag{C.2}$$

Due to smearing effects (see Sec. 3.3.1), the experimental yields $\vec{X}^{\pm}$ are different from the Born yields $\vec{B}^{\pm}$, a relation which can generally be formulated by the smearing equations

$$X^+(i) = k(i)S^+(i,j)B^+(j), \tag{C.3}$$

$$X^-(i) = k(i)S^-(i,j)B^-(j), \tag{C.4}$$

where the $n \times (n+1)$-matrix $S^{\pm}$ is the smearing matrix for target spin $\pm$, its entry $S^{\pm}(i,j)$ describing the event migration[2] from the observed bin i to Born bin j, where

[1] Count rate per luminosity.

[2] Separately for each target spin state, as radiative effects can be spin-dependent.

Born bin $j = 0$ integrates all background which smears into the acceptance[3], including elastic and quasi-elastic contributions, and $k(i)$ is a normalization constant. Such a smearing matrix $S^{\pm}(i,j)$ is obtained by generating the Born cross section $\sigma^{\pm}_{\rm Born}$ and in a separate data sample the experimental cross section $\sigma^{\pm}_{\rm X}$ by a Monte Carlo simulation (Sec. C.6) which contains the information about the bin migration both due to QED radiative and detector smearing effects (see Sec. 3.3.1). The migration matrix $M^{\pm}_{\rm X}(i,j)$ contains the absolute cross section which migrated from Born bin j to the observed bin i for the target spin state $\pm$ with

$$\sigma^{\pm}_{\rm X}(i) = \sum_{j=0}^{n} M^{\pm}_{\rm X}(i,j). \tag{C.5}$$

Note that the sum over i in Eq. C.5 would not recover $\sigma^{\pm}_{\rm Born}(j)$ because of the events that smeared out of the acceptance. In these terms, the unpolarized and polarized background $\Delta\sigma^{\rm U}(i)$ and $\Delta\sigma^{\rm P}(i)$ observed in bin i which have been introduced in Sec. 3.3.1 are written as:

$$\Delta\sigma^{\rm U}(i) = \sum_{\substack{j=0\\ j\neq i}}^{n} (2M^{+}_{\rm X}(i,j) + M^{-}_{\rm X}(i,j)), \tag{C.6}$$

$$\Delta\sigma^{\rm P}(i) = \sum_{\substack{j=0\\ j\neq i}}^{n} (2M^{+}_{\rm X}(i,j) - 2M^{-}_{\rm X}(i,j)), \tag{C.7}$$

thus *background* in the described formalism denotes all the cross section contributions which are observed in bin i, but stem from a *different* Born bin j. For the special case $j = 0$, $\Delta\widehat{\sigma}^{\rm P}(i)$ denotes the polarized background observed in bin i which smears *into* the acceptance:

$$\Delta\widehat{\sigma}^{\rm P}(i) = 2(M^{+}_{\rm X}(i,0) - M^{-}_{\rm X}(i,0)). \tag{C.8}$$

The unpolarized experimental cross section is shortly written as:

$$\sigma^{\rm U}_{\rm X}(i) = 2\sigma^{+}_{\rm X}(i) + \sigma^{-}_{\rm X}(i) = 2M^{+}_{\rm X}(i,i) + M^{-}_{\rm X}(i,i) + \Delta\sigma^{\rm U}(i), \tag{C.9}$$

containing a contribution which belongs to the bin on Born level (the main diagonal elements of $M_{\rm X}$) and a contribution which is background from other bins ($\Delta\sigma^{\rm U}$).
The unpolarized Born cross section $\sigma^{\rm U}_{\rm Born}(i)$ in bin i is obtained as

$$\sigma^{\rm U}_{\rm Born}(i) = 2\sigma^{+}_{\rm Born}(i) + \sigma^{-}_{\rm Born}(i). \tag{C.10}$$

The smearing matrix $S^{\pm}(i,j)$ is extracted as

$$S^{\pm}(i,j) := \frac{\partial\sigma^{\pm}_{\rm X}(i)}{\partial\sigma^{\pm}_{\rm Born}(j)} = \frac{M^{\pm}_{\rm X}(i,j)}{\sigma^{\pm}_{\rm Born}(j)}. \tag{C.11}$$

[3]Defined both by kinematic and geometry cuts.

The normalization with the BORN cross section causes the smearing matrix to be independent of the BORN model in the Monte Carlo because both numerator and denominator scale with the number of events generated in the given BORN bin j. An application of $S(i,j)$ to real data is thus reasonable, to the degree that QED radiative and detector smearing effects are correctly incorporated in the Monte Carlo simulation. The unpolarized BORN cross section (in terms of a parameterization of world data on F_2) which is used as input for the MC is assumed to hold for the experiment; so to speak, the unpolarized measured data is normalized to the MC:

$$2B^+(j) + B^-(j) = \sigma^{\mathrm{U}}_{\mathrm{Born}}(j). \tag{C.12}$$

With Eqs. C.3, C.4 and C.12 one has $(2+1)\cdot n$ equations with $(2+1)\cdot n$ unknowns: the $2n$ BORN yields $B^{\pm}(j)$ and the n normalization constants $k(i)$. Adding Eq. C.3 and Eq. C.4, one can deduce for $k(i)$:

$$k(i) = \frac{2X^+(i) + X^-(i)}{2\sigma^+_{\mathrm{X}}(i) + \sigma^-_{\mathrm{X}}(i)}, \tag{C.13}$$

with the assumption that the generic relation holds:

$$S(i,j)B(j) \equiv M_{\mathrm{X}}(i,j). \tag{C.14}$$

The $k(i)$ absorb for example detector inefficiencies like the $(1-\epsilon_{\mathrm{e.\ m.}})$ (Sec. 3.3.3) accounting for electromagnetic background showers. If the remaining $2n$ equations C.3 and C.4 can now be solved for the unknown BORN yields $B^{\pm}$, no iteration is needed to extract the BORN asymmetry. Subtracting Eq. C.4 from Eq. C.3, one obtains after using Eqs. C.1, C.13 and C.14 and separating the known (simulated) polarized background from outside the acceptance $\Delta\widehat{\sigma}^{\mathrm{P}}$ $(j=0)$ from the sum on the left hand side:

$$2\cdot\sum_{j=1}^{n}[S^+(i,j)B^+(j) - S^-(i,j)B^-(j)] = A_{\mathrm{X}}(i)\sigma^{\mathrm{U}}_{\mathrm{X}}(i) - \Delta\widehat{\sigma}^{\mathrm{P}}(i). \tag{C.15}$$

Eliminating $B^-(j)$ in favor of $B^+(j)$ by Eq. C.12, one has

$$2\cdot\sum_{j=1}^{n} B^+(j)[S^+(i,j)+2S^-(i,j)] = A_{\mathrm{X}}(i)\sigma^{\mathrm{U}}_{\mathrm{X}}(i)-\Delta\widehat{\sigma}^{\mathrm{P}}(i)+2\cdot\sum_{j=1}^{n} S^-(i,j)\sigma^{\mathrm{U}}_{\mathrm{Born}}(j). \tag{C.16}$$

Let $S'(i,j)$,

$$S'(i,j) = S^+(i,j) + 2S^-(i,j), \qquad i,j = 1..n, \tag{C.17}$$

be the well-conditioned (see [85] for details) square-matrix with the $j=0$-column removed; then $S'(i,j)$ can be inverted and Eq. C.16 can be solved for the BORN yield $B^+(j)$:

$$B^+(j) = \sum_{i=1}^{n}[S']^{-1}(j,i)\cdot\left[\frac{1}{2}A_{\mathrm{X}}(i)\sigma^{\mathrm{U}}_{\mathrm{X}}(i) - \frac{1}{2}\Delta\widehat{\sigma}^{\mathrm{P}}(i) + \sum_{k=1}^{n} S^-(i,k)\sigma^{\mathrm{U}}_{\mathrm{Born}}(k)\right]. \tag{C.18}$$

Re-writing Eq. C.2 as

$$A_{\mathrm{Born}}(j) = 2 \cdot \frac{3B^{+}(j) - \sigma^{\mathrm{U}}_{\mathrm{Born}}(j)}{\sigma^{\mathrm{U}}_{\mathrm{Born}}(j)}, \tag{C.19}$$

one obtains the final result for the unfolded tensor asymmetry A_{zz}:

$$A_{\mathrm{Born}}(j) = -2 + \frac{6}{\sigma^{\mathrm{U}}_{\mathrm{Born}}(j)} \cdot \sum_{i=1}^{n} [S']^{-1}(j,i) \cdot \left[\frac{1}{2} A_{\mathrm{X}}(i) \sigma^{\mathrm{U}}_{\mathrm{X}}(i) - \frac{1}{2} \Delta \widehat{\sigma}^{\mathrm{P}}(i) + \sum_{k=1}^{n} S^{-}(i,k) \sigma^{\mathrm{U}}_{\mathrm{Born}}(k) \right]. \tag{C.20}$$

Due to the rather complicated analytical form, it is not straight forward to deduce from Eq. C.20 the form of Eq. 3.7. It can be easily seen, however, that A_{Born} is obtained from A_{X} by the combination of a multiplicative and an additive term, the first containing the ratio of the unpolarized background to the unpolarized BORN cross section $\Delta\sigma^{\mathrm{U}}/\sigma^{\mathrm{U}}_{\mathrm{Born}}$ and the latter the ratio of the polarized background from outside the acceptance to the unpolarized BORN cross section $\Delta\widehat{\sigma}^{\mathrm{P}}/\sigma^{\mathrm{U}}_{\mathrm{Born}}$.
The division by $\sigma^{\mathrm{U}}_{\mathrm{Born}}$ in Eq. C.20 eliminates the dependence on the BORN input model of A_{Born} except in the $\Delta\widehat{\sigma}^{\mathrm{P}}$ term which contains information about the model outside the acceptance. This information is not provided by $\sigma^{\mathrm{U}}_{\mathrm{Born}}(j)$, $j = 1...n$, however, such that A_{Born} is left with a residual dependence on the BORN model employed outside the acceptance (see Sec. 3.4.4). Apart from that, A_{Born} depends only on the radiative corrections and the GEANT detector model which are used to extract $\sigma^{\mathrm{U}}_{\mathrm{X}}$ from Monte Carlo.
The result C.20 has the same form as the result obtained for the unfolded vector asymmetry $A_{\parallel}$ [97] except for single signs and prefactors which arise from the respective different definitions of the asymmetries between target spin yields.

C.2 Statistical error of the BORN asymmetry

The radiative dilution matrix[4]

$$D(j,i) := \frac{\partial A_{\mathrm{Born}}(j)}{\partial A_{\mathrm{X}}(i)} = \frac{3\sigma^{\mathrm{U}}_{\mathrm{X}}(i)}{\sigma^{\mathrm{U}}_{\mathrm{Born}}(j)} [S']^{-1}(j,i) \tag{C.21}$$

enters linearly the formula connecting A_{Born} and A_{X} (Eq. C.20):

$$A_{\mathrm{Born}}(j) \sim \sum_{i=1}^{n} D(j,i) A_{\mathrm{X}}(i). \tag{C.22}$$

[4]The explicit expressions in this section hold for the tensor asymetry A_{zz}.

In these terms, the covariance matrix of the statistical error on the Born asymmetry is written as

$$\mathrm{cov}(j,i) = \sum_{k=1}^{n} D(j,k)D(i,k)\delta A_{\mathrm{X}}^2(k), \tag{C.23}$$

see Tab. D.11 for the resulting values. Its diagonal elements represent the statistical error on the Born level asymmetry δA_{Born} which is expressed by the error bars accompanying the data points in a plot:

$$\begin{aligned}\delta A_{\mathrm{Born}}(j) &= \sqrt{\mathrm{cov}(j,j)} = \sqrt{\sum_{i=1}^{n} D(j,i)^2 \delta A_{\mathrm{X}}^2(i)} \\ &= 3\sqrt{\sum_{i=1}^{n}\left(\frac{\sigma_{\mathrm{X}}^{\mathrm{U}}(i)}{\sigma_{\mathrm{Born}}^{\mathrm{U}}(j)}\right)^2 \left([S']^{-1}(j,i)\right)^2 \delta A_{\mathrm{X}}^2(i)}.\end{aligned} \tag{C.24}$$

The ratio $\delta A_{\mathrm{Born}}/\delta A_{\mathrm{X}}$ is larger the more events have to be "unsmeared", see Sec. C.5. The matrix containing the correlation between the errors from kinematic bin to bin after the unfolding procedure is obtained by scaling with the errors on the Born asymmetry δA_{Born}:

$$\mathrm{corr}(j,i) = \frac{\mathrm{cov}(j,i)}{\delta A_{\mathrm{Born}}(j)\cdot\delta A_{\mathrm{Born}}(i)}, \tag{C.25}$$

see Fig. 3.22 for a graphical representation. It is

$$\mathrm{corr}(j,j) = 1, \tag{C.26}$$

i.e. in contrast to the covariance matrix, the correlation matrix contains numbers which do not display the numerical value of the errors, but lie (in absolute values) between $\mathrm{corr}(j,i) = 1$ (the errors in bin j and i are 100% correlated) and $\mathrm{corr}(j,i) = 0$ (the errors in bin j and i are not correlated).

For an error which is before unfolding 100% correlated between individual kinematic bins (like certain systematic uncertainties which are assumed to be valid for the entire considered kinematic range), the error on Born level is obtained by considering all possible bin combinations on the measured level:

$$\delta A_{\mathrm{Born}}^{\mathrm{corr}}(j)^2 = \sum_{i_1=1}^{n} D(j,i_1)\delta A_{\mathrm{X}}^{\mathrm{corr}}(i_1)\cdot\sum_{i_2=1}^{n} D(j,i_2)\delta A_{\mathrm{X}}^{\mathrm{corr}}(i_2) \equiv \left(\sum_{i=1}^{n} D(j,i)\delta A_{\mathrm{X}}^{\mathrm{corr}}(i)\right)^2. \tag{C.27}$$

Eq. C.27 reduces to one single sum given the case that the errors are not correlated before unfolding (which especially applies to the statistical error):

$$\delta A_{\mathrm{Born}}^{\mathrm{nocorr}}(j)^2 = \sum_{i=1}^{n} D^2(j,i)\delta A_{\mathrm{X}}^{\mathrm{nocorr}}(i)^2. \tag{C.28}$$

The inflation of the statistical error coming along with the unfolding, $\delta A_{\mathrm{Born}}/\delta A_{\mathrm{X}}$, is shown in Fig. 3.21. Generally, the error inflation will be smaller for the correlated case in Eq. C.27, because the two separate sums allow for negative contributions which don't appear in Eq. C.28 due to the fact that the dilution matrix enters squared.

C.3 Monte Carlo statistical error

To estimate an uncertainty due to the limited Monte Carlo statistics, the cross section determined from the experimental Monte Carlo sample σ_{X} and the BORN cross section σ_{Born} were subject to a GAUSSIAN variation within one standard deviation, respectively [104]: the cross section σ_{X} in every bin of x-BJØRKEN was varied 10000 times in the intervall $\sigma_{\mathrm{X}} \pm \delta\sigma_{\mathrm{X}}$ (the box in Fig. A.1); only that part of the resulting distribution was kept which lied below the GAUSSIAN curve with $\mu \equiv \sigma_{\mathrm{X}}$ and $\sigma \equiv \delta\sigma_{\mathrm{X}}$ (the shaded area in Fig. A.1). This procedure was performed in the same manner for σ_{Born}. Subsequently, 10000 varied smearing matrices $S'(i,j)$ (Eq. C.17) were constructed and inverted which allowed for the determination of 10000 unfolded asymmetries $A_{\mathrm{Born}}(j,k)$, $k = 1...10000$, for every BORN bin j.[5] The statistical error arising from the Monte Carlo data sample $\delta(\mathrm{MC})(j)$ in BORN bin j was calculated as the standard deviation (Eq. A.4) of the distribution found for each bin:

$$\delta(\mathrm{MC})(j) = \frac{\sqrt{\sum_{k=1}^{10000}(A_{\mathrm{Born}}(j,0) - A_{\mathrm{Born}}(j,k))^2}}{10000}. \tag{C.29}$$

C.4 Kinematic averages on BORN level

Due to bin migration effects, not only the central value of the asymmetry and its statistical error are subject to modifications, but also the average kinematic values for each kinematic bin. Thus, the measured and BORN level kinematic averages are not identical. The precise knowledge of the latter, however, is needed for instance for the calculation of the structure functions from the BORN asymmetry. To obtain the kinematic averages $\langle K_{\mathrm{Born}}\rangle$ for each bin on BORN level, the measured average for the variable $\langle K_{\mathrm{X}}\rangle$ (like x_{Bj}, Q^2, γ) is rescaled with the ratio of the average kinematic values obtained from the BORN and experimental Monte Carlo samples $\langle K^{\mathrm{MC}}_{\mathrm{Born}}\rangle$ and $\langle K^{\mathrm{MC}}_{\mathrm{X}}\rangle$, respectively (see also Sec. C.6):

$$\langle K_{\mathrm{Born}}\rangle = \frac{\langle K^{\mathrm{MC}}_{\mathrm{Born}}\rangle}{\langle K^{\mathrm{MC}}_{\mathrm{X}}\rangle}\langle K_{\mathrm{X}}\rangle. \tag{C.30}$$

As an example, compare $\langle x_{\mathrm{X}}\rangle$ from Tab. D.7 and $\langle x_{\mathrm{Born}}\rangle$ from Tab. D.10 with each other.

[5]The default BORN asymmetry was obtained from non-varied cross sections.

C.5 A simple unfolding example

A simple example with four bins in x-Bjørken (see Fig. C.1) is supposed to illustrate

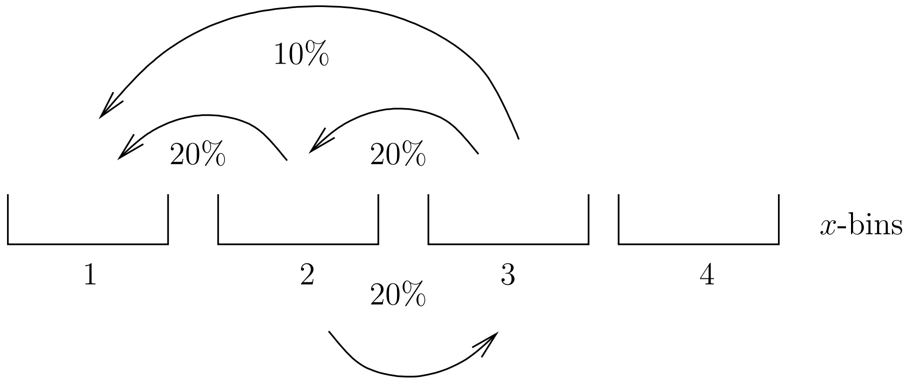

Figure C.1: Quantitative example for bin migrations between four bins in x-Bjørken, without events entering or leaving the acceptance. The corresponding smearing matrix and its inverse are given in the text.

the principle of the unfolding procedure, restricting the investigation to the multiplicative term from Eq. C.20:

$$A_{\mathrm{Born}}(j) \sim 3 \sum_{i=1}^{n} c_{ij} [S']^{-1}(j,i) A_{\mathrm{X}}(i), \tag{C.31}$$

with $c_{ij} = \sigma_{\mathrm{X}}^{\mathrm{U}}(i)/\sigma_{\mathrm{Born}}^{\mathrm{U}}(j)$, in which terms the full expression for the statistical error δA_{Born} reads

$$\delta A_{\mathrm{Born}}(j) = 3 \sqrt{\sum_{i=1}^{n} c_{ij}^2 \left([S']^{-1}(j,i)\right)^2 \delta A_{\mathrm{X}}^2(i)}. \tag{C.32}$$

No smearing from or into the outside of the acceptance is considered, i. e. $i, j = 1...4$. Let 20% of the events in Born bin number 3 due to smearing effects migrate to bin number 2, where they are observed, and similarily for the bin pairs 2→1 and 2→3, and only 10% of the events from Born bin 3 to the observed bin 1. Then the smearing matrix $S(i,j)$ and its inverse (the "unsmearing" matrix) $S^{-1}(j,i)$ explicitly read:

$$S(i,j) = \begin{array}{c} \begin{matrix} \mathbf{1} & \mathbf{2} & \mathbf{3} & \mathbf{4} \end{matrix} \\ \begin{pmatrix} 1 & 0.2 & 0.1 & 0 \\ 0 & 0.6 & 0.2 & 0 \\ 0 & 0.2 & 0.7 & 0 \\ 0 & 0 & 0 & 1 \end{pmatrix} \end{array}, \quad S^{-1}(j,i) = \begin{pmatrix} 1 & -0.3158 & -0.05263 & 0 \\ 0 & 1.842 & -0.5263 & 0 \\ 0 & -0.5263 & 1.579 & 0 \\ 0 & 0 & 0 & 1 \end{pmatrix} \begin{matrix} \mathbf{1} \\ \mathbf{2} \\ \mathbf{3} \\ \mathbf{4} \end{matrix}, \tag{C.33}$$

the numbers in bold indicating the Born bin number (columns or rows, respectively). If no events migrate from Born bin j into another bin, then $S(j,j) = 1$. As no events are considered to leave the acceptance, the continuity equation $\sum_{i=1}^{4} S(i,j) = 1$ holds. The losses in Born bin j due to smearing are compensated by the terms $S^{-1}(j,j) > 1$ in the unsmearing matrix. The corresponding contaminations in the observed bin i are retracted by the negative terms $S^{-1}(j,i) < 0$, $i \neq j$. Thus, when it comes to calculating for example the Born asymmetry in bin 2, $A_{\text{Born}}(2)$, the sum over i in Eq. C.31 accounts for the loss of each 20% of the events to bin 1 and 3 by multiplying $A_{\text{X}}(2)$ by the factor 1.842, and the contamination by 20% of the events from bin 3 is considered by subtracting 0.5263 times the asymmetry observed in bin 3, $A_{\text{X}}(3)$. For the calculation of δA_{Born}, there is no subtraction, as all terms in the sum of Eq. C.32 enter quadratically.
Due to the Born model-independence of the algorithm (within the acceptance, which is exclusively considered here), there are no intra-bin correlations, which allows for the unfolding also of asymmetries which are rather unsmooth or even not continuous. On the other hand, this causes the netto-effect in a given bin to be unknown *a priori*. Thus, the statistical error of the asymmetry in a given bin is inflated both due to event migrations into and out of the bin. However, the information of the double-counting is stored in the covariance matrix, of which the (squared) statistical error constitutes the main diagonal.

C.6 The inclusive Hermes Monte Carlo

The fully tracked (HRC) Monte Carlo samples run through three production stages: the generation of DIS events in accordance to the Born cross section (GMC); the application of QED radiative effects (RADGEN); and tracking of the events through a model of the detector (GEANT and HRC). For the HSG productions, the third stage is replaced by simulating the detector as one uniform piece of material. In the Born MC productions, only the first stage is incorporated, providing the Born cross section.

Generation. There are two basic principles to generate Monte Carlo samples of DIS leptons: the first is to generate events according to the cross section (like the generator Phythia [6]) and let the algorithm then decide wether to “accept” or to “reject” the event; one accepted event then corresponds to one Monte Carlo event.
The second principle is to use MC weights (like the generator `gmc_disNG` employed for this analysis): DIS events with kinematics (Q^2, ν) are randomly generated in a certain box interval[6] in $\log Q^2$ and ν. The weight $\omega_{\text{gen}}(k)$ which is generated for the kth event

[6] An extraweight accounts for the limited size of this box. For the MC samples produced for this analysis, extraweight=1. It is therefore skipped in the further discussion; generally, it multiplies with

accounts for the modulation of the BORN cross section σ_{Born} which is given as input to the MC in terms of an F_2 parameterization.
For the kth MC event, the MC generator dices iEvGen(k) times until it generates one event in the box interval. This number is used for correct luminosity weighting; the iEvGen(k) is summed up for every target spin state separately[7] before kinematic and geometry cuts[8]:

$$\Sigma(\mathrm{iEvGen}) = \sum_{k=1}^{N_{\mathrm{MC}}} \mathrm{iEvGen}(k), \tag{C.34}$$

where N_{MC} is the total number of generated MC events.

Radiative corrections. An event which is observed with kinematics (Q^2, ν) *can* have undergone second-oder QED processes (Sec. 3.3.1). This uncertainty is met by the Monte Carlo: the radiative correction code RADGEN randomly selects the scattering channel of the event, taking into account the respective probability in the total observed cross section (Eq. 3.2): non-radiative or radiative (either elastic, quasi-elastic, or inelastic). If the non-radiative channel is selected, the kth event delivers an observed[9] cross section of:

$$\sigma_{\mathrm{obs}}^{\mathrm{non-rad}}(k) = \frac{\omega_{\mathrm{gen}}(k)}{\mathrm{iEvGen}(k)}. \tag{C.35}$$

If the radiative channel is selected, an additional weight SigRadCorr is assigned to the event according to the chosen radiation type and the diced (Q^2, ν) pair, accounting for the additional contribution to the observed cross section which is coming along with the radiation of the real photon:

$$\mathrm{SigRadCorr}(k) := \frac{\sigma_{\mathrm{obs}}}{\sigma_{\mathrm{Born}}} > 1. \tag{C.36}$$

A radiative event contributes an observed cross section of:

$$\sigma_{\mathrm{obs}}^{\mathrm{rad}}(k) = \frac{\omega_{\mathrm{gen}}(k) \cdot \mathrm{SigRadCorr}(k)}{\mathrm{iEvGen}(k)}. \tag{C.37}$$

σ_{obs} has then the unit μbarn. Let ω_k denote the total weight of the kth event (i. e. the product of all involved weights, depending on wether the event is a radiative one or not). The total observed MC cross section $\sigma_{\mathrm{obs}}(i)$ in the kinematic bin i is calculated separately for every target spin state[10]:

$$\sigma_{\mathrm{obs}}(i) = \frac{1}{\Sigma(\mathrm{iEvGen})} \cdot \sum_k \omega_k, \tag{C.38}$$

every event weight ω_k, however.

[7] To obtain luminosity balance between the target spin states.

[8] Also luminosity in the real experiment is summed up *before* any cuts.

[9] *Observed* means *generated* here: the generated events are treated as observed events.

[10] The target state index is skipped for simplicity.

as well as its statistical error:

$$\delta\sigma_{\mathrm{obs}}(i) = \frac{1}{\Sigma(\mathrm{iEvGen})} \cdot \sqrt{\sum_k \omega_k^2}. \tag{C.39}$$

Both times the sum runs only over events k which fall into bin i. By considering the kinematics of the emitted real photon, the BORN level kinematics (Q^2_{Born}, ν_{Born}) of the event are calculated. If the event is non-radiative and thus no photon is emitted, the generated kinematics are equal to the BORN level kinematics. The knowledge of the BORN kinematics is crucial for the construction of the migration matrices $M_{\mathrm{X}}(i,j)$.

A separate BORN MC sample is required because the starting point for the MC production is the observed kinematics, and it is not *a priori* known how large the size of the generation box in the experimental MC would have to be in order to obtain the full BORN cross section within the acceptance of the detector, unless it is known how far away events migrate *at most* from the edges of the acceptance. For the BORN MC sample, as no radiative corrections are applied, the generated kinematics correspond to the true (BORN) kinematics. The BORN cross section $\sigma_{\mathrm{Born}}(k)$ for the single event k is

$$\sigma_{\mathrm{Born}}(k) = \frac{\omega_{\mathrm{gen}}(k)}{\mathrm{iEvGen}(k)}. \tag{C.40}$$

$\sigma_{\mathrm{Born}}(j)$ and its error $\delta\sigma_{\mathrm{Born}}(j)$ in bin j are obtained as

$$\sigma_{\mathrm{Born}}(j) = \frac{1}{\Sigma(\mathrm{iEvGen})} \cdot \sum_k \omega_{\mathrm{gen}}(k), \tag{C.41}$$

$$\delta\sigma_{\mathrm{Born}}(j) = \frac{1}{\Sigma(\mathrm{iEvGen})} \cdot \sqrt{\sum_k \omega_{\mathrm{gen}}(k)^2}, \tag{C.42}$$

respectively.

Tracking. For an HRC production, the generated events with kinematics (Q^2, ν) are then run through a model of the detector, employing the GEANT tool, and are reconstructed by HRC (the two stages are denoted as *tracking* in summary). This procedure alternates the kinematics of the event by simulating interactions in the detector material (e. g. by applying the BETHE-BLOCH formula). HRC passes the reconstructed momentum and scattering angle from which the experimental kinematics (Q^2_{X}, ν_{X}) can be calculated. The assigned weight and thus the cross section delivered by a single event is not changed, but the reconstructed cross section $\sigma_{\mathrm{X}}(i)$ in the kinematic bin i differs from the generated cross section $\sigma_{\mathrm{obs}}(i)$ in the same bin due to the smearing in the detector.

Exploitation of the MC productions. The so far obtained experimental and Born cross sections σ_{X} and σ_{Born}, respectively, are employed in the unfolding algorithm in App. C.1. Further quantities need to be extracted:

The average $\langle K^{\mathrm{MC}}\rangle(i)$ of a kinematic quantity K in the kinematic bin i (like the average x-Bjørken for a certain x-bin) is calculated as the weighted sum over all single contributions $K(k)$:

$$\langle K^{\mathrm{MC}}\rangle(i) = \frac{\sum_k K(k)\cdot\omega_k}{\sum_k \omega_k}, \tag{C.43}$$

where the sum runs only over events k falling into the kinematic bin i in question. $\langle K^{\mathrm{MC}}_{\mathrm{X}}\rangle$ is obtained by summing the $K(k)$ of the tracked[11] events of the experimental MC according to Eq. C.43, and $\langle K^{\mathrm{MC}}_{\mathrm{Born}}\rangle$ analogously from the Born MC. The multiplication by the MC weight in the numerator accounts for the fact that every kinematic distribution was originally generated flat, i. e. without any modulation resembling the cross section.

The migration matrix $M_{\mathrm{X}}(i,j)$ is constructed from the experimental Monte Carlo sample. The experimental and Born x-Bjørken for each event are known through $x_{\mathrm{X}} = Q^2_{\mathrm{X}}/2M\nu_{\mathrm{X}}$ and $x_{\mathrm{Born}} = Q^2_{\mathrm{Born}}/2M\nu_{\mathrm{Born}}$, respectively. For event k, the weight ω_k is filled into the ijth element of $M_{\mathrm{X}}(i,j)$, where i is the x-bin into which x_{X} falls and j the x-bin into which x_{Born} falls. After all events have been processed, normalization is performed by division by Σ(iEvGen) (Eq. C.34), such that every entry of the matrix has the unit μbarn. This calculation is carried out separately for every target spin state. Identical binning schemes in x-Bjørken are used for the experimental and the Born level with a total of n bins and $i = 1,...,n$ and $j = 0,...,n$, where $j = 0$ integrates the part of the cross section which migrates *into* the acceptance defined by kinematic and geometry cuts.

The tensor asymmetry A^{MC}_{zz} reconstructed from the Monte Carlo is calculated as:

$$A^{\mathrm{MC}}_{zz} = 2\cdot\frac{\sigma^+_{\mathrm{X}} - \sigma^-_{\mathrm{X}}}{2\cdot\sigma^+_{\mathrm{X}} + \sigma^-_{\mathrm{X}}}, \tag{C.44}$$

where $\sigma^{+(-)}_{\mathrm{X}}$ is the experimental cross section obtained for a target with tensor polarization $|\,P_{zz}\,| = 2(1)$ in the MC, and the statistical error on the MC tensor asymmetry $\delta A^{\mathrm{MC}}_{zz}$ is

$$\delta A^{\mathrm{MC}}_{zz} = \frac{6}{(2\cdot\sigma^+_{\mathrm{X}} + \sigma^-_{\mathrm{X}})^2}\cdot\sqrt{(\sigma^+_{\mathrm{X}})^2(\delta\sigma^-_{\mathrm{X}})^2 + (\sigma^-_{\mathrm{X}})^2(\delta\sigma^+_{\mathrm{X}})^2}. \tag{C.45}$$

[11] Or smeared in the case of HSG.

D Tables of results

Table D.1: The average HERA positron beam polarizations for the tensor data period, total and splitted for different beam helicities (top) and additionally for different target states (bottom). Statistical uncertainties are negligible. No systematic uncertainties are quoted as they are not relevant for the presented analysis.

Beam polarization			
Total average: $\|P_\mathrm{B}\| = 54.0\%$			
negative helicity: $\|P_\mathrm{B}^-\| = 54.7\%$ (statistics: $\approx 62\%$)		positive helicity: $\|P_\mathrm{B}^+\| = 52.9\%$ (statistics: $\approx 38\%$)	
Relative difference between $\|P_\mathrm{B}^-\|$ and $\|P_\mathrm{B}^+\|$: 3%			
`vector plus`:	$\|P_\mathrm{B}^-\| = 54.7\%$	`vector plus`:	$\|P_\mathrm{B}^+\| = 52.9\%$
`vector minus`:	$\|P_\mathrm{B}^-\| = 54.7\%$	`vector minus`:	$\|P_\mathrm{B}^+\| = 52.9\%$
`tensor plus`:	$\|P_\mathrm{B}^-\| = 54.7\%$	`tensor plus`:	$\|P_\mathrm{B}^+\| = 52.9\%$
`tensor minus`:	$\|P_\mathrm{B}^-\| = 54.6\%$	`tensor minus`:	$\|P_\mathrm{B}^+\| = 53.0\%$

Table D.2: The average target polarization values $P = \alpha_\mathrm{eff} \cdot P_a$ for the data taking year 2000 [62] with the dilution factor $\alpha_\mathrm{eff} = 0.918 \pm 0.026$ (sys). See Tab. 2.2 on Pg. 28 for the notation. The quoted errors are systematic only: $\delta P = \sqrt{\alpha_\mathrm{eff}^2 \delta P_a^2 + P_a^2 \delta\alpha_\mathrm{eff}^2}$; the statistical uncertainty is negligible. The vector polarization of *both* tensor states has actually a slight negative value, the *residual vector polarization*.

Target polarization	
$P_z^+ = +0.851 \pm 0.029$	$P_{zz}^+ = +0.800 \pm 0.025$
$P_z^- = -0.840 \pm 0.026$	$P_{zz}^- = +0.853 \pm 0.027$
$P_z^\Leftrightarrow = -0.010 \pm 0.003$	$P_{zz}^\Leftrightarrow = +0.891 \pm 0.027$
$P_z^0 = -0.010 \pm 0.005$	$P_{zz}^0 = -1.656 \pm 0.049$

Table D.3: Integrated deadtime corrected relative luminosity $L = \sum_i \Delta\tau_i \epsilon_i \mathcal{L}_i$ (in 10^7), where $\Delta\tau_i$ is the burstlength, ϵ_i the dead time correction and $\mathcal{L}_i$ the measured relative luminosity ("lumirate", in Hz), respectively, for burst i. Values for L are given separately for detector half, target states and beam helicity. The top/bottom averaged total value of the relative luminosity $L = 5.1 \cdot 10^7$ corresponds to an absolute luminosity of $L_{\text{abs}} = L \cdot C_{\text{Lumi}} = (5.1 \cdot 10^7 \cdot 417 \cdot 10^{-9})/\text{pb} \approx 21\ \text{pb}^{-1}$, where $C_{\text{Lumi}} = 417/\text{mb}$ is a lumi constant [105] $\langle L \rangle$ denotes the luminosity difference between negative and positive beam helicity. See Tab. 2.2 for the notation of the target injection modes and Eq. B.3 for the double superscript notation.

L	L_{Top} in 10^7			L_{Bottom} in 10^7		
total	5.0731			5.0904		
$L^{\leftrightarrows} = L^{+-} + L^{-+}$	1.2689			1.2739		
$L^{\rightrightarrows} = L^{++} + L^{--}$	1.2706			1.2743		
$L^{\Leftrightarrow} = L^{+\Leftrightarrow} + L^{-\Leftrightarrow}$	1.2715			1.2744		
$L^{0} = L^{+0} + L^{-0}$	1.2621			1.2678		
	max.deviation=$\frac{L^{\Leftrightarrow}-L^{0}}{L^{0}} = 0.0075$, $\langle L \rangle = 1.2683$			max.deviation=$\frac{L^{\Leftrightarrow}-L^{0}}{L^{0}} = 0.0052$, $\langle L \rangle = 1.2726$		
target mode	neg. beam hel.	pos. beam hel.	$\frac{\Delta L}{\langle L \rangle}$	neg. beam hel.	pos. beam hel.	$\frac{\Delta L}{\langle L \rangle}$
`vector plus`	$L^{-+} = 0.7730$	$L^{++} = 0.4959$	0.2185	$L^{-+} = 0.7763$	$L^{++} = 0.4964$	0.2199
`vector minus`	$L^{--} = 0.7747$	$L^{+-} = 0.4959$	0.2198	$L^{--} = 0.7779$	$L^{+-} = 0.4976$	0.2203
	$\frac{L^{-+}-L^{--}}{L^{--}} = -0.0022$	$\frac{L^{++}-L^{+-}}{L^{+-}} < 0.0001$		$\frac{L^{-+}-L^{--}}{L^{--}} = -0.0021$	$\frac{L^{++}-L^{+-}}{L^{+-}} = 0.0024$	
`tensor plus`	$L^{-\Leftrightarrow} = 0.7754$	$L^{+\Leftrightarrow} = 0.4961$	0.2202	$L^{-\Leftrightarrow} = 0.7778$	$L^{+\Leftrightarrow} = 0.4967$	0.2209
`tensor minus`	$L^{-0} = 0.7753$	$L^{+0} = 0.4868$	0.2275	$L^{-0} = 0.7788$	$L^{+0} = 0.4890$	0.2277

Table D.4: The applied kinematic cuts (left) and the binning in x-Bjørken used to extract the tensor asymmetry from Hermes data (right).

Kinematic cuts
$0.0021 < x < 0.8500$
$0.1\ \mathrm{GeV}^2 < Q^2$
$W^2 > 3.24\ \mathrm{GeV}^2$
$\nu > 1\ \mathrm{GeV}$
$0.10 < y < 0.91$

Binning in x-Bjørken		
bin	x_{min}	x_{max}
1	0.0021	0.0212
2	0.0212	0.0430
3	0.0430	0.0872
4	0.0872	0.1770
5	0.1770	0.3580
6	0.3580	0.8500

Table D.5: The number of collected DIS events entering the analysis. The number has been corrected for the charge symmetric background (see Tab. D.6) per x-bin, spin state and detector half. Altogether, 2.9 M DIS events have been collected. The ratio of charge symmetric and DIS events versus x-Bjørken is depicted in Fig. 2.9 on Pg. 38.

Top DIS events: 1398872				
bin	$\overleftarrow{\Leftarrow}$ (antiparallel)	$\overrightarrow{\Rightarrow}$ (parallel)	$\Leftrightarrow$ (`tensor plus`)	0 (`tensor minus`)
1	80951	79743	80255	79771
2	61747	60869	61031	61290
3	72558	71183	71990	72230
4	74070	71177	72695	72315
5	53042	50829	51755	51376
6	12445	11688	12147	11715

Bottom DIS events: 1531814				
bin	$\overleftarrow{\Leftarrow}$ (antiparallel)	$\overrightarrow{\Rightarrow}$ (parallel)	$\Leftrightarrow$ (`tensor plus`)	0 (`tensor minus`)
1	87691	87592	86851	87529
2	66535	66435	65946	66702
3	78387	76983	77572	77923
4	80050	78687	79437	79183
5	59295	57202	58294	58114
6	14535	13483	13712	13676

Table D.6: The number of collected charge symmetric events entering the analysis per x-bin, spin state and detector half.

Top charge symmetric events: 90281				
bin	$\overleftarrow{\Leftarrow}$ (antiparallel)	$\overrightarrow{\Rightarrow}$ (parallel)	$\Leftrightarrow$ (`tensor plus`)	0 (`tensor minus`)
1	14475	14849	14770	14712
2	5856	5968	6078	6007
3	1773	1709	1725	1793
4	140	143	117	131
5	9	7	8	5
6	3	0	1	2

Bottom charge symmetric events: 90078				
bin	$\overleftarrow{\Leftarrow}$ (antiparallel)	$\overrightarrow{\Rightarrow}$ (parallel)	$\Leftrightarrow$ (`tensor plus`)	0 (`tensor minus`)
1	14470	14858	14695	14433
2	6045	5854	5935	5997
3	1817	1852	1762	1814
4	131	131	126	128
5	5	10	5	6
6	1	1	0	2

Table D.7: Results of the measured $A_{zz}(6)$ for each x-bin, its statistical error and the average kinematics for each bin.

Measured A_{zz}			
$\langle x \rangle$	$\langle Q^2 \rangle/\mathrm{GeV}^2$	A_{zz}	δA_{zz}(stat)
0.0117	0.4830	-0.0028	0.0026
0.0312	1.0692	-0.0076	0.0028
0.0628	1.6645	-0.0078	0.0025
0.1263	2.3613	-0.0017	0.0024
0.2455	3.1906	0.0001	0.0028
0.4489	4.8425	0.0145	0.0058

Table D.8: Results of the measured $A_{zz}(1)$, $A_{zz}(5)$ and $A(4)$, their statistical error and the average kinematics for each bin.

Tensor mismatch							
$\langle x \rangle$	$\langle Q^2 \rangle/\mathrm{GeV}^2$	$A_{zz}(1)$	$\delta A_{zz}(1)(\mathrm{stat})$	$A_{zz}(5)$	$\delta A_{zz}(5)(\mathrm{stat})$	$A(4)$	$\delta A(4)(\mathrm{stat})$
0.0117	0.4830	-0.0011	0.0028	-0.0059	0.0032	0.0041	0.0023
0.0312	1.0692	-0.0057	0.0030	-0.0112	0.0034	0.0048	0.0025
0.0628	1.6645	-0.0076	0.0026	-0.0081	0.0030	0.0005	0.0022
0.1263	2.3613	-0.0018	0.0025	-0.0017	0.0029	-0.0001	0.0021
0.2455	3.1906	0.0007	0.0030	-0.0009	0.0034	0.0014	0.0025
0.4489	4.8425	0.0170	0.0061	0.0095	0.0069	0.0061	0.0051

Table D.9: Experimental systematic errors $\delta A_{zz}^{\mathrm{sys}}$ (not inflated) for each x-bin, the single contributions (tensor mismatch *mismatch*, nuclear target polarization *tarpo*, target density *tardens*, residual electron polarization *reselpol* and hadron contamination *hadcont*) and their quadratic sum (total) which is dominated by the contribution from the mismatch.

Experimental systematic uncertainties on A_{zz}						
$\langle x \rangle$	total	$\delta A^{\mathrm{sys}}_{\mathrm{mismatch}}$	$\delta A^{\mathrm{sys}}_{\mathrm{tarpo}}$	$\delta A^{\mathrm{sys}}_{\mathrm{tardens}}$	$\delta A^{\mathrm{sys}}_{\mathrm{reselpol}}$	$\delta A^{\mathrm{sys}}_{\mathrm{hadcont}}$
0.0117	0.00112	0.00106	0.00004	0.00030	0.00023	0.00003
0.0312	0.00113	0.00106	0.00010	0.00030	0.00023	0.00000
0.0628	0.00113	0.00106	0.00010	0.00030	0.00023	0.00001
0.1263	0.00112	0.00106	0.00002	0.00030	0.00023	0.00000
0.2455	0.00112	0.00106	0.00000	0.00030	0.00023	0.00000
0.4489	0.00114	0.00106	0.00019	0.00030	0.00023	0.00000

Table D.10: A_{zz} on Born level ("unfolded", including electromagnetic shower background) for each x-bin and its statistical error δA_{zz}(stat) and total systematic error δA_{zz}(sys), and the average Born kinematics for each bin. δ(MC) is the statistical error arising from the default Monte Carlo sample (Sec. 3.3.2) used to unfold A_{zz} (Eq. C.29).

A_{zz} on Born level					
$\langle x \rangle$	$\langle Q^2 \rangle$	A_{zz}	δA_{zz}(stat)	δA_{zz}(sys)	δ(MC)
0.0122	0.5075	-0.0106	0.0052	0.0026	0.0015
0.0315	1.0641	-0.0107	0.0049	0.0036	0.0013
0.0635	1.6542	-0.0132	0.0038	0.0021	0.0012
0.1277	2.3319	-0.0019	0.0034	0.0029	0.0012
0.2481	3.1066	-0.0039	0.0039	0.0032	0.0014
0.4521	4.6923	0.0157	0.0068	0.0013	0.0016

Table D.11: The covariance matrix of the statistical error of A_{zz} (Born level), Eq. C.23. It is symmetrical with respect to the main diagonal; the entries of the latter are the square of δA_{zz}(stat) from in Tab. D.10.

Covariance matrix of δA_{zz} (in 10^{-4})						
x-bin	1	2	3	4	5	6
1	0.272	-0.040	-0.007	-0.005	-0.003	0.002
2	-0.040	0.241	-0.035	-0.005	-0.006	-0.006
3	-0.007	-0.035	0.146	-0.030	-0.002	-0.013
4	-0.005	-0.005	-0.030	0.118	-0.038	-0.002
5	-0.003	-0.006	-0.002	-0.038	0.148	-0.105
6	0.002	-0.006	-0.013	-0.002	-0.105	0.464

Table D.12: BORN level (inflated) experimental systematic errors $\delta A_{zz}^{\rm sys}$ for each x-bin, the single contributions (tensor mismatch *mismatch*, nuclear target polarization *tarpo*, target density *tardens*, residual electron polarization *reselpol* and hadron contamination *hadcont*) and their quadratic sum $\delta A_{\rm Born}^{\rm sys}(\rm exp)$ (Eq. 3.16) which is dominated by the contribution from the mismatch.

Inflated experimental systematic uncertainties on A_{zz}						
$\langle x \rangle$	$\delta A_{\rm Born}^{\rm sys}(\rm exp)$	$\delta A_{\rm mismatch}^{\rm sysinfl}$	$\delta A_{\rm tarpo}^{\rm sysinfl}$	$\delta A_{\rm tardens}^{\rm sysinfl}$	$\delta A_{\rm reselpol}^{\rm sysinfl}$	$\delta A_{\rm hadcont}^{\rm sysinfl}$
0.0122	0.00163	0.00154	0.00005	0.00044	0.00033	0.00005
0.0315	0.00126	0.00118	0.00019	0.00034	0.00025	0.00001
0.0635	0.00118	0.00110	0.00021	0.00031	0.00024	0.00002
0.1277	0.00113	0.00107	0.00004	0.00030	0.00023	0.00000
0.2481	0.00113	0.00106	0.00006	0.00030	0.00023	0.00000
0.4521	0.00118	0.00106	0.00034	0.00031	0.00022	0.00000

Table D.13: BORN level systematic errors $\delta A_{zz}^{\rm sys}$ for each x-bin; the total uncertainty $\delta A_{\rm Born}^{\rm sys}(\rm tot)$ is obtained by adding the contribution from the experiment $\delta A_{\rm Born}^{\rm sys}(\rm exp)$ (Eq. 3.16) and the contribution from the Monte Carlo studies $\delta A_{\rm Born}^{\rm sys}(\rm MC)$ (Eq. 3.17) in quadrature (Eq. 3.18). To obtain the latter error, the uncertainty on the misaligment (*misali*) (Eq. 3.15) and the uncertainty on the determination of the radiative corrections (RC) (Eq. 3.14) have been added in quadrature (Eq. 3.17).

BORN level systematic uncertainties on A_{zz}					
$\langle x \rangle$	$\delta A_{\rm Born}^{\rm sys}(\rm tot)$	$\delta A_{\rm Born}^{\rm sys}(\rm exp)$	$\delta A_{\rm Born}^{\rm sys}(\rm MC)$	$\delta A_{\rm misali}^{\rm sysMC}$	$\delta A_{\rm RC}^{\rm sysMC}$
0.0122	0.00262	0.00163	0.00205	0.00066	0.00194
0.0315	0.00357	0.00126	0.00334	0.00014	0.00334
0.0635	0.00209	0.00118	0.00172	0.00065	0.00159
0.1277	0.00286	0.00113	0.00263	0.00263	0.00010
0.2481	0.00320	0.00113	0.00299	0.00299	0.00002
0.4521	0.00125	0.00118	0.00043	0.00034	0.00026

Table D.14: b_1^{d} on Born level ("unfolded", including electromagnetic shower background) for each x-bin and its statistical error $\delta b_1^{\mathrm{d}}(\mathrm{stat})$ and total systematic error $\delta b_1^{\mathrm{d}}(\mathrm{sys})$ propagated from $\delta A^{\mathrm{sys}}_{\mathrm{Born}}(\mathrm{tot})$ (Tab. D.13) to b_1, and the average Born kinematics for each bin.

b_1^{d} on Born level				
$\langle x\rangle$	$\langle Q^2\rangle$	b_1^{d}	$\delta b_1^{\mathrm{d}}(\mathrm{stat})$	$\delta b_1^{\mathrm{d}}(\mathrm{sys})$
0.0122	0.5075	0.1120	0.0551	0.0277
0.0315	1.0641	0.0550	0.0253	0.0184
0.0635	1.6542	0.0382	0.0111	0.0060
0.1277	2.3319	0.0029	0.0053	0.0044
0.2481	3.1066	0.0029	0.0028	0.0024
0.4521	4.6923	-0.0038	0.0016	0.0003

Table D.15: $b_2^{\mathrm{d}} = -\frac{3}{2}A_{zz}F_2^{\mathrm{d}}$ and $b_1^{\mathrm{d}}/F_1^{\mathrm{d}} = -\frac{3}{2}A_{zz}$ on Born level ("unfolded", including electromagnetic shower background) and the average Born kinematics for each x bin. The systematic errors on $b_1^{\mathrm{d}}/F_1^{\mathrm{d}}$ and b_2^{d} can be obtained by propagation of the systematic errror $\delta A_{zz}(\mathrm{sys})$ from Tab. D.10. The values of F_2^{d}, F_1^{d} and R were calculated from world data fits (default parameterizations, see Sec. 3.3.2) at the quoted average kinematics.

b_2^{d}, $b_1^{\mathrm{d}}/F_1^{\mathrm{d}}$, F_2^{d}, F_1^{d} and $R=\sigma_L/\sigma_T$ on Born level								
$\langle x\rangle$	$\langle Q^2\rangle$	b_2^{d}	δb_2^{d}	$b_1^{\mathrm{d}}/F_1^{\mathrm{d}}$	$\delta(b_1^{\mathrm{d}}/F_1^{\mathrm{d}})$	F_2^{d}	F_1^{d}	R
0.0122	0.5075	0.0035	0.0017	0.0159	0.0078	0.2209	7.0591	0.2817
0.0315	1.0641	0.0046	0.0021	0.0160	0.0074	0.2898	3.4402	0.3401
0.0635	1.6542	0.0064	0.0018	0.0198	0.0057	0.3218	1.9294	0.3250
0.1277	2.3319	0.0009	0.0017	0.0028	0.0052	0.3265	1.0218	0.2818
0.2481	3.1066	0.0016	0.0016	0.0058	0.0058	0.2738	0.4922	0.1992
0.4521	4.6923	-0.0033	0.0015	-0.0236	0.0102	0.1417	0.1606	0.1256

Table D.16: First moment $M = \int b_1^{\mathrm{d}}(x, Q_0^2 = 5\ \mathrm{GeV}^2)\mathrm{d}x$ within two different ranges, its statistical and systematic error (Eq. 3.36) and the contributions to the latter one: experimental (Eq. 3.34) and from Monte Carlo studies (Eq. 3.35).

First moment of b_1^{d} ($Q_0^2 = 5$ GeV^2)						
x-range	M	δM(stat)	δM(sys)	δM^{sys}(exp)	δM^{sys}(MC)	$\int F_1^{\mathrm{d}}(x, Q_0^2)\mathrm{d}x$
0.0021..0.85	0.0105	0.0034	0.0035	0.0019	0.0030	0.8763
0.02..0.85	0.0035	0.0010	0.0018	0.0008	0.0016	0.4359

List of Tables

List of Figures

Bibliography

[1] C. G. Callan and D. Gross, Phys. Lett. B**22** (1969) 156

[2] J. Ashman *et al.* (EMC), Phys. Lett. B**206** (1988) 364

[3] B. W. Filippone and Xiangdong Ji, Adv. Nucl. Phys. **26** (2001) 1

[4] M. C. Vetterli, hep-ph/9812420 (1998)

[5] A. V. Belitsky, D. Müller and A. Kirchner, Nucl. Phys. **B**629 (2002) 323

[6] P. Liebing, PhD thesis, Universität Hamburg (2004), DESY-thesis-2004-036

[7] A. Airapetian *et al.* (HERMES), Phys. Rev. Lett. **94** (2005) 012002

[8] V. Barone *et al.*, Phys. Rep. **359** (2002) 1

[9] A. W. Thomas and W. Weise, *The Structure of the Nucleon*, Wiley-VCH, Berlin (2001)

[10] A. Deshpande, Talk given at the 16th international spin physics symposium, Trieste (2004)

[11] K. Rith, Prog. Part. Nucl. Phys. **49** (2002) 245

[12] F. E. Close, Rep. Prog. Phys. **42** (1979) 1286

[13] B. Povh, K. Rith, C. Scholz, F. Zetsche, *Teilchen und Kerne*, Springer-Verlag (1995)

[14] P. Hoodbhoy, R. L. Jaffe and A. Manohar, Nucl. Phys. B**312** (1989) 571

[15] R. L. Jaffe, Comm. Nucl. Part. Phys. **19** (1990) 239

[16] R. Devenish and A. Cooper-Sarkar, *Deep Inelastic Scattering*, Oxford University Press (2004)

[17] J. Edelmann, G. Piller and W. Weise, Z. Phys. A**357** (1997) 129, Phys. Rev. C**57** (1998) 3392

[18] B. Lampe and E. Reya, Phys. Rep. **332** (2000) 1

[19] B. Adeva *et al.* (SMC), Phys. Rev. D**60** (1999) 072004, and erratum, Phys. Rev. D**62** (2000) 079902

[20] P. Amaudruz *et al.* (NMC), Z. Phys. C**51** (1991) 387

[21] R. G. Roberts, *The Structure of the Proton: deep inelastic scattering*, Cambridge University Press (1990)

[22] M. Garcon, *Elastic Scattering Studies of Deuterium*, DAPNIA-SPHN-99-77 (1999)

[23] J. L. Forest *et al.*, Phys. Rev. C**54** (1996) 646

[24] V. Franco and R. J. Glauber, Phys. Rev. Lett. **22** (1969) 370

[25] J. -F. Germond and C. Wilkin, Phys. Lett. B**59** (1975) 317

[26] E. Passchier, PhD thesis, Universiteit Utrecht (1996)

[27] R. L. Jaffe and A. Manohar, Nucl. Phys. B**321** (1989) 343

[28] S. Kumano, Talk given at the 14th international spin physics symposium, Osaka (2000)

[29] S. Kumano, The ELFE project, an Electron Laboratory For Europe, Conference Proceedings of the Italian Physical Society Vol. **44**, Mainz (1993) p. 371

[30] HERMES Collaboration, *Technical Design Report*, DESY-PRC 93/06 (1993)

[31] M. Düren, habilitation thesis, FRIEDRICH-ALEXANDER-Universiät Erlangen-Nürnberg (1995), DESY HERMES-95-02

[32] A. Pais, Phys. Rev. Lett. **19** (1967) 544

[33] L. L. Frankfurt and M. I. Strikman, Nucl. Phys. **A**405 (1983) 557

[34] R. L. Jaffe, in *Relativistic Dynamics and Quark Nuclear Physics*, eds. M. B. Johnson and A. Picklesimer (Wiley, New York 1986)

[35] H. Khan and P. Hoodbhoy, Phys. Rev. C**44** (1991) 1219

[36] G. A. Miller, in *Electronuclear Physics with Internal Targets*, ed. R. G. Arnold (World Scientific, Singapore 1989) p. 30

[37] L. Mankiewicz, Phys. Rev. D**40** (1989) 255

[38] R. L. Jaffe and A. Manohar, Phys. Lett. B**223** (1989) 218

[39] E. Sather and C. Schmidt, Phys. Rev. D**42** (1990) 1424

[40] N. N. Nikolaev and W. Schäfer, Phys. Lett. B**398** (1997) 245

[41] K. Bora and R. L. Jaffe, Phys. Rev. D**57** (1998) 6906

[42] G. Niesler, G. Piller and W. Weise, Z. Phys. A**358** (1997) 407

[43] H. Khan and P. Hoodbhoy, Phys. Lett. B**298** (1993) 181

[44] N. N. Nikolaev, private communication (2003, 2004)

[45] M. Strikman, in *Proceedings of the Symposium on Spin Structure of the Nucleon*, ed. V. H. Hughes and C. Cavata (World Scientific, Singapore 1995) p. 153

[46] M. Arneodo *et al.* (NMC), Phys.Rev. D**50** (1994) 1

[47] J. D. Bjørken, Phys. Rev. **148** (1966) 1457

[48] J. D. Bjørken, Phys. Rev. D**1** (1970) 1367

[49] F. E. Close and S. Kumano, Phys. Rev. D**42** (1990) 2377

[50] A. V. Efremov and O. V. Teryaev, Sov. J. Nucl. Phys. **36** (1982) 557

[51] A. Schäfer, L. Szymanowski and O. V. Teryaev, Phys. Lett. B**464** (1999) 94

[52] P. Newman, hep-ex/9901026 (1999)

[53] P. Abreu *et al.* (DELPHI), Phys. Lett. B**406** (1997) 271

[54] K. Ackerstaff *et al.* (HERMES), Nucl. Instr. and Meth. A**417** (1998) 230

[55] A. Sokolov and I. Ternov, Sov. Phys. Doklady **8** (1964) 1203

[56] J. Buon and K. Steffen, Nucl. Instr. and Meth. A**245** (1986) 248

[57] D. Barber *et al.*, Nucl. Instr. and Meth. A**329** (1993) 79

[58] D. Barber *et al.*, Nucl. Instr. and Meth. A**338** (1994) 166

[59] M. Beckmann *et al.*, Nucl. Instr. and Meth. A**479** (2002) 334

[60] Madison convention, in *Polarization Phenomena in Nuclear Reactions* (University of Wisconsin Press, Madison 1971) XXV

[61] Z. -L. Zhou *et al.*, Phys. Rev. Lett. **82** (1999) 687

[62] A. Airapetian *et al.* (HERMES), Nucl. Instr. and Meth. A**540** (2005) 68

[63] A. Nass *et al.*, Nucl. Instr. and Meth. A**505** (2003) 633

[64] C. Baumgarten *et al.*, Nucl. Instr. and Meth. A**496** (2003) 277

[65] C. Baumgarten *et al.*, Nucl. Instr. and Meth. A**508** (2003) 268

[66] C. Baumgarten *et al.*, Nucl. Instr. and Meth. A**482** (2002) 606

[67] D. Reggiani, PhD thesis, Universita degli Studi di Ferrara (2002)

[68] HERMES target group, HERMES internal note 02-010 (2002)

[69] E. Steffens, W. Haeberli, Rep. Prog. Phys. **66** (2003) 1887

[70] Th. Benisch *et al.*, Nucl. Instr. and Meth. A**471** (2001) 314

[71] N. C. R. Makins, HERMES *Analysis Boot Camp* (online), unpublished

[72] A. Airapetian *et al.* (HERMES), Phys. Rev. D**71** (2005) 012003

[73] G. D'Agostini, Nucl. Instr. and Meth. A**362** (1995) 487

[74] J. Wendland, *Particle Identification for HERMES Run I*, unpublished (2001)

[75] HERMES Collaboration, publication on g_1 in preparation

[76] M. Contalbrigo, L. De Nardo, M. Ehrenfried, D. Reggiani and C. Riedl, HERMES internal report on g_1 release (September 2004)

[77] I. Akushevich, H. Böttcher and D. Ryckbosch, hep-ph/9906408 (1999)

[78] A. Airapetian *et al.* (HERMES), Phys. Lett. B**475** (2000) 386, and erratum A. Airapetian *et al.*, Phys. Lett. B**567** (2003) 339

[79] B. Adeva *et al.* (SMC), Phys. Rev. D**60** (1999) 072004

[80] I. V. Akushevich and N. M. Shumeiko, J. Phys. G**20** (1994) 513

[81] K. Abe *et al.* (E143), Phys. Rev. D**58** (1998) 112003

[82] P. L. Anthony *et al.* (E155), Phys. Lett. B**463** (1999) 339

[83] S. Kuhn and F. Wesselmann, E155 technical note (1998) 59

[84] F. Wesselmann and S. Kuhn, E155 technical note (1999) 100

[85] A. Miller, *Applying Radiative Corrections to Polarisation Asymmetries for Deeply Inelastic Scattering*, unpublished (2002)

[86] L. Mankiewicz, A. Schäfer and M. Veltri, Comp. Phys. Comm. **71** (1992) 305

[87] R. Brun, R. Hagelberg, M. Hansroul and J. Lassalle, CERN-DD-78-2-REV (1978)

[88] A. Hillenbrand, PhD thesis, FRIEDRICH-ALEXANDER-Universität Erlangen-Nürnberg (2005)

[89] D. Abbott *et al.* (JLAB), Eur. Phys. J. A **7** (2000) 421

[90] S. Stein *et al.*, Phys. Rev. **12** (1975) 1884

[91] L. W. Whitlow *et al.*, Phys. Lett. B**250** (1990) 193

[92] H. Abramowicz and A. Levy, hep-ph/9712415 (1997)

[93] P. Amaudruz *et al.* (NMC), Nucl. Phys. B**371** (1992) 3

[94] B. Adeva *et al.* (SMC), Phys. Rev. D**58** (1998) 112001

[95] I. V. Akushevich, A. Ilyichev, N. Shumeiko, A. Soroko and A. Tolkachev hep-ph/9706516v1 (1997)

[96] M. Contalbrigo, private communication (2004)

[97] M. Ehrenfried, PhD thesis, Friedrich-Alexander-Universität Erlangen-Nürnberg (2005)

[98] C. Weiskopf, PhD thesis, Friedrich-Alexander-Universität Erlangen-Nürnberg, DESY-thesis-2003-039 (2002)

[99] A. Brüll, E. Aschenauer, private communication (2004)

[100] A. Airapetian *et al.* (Hermes), hep-ex/0506018 (submitted to Phys. Rev. Lett.)

[101] C. Riedl, Proceedings of the 16th international spin physics symposium, Trieste 2004, hep-ex/0411087 (2004)

[102] I. N. Bronstein, K. A. Semendjajew, G. Musiol, H. Mühlig, *Taschenbuch der Mathematik*, Verlag Harri Deutsch, Frankfurt am Main, Thun (1997)

[103] L. De Nardo, *On the Propagation of Statistical Errors*, unpublished (2002)

[104] J. Wendland, PhD Thesis, Simon Fraser University Vancouver, DESY-thesis-2003-032 (2003)

[105] U. Elschenbroich, Hermes internal note 02-013 (2002)

Danke! Grazie! Thank you!

Mühsam ernährt sich das Eichhörnchen.
(Volksweisheit)

I thank Klaus Rith for giving me the inspiration for this thesis in the first place and being the guide field afterwards. He taught me to see the crucial point of things.
Without the input and engagement of Elke Aschenauer, I could not have carried out the analysis in the form I did. She always had an open ear for my questions and concerns.
Christoph Weiskopf provided me with the starting point for my analysis and patiently introduced me to programming.
Together with the HERMES inclusive group, I spent numerous fruitful meetings, phone conferences and discussions mainly in our *hot phase* 2004/2005. Thanks and cheers to Marco Contalbrigo, Lara De Nardo, Davide Reggiani and Markus Ehrenfried and thank you Wolf-Dieter Nowak and Helmut Böttcher for supporting discussions! In any case, a special thank goes to Marco who supported me as junior in the b_1-duo.
Uli is another useful and patient source of HERMES analysis knowledge, thanks! And thank you to Delia and Patty for the one or the other discussion. Indeed I like the fact that at HERMES the percentage of women is higher than in average physics.
HERMES is a large collaboration which implies that performing an analysis and writing a thesis about HERMES physics is not possible without *collaboration*. This starts with hardware and does not end with software. I therefore thank the collaboration as a whole. Without computers, nothing would run in our business. This is a trivial statement which is connected to a non-trivial job. I bow to the administrators Martin, Chris and Nils (Erlangen); Larry, Eduard and Alexander K. (Hamburg). I thank Ellen for organizing the "chaos" in Erlangen and Sörne, Sabine and recently Evelyn the one in Hamburg. I enjoyed sharing the office with Christoph, Larry and Marc. Ralf and I took turns not only sharing the office, but also the appartment.
I especially enjoy the giggling phases of Yorck and Matthias and generally the atmosphere when everybody in 1e is crawling out of his/her office and gathering in front of Elke's office to catch the latest gossip. I once more thank Larry for *never* disturbing my biological experiments. Thank you Beni for helping me when I do stupid things and for making me laugh when I feel like banging my head on the table.
Last but not least, indeed many roads seem to lead to Rome (or its vicinity). Thank you Pasquale for guiding me!
We have to accept the fact that the COOKIE MONSTER has not only changed its color from blue to orange but also *is not supposed to eat cookies anymore*! Thank you Markus that you went the way together with me. Inklusive freier Entfaltung und italienischem Superpartner. My hair dryer still remembers its (and my) trip to Zeuthen with you. I hope you (and the other persons on the train) even more enjoyed our recent migrations

as coffee spillers and border crossers to Bavaria.
I thank Achim, Phil, Davide and Markus D.+E. for the experiences we were able to share during the Medizinerpraktikum.
The Hermes family shares a lot of activities, like elastic pool ball scattering (Fridays), (sometimes inelastic) squash ball scattering (Tuesdays) and some Hermes Movie Nights (Wednesdays). On Thursdays, the factorization theorem of high energy physics applies to Hermesians, see figure. The offsite contribution to the cross section can contain an infinite tower of Familieneck operators involving a health-flip amplitude. The bottom right part of the figure indicates that under certain conditions an inter-

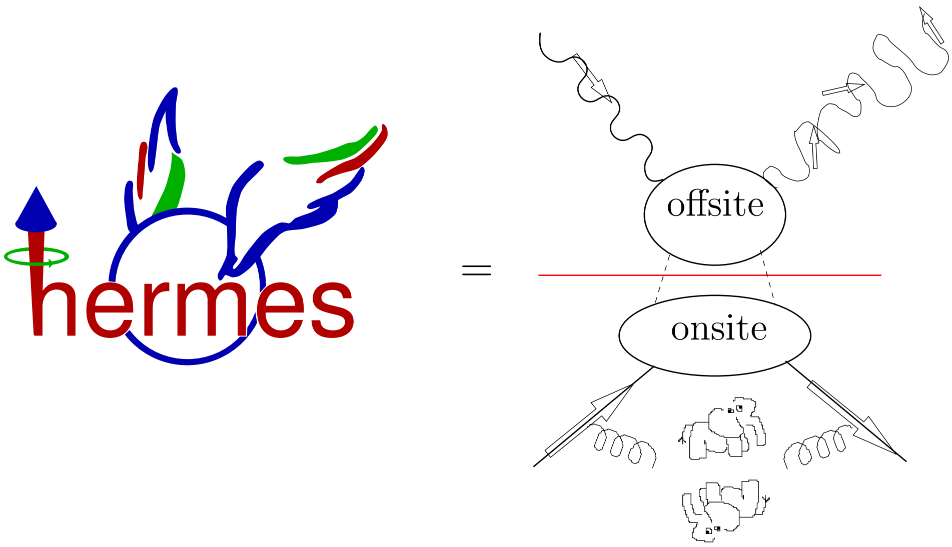

mediate elephant ( ) - anti-elephant ( ) -quark pair can be generated, a process which has been discovered at DESY in September 1999.
Hamburg, Du Elbperle! Zwar bist Du streng in der Zuweisung Deiner Regentage, aber *wenn* Du und Dein Fluß und Dein Hafen prächtig glitzern im Sonnenlicht, dann bist Du unschlagbar.
Aber auch die erste Hälfte meiner Doktorarbeit, die ich in meiner fränggischen Heimat Erlangen am Physikalischen Institut II verbrachte, darf nicht unerwähnt bleiben. In den Kaffeepausen lauschte ich gemeinsam mit den Gruppenmitgliedern Martin, Stefan, Jürgen, Nils, Christian, Rezo, Christoph, Bernhard und manchmal Herrn Steffens den (Inter)Nationalhymnen aus aller Herren Länder und verfolgte atemlos den Ausgang der Bundestagswahlen 2002. Wir verzierten geeignete Oberflächen mit Handtaschendiagrammen und gewannen den inoffiziellen Wettbewerb für die kitschigste Weihnachtsdekoration, worüber sich Rudy, the red nose reindeer, sehr freute. Chris war mir manchmal eine unsagbare Hilfe beim Liefern von für ihn – schwups! – trivialen Algorithmen.
Und schließlich danke ich meiner Familie für jedwede Unterstützung, die mir zugeflossen ist.
Ich widme diese Arbeit allen gequälten Kreaturen. Go vegan!

Curriculum vitae

Persönliche Daten

Name: Caroline Kathrin Riedl

Geburtsdatum: 8. Juli 1977

Geburtsort: Erlangen, Deutschland

Staatsangehörigkeit: deutsch

E-Mail: criedl@mail.desy.de

Ausbildung

1983-1985: Loschge-Grundschule, Erlangen

1985-1987: Grundschule Uttenreuth

1987-1996: Emil-von-Behring-Gymnasium, Spardorf

Juni 1996: Abitur

1996-2001: Friedrich-Alexander-Universität Erlangen-Nürnberg

1998: Vordiplom Physik

Aug.-Sep. 1999: Sommerstudentin am DESY, Hamburg

Apr. 2000-Juli 2001: Diplomarbeit bei Prof. M. Thies am Lehrstuhl für Theoretische Physik III der Friedrich-Alexander-Universität Erlangen-Nürnberg, Betreuung von Theoretika

2001: Diplom Physik

Jan.-März 2002: Praktikum bei der november AG, Erlangen

April 2002-Mai 2005: Doktorarbeit bei Prof. K. Rith am Lehrstuhl für Physik der Friedrich-Alexander-Universität Erlangen-Nürnberg im Rahmen des Hermes-Experiments (sowohl in Erlangen als auch in Hamburg), Betreuung von Praktika und Übungen in Experimentalphysik, Teilnahme an deutschen und internationalen Konferenzen

seit Juni 2005: Wissenschaftliche Mitarbeiterin am Istituto Nazionale di Fisica Nucleare (INFN), Frascati